

Cr(VI) and Cr(III)-Based Conversion Coatings on Zinc

Xiaolong Zhang

Cr(VI) and Cr(III)-Based Conversion Coatings on Zinc

Proefschrift

ter verkrijging van de graad van doctor
aan de Technische Universiteit Delft,
op gezag van de Rector Magnificus prof. dr. ir. J.T. Fokkema,
voorzitter van het College voor Promoties,
in het openbaar te verdedigen
op woensdag 9 februari 2005 om 10.30 uur

door

Xiaolong ZHANG

Master of Science
Hunan University, China
geboren te Hunan, China

Dit proefschrift is goedgekeurd door de promotoren:

Prof. dr. J.H.W. de Wit

Prof. dr. ir. H. Terry

Samenstelling promotiecommissie:

Rector Magnificus	voorzitter
Prof. dr. J.H.W. de Wit	Technische Universiteit Delft, promotor
Prof. dr. ir. H. Terry	Vrije Universiteit Brussel, promotor
Prof. dr. P.L. Bonora	Università degli Studi di Trento, Italië
Prof. dr. R. van der Linde	Technische Universiteit Eindhoven
Prof. dr. R. Boom	Technische Universiteit Delft
Dr. A. Hovestad	TNO Eindhoven
Dr. C. Van den Bos	Technische Universiteit Delft
Prof. ir. L. Katgerman	Technische Universiteit Delft, reservelid

This research was carried out under the project number IZW98102 in the framework of the Innovation Research Program for Environmental Technology/Heavy Metals in The Netherlands.

Printed by Pasmans Offsetdrukkerij, Den Haag

ISBN 90-9019089-9

Keywords: chromium, conversion coating, corrosion, zinc

Copyright © 2005 by Xiaolong Zhang

All rights reserved.

Email: info@library.tudelft.nl

Printed in The Netherlands

Contents

Chapter 1 Introduction

1.1	Background	1
1.2	Research aim	2
1.3	Research approach	2
	References	4

Chapter 2 Literature survey: Corrosion of zinc

2.1	Introduction	7
2.2	Physical natures	8
2.3	Corrosion of zinc in atmosphere	9
2.4	Corrosion of zinc in aqueous environment	10
2.5	Summary	15
	References	16

Chapter 3 Literature survey: Conversion coatings

3.1	Introduction	17
3.2	Formation of chromate conversion coatings	18
3.3	Properties of chromate conversion coatings	23
3.4	Protective mechanism of chromate coatings	28
3.5	Alternatives to chromates	30
3.5.1	Phosphate	30
3.5.2	Molybdate	31
3.5.3	Permanganate	32
3.5.4	Tungstate	34
3.5.5	Cerium compounds	34
3.5.6	Trivalent chromium	36
3.5.7	Silanes	37
3.5.8	Miscellaneous	38
3.6	Conclusions	39
	References	40

Chapter 4 Physical characterization of Cr(VI)-based conversion coatings

4.1	Introduction	43
4.2	Sample preparation	43
4.3	Morphology of the coatings	44
4.4	Determination of coating thickness	46
4.4.1	Spectroscopic ellipsometry (SE)	46
4.4.2	Thickness of conversion coatings	47
4.5	AES analysis	52
4.5.1	Auger effects	52
4.5.2	Auger depth profiles of conversion coatings	54
4.6	XPS analysis	56

4.6.1	Basic principle of XPS	56
4.6.2	XPS analysis of Cr(VI)-based conversion coatings	57
4.6.3	Photo-reduction of Cr(VI) species	63
4.6.4	Chromate layer after exposure to NaCl solution	65
4.7	FTIR analysis	66
4.8	Discussion	68
4.9	Conclusions	70
	References	71

Chapter 5 Electrochemical characterization of Cr(VI)-based conversion coatings

5.1	Introduction	73
5.2	Experimental	74
5.2.1	Open circuit potential and polarization measurements	74
5.2.2	Impedance measurements	74
5.2.3	Determination of corrosion rate	74
5.3	Results and discussion	81
5.3.1	Polarization measurements	81
5.3.2	Impedance measurements	85
5.4	Conclusions	102
	References	103

Chapter 6 Heat effect on corrosion performance of Cr(VI)-based conversion coatings

6.1	Introduction	105
6.2	Experimental	106
6.2.1	Sample preparation	106
6.2.2	Morphology of the chromate coatings	108
6.2.3	FTIR and XPS analyses	108
6.2.4	Open circuit potential and polarization measurements	109
6.2.5	Impedance measurements	109
6.3	Results	110
6.3.1	Heat effect on morphology of Cr(VI)-based conversion coatings	110
6.3.2	Thermal reduction of Cr(VI) species in the coatings	116
6.3.3	Open circuit potential	120
6.3.4	Polarization curves	121
6.3.5	Impedance measurements	125
6.4	Discussion	133
6.5	Conclusions	136
	References	137

Chapter 7 Investigation of Cr(VI) and Cr(III)-based conversion coatings on zinc using SKP and SKPFM

7.1	Introduction	139
7.2	Principles of Kelvin probe and Scanning Kelvin probe force microscopy	140
7.2.1	Kelvin probe technique	140
7.2.2	Scanning Kelvin probe force microscopy	142
7.3	Experimental methods	144

7.3.1	Sample preparation	144
7.3.2	Kelvin probe measurements	144
7.3.3	Scanning Kelvin probe force microscopy measurements	145
7.4	Results and discussion	145
7.4.1	Cr(VI) treated zinc	145
7.4.2	Cr(III)-A treated zinc	150
7.4.3	Open circuit potential	153
7.5	Conclusions	156
	References	157

Chapter 8 Physical and electrochemical characterization of Cr(III)-based conversion coatings

8.1	Introduction	159
8.2	Experimental	160
8.2.1	Materials	160
8.2.2	Cr(VI) and Cr(III) treatments	160
8.2.3	Analysis of morphology and thickness of the coatings	161
8.2.4	Composition analysis of the coatings	162
8.2.5	Open circuit potential and polarization measurements	162
8.2.6	Impedance measurements	163
8.3	Results	163
8.3.1	Morphology of the coatings	163
8.3.2	Thickness of the coatings	165
8.3.3	Composition of the coatings	168
8.3.4	Corrosion resistance of the Cr(VI) and the Cr(III)-A coated zinc discs	173
8.3.5	Corrosion inhibition through the reduction of Cr(VI) in the solution	183
8.3.6	Corrosion resistance of the Cr(VI), the Cr(III)-A and the Cr(III)-B coated EG steel	187
8.4	Discussion	195
8.5	Conclusions	197
	References	199

Chapter 9 Salt spray testing of Cr(VI) and Cr(III) treated zinc

9.1	Introduction	201
9.2	Experimental	201
9.3	Results and discussion	203
9.4	Conclusions	208
	References	208

Chapter 10 General discussion

10.1	The corrosion of zinc	209
10.2	Inhibition effect of Cr(III) and Cr(VI)-based conversion coatings	210
10.3	Topics for future research	213
	References	216

	Summary	217
--	----------------	-----

Samenvatting	221
Publications	225
Acknowledgements	227
Curriculum vitae	231

Chapter 1

Introduction

1.1 Background

Zinc is widely used in the building and coating industry. Zinc coating is regarded as one of the most economical and effective means of protecting carbon steel against corrosion [1]. Zinc coatings offer protection to steel by two mechanisms [2]. First, zinc is more corrosion resistant than steel in most natural atmospheres, because zinc oxidizes easily in air to form a corrosion resistant film of zinc oxide. The zinc oxide layer becomes zinc hydroxide when it is exposed to moisture or rainfall. During drying, the zinc hydroxide reacts with carbon dioxide in the atmosphere and is converted into a thin, compact and adherent layer, basic carbonate, which provides barrier protection. Second, zinc coatings provide galvanic protection to exposed steel because zinc is anodic with respect to iron. When zinc-coated surfaces are subjected to mechanical damage so that the steel is exposed to corrosion agents, zinc is slowly corroded, while steel is protected.

With the increasing demands for corrosion resistance from industry, additional treatments on zinc coatings are required [3]. One of these processes is conversion coating, which provides more corrosion resistance and increases the adhesion between primer coatings and metal substrates [4]. Among the used conversion coatings, chromate conversion coating (CCC) is the best in increasing the corrosion resistance of metals [5,6]. Chromate film forms easily on zinc and its alloys, because chromates are very powerful oxidizing agents which react fast with zinc, and there is a large difference in the solubility of Cr(VI) and Cr(III) ions in aqueous media. Cr(III) oxides/hydroxides in the film act as protective barrier while hexavalent chromium adsorbed in the film can provide active protection, “repairing” wherever the layer gets damaged [7]. However, hexavalent chromium compounds are classed as carcinogenic [8,9]. In European countries, the use of hexavalent chromium will be forbidden in protective coatings in the vehicle industry from 1st July 2007 [10]. Therefore, extensive investigations have

been done to understand the protective mechanism of the CCC and to find alternatives for chromate conversion coatings [11-15].

1.2 Research aim

The main objective of this work is to gain a better understanding of the formation and degradation of chromate conversion coatings (CCCs) on zinc. An understanding of the protective mechanism of chromate conversion coatings will be useful in the development of alternative conversion treatment processes. Cr(III)-based treatment of zinc is investigated to determine if this type of treatment could be an alternative to hexavalent chromium treatments.

1.3 Research approach

Pure zinc (99.95%) sheets or discs and electrodeposited zinc on carbon steel are used as substrates in this research. A conversion coating generated in a Cr(VI)-containing bath is named as “Cr(VI)-based coating” or simply “Cr(VI) coating”, in order to distinguish it from the conversion coating generated in a trivalent chromium bath (named as “Cr(III)-based coating” or “Cr(III) coating”). The physical nature and the corrosion properties of Cr(VI) coatings on zinc with different dipping times are investigated to see how the conversion coatings are built and how these coatings affect performance. The effect of heat on the corrosion performance of the Cr(VI) coatings is investigated to see how the drying temperature affects the structure and the role of the Cr(VI) compounds in the coatings. A comparison of the morphology, composition and corrosion performance of Cr(VI) and Cr(III) coatings is made to understand the roles that the Cr(VI) and the Cr(III) play in the coatings.

Fig. 1.1 shows the contents of this thesis schematically. In chapters 2 and 3, literature surveys of zinc corrosion and conversion coatings are made respectively.

In chapter 4, the morphology, the thickness, and the compositions of the Cr(VI)-based coatings on zinc after different dipping times are studied using scanning electron

microscopy (SEM), spectroscopic ellipsometry (SE)[16,17], Auger electron spectroscopy (AES), X-ray photoelectron spectroscopy (XPS), and Fourier transform infrared spectroscopy (FTIR). The chemical states of chromium in the conversion coatings before and after immersion in 0.01 M NaCl solution are analyzed by means of XPS.

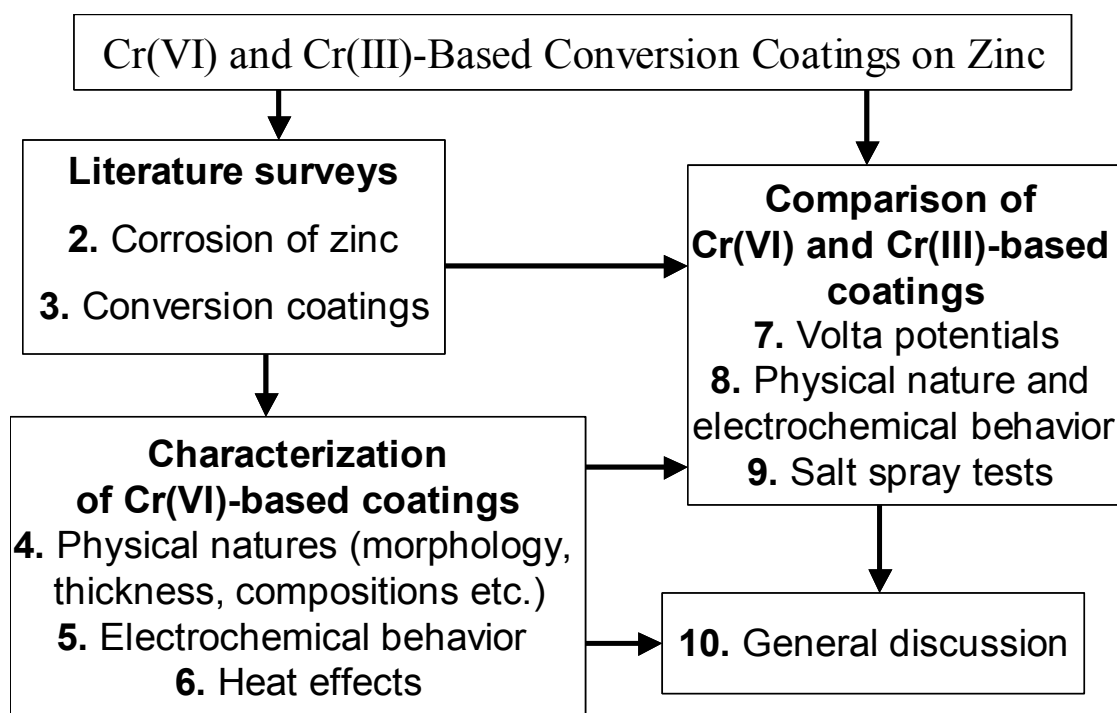


Fig. 1.1 Schematic illustration of contents of the thesis.

In chapter 5, the corrosion behavior of untreated and Cr(VI) treated zinc (with different dipping times) is studied using polarization and electrochemical impedance spectroscopy (EIS) measurements. Modeling of the impedance response for bare zinc and Cr(VI) treated zinc in 0.01 M NaCl solution is discussed.

It was reported many years ago that the drying operation performed after the chromating process can degrade the coating[18], but the mechanism is not fully understood. In chapter 6, the influence of the drying temperature on the corrosion performance of Cr(VI) and Cr(III)-based conversion coatings on galvanized steel and on pure zinc sheets are investigated. A possible mechanism for the degradation of the conversion coatings during heating is discussed.

In an atmospheric environment, a thin water layer is often present on the metal surface. This water layer is thin, so it is difficult to use conventional electrochemical techniques to study atmospheric corrosion. It has been reported that the Volta potential is correlated to the corrosion potential of a metal [19,20]. So, in chapter 7, Cr(VI) and Cr(III)-A coatings on zinc are studied using a scanning Kelvin probe (SKP) and a scanning Kelvin probe force microscopy (SKPFM). A boundary between the Cr(VI) or Cr(III)-A treated zinc and untreated zinc was made by treating only half of the zinc surface. The Volta potential across the boundary between untreated and treated zinc areas was scanned using a Kelvin probe in a humid chamber and using SKPFM in air.

In chapter 8, the nature and corrosion properties of Cr(III) coatings on pure zinc discs and on electro-galvanized (EG) steel sheets are studied and compared with Cr(VI) coatings. The inhibition of zinc corrosion in solutions containing Cl^- by Cr(VI) and Cr(III) are discussed.

In chapter 9, the corrosion resistance of Cr(VI) and Cr(III)-treated zinc has been compared using salt spray test following the standardized DIN 50021 protocol. In chapter 10, a general discussion about the corrosion of zinc and the role of Cr(VI) and Cr(III) species in conversion coatings is given, and topics for future research are suggested.

References

1. D. C. H. Nevison, in: *ASM Handbook*, 9th ed., ASM International, Materials Park, Ohio, 1987, Vol. 13, p. 755-769.
2. X. G. Zhang, *Corrosion and Electrochemistry of Zinc*, (Plenum Press, New York, 1996).
3. P. McCluskey, *Trans IMF*, 74 (1996) 119.
4. T. Biestek and J. Weber, *Conversion Coatings*, (Portcullis Press Ltd., Redhill, 1976).
5. G. D. Wilcox and J. A. Wharton, *Trans IMF*, 75 (1997) B140-B142.
6. P. C. Wynn and C. V. Bishop, *Trans IMF*, 79 (2001) B27-B30.

7. D. Gilroy, P. J. Eddowes, I. M. Dalrymple, V. Madina, F. Seco, A. del Barrio, J. Parkes, M. Byrne, R. Byrne and E. M. Almeida, *Metal Finishing*, 94 (1996) 14.
8. K. A. Korinek, in: *ASM Handbook*, ASM International, 1987, Vol. 13, p. 389-395.
9. P. L. Hagans, in: *ASM Handbook*, ASM International, 1994, Vol. 5, p. 405-411.
10. Official Journal of the European Communities, L 170, 29.6.2002 (2002) 81.
11. M. Kendig and S. Jeanjaquet, *J. Electrochem. Soc.*, 149 (2002) B47-B51.
12. G. O. Ilevbare and J. R. Scully, *J. Electrochem. Soc.*, 148 (2001) B196-B207.
13. G. Goeminne, H. Terryn, A. Hubin and J. Vereecken, *Electrochim. Acta*, 47 (2002) 1925.
14. P. Campestrini, *Microstructure-related Quality of Conversion Coatings on Aluminium Alloys*, thesis, Delft University of Technology, The Netherlands, 2002.
15. P. Campestrini, G. Goeminne, H. Terryn, J. Vereecken and J. H. W. de Wit, *J. Electrochem. Soc.*, 151 (2004) B59-B70.
16. P. Campestrini, S. Bohm, T. Schram, H. Terryn and J. H. W. de Wit, *Thin Solid Film*, 410 (2002) 76.
17. T. Schram, J. De Laet and H. Terryn, *Thin Solid Film*, 313-314 (1998) 727.
18. A. Gallaccio, F. Pearlstein and M. R. D'Ambrosio, *Metal Finishing*, (1966) 50, 57.
19. M. Stratmann and H. Streckel, *Corros. Sci.*, 30 (1990) 681.
20. P. Schmutz and G. S. Frankel, *J. Electrochem. Soc.*, 145 (1998) 2285.

Chapter 2

Literature survey: Corrosion of Zinc

2.1 Introduction

Each year, over 40 million tonnes of steel are coated with zinc or zinc alloys and more than 2.2 million tonnes of zinc are used worldwide for coatings [1]. In western countries, about 37% zinc is used as coating. The adherent coatings of zinc on iron have many times the corrosion resistance of the carbon steel. For example, the corrosion rate of zinc is about 1/25 that of carbon steel in seacoast atmosphere [2]. As zinc is electronegative to iron, it supplies galvanic protection to the exposed steel. Zinc coating can be performed by various methods such as hot dipping, electroplating, spraying, mechanical coating and sherardizing.

Hot dip galvanizing has a number of advantages, including the ability to coat recessed areas with a standard minimum coating thickness, good resistance to mechanical damage and to corrosion in a number of environments, attributed to the zinc-iron alloys metallurgically bounded to the steel. The limiting factors of this process are that coating has to be performed at a reasonably high temperature (to melt zinc and alloy elements) and the steel must not undergo undesirable property changes during the coating process.

Electroplating offers special advantages: it can be done at room temperature, the plating duration can be adjusted to obtain desired thickness, and coatings are adequately uniform. Various electroplating baths based on zinc sulfate (pH 1.5-5.5), zinc chloride (pH 4.0-5.5), zinc fluoroborate (pH 1.5-3.5), zinc pyrophosphate (pH 7-10), alkaline as well as cyanide can be used to produce dull or bright coatings. However, electroplating cannot be competitive in price with hot dip galvanizing for thickness greater than about 15 - 20 μm due to the high costs of the electroplating process.

Zinc alloy coatings, such as Galfan (Zn-5% Al) and Galvalume (Zn-55% Al-1.5% Si), have been widely adopted for the continuous coating of steel sheet and wire [1]. Alloys of zinc with iron are not only an inherent part of the hot dip galvanized coating, but also developed for the electroplating. This kind of zinc alloy coating is particularly easy to paint. Zinc-Nickel (up to 14%) alloy coatings have also been developed for the continuous electroplating industry. Other additions such as cobalt and chromium (in a smaller quantity) have been developed for electroplating strip or products. For hot dip galvanizing, some elements are added in very small amount to develop special properties or to assist in processing. For example, lead, tin and antimony can be added to lower the surface tension; titanium and zirconium can be added to act as refiners; nickel and vanadium are suitable for controlling the reaction of semi-killed steels with molten zinc [1].

In order to simplify the study systems, this thesis is mainly focused on the pure zinc substrate. Electro-deposited zinc on low carbon steel, as substrate to be treated with a chromium based solution, will be also studied. In order to study the mechanism by which chromium-based conversion coating protects zinc, understanding of the basic nature and corrosion properties of zinc is necessary. In the following sections, the physical natures and basic corrosion properties of zinc under ambient and aqueous conditions are described.

2.2 Physical natures

Zinc is a bluish-white, lustrous metal with a relatively low melting point (419.5°C) and boiling point (907°C). Zinc crystals have a close-packed hexagonal structure. The lattice constants a and c are 0.2664 and 0.4947 nm, respectively [3]. Every zinc atom has 12 near neighbors. Among them, 6 are at a distance of 0.2664 nm and the other 6 are at 0.2907 nm. The bonds between the atoms in the hexagonal basal layer are stronger than those between the layers. This accounts for the deformation behavior and anisotropy of the zinc crystals. Zinc has low creep resistance due to grain boundary migration. It is brittle at ambient temperatures but is malleable at 100 to 150°C. It is a reasonable conductor of electricity. Its density is 7.14 g/cm³ at room temperature.

The use of zinc in engineering applications is restricted by its mediocre physical properties, but it is used extensively in alloys [4]. For example, it forms a series of excellent die-casting alloys with aluminum (4 %). The addition of up to 45 % of zinc to copper forms the long-established series of brass alloys. Zn-Fe alloy is the basis of the corrosion protection of steel by galvanizing.

2.3 Corrosion of zinc in atmosphere

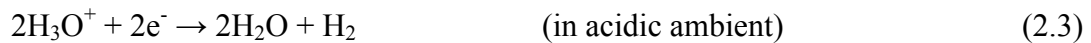
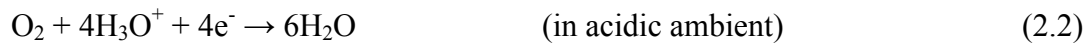
The atmospheric corrosion of zinc is influenced by the environmental conditions, such as humidity, temperature, air pollutants, rainfall, wind, and solar radiation. The influence of these factors on the corrosion of zinc is related to their effect on the initiation and growth of protective films.

In a relative dry ambient, zinc corrodes slowly at room temperature with the formation of ZnO. Zinc oxide is an n-type semiconductor with a band-gap of 3.2 eV[5].

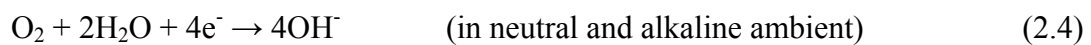
In a more humid environment, water layers adsorbed on the zinc surface provide a medium for the mobilization of zinc ions. A thin film of zinc hydroxide forms rapidly on zinc surface. The zinc corrosion in a humid environment can be described as[6]



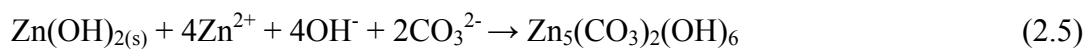
which is balanced by



and/or



Zinc hydroxide reacts further with carbon dioxide dissolved in the adsorbed water, which forms the relatively less soluble basic zinc carbonate. Zinc hydroxide combines with zinc carbonate to form hydrozincite $[\text{Zn}_5(\text{CO}_3)_2(\text{OH})_6]$ [6]:



Hydrozincite is a metastable product. Under continuous exposure to different environments, the corrosion products can be transformed to different compounds, such as zinc hydroxysulfate $[\text{Zn}_4\text{SO}_4(\text{OH})_6 \cdot n\text{H}_2\text{O}]$ in the rural atmosphere, zinc chlorohydroxysulfate $[\text{NaZn}_4\text{Cl}(\text{OH})_6\text{SO}_4 \cdot 6\text{H}_2\text{O}]$ in the marine atmosphere, and another zinc chlorohydroxysulfate $[\text{Zn}_4\text{Cl}_2(\text{OH})_4\text{SO}_4 \cdot 5\text{H}_2\text{O}]$ in urban and industrial atmospheres[7].

The amount of water adsorbed onto a zinc surface varies with relative humidity (RH) and with temperature. At temperatures 0 - 20°C, about 10 monolayers of water is present on the zinc surface at 93% RH. The amount of surface water decreases as temperature increases from 0 to 80°C. It was reported that the highest average corrosion rate of zinc is at about -2°C in moist oxygenated atmospheres (RH > 80%)[8]. This occurs because in the adsorbed layer the adsorbed water suffers depression of the freezing point and remains liquid at temperatures below 0°C. The corrosion rate of zinc in the region of positive temperatures is determined by the thickness of the adsorbed water layer, and in the region of negative temperatures, the surface reactions are retarded with decrease of temperatures.

Zinc is lost from the corrosion layer by dissolution of the zinc salts in rain, followed by washing from the surface. An enhanced process occurs in urban or industrial environment where atmospheric concentration of sulfur compounds is high.

2.4 Corrosion of zinc in aqueous environment

Zinc is divalent in all its compounds. The standard potential value of the zinc electrode is -0.763 V_{SHE}, slightly lower than the standard potential of iron (-0.401 V_{SHE}, Fe-Fe²⁺) [5]. The potential-pH equilibrium diagram for the zinc-water system at 25 °C is shown in Fig. 2.1 [9]. Zinc is thermodynamically unstable in water and aqueous

solutions. When zinc is exposed to water, positively charged zinc ions go into solution and the reduction of dissolved oxygen occurs at the zinc surface. Once the dissolved oxygen has become depleted, or there is insufficient diffusion of oxygen to support the cathodic reaction, hydrogen evolution will be the dominated cathodic reaction:



In stagnant water, zinc may be attacked rapidly at local areas, since the oxygen in a near region of zinc surface is consumed in the corrosion process and an oxygen concentration cell may form locally. As more oxygen is made available, the corrosion becomes more uniform [2].

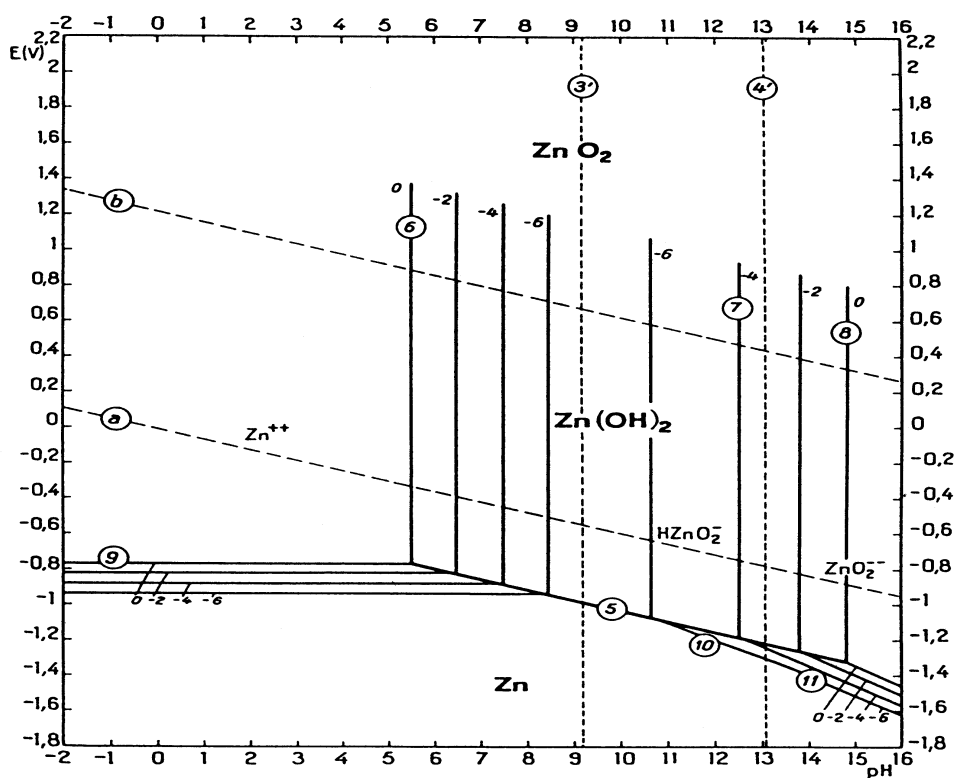
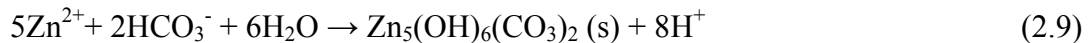
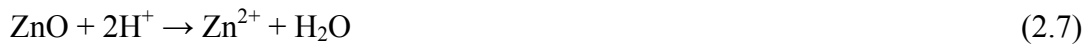


Fig. 2.1 Potential-pH equilibrium diagram for the system zinc-water, at 25°C. Source: Ref. [9]

However, from Potential-pH equilibrium diagram in Fig. 2.1, in solutions of pH between approximately 8.5 and 10.5, zinc may form a hydroxide film on the surface. This film has the effect of inhibiting zinc dissolution. The stability of zinc oxides and hydroxides in aqueous solutions depends on pH. Zinc oxides and hydroxides are amphoteric. They dissolve in acid solutions as Zn^{2+} and in alkaline solutions as zincate ions $HZnO^-$ and ZnO^{2-} . At room temperature, ϵ - $Zn(OH)_2$ is the most stable compound whereas amorphous $Zn(OH)_2$ is the most unstable. Galvanized surfaces have a good tolerance to various chemicals within pH 4 to 12.5 (see Fig. 2.2) [10].

Furthermore, zinc can form insoluble compounds with some chemicals such as carbonate and sulfate. Zinc carbonate is of particular importance because it has been found to be responsible for the high corrosion resistance of zinc in atmospheric environments. The formation of zinc carbonate can occur in solutions containing carbonates and bicarbonates according to the following reactions [11]:



The pH-potential diagram for the zinc-water-carbonate system is shown in Fig. 2.3 [11]. In the presence of carbonate and bicarbonate the possible zinc passivation region extends to near neutral pH values.

In a solution containing chloride, zinc chloro-hydroxo complexes can be formed by the following reaction:



This corrosion product has been found on an electro-galvanized (EG) steel sample after exposure to 0.6 M NaCl solution for 24 hours [12]. Simonkolleite, $\text{ZnCl}_2 \cdot 4\text{Zn}(\text{OH})_2 \cdot \text{H}_2\text{O}$, has been identified by means of X-ray diffraction (XRD) (see Fig. 2.4). This corrosion product was also observed by other authors [13,14].

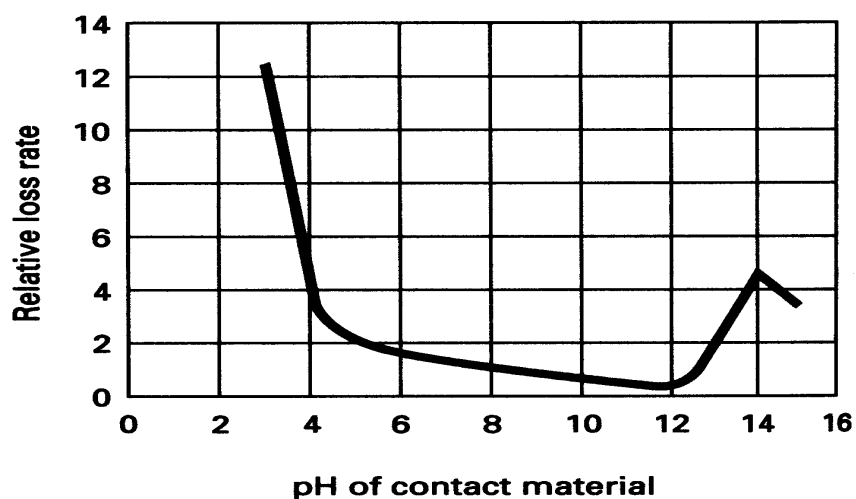


Fig. 2.2 Effect of pH on corrosion of zinc. Source: Ref. [10]

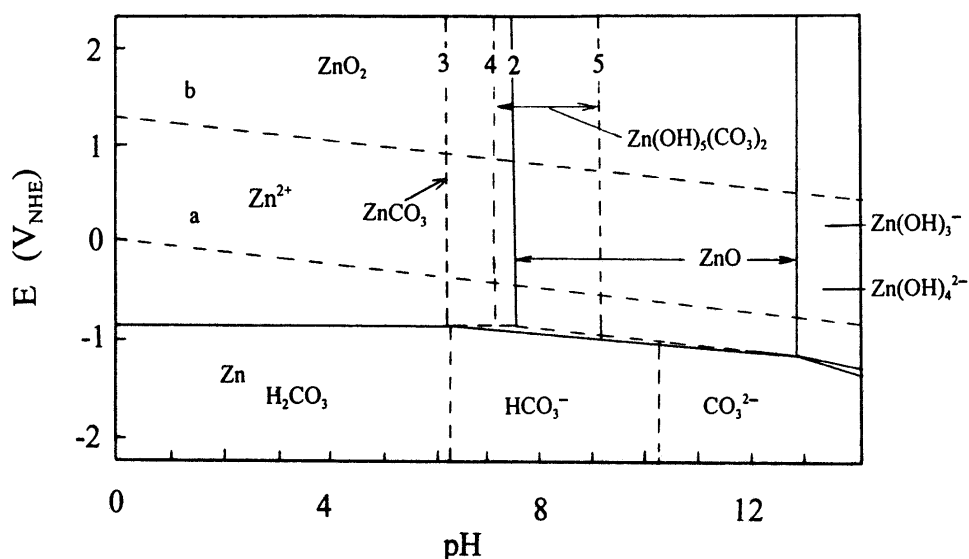
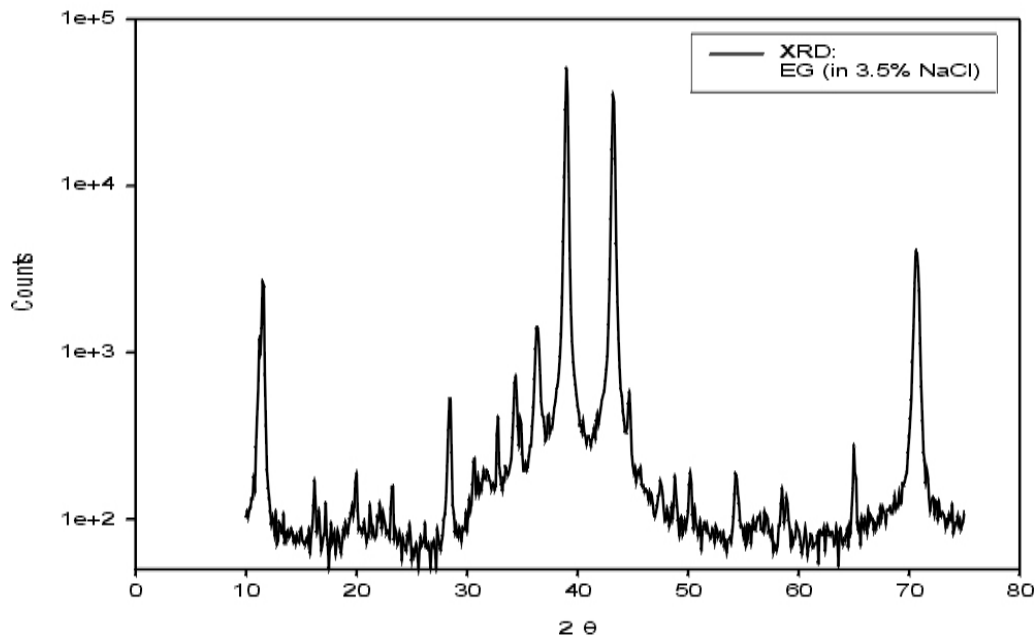


Fig. 2.3 Potential –pH diagram for the zinc-carbonate-water system at 25°C. $a_{\text{Zn}} = 10^{-4}$ mol/dm³ (dissolved zinc species); $a_{\text{c}} = 10^{-2}$ mol/dm³ (dissolved carbonate species). Source: Ref. [11]



Data observed	$\text{Zn}_5(\text{OH})_8\text{Cl}_2 \cdot \text{H}_2\text{O}$, Simonkolleite no. 7-155, JCPDS-ICDD, 1997		
2θ	2θ	Intensity	hkl
11.5	11.243	100	003
16.6	16.570	20	101
20.0		not attributed	
22.1	22.112	20	104
24.8	24.871	25	015
28.5	28.150	35	110
30.7	30.403	30	113
32.8	32.868	55	021
34.4	34.482	20	018
36.4	36.373	10	116
	(36.328)	(Zn 53)	(002)
39.0	(39.026)	(Zn 40)	(100)
43.2	(43.269)	(Zn 100)	(101)
44.7	44.801	20	119
	(44.712)	(Fe 100)	(110)
47.5	47.876	8	125
50.2	49.829	4	300
54.3	(54.384)	(Zn 28)	(102)
58.5	58.207	35	220
65.1	(65.082)	(Fe 20)	(200)
70.7	(70.728)	(Zn 21)	(110)

Fig. 2.4 XRD spectra from an electro-galvanized steel exposed to 0.6 M NaCl solution for 24 h. Ref. [12,15]

The environment temperature has also an effect on the corrosion rate of zinc. It is reported that a corrosion peak at approximately 65°C occurs both in waters under a pure oxygen atmosphere and under a CO₂-free air atmosphere (see Fig. 2.5) [16]. Electrochemical measurements showed that in many cases zinc was anodic to iron at temperatures below 60°C, but iron was anodic to zinc at 77°C.

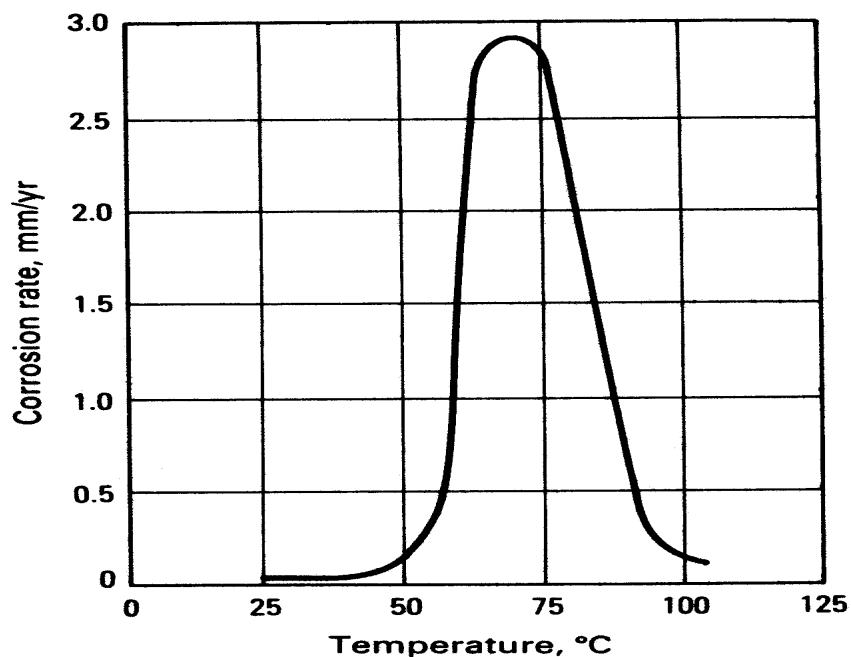


Fig. 2.5 Effect of temperature on corrosion of zinc in distilled water. Source: Ref. [16]

2.5 Summary

Zinc is widely used as a coating to protect carbon steel against corrosion. Zinc corrodes slower than steel in most atmospheric environments, since zinc carbonate formed on the zinc surface in air is very protective. The zinc electrode has a standard potential value of $-0.763 V_{SHE}$, which is more negative than that for iron. Zinc can provide sacrificial or cathodic protection to carbon steel when the zinc coating is broken and the steel is exposed to a humid environment.

Zinc may form a hydroxide film on the surface in solutions of pH between approximately 8.5 and 10.5. In the presence of carbonate and bicarbonate the possible

zinc passivation region extends to near neutral pH values. The corrosion product for zinc in NaCl solution is $ZnCl_2 \cdot 4Zn(OH)_2 \cdot H_2O$. Galvanized surfaces have a good tolerance to various chemicals within pH 4 to 12.5.

References

1. F. C. Porter, A. M. Stoneman and R. G. Thilthorpe, *Trans IMF*, 66 (1988) 28.
2. D. C. H. Nevison, in: *ASM Handbook*, 9th ed., ASM International, Materials Park, Ohio, 1987, Vol. 13, p. 755-769.
3. X. G. Zhang, *Corrosion and Electrochemistry of Zinc*, (Plenum Press, New York, 1996).
4. S. W. K. Morgan, *Zinc and Its Alloys and Compounds*, (Ellis Horwood Limited, Chichester, 1985).
5. *Handbook of Chemistry and Physics*, 56 ed., (CRC Press, Inc., USA, 1975).
6. T. E. Graedel, *J. Electrochem. Soc.*, 136 (1989) 193c.
7. I. Odnevall and C. Leygraf, *Corros. Sci.*, 36 (1994) 1551.
8. P. V. Strekalov, V. V. Agafonov and Yu. N. Mikhailovskii, *Prot. Met.*, 8 (1972) 521.
9. M. Pourbaix, *Atlas of Electrochemical Equilibria in Aqueous Solutions*, 2nd ed., (National Association of Corrosion Engineers, Houston, 1974).
10. D. Wetzel, in: *ASM Handbook*, ASM International, 1994, Chap. 5, p. 360-371.
11. D. C. W. Kannangara and B. E. Conway, *J. Electrochem. Soc.*, 134 (1987) 894.
12. X. Zhang, S. Bohm, A. J. Bosch, E. P. M. van Westing and J. H. W. de Wit, in: *Eurocorr 2001*, 30 Sept. - 4 Oct., paper No. 193 (European Federation of Corrosion, Riva del Garda, Italy, 2001).
13. C. Pérez, A. Collazo, M. Izquierdo, P. Merino and X. R. Nóvoa, *Corrosion*, 56 (2000) 1220.
14. N. R. Short, A. Abibsi and J. K. Dennis, *Trans IMF*, 67 (1989) 73.
15. M. King, W. F. McClune, L. C. Andrews and M. A. Holomany, *Powder Diffraction File*, (International Centre for Diffraction Data, USA, 1992).
16. H. Grubitsch and O. Illi, *Korros. Metall.*, 16 (1940) 197.

Chapter 3

Literature survey: Conversion Coatings

3.1 Introduction

Generally, a conversion coating process is an artificially induced and controlled corrosion process yielding on the metal surface a layer firmly bonded to the basis metal, practically insoluble in water or a given medium, and having electrical insulating properties [1]. Surface conversion treatments consist of chemical conversion, obtained by dipping, spraying, brushing or swabbing without the use of external current, and anodic conversion that occurs when the part is made the anode in an electrolytic cell. Depending on the treatment selected, conversion coatings can be used to: 1) promote paint bonding; 2) provide a decorative surface; 3) provide a protective barrier against corrosion; and 4) serve as an absorptive carrier for lubricants [2]. Traditional conversion coatings are mainly chromates, phosphates and oxides, or combinations of these.

Chromate conversion coatings became popular during World War II for protecting zinc and cadmium plated articles in tropical environments. Since then they have been widely used in commercial metal finishing. Hexavalent chromium or chromate is currently the most effective way to inhibit corrosion of metals. However, the use of chromates and other chromium containing compounds has been limited since 1982 due to their carcinogenic effects [3,4]. Recently, much interest has been focused on developing new technology concerning the formulation and application of the conversion coatings. Among the most promising candidates being investigated as active inhibitors are phosphates, molybdates, permanganates and tungstates. Treatments based on cerium, zirconium compounds, Cr(III) treatments and silane/polymer are also considered. In this chapter, a literature survey on the formation and properties of chromate conversion coatings and some potential alternatives are presented.

3.2 Formation of chromate conversion coatings

Chromates may take part in a number of complex reactions, particularly in the presence of certain additives, giving deposits of mixed compounds including ions of the treated metal.

1) Chromates, being strongly oxidizing agents in acidic solutions, may promote the formation of insoluble salts on the metal surface or increase the thickness of natural oxide films.

2) Reduction products of chromic acid are usually insoluble, as for example chromium sesqui-oxide Cr_2O_3 or hydroxide $\text{Cr}(\text{OH})_3$.

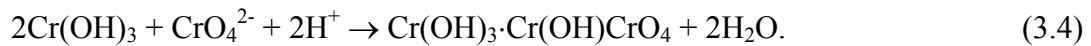
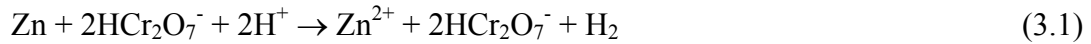
3) Metal chromates are often insoluble (for example ZnCrO_4).

In principle, the most frequently applied chromating method consisting of a simple immersion process does not differ in operation from the electrochemical treatment. In both cases the general processing cycle is as follows[1]:

- a) surface preparation (cleaning, degreasing),
- b) rinsing in water,
- c) immersion in a chromating bath,
- d) rinsing in running water,
- e) brightening or dyeing the produced coating(if required),
- f) rinsing in running water,
- g) drying,
- h) application of additional protective film (grease) or paint.

The formation of chromate coating involves oxidation of the metal surface in the chromating solution with simultaneous transition of the basis metal ions to the solution and reduction of hexavalent chromium to the trivalent state. Dissolution of the metal substrate produces electrons that are consumed by cathodic reactions. The cathodic reactions consume protons, leading an increase of local pH at the metal solution interface up to a value at which trivalent chromium precipitates in the form of gelatinous chromium hydroxide. Certain amounts of hexavalent chromium from the solution and compounds formed like zinc chromate are occluded in the gel.

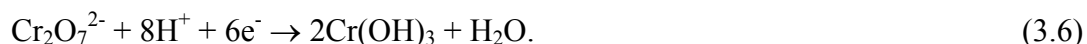
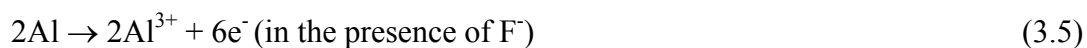
Roper [5] reported that films formed from the acidified dichromate solution of the Cronak type consist of basic chromium chromate formed in accordance with the following processes:



The adsorptive nature of such coatings is so strong that a proportion of soluble Cr^{6+} is likely retained even after the rinsing and drying procedure. This quantity is likely to be related to the chromium concentration in the processing solution.

In practice, the chromating bath contains a hexavalent chromium compound and one or more activators. Williams reported that the mechanism of formation of chromate conversion coatings on zinc is known to depend on the anions added to the acidic dichromate solution [6]. Sulfate, chloride, nitrate and fluoride are typical of those anions used in various solutions for the chromating of zinc. Thin films are formed in pure chromic solutions, while the formation of iridescent films requires the presence of anions such as sulfate or chloride. Fluoride is used for blue bright films, whilst nitrate has little effect on the chromating reaction. On additions of larger concentrations of sulfate, a maximum film weight is achieved, after which further additions of sulfate result in a thinner film. Chloride ions additions do not result in a similar maximum. Fluoride additions to the chromic acid solution also activate the zinc dissolution, but result in a relatively thin clear film. Anions such as sulfate, chloride and dichromate can adsorb on the chromium hydroxides, resulting in their incorporation in the film. The reason for the activation by the anions, which are not directly involved in the electron transfer reaction, has not been fully explained [7].

For chromating Al and Al alloys, fluorides are usually added in the bath as activators. The oxidation of aluminum in the presence of the complexing F^- produces electrons to reduce the hexavalent Cr of the dichromate ion ($\text{Cr}_2\text{O}_7^{2-}$) and form a protective hydrated 3-valent $\text{Cr}(\text{OH})_3$ film[8]:



The coating formation involves hydrolysis, polymerization, and condensation of Cr(III) (see Fig. 3.1 a)[9-11]. This process produces a chromium hydroxide polymer “backbone”, which has edge- and corner-sharing Cr(III) octahedral units. The adsorption of Cr(VI) oxo-anions to the solid Cr(III) hydroxide forms a reversible Cr(III)-O-Cr(VI) mixed oxide (see Fig. 3.1 b) [11].

The parameters that affect the properties of chromate films formed by solutions of definite composition are pH, temperature, immersion time, degree of agitation, rinsing temperature and drying temperature.

1) pH of solutions

The most important factor, decisive for the formation of chromate coatings is the pH of the chromating solution. The pH range of importance for the zinc chromating process lies between 1 and 4 [1]. The lower the pH, the stronger a zinc substrate is attacked and the higher the probability that the solution will also exert brightening action. Aluminum, on the contrary, may be chromated in both acidic and alkaline solution owing to its amphoteric character.

2) Temperature of solutions

Generally, most chromating processes are carried out at room temperature, and are not seriously affected by variation within the range 16 to 30 °C. Lower temperatures cause chromate coatings to form very slowly and lose some of the characteristic fluorescence[12]. Higher temperatures increase the degree of metal removal and coatings lose abrasion resistance, probably because of the formation of a thick, less densely packed film. Although at higher temperatures film deposition proceeds more rapidly to yield thin coatings whose further build-up is considerably inhibited, relatively thick coatings may be obtained even at the boiling temperature, provided sulfates are replaced by chlorides in the conventional chromating bath containing sodium

dichromate [1]. No explanation of this phenomenon has been found in the available literature.

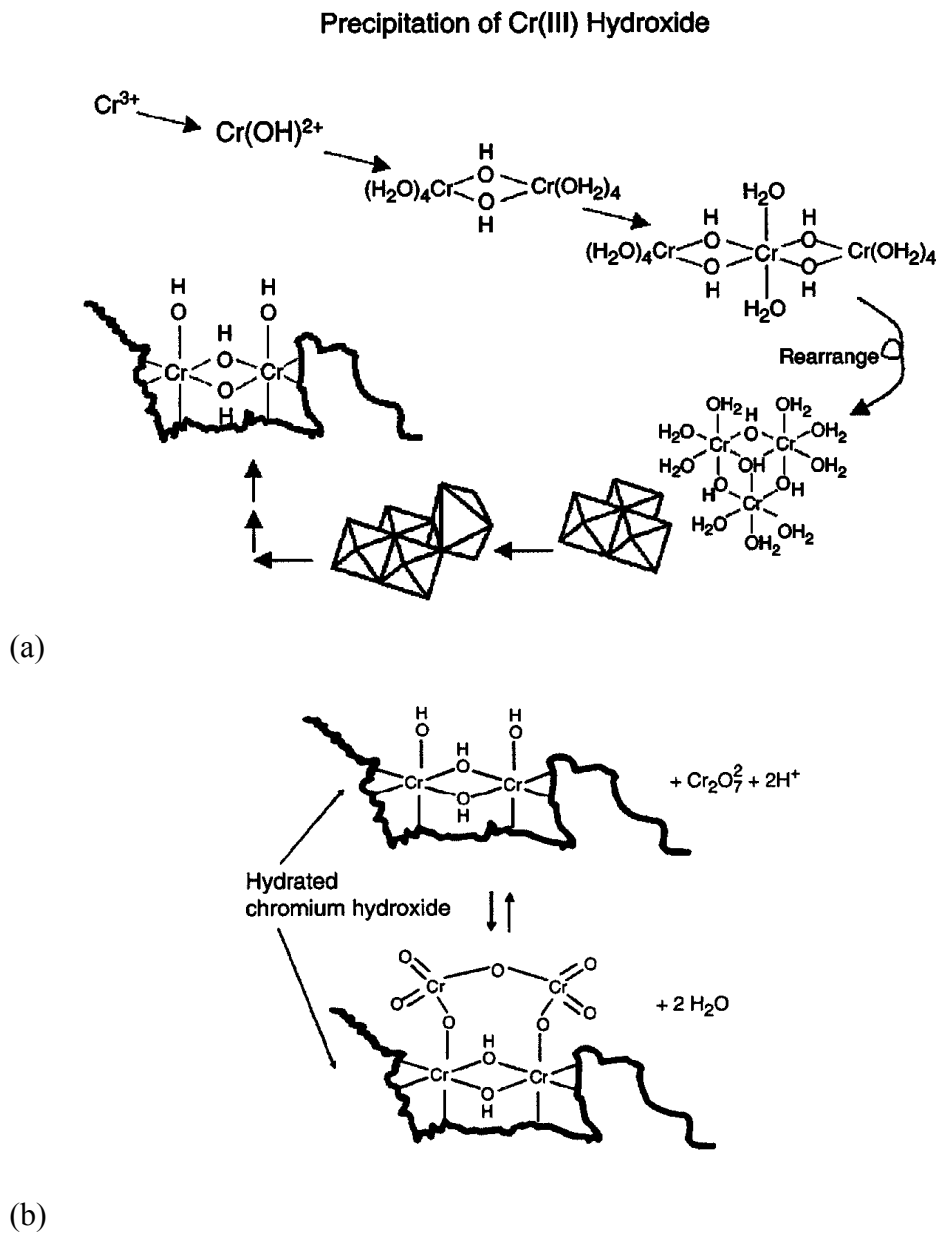


Fig. 3.1 Schematic illustrations of (a) the formation of $\text{Cr}(\text{OH})_3$ backbones [9] and (b) the possible structures of the Cr(III)/Cr(VI) mixed oxide present in a chromate coating [11].

3) Immersion time

The thickness and color of chromate coatings increase with rise of immersion time. With solutions producing colorless coatings, the coating thickness increases at a rate

that is dependent upon the pH, agitation and temperature, until an equilibrium state is established between formation and dissolution of the film. With solutions producing colored coatings the thickness and color intensity of chromate coatings gradually increase with immersion time until film detachment occurs [12].

4) Agitation of solutions

Generally, some form of agitation is recommended with most types of passivating processes as it leads to the formation of uniform films [12]. Zinc dissolution in an acidic solution results in depletion of hydrogen ions in the solution layer in contact with the zinc surface. If the workpiece and the solution remain unagitated, hydrogen ions are replenished by relatively slow diffusion from the main body of the bath, and further reaction with zinc occurs through the gelatinous film. In agitated solutions film formation is more rapid as hydrogen ions are continuously replenished at the zinc surface.

5) Rinsing temperature

Residues of the chromating solution on the treated surface offer difficulties in rinsing and reduce the corrosion resistance of the chromate coatings. A rigorously agitated rinse immediately after the passivation step is generally recommended as this results in a clearer and more uniform appearance. However, it was reported that the properties of chromate coatings were altered considerably by immersion in hot water, both appearance and corrosion resistance being adversely affected. In automatic plant it is recommended that the final rinse temperatures should not exceed 40 °C. Non-rinse chromate coating has also been applied for the treatment of galvanized steel and aluminum sheet stock in 1990's [13]. The advantage of this non-rinse coating is that the process is not accompanied by wastewater problem.

6) Drying temperature

Chromate coatings should be dried as rapidly and at the same time as carefully as possible. Removal of water by slow evaporation results in poor adhesion, pore formation and even crack development [1]. The drying temperature has less effect on the appearance of chromate coatings than the final rinse temperature, but it is often responsible for the formation of film cracks and transition of chromium compounds into insoluble forms. Gallaccio et al. [14] found that chromate coatings produced on zinc

from Cronak solutions suffered losses in corrosion resistance by heating in dry air at 70°C for 2 hours. It is of interest to note that films heated to the same temperature in steam did not crack and the corrosion resistance was not impaired. The benefit of “pre-paint chromating” will only be obtained if careful and thorough rinsing and drying procedures are carried out.

3.3 Properties of chromate conversion coatings

a. Composition and structure

The composition of chromate coatings has not been precisely determined, as it has been found to depend largely on the metal substrate, the bath composition and other parameters of the process. The main constituents of chromate coatings are trivalent chromium, hexavalent chromium, the basis metal, various oxides and water. Originally, it was proposed that chromate coatings consisted of a basic chromium chromate, chromium hydroxide and soluble chromates, which can be represented as [1,6,15] :



Van de Leest [16] reported that by means of precipitation titration and EDAX the yellow chromate conversion coating was shown to be a basic zinc chromate salt, which can be represented as $x\text{ZnCrO}_4 \cdot y\text{ZnX} \cdot z\text{Zn}(\text{OH})_2$, where X is an anion. To obtain the most accurate information about the composition of the coatings, it is necessary to conduct a surface analysis, preferably by several complementary techniques, such as Auger electron spectroscopy (AES) [17,18], X-ray photoelectron spectroscopy (XPS) [19-21] and X-ray absorption near edge spectroscopy (XANES) [22] etc..

Townsend and Hart measured the composition of chromate films on zinc and Al-Zn alloy-coated sheet steel by means of XPS [23]. Prior to chromating (Fig. 3.2 a), the surface of zinc is covered with a thin layer of zinc oxide. After chromating (Fig. 3.2 b), only two layers containing chromium have been observed, an outer layer of hexavalent chromium and an inner layer of trivalent chromium oxide. Corresponding analyses of the Al-Zn coating surface showed that it is covered with a thin layer of trivalent aluminum oxide (Fig. 3.3a). The paucity of zinc in the oxide film is attributed to

preferential oxidation of the more active aluminum component during solidification of the hot-dip coating in air. After chromating (Fig. 3.3 b), a passive film that comprises chromium in three oxidation states was observed. At the outer surface of the film, chromium is present in the hexavalent form. Following sputter removal of the hexavalent chromium, the major components of the film were found to be trivalent oxides of aluminum and chromium. With continued sputtering, the trivalent components diminish, and a peak in metallic chromium occurs. The chromate passivation films formed on Al-Zn alloy differ from that on zinc in two ways: (i) an intermediate layer containing aluminum oxide and (ii) an inner layer of metallic chromium (probably due to the Ar^+ sputter effect). These additional features could account for the greater degree of protection offered by chromate passivation to Al-Zn coatings as compared to zinc coatings.

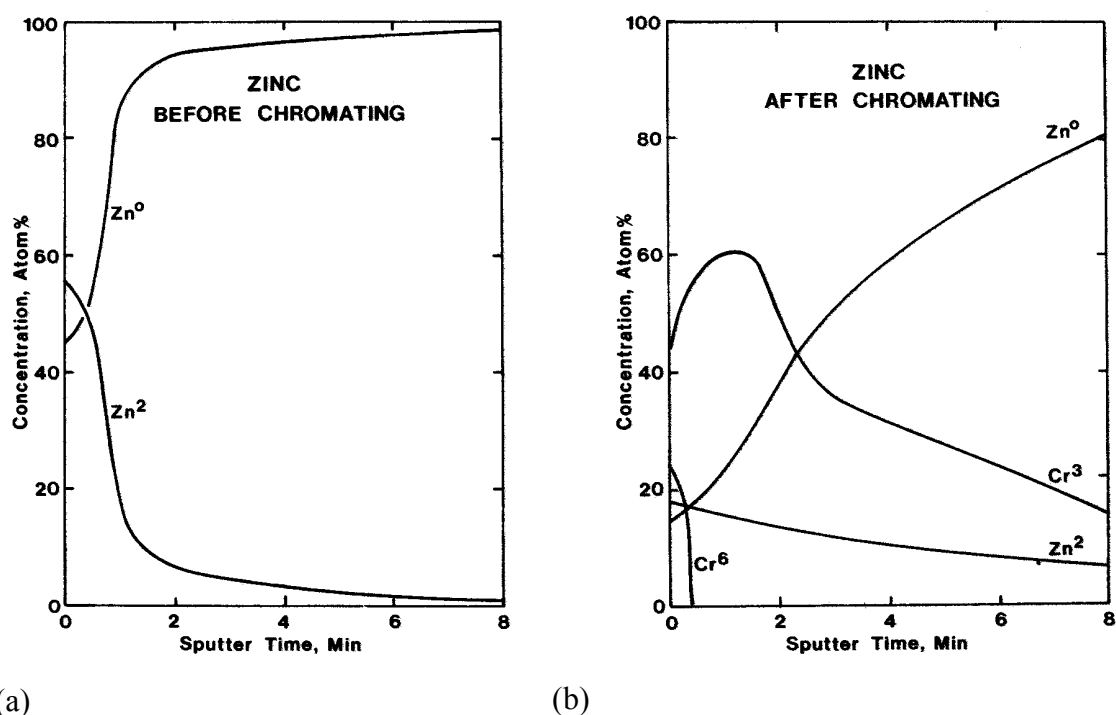


Fig. 3.2 XPS analysis of zinc sheet: (a) before chromating, (b) after chromating. Source: Ref. [23].

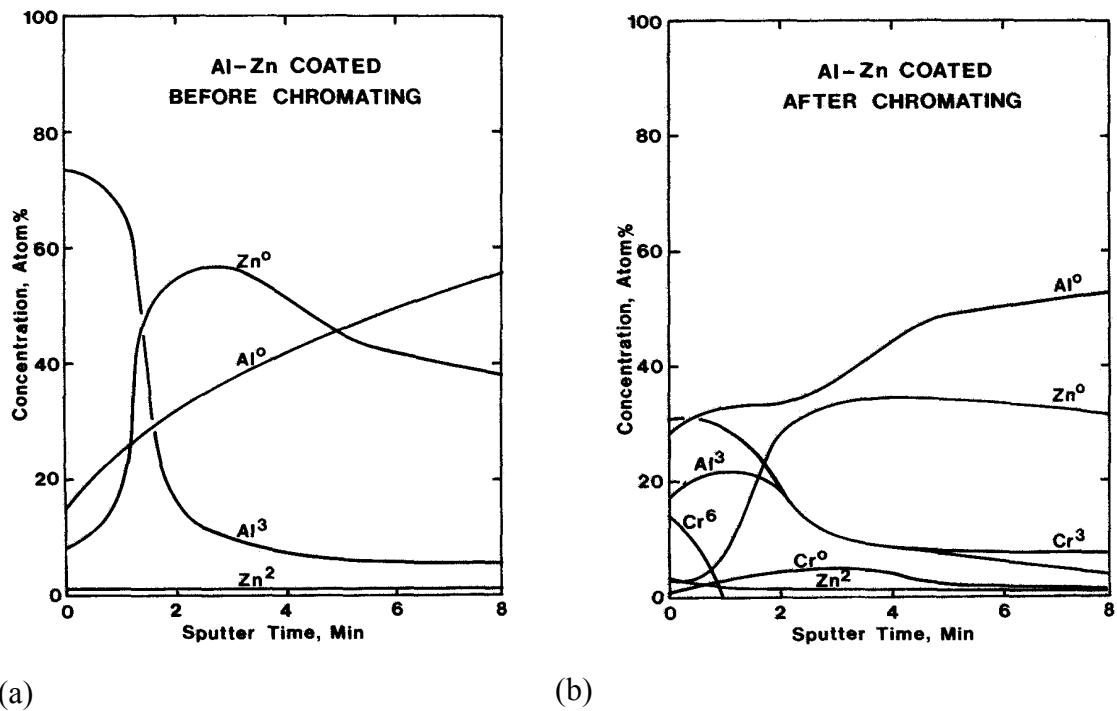


Fig. 3.3 XPS analysis of Al-Zn alloy-coated sheet steel: (a) before chromating, (b) after chromating. Source: Ref. [23].

Kendig and coworkers [8] reported that the ratio of Cr(VI) to total Cr in the chromate conversion coatings on Al 2024-T3 was about 20%, measured by XANES. The Cr(III) in the conversion coating is not crystalline Cr_2O_3 , but has a closer resemblance to an amorphous hydrated $\text{Cr}(\text{OH})_3$. Jeffcoat and coworkers [24] have also reported that approximately 20% of the total chromium in a chromate conversion coating on pure aluminum is Cr(VI). This suggested that Cr(VI) remains a major constituent of the chromate conversion coatings on Al and Al alloys. No quantitative results have been found about the composition of chromate conversion coatings on zinc or zinc alloys.

L. Xia and coworkers [11] reported that a Cr(III)/Cr(VI) mixed oxide was a significant component of the chromate conversion coating on AA 2024-T3 surface. The Infrared and Raman spectroscopic results are consistent with reversible formation of a covalent Cr(III)-O-Cr(VI) bond which binds the chromate species to the insoluble Cr(III) oxide.

The majority of chromate coatings are amorphous and gelatinous when just formed and while still wet, they are soft and exhibit absorptive properties. On drying, they shrink, harden and become hardly wettable and resistant to water solutions [1]. Chromate coatings usually exhibit microcracks due to the tensile stress [25-27]. Mattyak measured the internal stresses of the zinc deposition on a low carbon steel substrate and zinc chromate coatings. As-deposited bright zinc coatings (6 μm) exhibit a compressive stress of about -48 MPa. Once chromated, the zinc-chromate films exhibit a tensile stress dependent upon the immersion time and composition of the chromating solution. After chromating the zinc deposits in the yellow chromating solution, the stress rises from about 27.6 MPa after 30 s to about 69 MPa after 5 min. Galvanostatic studies show that corrosion in black, green, and yellow chromate films starts and propagates along cracks within the chromate coatings. Generalized corrosion is seen in blue chromate films [28]

b. Color and thickness

The color and thickness of chromate coatings vary with the conditions of chromating, and particularly with the composition, pH and temperature of the bath and time of treatment. The color of chromate coatings on zinc ranges from colorless to olive green and even to black. It depends considerably on the substrate and the type of chromating process used. To improve their decorative finish, freshly formed chromate coatings can be easily colored with pigments or dyes to create various color finishes. After drying, the coatings lose their absorbency, become hydrophobic, and cannot be dyed.

The thickness of chromate coatings can range from 10 to 1000 nm. For a given combination of substrate and conversion coating, the color of the coatings can be used as an indicator of the coating thickness [29]. The thinner films are often used as a paint base or when a colorless appearance is required. Thicker coatings are used for corrosion protection and decorative applications.

c. Corrosion resistance

Chromate coatings offer the greatest degree of corrosion resistance in all environments. In unpainted applications, corrosion resistance increases with increasing

coating thickness, particularly if the coatings contain a high proportion of Cr^{6+} . In painted applications, the conversion coatings must improve corrosion resistance and provide for good paint adhesion. The protection provided by chromate coatings increases with thickness up to a certain point, after which the protective nature is sacrificed due to the formation of a porous, non-adherent film [3,30].

Martyak measured the potentiodynamic polarization curves for zinc electro-deposit and chromated zinc in 4% NaCl at pH 6.8 – 7.0 (see Fig. 3.4) [28]. Air was bubbled through the solution before each experiment, but no during the experiments. The Tafel plots show that the anodic branch for the zinc deposit without a chromate coating exhibits no passivity, while for the green chromate deposit, the passive region occurs at a smaller critical current density and causes the cathodic branch of Tafel plot to intersect the anodic branch in a passive domain.

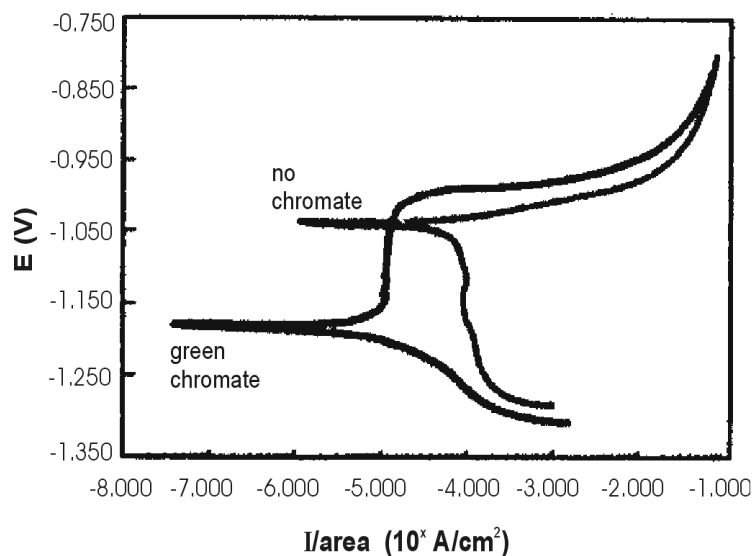


Fig. 3.4 Tafel plots of zinc deposit and green chromated zinc deposit (in 4% NaCl solution). The potentials were measured against a standard calomel electrode (SCE). Source: Ref. [28].

d. Hardness and abrasion resistance

The hardness of chromate coatings depends on the conditions of their formation, especially on the temperature during chromating and drying. Freshly made wet coatings are very soft and can be easily damaged by abrasion. After drying, the coatings become

hard, which allows for safe handling. However, even the dry coatings are sensitive to severe scratching or abrasion.

e. Adhesion

Generally chromate coatings have excellent adhesion to the metal surface, because the coating is bonded to the metal surface and no clear interface exists between the coating and the substrate. Coatings are usually sufficiently ductile to withstand pressing and forming operations, and although abrasion will occur, a degree of corrosion resistance will be obtained as the underlying zinc is re-passivated by soluble chromium from surrounding area [5].

f. Porosity

In principle, coatings of suitable thickness and produced in a proper way have no pores. Chromate coatings are porous before drying and may absorb dyes, so their color may be modified. Thin films and films produced on coarse surfaces tend to be more porous, while thicker coatings and coatings produced on smooth surface are less porous. Passivating solutions containing suspended particles produce very porous deposits [5].

g. Electrical resistance

The electrical resistance of chromate coatings varies with the type of base metal and its roughness, the coating thickness and the load applied. Chromate coatings have a relatively low electrical resistance. The reported value ranges from 8 to 300 $\mu\Omega/\text{cm}^2$ for chromated zinc at contact pressure of 7 kg/cm^2 , as compared with the 14 Ω/cm^2 for the anodized aluminum at the same contact load [1]. The resistance of thin films is sufficiently low to allow for the use of chromated metals in electric or electronic applications.

3.4 Protective mechanism of chromate coatings

The chemical and electrochemical methods of treatment of metals in chromate solutions have been known for many years, but to date there is no established and uniform opinion on the mechanism of metal protection by chromate coatings. Burns and Bradley gave two reasons for the protective activity shown by chromate coatings [31]. The first consists in the tightness of these coatings, ensuring an advanced degree of

isolation of the metal surface from the corrosive environment. Secondly, hexavalent chromium compounds, which are partly soluble, show well-known inhibiting properties at areas of bare metal corresponding to discontinuity in the coating.

The “self-healing” effect of hexavalent chromium compounds is supported by the fact that when a chromate coating is scratched, the base metal is protected against corrosion due to the evolution of chromates emerging from the surface around the damaged site. However, some authors regarded that the insoluble part of the chromate coatings was decisive for corrosion resistance, while the soluble part had only an additional effect.

Another theory concluded that the overall protective action of chromate coatings is attributed to the adsorption of polar molecules from the chromating solution [32]. The adsorbed molecules or ions form a dipole film with positive charges on the metal surface moving the electrochemical potential of the metal toward more positive values. However, Elze found that the stationary potentials of unchromated and chromated zinc and cadmium coatings differ only slightly[33]. These investigations were conducted in zinc sulfate solutions of various concentrations in which oxygen was removed and replaced by nitrogen. It was found that the chromate films do not inhibit the zinc dissolution in the vicinity of corrosion potential. Inhibition of anodic transition of ions into the corrosive medium is possible only when this transition proceeds through pores that are clogged in the initial stage of corrosion. The decrease in the rate of corrosion might also occur when the cathodic reaction is inhibited. Elze reported that the inhibition effect offered by chromate coatings depends on the corrosive environment. In seawater, the corrosion is inhibited in the initial stage due to the clogging of pores in the coatings. On the other hand, in chloride-free, weakly acidic (pH 6.0) corrosion media the protective action of chromate coatings involves primarily inhibition of the cathodic reaction.

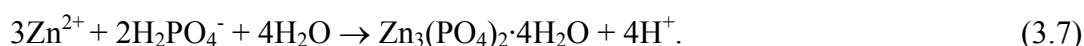
The loss of corrosion resistance after drying at higher temperatures may be explained by dehydration and cracking of the chromate coatings. Heating of the chromate coatings up to 200 °C and above results in the transition of soluble chromates into insoluble form [14]. X-ray absorption near edge structure (XANES) analysis results revealed that the relative quantity of hexavalent Cr in the chromate conversion coatings

decreases with the time of exposure in air-equilibrated 0.5 M NaCl solution [8]. *In situ* and *ex situ* microscopic Raman spectroscopy have been used to study the chromate effects on corrosion of aluminum alloy 2024-T3 [34-36]. Their results showed that dilute Cr(VI) was released from chromate coatings and transported to a nearby uncoated area or into pits in AA-2024-T3 by diffusion and/or migration, where it adsorbs to Al(OH)_x via electrostatic or covalent binding. Binding of Cr(VI) to Al(OH)_x reduces the surface charge due to neutralization of cationic sites on the Al(OH)_x. The reduction in surface charge may reduce chloride adsorption and possibly stabilize the oxide film. Chromate or its reduction product is an effective cathodic passivator that inhibits the rate of the cathodic reaction.

3.5 Alternatives to chromates

3.5.1 Phosphate

Zinc phosphates have been using extensively. They are not toxic and provide some corrosion protection to metals by forming a Zn₃(PO₄)₂·4H₂O film [4,37]. Phosphate coatings usually consist of crystalline salts of the metal being treated or of metal ions added to the phosphating bath. In acid solution, the intended coating process is [38,39]



The acidity of the phosphating bath varies, depending on the type of phosphating compound and its method of application. Immersion zinc phosphating baths are operated in a pH range of 1.4 to 2.4, whereas spray zinc phosphating solutions can be operated at a pH as high as 3.4, depending on the bath temperature.

Zinc phosphate coatings vary from light to dark gray in color. They are seldom used bare, serving mostly as a base for organic coatings to improve the protection of the base metal. In addition to increasing adhesion and retention of paints, phosphate coatings also tend to improve corrosion resistance under the coatings. Phosphate coatings are inert barrier layers that can confine corrosion to a limited area when the paint film is

damaged. Phosphate coatings have also been used to reduce friction in wire, tube, and deep drawing applications.

3.5.2 Molybdate

Molybdates have been tested extensively as possible chromate replacements due to their oxidizing power and stability of their reduction products, which form a passivating layer. Magalhaes et al.[40] compared the effects of Na_2MoO_4 and Na_2CrO_4 on zinc surfaces in NaCl solutions. It was reported that the inhibiting mechanism of molybdate films prepared in phosphoric acid baths is similar to chromate, but molybdate coatings are not as good as chromate coatings in corrosion resistance. The protective effect of steel by using molybdate anion has been described as the reduction of the Mo^{6+} to Mo^{4+} (as MoO_2) during film formation [41],



The oxide layer functions as a barrier layer to the corrosive media. MoO_4^{2-} anions adsorb on the oxide surface through hydrogen bonding between hydrogen atoms of dangling hydroxyl groups on the oxides and the oxygen atom of the MoO_4^{2-} ion. Such a MoO_4^{2-} -adsorbed surface is negatively charged and it repels other aggressive anions such as Cl^- , which ensures the protection and stability of the oxide layer [42].

Bresline et al. compared the effects of Na_2MoO_4 and $\text{Na}_2\text{Cr}_2\text{O}_7$ on aluminum alloys in NaCl solutions [43]. They postulated formation of Mo, Mo^{3+} and MoO_2 species followed by the formation of molybdenum oxides with different oxidation states. The oxidizing power of MoO_4^{2-} was not strong as the dichromate species ($\text{Cr}_2\text{O}_7^{2-}$) and the molybdate species was too large to accumulate at flawed areas, therefore unable to effectively passivate the region. Shaw et al. reported the presence of Mo^{4+} , MoO_4^{2-} and MoO_3 species in the passive regions[44].

Almeida et al.[45] have reported that molybdate-based conversion layers on galvanized steel (4 μm thick zinc) showed a better anticorrosive behaviour with respect to permanganate, tungstate and vanadate conversion coatings in the neutral salt spray

test (5% NaCl) (see Table 3.1). However, the behaviour of molybdate conversion coatings is not as good as that presented by chromate conversion coatings.

Table 3.1 Corrosion behavior in salt spray (average of three samples) of layers obtained with ammonium molybdate (10 g/l, 60°C and 300 s with ammonium chloride 40 g/l), sodium molybdate, permanganate, tungstate and vanadate baths (1M; 20°C; 300 s and pH 5 adjusted with H₂SO₄)(already optimized)[†]. Source: Ref. [45]

Oxidizing species	Time of beginning of rust (h)		
	White rust	First point of red rust	10% red rust
Sodium molybdate	7	75	85
Ammonium molybdate	3	49	58
Sodium permanganate	2	27	30
Sodium tungstate	2	24	26
Sodium vanadate	2	27	30
Chromate bath (reference)		340	350

[†]Zinc galvanized steel substrate without passivation shown white rust after 1 hour and 10% red rust after 20 h of salt spray exposure.

3.5.3 Permanganate

Potassium permanganate is known as an oxidizing agent, consequently it has the potential to produce a coating containing some residual permanganate to act as a passivator. Permanganate solutions are intrinsically unstable, acidic solutions decompose slowly to form a brown precipitate of MnO₂. If a coating mechanism similar to a chromate coating is considered for the permanganate treatment the evolution of hydrogen, accompanying the zinc dissolution reaction, at the metal-solution interface could be capable of reducing permanganate to Mn(II). The residual permanganate

component of the coating could oxidize the Mn(II) to Mn (IV) (MnO_2) as following reaction [46]:



Wharton et al. [46] have investigated the permanganate conversion coatings on Zinc-Nickle alloys in a solution containing 10g/l KMnO_4 at pH 2.2. The permanganate conversion coatings were reported to undergo rapid deterioration, with the formation of voluminous white corrosion products over the surface. This behavior could be as a consequence of an increased acidity within the coatings due to a reaction such as the oxidation of Mn(II) by entrapped permanganate species (3.10).

Umehara et al.[47] studied the permanganate conversion coatings on magnesium alloy with some acidic additives such as HNO_3 , H_2SO_4 , and HF. As a cathodic reaction, permanganate could be reduced to MnO_2 . With the pH rising locally in the cathodic area, reduction reactions from MnO_2 to lower-order oxides will occur and form a surface layer where various oxides coexist. The reactions are as follows:



It has been reported that the conversion layer formed in an HF-added bath has an amorphous structure, a very thin layer containing magnesium fluoride, hydroxides, and manganese oxides. The corrosion resistance of permanganate conversion coatings on magnesium alloy is comparable with that of chromium conversion coatings on this alloy [47].

Dual formulation treatments on electrodeposited Zn-Ni alloys have been performed by Warton et al. [46], which consists of a simple molybdate, then a permanganate immersion (molybdate/permanganate) or reverse treatment procedure (permanganate/molybdate). The formulations consisted of 10g/l $\text{Na}_2\text{MoO}_4 \cdot 2\text{H}_2\text{O}$ at pH

5.5 and 10 g/l KMnO_4 at pH 2.2. Immersion times in each solution were for 300 seconds. The average corrosion current density, determined from linear polarization measurements, for the molybdate/permanganate and permanganate/molybdate coatings is smaller than for an untreated zinc-nickel alloy electrodeposit in a quiescent 3.5% NaCl solution. No synergistic effect was found between the two coating systems. The corrosion tests indicated behaviors corresponding to the performances achieved by either a simple molybdate or permanganate coating, depending upon which was the final treatment.

3.5.4 Tungstate

The application of this type of solution to form conversion coatings is not widely reported. The cathodic polarization characteristics of zinc in tungstate solutions have been investigated by Wilcox et al. [48-50]. It was suggested that H^+ ions discharge on the cathode before WO_4^{2-} reduction. Evolved hydrogen then reduces the WO_4^{2-} ions. Passivation treatment for tin-zinc alloy have been reported by Cowieson et al. [51]. The tungstate treatment appeared to offer a similar degree of protection as the molybdate treatment with respect to the onset of zinc corrosion, but the former does not appear to have a retarding effect on the breakdown of the alloy coating. The tungstate based treatment provided a lesser degree of protection than the molybdate ion in both the salt fog test and the cycled temperature humidity test.

3.5.5 Cerium compounds

The soluble salts of rare earth metals such as cerium, lanthanum and yttrium have been recognized as effective corrosion inhibitors for aluminum alloys in aqueous chloride solutions[52,53]. Hinton et al. [53] reported that a CeCl_3 solution was effective at lowering the oxygen reduction rate at cathodic sites on zinc in NaCl solutions. Cathodic polarization curves obtained after a hold time at open circuit of 15 min in 0.1 M NaCl or 0.1 M NaCl plus 1000 ppm $\text{CeCl}_3 \cdot 7\text{H}_2\text{O}$ showed that the open circuit potential for zinc was reduced in the second solution (Fig. 3.5). When the test specimen was kept at open circuit potential in the second solution for 64 h, the entire cathodic

curve was shifted to much lower current densities. A yellow film was observed on the specimen surface in tests conducted in the second solution.

Passivation of an 80% Sn-20% Zn electrodeposited alloy in cerium containing solutions afforded a level of corrosion protection similar to that evidenced with conventional dichromate passivation treatments [54]. The presence of cerous ions in solution leads to the formation of a protective film of complex hydrated cerium oxides containing Ce^{3+} and Ce^{4+} on the zinc surface. The yellow color of the film formed on the zinc species indicates the presence of Ce^{4+} ions [53]. The cerium-rich film formation is dependent on reduction of oxygen which influences the oxidation of Ce(III) to Ce(IV) in solution and precipitation of the film by changing the local pH at the electrode [55]. The generation of hydrogen peroxide by oxygen reduction is considered to enhance cerium-rich film formation by oxidizing Ce(III) to Ce(IV) in solution

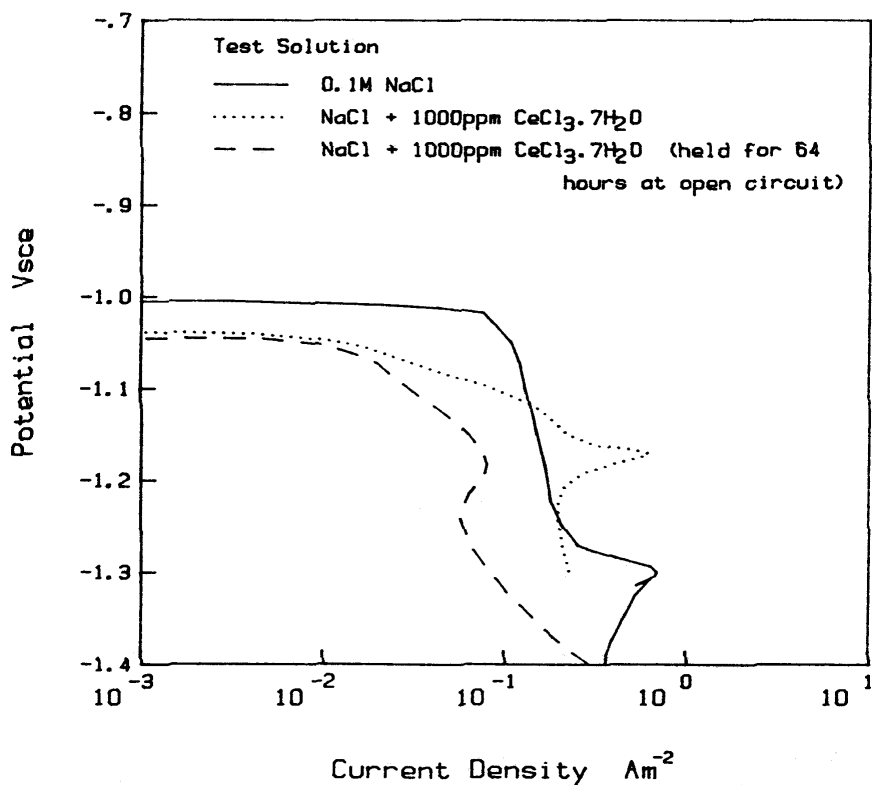


Fig. 3.5 Cathodic polarization curves for zinc in 0.1 M NaCl with an addition of $\text{CeCl}_3 \cdot 7\text{H}_2\text{O}$. Source: Ref. [53]

The treatment of zinc surface in cerium nitrate solution has been reported by Aramaki [56]. A film composed of hydrated Ce_2O_3 and CeO_2 was formed on the zinc surface. Since the solubility of $\text{Ce}(\text{OH})_3$ is lower (1.6×10^{-20}) than that of $\text{Zn}(\text{OH})_2$ (3×10^{-17}), $\text{Ce}(\text{OH})_3$ precipitates on the zinc surface in a solution containing Ce^{3+} preferentially,



and changes to the oxide,



The presence of Ce^{4+} within the film was confirmed by XPS. Ce^{4+} may also be reduced to Ce^{3+} by the cathodic process,



which results in an increase of the cathodic current.

This film was protective against corrosion of zinc in an aerated 0.5 M NaCl solution at 30 °C, but its self-healing ability was poor at the scratched zinc surface.

3.5.6 Trivalent chromium

Trivalent chromium based conversion treatments are far less toxic than chromates. Barnes et al. have developed a trivalent chromium system for zinc [57]. These conversion coating solutions contain nitrate as an oxidant and sodium hypophosphite as a complexant to increase the stability of the Cr(III) in the bath. The color and the thickness of the conversion coatings can be altered by variation of solution composition, pH, temperature, and time of immersion. The solution temperature is not critical, but higher temperatures enhance the rate of film formation. The pH of non-complexed

solutions must be less than 3.0 to avoid bulk precipitation of chromium hydroxide, but when a complexant is present, the pH values up to pH 4.5 can be tolerated. It is reported that, with this type of solution, the conversion coatings with corrosion resistance equivalent to that of chromate coatings could be produced.

Bellezze et al. [58] have compared the corrosion resistance of Cr(III)- and Cr(VI)-based conversion layers on zinc coatings in quiescent aerated 5% NaCl solution. They reported that the corrosion behavior of the Cr(III) passivated coating with sealing treatment is comparable to that of the coatings submitted to Cr(VI) conversion treatment without sealant coatings

Gardner et al. [59] have reported that the corrosion resistance of the trivalent coatings do not significantly diminish after thermal shock, as is the case with hexavalent chromates. This new generation of trivalent passivators work particularly well on plated zinc-iron. The coatings give a clear to light coating with exceptionally good corrosion resistance.

3.5.7 Silanes

The use of silanes as a potential alternative to chromates was reported recently [60,61]. The bis-silane, bis-1,2-[triethoxysilyl] ethane (BTSE), after complete hydrolysis in water/alcohol mixtures, can be applied in thin films and provides protection against corrosion [62]. As BTSE has no functional group, it cannot be bonded well to many polymers[61]. Therefore, a two-step process, including coating the metal with a layer of a non-functional silane topped with a layer of a functional silane, or a mixture of BTSE with an organofunctional silane such as γ -aminopropyltriethoxysilane (γ -APS) seems to be the best approach.

The initially hydrophilic nature of organofunctional silanes is an important aspect. Organofunctional silanes are chemicals with a hydrolysable Si group at one end and a functional group at the other. Upon hydrolysis in water/ alcohol/acid, the silicon end groups produce Si-OH groups, through which they can be absorbed by metal oxide surfaces forming hydrogen bonds. Upon curing, such bonds are replaced by metallosiloxane bonds, -Me-O-Si. The remaining silanol groups in the film condense

and form hydrophobic Si-O-Si bonds. The other end of the silane molecule consists of a functional group that can bond with the paint. The conversion from hydrophobic to temporarily hydrophilic, followed by curing to a hydrophobic film, is an important property of silanes[61].

Sundararajan and van Ooij reported that bis-amino and bis-sulphur silanes deposited on EG steel, HDG steel and Al6061 under optimum conditions could provide adhesion and corrosion performance equivalent to the phosphated system [63]. The paint adhesion and corrosion properties of silane films on metals depend upon cleaning procedure, silane concentration, pH of application, and post-treatment. In the case of bis-sulphur silane, only the 5% bis-sulphur silane has comparable performance to the phosphated systems on EG steel, while lower concentrations gives inferior results. For the bis-amino silane films on Eg steel, bis-amino films deposited at acidic pH result in inferior performance. The corrosion inhibition is mainly due to the hydrophobic interface of condensed siloxane units. It is not related to the hydrolytic resistance of the metallosiloxane bond, because the Me-O-Si bond can be expected to be polarized and subject to hydrolysis[61].

3.5.8 Miscellaneous

Other treatments such as vanadate, zirconate, titanate as well as anodizing can also provide a certain degree's protection on metals, but these treatments have been applied less widely to zinc-based metal surfaces. Almeida and coworkers have compared the effect of oxidizing species treatments on galvanized steel with an average zinc thickness of 4 μm using the salt spray test (ASTM-B-117) [45]. The results are shown in Table 3.1. Vanadate can supply moderate protection to zinc (less than molybdate does), and it is also toxic.

Recently, zirconate and titanate based coatings are found which supply better adhesion properties on aluminum [64]. Most of these treatments are recognized as a pretreatment for a subsequent paint finish and they would not presumably have the "stand alone" capabilities for some end-uses of unpainted galvanized zinc surfaces [50].

Anodizing is an electrochemical method whereby the surface of a metal, chiefly aluminum, is converted to an oxide when the metal is made the anode in certain electrolytes. The anodizing coating on zinc is of the barrier-layer type with a porous outer layer over an initial barrier layer. Compared to chromate and phosphate conversion coatings for zinc, the anodized coatings are harder, thicker and more corrosion resistant [2]. However, the cost of electricity needed during the process makes the anodizing treatment less attractive.

3.6 Conclusions

Conversion coatings are employed to passivate metal surfaces to enhance their corrosion resistance, increase the adhesion between the paint and the underlying metal, and get a pleasing appearance. To date, chromate conversion coating exhibits best performance in practical use. Chromate can passivate almost the all base metals used in industry. Its good corrosion resistance benefits from the particularly protective, inert and hydrophobic barrier layer, Cr(III) oxide/hydroxide, and its unique “self-healing” effect due to the soluble hexavalent chromium. However, it will be abolished in due time because it is highly toxic.

It is clear that, at present, no other solution appears to offer a complete replacement to chromates. Molybdate and soluble salts of rare earth metals such as cerium and lanthanum compound based solutions do show promise, although their neutral salt spray (NSS) corrosion resistance is still inferior to chromates. Silanes and plasma polymerization coatings do supply protection to metals, however, compared to chromate treatments, the corrosion resistance or the cost of these alternatives is unfavorable. There is a growing realization that the Cr(III) is, as an intermediate stage, the most commercially acceptable alternative to Cr(VI). Its adoption into industry offers the best available technology not requiring too much excessive cost and when applied to a zinc alloy can obtain suitable corrosion protection.

In any case, understanding the protective mechanism of chromate conversion coatings becomes a critical step to facilitate searching for alternatives. In this thesis, we will focus on comparison of Cr(VI)- and Cr(III)-based conversion coatings, in order to

understand the protective mechanism of chromate conversion coatings on zinc, eventually this may lead to alternative Cr-free solution.

References

1. T. Biestek and J. Weber, *Conversion Coatings*, (Portcullis Press Ltd., Redhill, 1976).
2. J. A. Mock, *Materials Engineering*, 70 (1969) 52.
3. P. L. Hagans, in: *ASM Handbook*, ASM International, 1994, Vol. 5, p. 405-411.
4. R. L. Twite and G. P. Bierwagen, *Prog. Org. Coat.*, 33 (1998) 91.
5. M. E. Roper, *Metal Finishing Journal*, 14 (1968) 320.
6. L. F. G. Williams, *Plating*, (1972) 931.
7. L. F. G. Williams, *Surf. Technol.*, 4 (1976) 355.
8. M. W. Kendig, A. J. Davenport and H. S. Isaacs, *Corros. Sci.*, 34 (1993) 41.
9. M. W. Kendig and R. G. Buchheit, *Corrosion*, 59 (2003) 379.
10. H. Stünzi and W. Marty, *Inorg. Chem.*, 22 (1983) 2145.
11. L. Xia and R. L. McCreery, *J. Electrochem. Soc.*, 145 (1998) 3083.
12. M. E. Roper, *Metal Finishing Journal*, 14 (1968) 286, 294.
13. Y. Yoshikawa and J. F. Watts, *Surf. Interface Anal.*, 20 (1993) 379.
14. A. Gallaccio, F. Pearlstein and M. R. D'Ambrosio, *Metal Finishing*, (1966) 50, 57.
15. J. P. G. Farr and S. V. Kulkarni, *Trans IMF*, 44 (1966) 21.
16. R. E. Van de Leest, *Trans IMF*, 56 (1978) 51.
17. A. G. Schrott, G. S. Frankel, A. J. Davenport, H. S. Isaacs, C. V. Jahnes and M. A. Russak, *Surf. Sci.*, 250 (1991) 139.
18. J.-O. Nilsson, S.-E. Hörnström, E. Hedlund, H. Klang and K. Uvdal, *Surf. Interface Anal.*, 19 (1992) 379.
19. A. E. Hughes and R. J. Taylor, *Surf. Interface Anal.*, 25 (1997) 223.
20. S.-E. Hörnström, E. Hedlund, H. Klang, J.-O. Nilsson and M. Backlund, *Surf. Interface Anal.*, 20 (1993) 427.
21. E. Desimoni, C. Malitesta, P. G. Zambonin and J. C. Rivière, *Surf. Interface Anal.*, 13 (1988) 173.
22. F. W. Lytle, R. B. Gregor, G. L. Bibbins, K. Y. Blohowiak, R. E. Smith and G. D. Tuss, *Corros. Sci.*, 37 (1995) 369.
23. H. E. Townsend and R. G. Hart, *J. Electrochem. Soc.*, 131 (1984) 1345.
24. C. S. Jeffcoate, H. S. Isaacs, A. J. Aldykiewicz Jr and M. P. Ryan, *J. Electrochem. Soc.*, 147 (2000) 540.

25. N. M. Martyak, J. E. McCaskie, T. Hulsmann and D. Schroer, in: Interfinish 96 World Congress, 10-12 Sept., 1996, Birmingham, England, 96 A.D.; 1996).
26. N. M. Martyak, *Plat. and Surf. Fin.*, 87 (2000) 77.
27. N. M. Martyak, *Surf. Coat. Technol.*, 88 (1996) 139.
28. N. M. Martyak, J. E. McCaskie and L. Harrison, *Metal Finishing*, 94 (1996) 65.
29. K. A. Korinek, in: *ASM Handbook*, ASM International, 1987, Vol. 13, p. 389-395.
30. D. Ende, W. Kessler, D. Oelkrug and R. Fuchs, *Electrochim. Acta*, 38 (1993) 2577.
31. R. M. Burns and W. W. Bradley, *Protective Coatings for Metals*, 3rd ed., (Reinhold Publishing Corp., New York, 1967).
32. F. J. Bubsey, *Metal Progress*, 66 (1954) 122.
33. J. Elze, *Metall*, 13 (1959) 740.
34. J. Ramsey and R. McCreery, *J. Electrochem. Soc.*, 146 (1999) 4076.
35. J. Zhao, G. Frankel and R. McCreery, *J. Electrochem. Soc.*, 145 (1998) 2258.
36. J. Zhao, L. Xia, A. Sehgal, D. Lu, R. L. McCreery and G. S. Frankel, *Surf. Coat. Technol.*, 140 (2001) 51.
37. A. Amirudin and D. Thierry, *Prog. Org. Coat.*, 28 (1996) 59.
38. X. G. Zhang, *Corrosion and Electrochemistry of Zinc*, (Plenum Press, New York, 1996).
39. J. A. Kargol and D. L. Jordan, *Corrosion*, 38 (1982) 201.
40. A. A. O. Magalhães, I. C. P. Margarit and O. R. Mattos, in: 7th International symposium on electrochemical methods in corrosion research, EMCR 2000, May 28 - 1 June, Budapest, Hungary, 2000).
41. S. A. M. Refaey, S. S. Abd El-Rehim, F. Taha, M. B. Saleh and R. A. Ahmed, *Appl. Surf. Sci.*, 158 (2000) 190.
42. C. M. Mustafa and S. M. Shahinoor Islam Dulal, *Corrosion*, 52 (1996) 16.
43. C. B. Breslin, G. Treacy and W. M. Carroll, *Corros. Sci.*, 36 (1994) 1143.
44. B. A. Show, G. D. Davis, T. L. Fritz and K. A. Olver, *J. Electrochem. Soc.*, 137 (1990) 359.
45. E. Almeida, T. C. Diamantino, M. O. Figueiredo and C. Sad, *Surf. Coat. Technol.*, 106 (1998) 8.
46. J. A. Wharton, G. D. Wilcox and K. R. Baldwin, *Trans IMF*, 77 (1999) 152.
47. H. Umehara, M. Takaya and Y. Kojima, *Mater. Trans.*, 42 (2001) 1691.
48. G. D. Wilcox and D. R. Gabe, *Br. Corros. J.*, 19 (1984) 196.
49. G. D. Wilcox and D. R. Gabe, *Br. Corros. J.*, 22 (1987) 254.
50. G. D. Wilcox and J. A. Wharton, *Trans IMF*, 75 (1997) B140-B142.
51. D. R. Cowieson and A. R. Scholefield, *Trans IMF*, 63 (1985) 56.

52. M. A. Arenas, M. Bethencourt, F. J. Botana, J. de Damborenea and M. Marcos, *Corros. Sci.*, 43 (2001) 157.
53. B. R. W. Hinton and L. Wilson, *Corros. Sci.*, 29 (1989) 967.
54. C. B. Breslin and M. Geary, *Corrosion*, 54 (1998) 964.
55. Jr. A. J. Aldykiewicz, A. J. Davenport and H. S. Isaacs, *J. Electrochem. Soc.*, 143 (1996) 147.
56. K. Aramaki, *Corros. Sci.*, 43 (2001) 2201.
57. C. Barnes, J. J. B. Ward, T. S. Sehmbhi and V. E. Carter, *Trans IMF*, 60 (1982) 45.
58. T. Bellezze, R. Fratesi and G. Roventi, *Eur. Fed. Corros. Publ.*, 28 (2000) 180.
59. A. Gardner and J. Scharf, *Soc. Automot. Eng.*, [Spec. Publ.], SP-1614 (2001) 91.
60. R. Duarte, A. M. Cabral, M. F. Montemor, J. C. S. Fernandes and M. G. S. Ferreira, in: *Proc. of 15th ICC ; Granada, Spain, 2002*) pp. 1-11.
61. W. J. van Ooij, D. Q. Zhu, G. Prasad, S. Jayaseelan, Y. Fu and N. Teredesai, *Surf. Eng.*, 16 (2000) 386.
62. V. Subramanian and W. J. van Ooij, *Surf. Eng.*, 15 (1999) 168.
63. G. P. Sundararajan and W. J. van Ooij, *Surf. Eng.*, 16 (2000) 315.
64. A. Kwakernaak and A. van den Berg, *Aluminium for its functional surface properties, Brussel, 2002*) pp. 1-7.

Chapter 4

Physical Characterization of Cr(VI)-Based Conversion Coatings on Zinc

4.1 Introduction

The morphology and the composition of a conversion coating play an important role in corrosion protection. It is well known that chromate conversion coatings (CCCs) contain Cr(VI) and Cr(III) species in the layer. Many reports on the nature of chromate coatings can be found in literature, however, the morphology and the composition of a chromate layer depends on the chromating process and the treated substrate. Martyak et al. [1] reported that the surface structure is related to the stress in the chromate layer. Some chromate coatings exhibit excellent corrosion protection, even though cracks exist in the layer, and this is attributable to the composition of the coatings[2,3]. In the work described in this chapter, the morphology, the thickness, and the compositions of the Cr(VI)-based coatings with different dipping times were studied by means of scanning electron microscopy (SEM), spectroscopic ellipsometry (SE), Auger electron spectroscopy (AES), X-ray photoelectron spectroscopy (XPS), and Fourier transform infrared spectroscopy (FTIR).

4.2 Sample preparation

In this study, pure zinc sheets, 0.5 – 1.0 mm thick, or electro-galvanized (EG) steel (carbon steel was polished and a 13 μm thick zinc layer was electrodeposited) were used as substrates. The specimens were cut into 2 \times 2 cm for SEM and SE analyses, 2 \times 1.6 cm for the XPS and AES analyses, and 7 \times 2.5 cm for the FTIR analysis. Before applying a chromate coating, the zinc sheet surface to be analysed was polished using 1

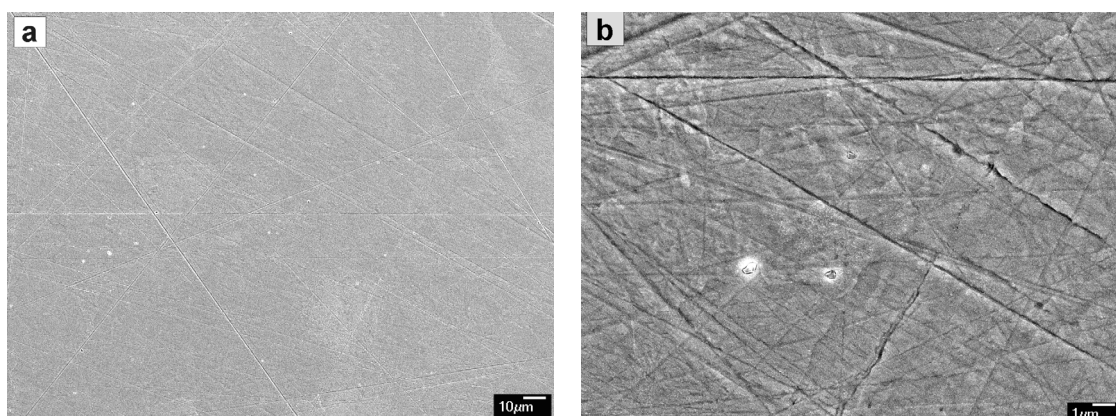
μm diamonds in the final step, ultrasonically cleaned in ethanol for 2 minutes, activated in 0.25% nitric acid for 10 seconds, and rinsed in de-ionised water.

The Cr(VI)-based coating was applied in a Cr(VI) bath containing 200 g/L $\text{Na}_2\text{Cr}_2\text{O}_7$ + 10 g/L H_2SO_4 (pH 1.1-1.3) for 1, 5, 10, 30 or 60 seconds at room temperature. After this chromating, the samples were rinsed in de-ionized water. The rinsed chromated specimens were first dried using a hair-dryer and then heated in an oven at 60°C for 30 minutes.

4.3 Morphology of the coatings

The samples were ultrasonically cleaned in 2-propanol for 2 minutes. The morphology of Cr(VI) coatings (as mentioned before, the Cr(VI) coating refers to the coating which was developed in the hexavalent chromium bath) was investigated under the Field Emission Scanning Electron Microscope, JSM-6500F.

Fig. 4.1 shows SEM images of Cr(VI) coatings on zinc with dipping times of 1, 5, 10, 30 and 60s. For specimens with a dipping time of 1 and 5 s, the polishing scratches are still visible because the layer is very thin. No cracks can be seen in these thin layers. For the specimens with dipping times longer than 10 s, microcracks are visible in the layers. The length of crack per unit area and the average crack width both increase with the dipping time.



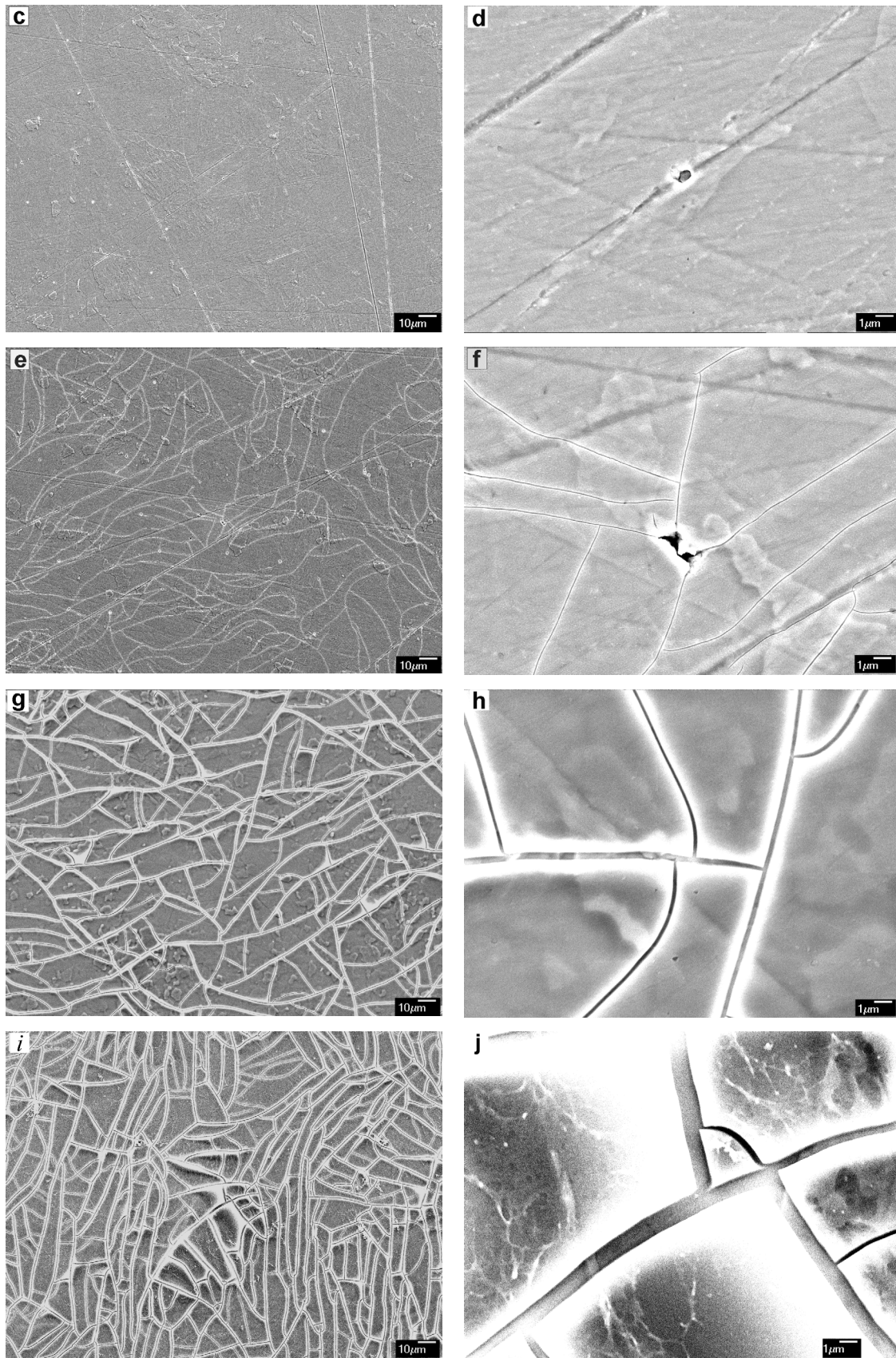


Fig. 4.1 SEM images for the Cr(VI) coatings on zinc with different dipping times: (a) and (b) 1 s, (c) and (d) 5s, (e) and (f) 10 s, (g) and (h) 30 s, (i) and (j) 60 s.

Fig. 4.2 shows a cross section view for a Cr(VI) treated EG steel specimen. The thickness of the zinc coating is about 13 μm , and the thickness of the chromate layer is about 600 nm.

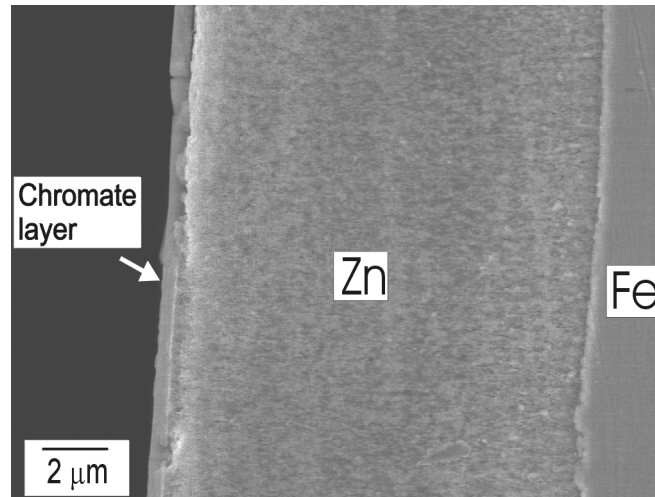


Fig. 4.2 Cross section view for a Cr(VI) treated EG steel. The zinc coating is about 13 μm thick, while the chromate layer is about 600 nm thick.

4.4 Determination of coating thickness

4.4.1 Spectroscopic ellipsometry (SE)

Variable angle spectroscopic ellipsometry is a powerful tool for non-destructively characterizing thin films. It operates by reflecting linearly polarized light from (or transmitting through) the surface of a material. The linearly polarized light undergoes a polarization change due to the reflection (or transmission) related to the thin film properties (thickness, index of refraction, etc.). Ellipsometry is a technique based on measurements of the polarization state of the reflected light, and describes the change in polarization caused by the sample with two parameters, psi (Ψ) and delta (Δ), which are related to the ratio of Fresnel reflection coefficients (\tilde{R}) of the sample (see Fig. 4.3) [4,5]:

$$\rho = \tan(\Psi) e^{j\Delta} = \frac{\tilde{R}_p}{\tilde{R}_s} = \frac{|\tilde{R}_p|}{|\tilde{R}_s|} e^{j(\delta_p - \delta_s)} \quad (4.1)$$

$$\tilde{R}_\alpha = \frac{\tilde{E}_{r\alpha}}{\tilde{E}_{i\alpha}} = \frac{|\tilde{E}_{r\alpha}|}{|\tilde{E}_{i\alpha}|} e^{j\delta_{r\alpha}} \quad \alpha = p, s \quad (4.2)$$

where the subscripts refer to incident (*i*) and reflected (*r*) waves parallel (*p*) or perpendicular (*s*) to the plane of incidence. Thus, Ψ is related to the ratio of reflected intensities of the parallel and perpendicular light components, while Δ contains information about the phase changes that have occurred between these two components. Useful information about thin films can be obtained by fitting the Ψ and Δ data to get the best match between the theoretical response and the experimental results.

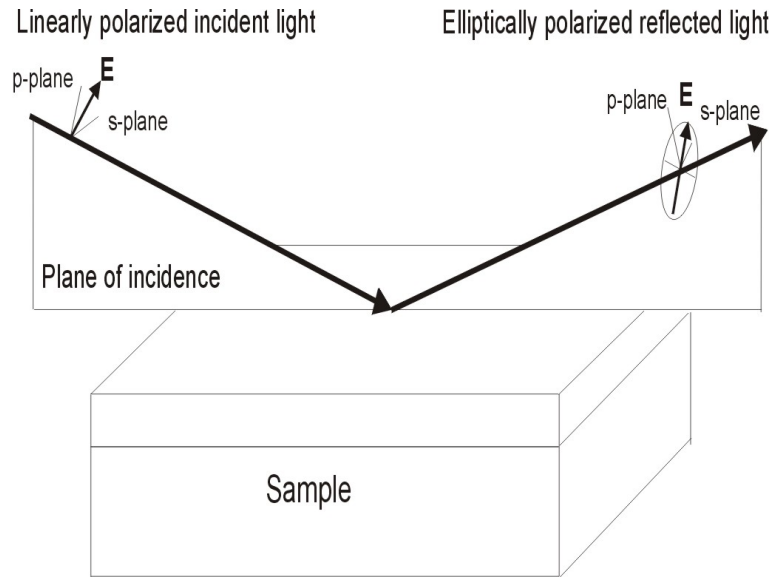


Fig. 4.3 Basic geometry of an ellipsometry measurement. Ref. [6]

4.4.2 Thickness of conversion coatings

The thickness of the Cr(VI) coatings was measured by means of Spectroscopic Ellipsometry (SE). The SE analysis was performed with a J.A. Woollam Co. VASE (variable angle spectroscopic ellipsometry) instrument. The angle of incidence was varied from 65° to 85° in steps of 10° . The spectra were recorded using a wavelength

range of 300 to 1700 nm. The thickness of each coating was calculated by fitting the acquired SE spectrum using a two-layer optical model previously used to model the optical properties of chromium conversion coatings on aluminium [7,8]. The two layers are the coating layer and an interface layer between the coating and the substrate. The refractive index n of the chromate layer is unknown and is modeled as a function of the wavelength λ using a Cauchy dispersion relation whose terms are fitted during the regression processing[5]:

$$n(\lambda) = A + \frac{B}{\lambda^2} + \frac{C}{\lambda^4} \quad (4.3)$$

where A, B and C are Cauchy coefficients and λ is the wavelength. Strictly, this dispersion relation describes the dependence of n on λ for a fully transparent dielectric material. For materials that are not fully transparent, an absorption factor should also be included. One of useful relationship for the extinction coefficient k is a simple exponent function[5]:

$$k(\lambda) = A_k e^{B_k(E-E_b)} \quad (4.4)$$

where A_k , B_k and E_b are parameters, but A_k and E_b are not independent. E is the photon energy, which is related to the wavelength by [5]

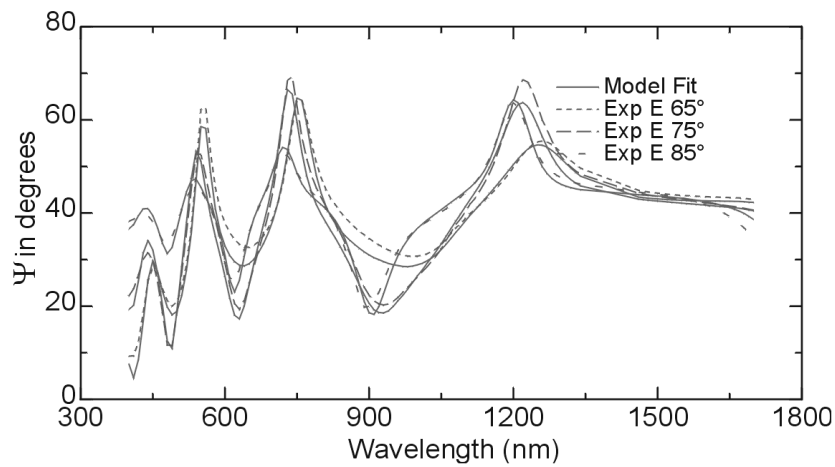
$$E \cong \frac{12400}{\lambda} \quad (4.5)$$

where E is given in electron volts and λ is given in angstroms. For chromate layers on galvanized steel, two main absorption bands were found at 270 and 370 nm due to the ligant-metal charge transfer [9]. Nevertheless, it has been confirmed that the use of this dispersion relationship to model the optical properties of chromium coatings is acceptable [7].

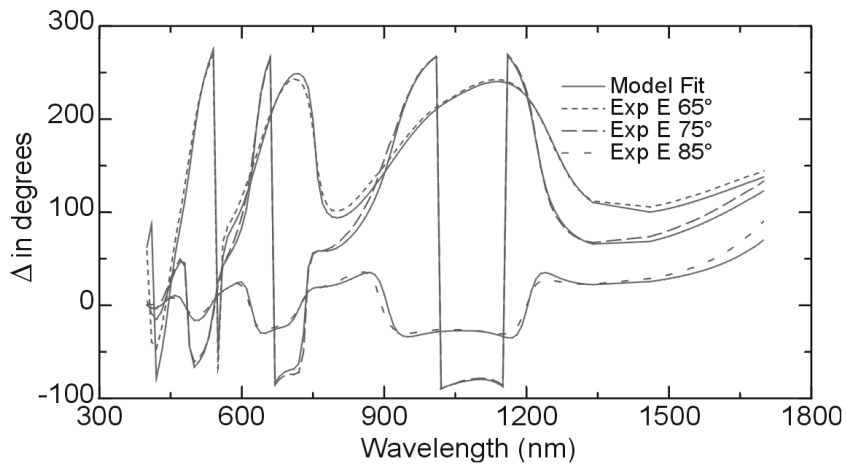
The measured ellipsometric data were analysed using software WVASE32TM [10]. Fig. 4.4 shows experimental and fitted ellipsometric data for the Cr(VI) coated zinc: (a) Ψ spectra and (b) Δ spectra. The fitted value of the refractive index, n , for a wavelength

of 600 nm is 1.7 ± 0.1 for the Cr(VI) coatings. This value of n is consistent with the values given in reference [7] for chromate conversion coatings on aluminum.

The thickness fitting results are shown in Fig. 4.5. For the Cr(VI) coatings on zinc or on the EG steel, the thickness of the coating initially increases fast with the dipping time. The thickness of the coating reaches a maximum at about 60 seconds and afterwards does not change much.



(a)



(b)

Fig. 4.4 Experimental and fitted ellipsometric data for the Cr(VI) coated zinc with dipping time 30 s: (a) Ψ spectra and (b) Δ spectra.

The thicknesses of the Cr(VI) coatings on the EG steel were also measured by means of positron beam analysis techniques using ^{22}Na as a positron source[11]. The positrons were injected in the samples with energies tuned between 100 eV to 30 keV. Positrons annihilate with electrons in the sample via the emission of 2γ -quanta. A non-zero component of the momentum of the electrons parallel to the γ emission results in a shift of the energy of the annihilation photons, which results in a Doppler broadening of the 511 keV ($= m_0c^2$) annihilation photo-peak by a few keV. This Doppler broadening effect can be detected by means of Ge detectors, and the results can be characterized by S (shape) and W (wing) parameters. The S parameter is defined as the ratio between the central part of the annihilation spectra (dN/dE versus E spectra) and the total spectra. This parameter indicates the fraction of positrons that annihilate with low momentum electrons, which is related to the open volume defects present in the sample. The W parameter indicates the fraction of the positrons that annihilate with high momentum electrons and is related to the chemical environment where the annihilation takes place[11].

The S and W parameters are measured as a function of the positron implantation energy E. The distribution function giving the fraction of positrons absorbed at depth z in a layer of single thickness is given by [12]

$$f(E, z) = \frac{pz^{p-1}}{z_0^p} \exp\left[-\left(\frac{z}{z_0}\right)^p\right] \quad (4.6)$$

where p is a shape parameter normally set to 2 and z_0 is related to the mean implantation depth (\bar{z}) given by

$$\bar{z} = \frac{\sqrt{\pi}}{2} z_0 = \frac{\alpha}{\rho} E^n \quad (4.7)$$

where $\alpha = 4.0 \text{ keV}^{-n} \mu\text{g}/\text{cm}^2$, $n = 1.62$, ρ is the density of the material and E the energy of the positrons in unit of keV.

Fig. 4.6 shows the S parameter as a function of the average positron implantation energy for the chromated galvanized steel with different dipping times. The S parameter has a value of 0.94 on the surface of the zinc coating (untreated) and of 1.01 inside the zinc coating. For the chromated samples the S parameter is about 0.88 on the surface

and 0.87 in the chromate layer. The zinc coatings are very thick (~13 μm) and positrons have not reached the steel substrate. The change in the chromate layer thickness with the dipping time can be clearly seen, since for positrons penetrating a thicker chromate layer needs higher implantation energy.

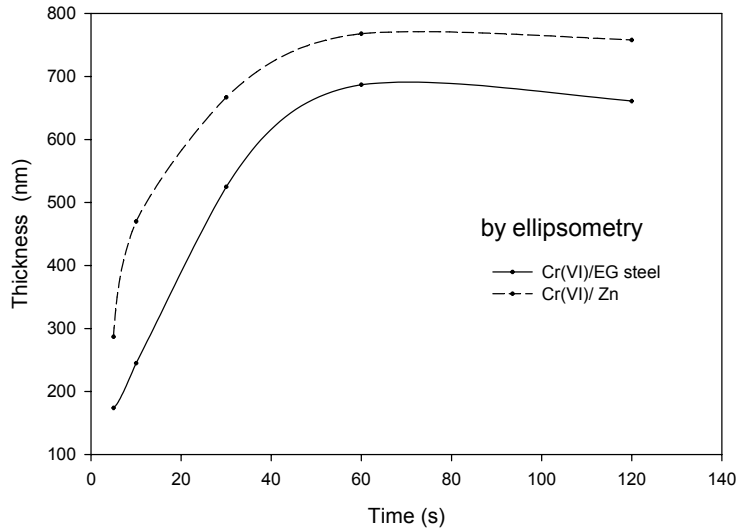


Fig. 4.5 Thickness of chromate conversion coatings obtained from SE plotted as a function of dipping time.

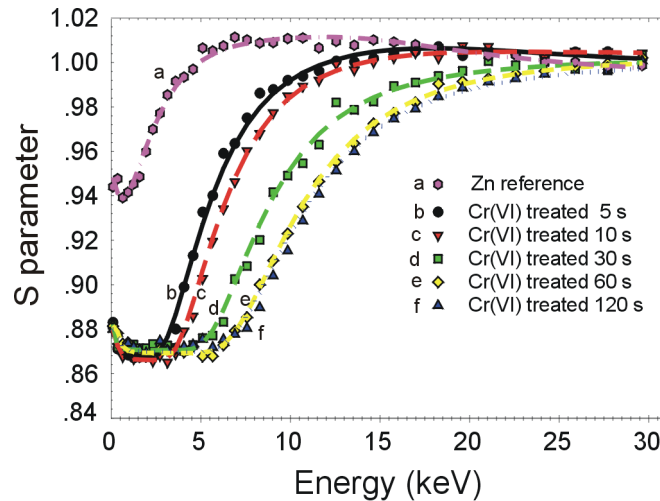


Fig. 4.6 S parameter as a function of the positron implantation energy for the chromated galvanized steel with different dipping times. The lines represent the VEPFIT analysis results and the S values were normalized to the crystal silicon parameters.

Fig. 4.7 shows the thickness of the chromate layer obtained from the Variable Energy Positron FITting (VEPFIT) analysis using 2 g/cm^3 as the density of the layer. It is in good agreement with the results obtained from the spectroscopic ellipsometry.

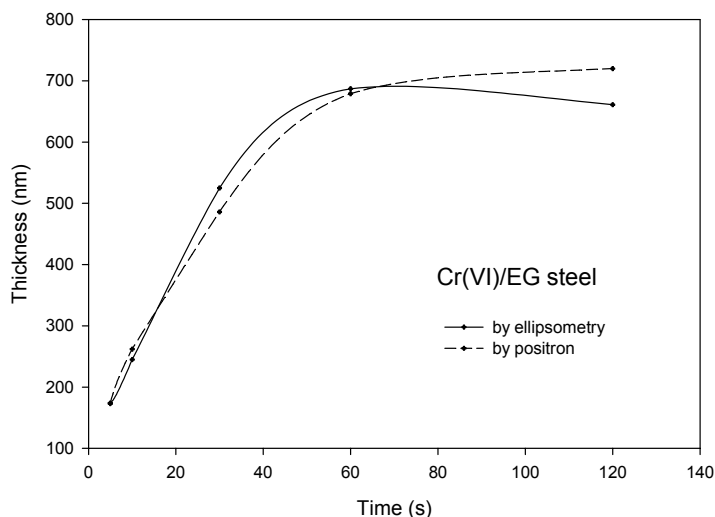


Fig. 4.7 The thickness of the chromate coatings obtained from positron (VEPFIT) analysis plotted as a function of dipping time compared with the results obtained from SE.

4.5 AES analysis

4.5.1 Auger effects

Auger electron spectroscopy (AES) is a useful technique to measure the chemical composition of the first few atomic layers of a given surface. The AES process is essentially a three-electron process (see Fig. 4.8). It is initiated by the ejection of a core electron by an incident high-energy electron, which creates a core hole in an atom. The core hole is filled by an electron from a higher energy shell, leaving the atom in an energetically excited state. The excited atom can lose energy either through the emission of X-ray fluorescence or through the ejection of another electron from a third energy level with a certain kinetic energy. This ejected electron is a so-called Auger electron

and is characteristic of the source atom. The basis of the AES technique is the measurement of the energy distribution of these Auger electrons.

The Auger electron energy, E_{Auger} , referenced to the Fermi level, can be written as [13]:

$$E_{Auger} = E_x - E_y - E_z - U_{eff} \quad (4.8)$$

where E_x , E_y and E_z are the binding energies of the three participating electrons and U_{eff} is the extra energy needed to remove an electron from a doubly ionised atom.

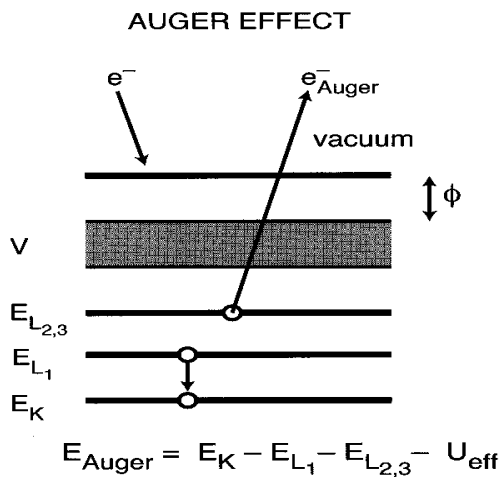


Fig. 4.8 Schematic diagram of the Auger effect in a solid. An incident electron creates a hole in the core level K by ionisation. The core hole (E_K) is filled by an electron from L_1 , releasing an amount of energy ($E_K - E_{L1}$), which causes the ejection of an electron (called an Auger electron) from a third energy level ($E_{L2,3}$) [13].

The most common method for quantification of surface concentration involves using sensitivity factors from pure elemental standards. Using bulk elemental standards, the surface concentration, C_A , of element A, can be calculated as [14]:

$$C_A = \frac{I_A / I_A^\infty}{\sum_i F_{iA} I_i / I_i^\infty} \quad (4.9)$$

where i is the number of elements on the surface, I_A is the Auger signal of element A, I_i^∞ is the intensity of the pure element standard and F_{iA} is the matrix correction factor.

The Auger matrix correction factor F_{iA}^A is related to the interaction of the primary beam with the target, which is approximately given by [14]:

$$F_{iA}^A = \left\{ \frac{1 + r_i(E_A)}{1 + r_A(E_A)} \right\} \frac{\lambda_i(E_A) a_A^3}{\lambda_A(E_A) a_i^3} \quad (4.10)$$

where $\lambda_i(E_A)$ is the electron attenuation length of electrons of energy E_A in the matrix i , $r_i(E_A)$ is the fractional contribution of Auger electron intensity arising from the backscattered electrons compared to those generated by the primary electron beam and a_i^3 is the total volume occupied by one i atom.

4.5.2 Auger depth profiles of conversion coatings

The elemental distribution as a function of depth through a layer can be obtained by means of AES combined with Ar^+ sputtering. AES measurements were performed using a PHI 4300 SAM with a LaB_6 cathode. A cylindrical mirror analyser (CMA) and a 5 keV ion-gun (PHI 04-303) were used. The capture angle of the CMA was $42^\circ \pm 6^\circ$. The spectrometer (CMA) was calibrated according to the method described in reference [15]. The base pressure in the analysis chamber was 3×10^{-10} Torr. A primary electron beam with energy of 5 keV and a current of 1 μA was incident on the sample surface at 30° to the normal. All the Auger electron spectra were acquired with an energy analyser resolution of $\Delta E/E = 0.6\%$.

For the AES analysis, a 40 nm gold layer was deposited on the chromated zinc in order to increase the conductivity of the surface. Alternate sputtering and data acquisition were performed to obtain the depth profile for two locations on each sample. The surface was rastered using a 2 keV Ar ion beam over an area of $4 \times 4 \text{ mm}^2$. The emission current was 20 mA and Ar pressure was 10 mPa. The ion beam was used at intervals of 1 minute and impinged on the sample surface at 50° to the normal. The Auger electron spectral regions recorded in the depth profiling are given in Table 4.1. Within each of these acquisition regions, data were recorded at 1.0 eV intervals except in the O1s region where a 0.5 eV interval was used.

The recorded spectra were analysed with Multipak 6.1A software (Physical Electronics). Firstly, the spectra were differentiated using a five-point Savitsky-Golay method [16]. The energy range for each element was redefined in order to isolate the peak for the transition of different elements (noted as analysis range in Table 4.1). For Zn, a linear least square fitting was performed to separate zinc metal from zinc oxide [16].

Table 4.1 The spectral line designations and acquisition details of the elements detected in the AES analysis.

Element	Auger line	Sensitivity factor @ 5keV [16]	Acquisition region (eV)	Analysis region (eV)
Au2	NNV	0.044	220 - 250	230 - 250
O1	KLL	0.296	450 - 600	500 - 518
Cr2	LMM	0.359	500 - 600	519 - 539
Zn1	LMM	0.296	960 - 1030	980 - 1000
S1	LMM	1.041	129.5 – 169.5	147 - 157

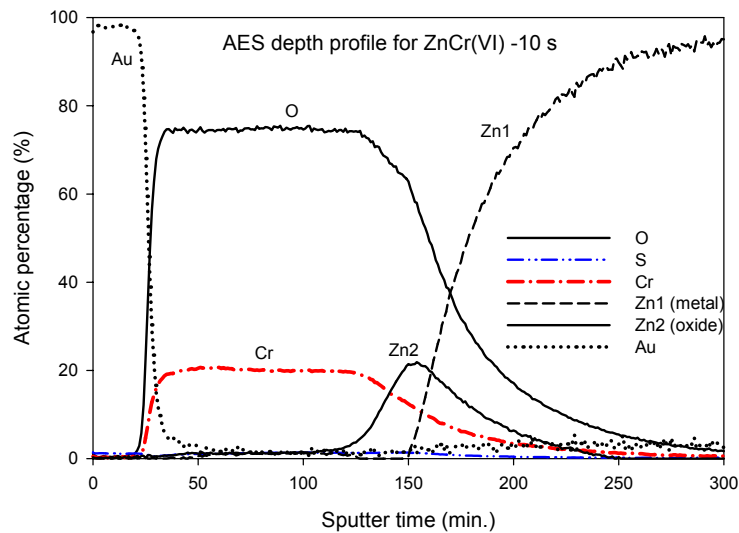


Fig. 4.9 AES depth profile analysis for a Cr(VI) coating (dipping time 10 s) on Zn.

Fig. 4.9 shows the AES depth profile analyses for the Cr(VI) coating on Zn with dipping time of 10 s. This figure shows that O, Cr, Zn and S are present in the coating.

The outmost layer of the Cr(VI) coating comprises mainly chromium oxides/hydroxides. Zinc oxide in the top layer is less than 4%. Zinc oxide is detected mainly at the interface between the chromium oxides/ hydroxides and the zinc metal substrate.

4.6 XPS analysis

4.6.1 Basic principle of XPS

X-ray photoelectron spectroscopy (XPS) is a powerful technique for study of the composition and chemical state of elements in a solid surface layer. Fig. 4.10 shows the schematic energy level diagrams of the photoemission process. The sample is irradiated with an X-ray beam of known energy ($h\nu$). Electrons of binding energy E_b , are ejected, where $E_b < h\nu$. The kinetic energy E_K of these electrons can be measured in the spectrometer, and is given by [17]:

$$E_K = h\nu - E_b - \Phi_{sp} \quad (4.11)$$

where Φ_{sp} is the work function of the spectrometer, which is the combination of the sample work function Φ_s and the work function induced by the analyser. Since the work function is a virtual constant, it can be compensated electronically. Thus, eliminating the work function term in equation (4.11) gives

$$E_K = h\nu - E_b \quad (4.12)$$

or

$$E_b = h\nu - E_K \quad (4.13)$$

Thus, by measuring the kinetic energy E_K of the photoelectrons, one knows the binding energy E_b of the electrons from equation (4.13). From the binding energy, the elements in the matrix can be distinguished.

From XPS, data can be obtained quantitatively by determining the area under the peaks in question and applying sensitivity factors. The concentration C_A of element A can be calculated using equation (4.9) with the XPS matrix factor, F_{iA}^x , which is given by[14]:

$$F_{iA}^x = \frac{\lambda_i(E_A) a_A^3}{\lambda_A(E_A) a_i^3} \quad (4.12)$$

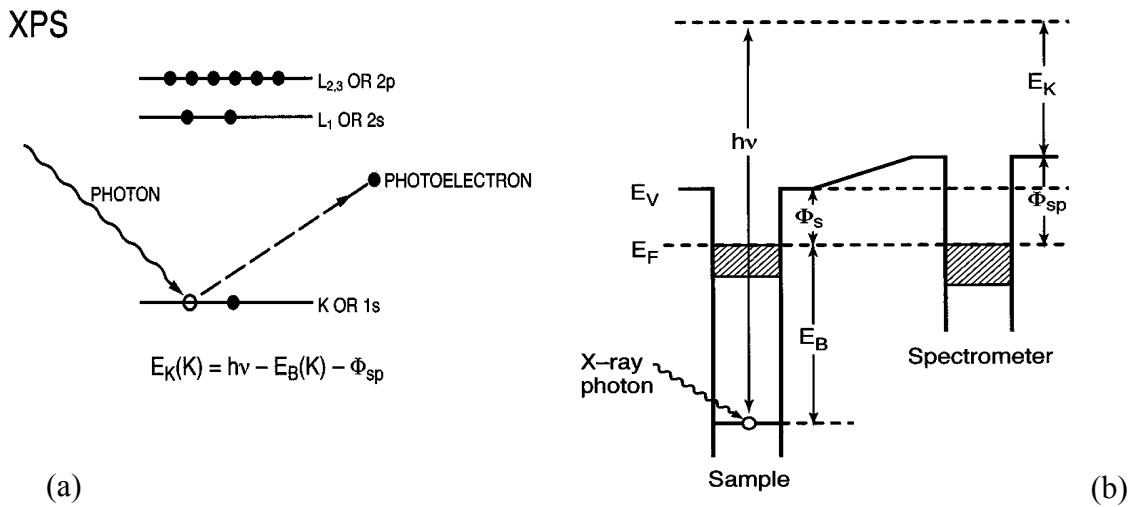


Fig. 4.10 (a) XPS process involves the removal of a core electron, (b) schematic diagram of the photoemission process. The sample is irradiated with an X-ray beam ($h\nu$) and electrons of binding energy E_b are ejected. The kinetic energy E_k of these electrons can be measured in the spectrometer. Φ_s and Φ_{sp} are the work functions of the sample and the spectrometer, respectively [17].

4.6.2 XPS analysis of Cr(VI)-based conversion coatings

The use of XPS to analyse chromate coatings on Al alloys and zinc alloys has been reported by some researchers [18,19]. When using XPS to study a chromate layer, the photo-reduction of hexavalent Cr under x-ray radiation has to be considered [20,21]. By controlling the analysis condition, it is still possible to use XPS to assess the Cr species in the chromate layers[22].

XPS analysis was carried out with a PHI 5400 ESCA using 400 Watt Mg K_{α} radiation (1253.6 eV). This instrument is equipped with a Spherical Capacitor Analyser (SCA) operating with a constant pass energy value. The energy scale of the spectrometer was calibrated according to Anthony et al.[23]. Overview spectra were obtained in the range of 0 – 1100 eV with an analyser pass energy of 71.55 eV. The intensities of Cr 2p, O 1s, C 1s, S 2p and Zn 2p photoelectron lines were recorded separately with an analyser pass energy of 35.75 eV. The electrons emitted from the specimens were detected at an angle of 45° with respect to the specimen surface. The C 1s peak (284.8 eV) was used as a reference to correct for electrostatic charging. The X-ray satellites, present in all measured spectra as a consequence of the non-monochromatic nature of the incident X-ray beam, were removed using the relative height and displacements with respect to the height and position of the Mg $K_{\alpha 1,2}$ line. The compositions were evaluated using atomic sensitivity factors supplied by Perkin-Elmer corporation[24]. In order to assess the relative amounts of the species constituting the photoelectron lines, curve fitting was performed with symmetrical Gaussian-Lorentzian peaks after smoothing of the curve and Shirley-type subtraction of the background. The number of components to be fitted to any particular spectrum was determined by choosing the fit with the minimum reduced chi-squared value (χ^2). Cr 2p spectra were fitted either in doublets, Cr $2p_{(3/2, 1/2)}$, or in singlets for the Cr $2p_{3/2}$ peak. For the doublets, Cr $2p_{3/2}$ to Cr $2p_{1/2}$ splitting of 9.4 eV was used for chromate, 9.5 eV for Cr_2O_3 and 9.5 eV for $Cr(OH)_3$ or $CrOOH$. Three-component fitting was performed for chromium in the form of Cr_2O_3 (576.3 ± 0.2 eV), $Cr(OH)_3$ or $CrOOH$ (577.3 ± 0.2 eV) and Cr(VI) (579.2 ± 0.2 eV) in the chromate layer [18,25,26].

Two Cr(VI) coated zinc samples for each dipping time were analyzed using XPS. In order to investigate the photo-reduction effect on the Cr(VI) species, detailed XPS spectra were acquired sequentially with intervals of 1 hour between each measurement for one specimen (which had chromating time of 60 s). During the intervals between acquisitions of spectra, the X-ray beam was off. Each measurement including all individual lines (see above) took about 45 min (under X-ray radiation).

The XPS overview spectra show that C, O, Cr and S are present in the chromate layer for an as-chromated sample with dipping time of 30 s (see Fig. 4.11). The signal

from zinc is not significant for this as-chromated sample. Carbon has been detected on all samples as an impurity from handling the samples in air. The compositions of the samples were calculated from the peak areas remaining after subtraction of the background intensity, applying the atom sensitivity factors[24]. The relative atomic percentages for O, S, Cr and Zn in the chromate coatings on zinc with different dipping times were calculated and are shown in Table 4.2 (the adventitious carbon was not calculated). For the chromate coating with dipping time 60 s, the oxygen content is 73 at.% and the chromium content is 23 at.%. This is in agreement with the AES results. The ratio of oxygen to chromium varies from 3.2 to 3.7 for coatings with different dipping times. The zinc content is at a level of 4 at.% for the coatings with a dipping time of 1 s, while it is less than 1 at.% for the coatings with dipping times longer than 10 s. The sulphur content is about 2% for most of the chromate coatings.

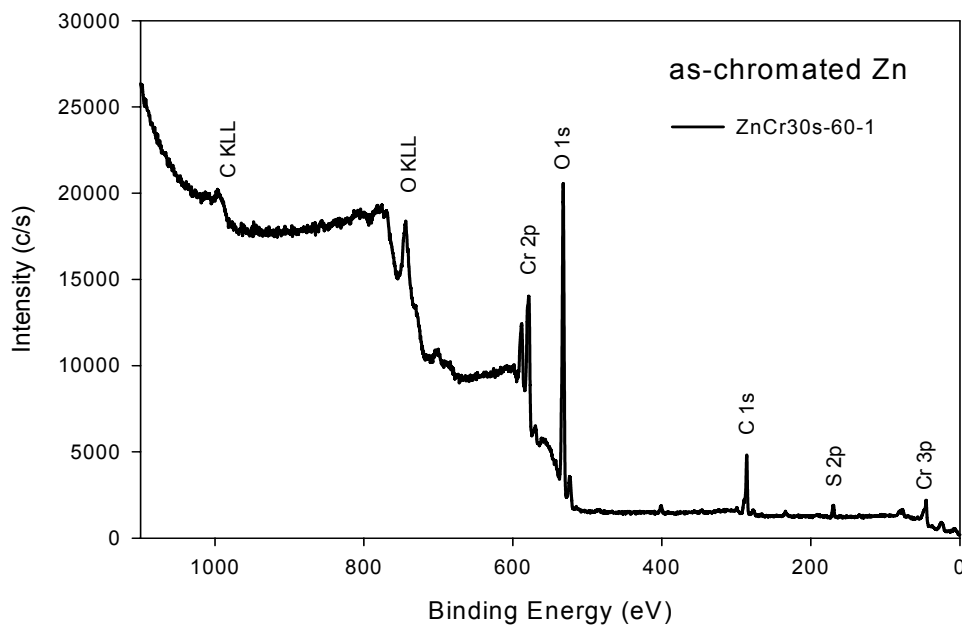


Fig. 4.11 XPS spectrum for a Cr(VI) coating on zinc with dipping time 30 s.

Cr 2p peaks, obtained from samples with different dipping time, are shown in Fig. 4.12. All the Cr 2p_{3/2} spectra show two peaks. A peak near 577 eV is attributable to Cr(III) and a shoulder near the binding energy of 579 eV is attributable to Cr (VI). Fig. 4.13 shows the fitted Cr 2p_{3/2} peaks for the sample with dipping time 30 s. The ratio of

Cr(VI) to Cr (III) is about 4 : 6. Other fitted results are shown in Table 4.3. The content of Cr(VI) varies from 32 to 42% of the total chromium as the dipping time changes from 1 to 60 s (see Fig. 4.14).

Table 4.2 Relative elemental percentage (at. %) for the Cr(VI) conversion coatings on zinc by XPS.

Chromating time (s)	O	S	Cr	Zn
1	73	2	21	4
5	76	2	22	0.2
10	77	2	21	0.2
30	75	2	23	0
60 (XPS-1)	73	3	23	0.8
60 (XPS-2)	74	3	23	0.6
60 (XPS-3)	72	3	24	0.9
60 (XPS-4)	72	2	25	1

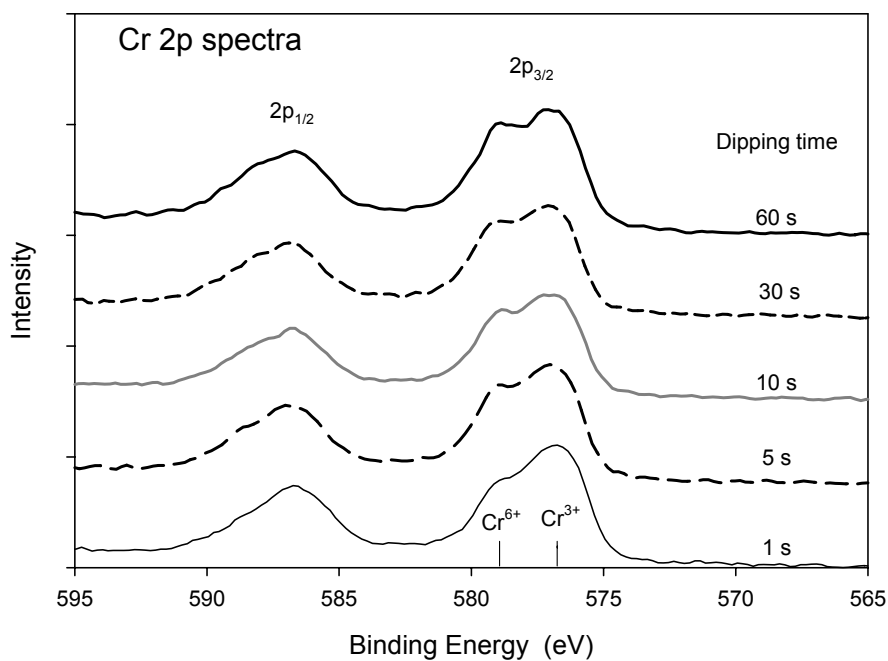


Fig. 4.12 Cr 2p spectra for the Cr(VI) coatings with different dipping times: 1 s, 5 s, 10 s, 30 s and 60 s.

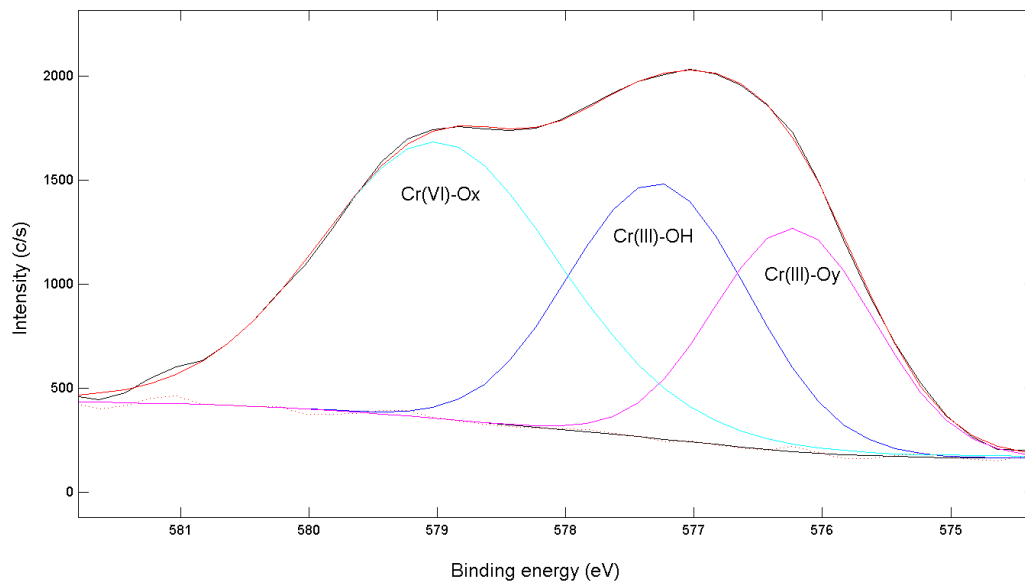


Fig. 4.13 Fitting of Cr 2p_{3/2} spectra for a chromated sample with dipping time of 30 s. (Cr_2O_3 : 576.3 ± 0.2 eV, $\text{Cr}(\text{OH})_3$ or CrOOH : 577.3 ± 0.2 eV and $\text{Cr}(\text{VI})$: 579.2 ± 0.2 eV).

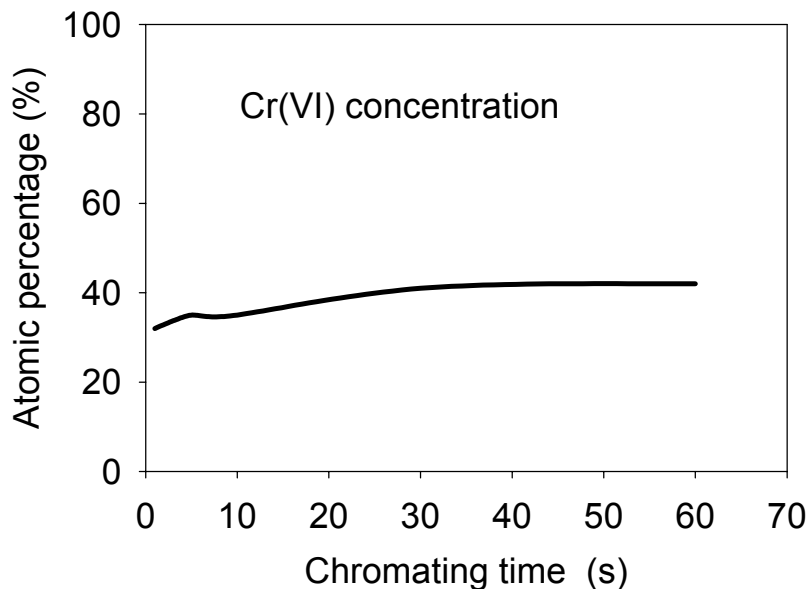


Fig. 4.14 Cr(VI) concentration in the chromate layer versus dipping time.

Table 4.3 Summary of Cr 2p_{3/2} spectrum fitting for the chromate layer on zinc.

Chromating time (s)	Cr 2p _{3/2} B.E.(eV)	Components	at. %	χ^2
1	576.4	CrO _{3/2}	16	1.01
	577.3	Cr(OH) ₃	52	
	579.3	Cr(VI)	32	
5	576.4	CrO _{3/2}	13	0.13
	577.3	Cr(OH) ₃	52	
	579.2	Cr(VI)	35	
10	576.3	CrO _{3/2}	23	1.34
	577.4	Cr(OH) ₃	42	
	579.1	Cr(VI)	35	
30	576.3	CrO _{3/2}	24	1.08
	577.4	Cr(OH) ₃	35	
	579.2	Cr(VI)	41	
60 (XPS-1)	576.1	CrO _{3/2}	18	0.89
	577.2	Cr(OH) ₃	40	
	579.1	Cr(VI)	42	
60 (XPS-2)	576.3	CrO _{3/2}	17	0.98
	577.3	Cr(OH) ₃	48	
	579.2	Cr(VI)	35	
60 (XPS-3)	576.1	CrO _{3/2}	19	0.65
	577.2	Cr(OH) ₃	47	
	579.1	Cr(VI)	34	
60 (XPS-4)	576.2	CrO _{3/2}	18	0.67
	577.3	Cr(OH) ₃	49	
	579.2	Cr(VI)	33	

The O 1s spectrum for the chromate coatings was fitted with three components at 530.1, 531.3 and 533.1 eV for oxide anions, hydroxyl groups and adsorbed water, respectively[18]. The integral intensity ratio of the three components is about 5:4:1 (see

Fig. 4.15). If the 10% O 1s peak attributed to adsorbed water in the coating is taken out, the ratio of the remaining oxygen to chromium becomes approximately 3.

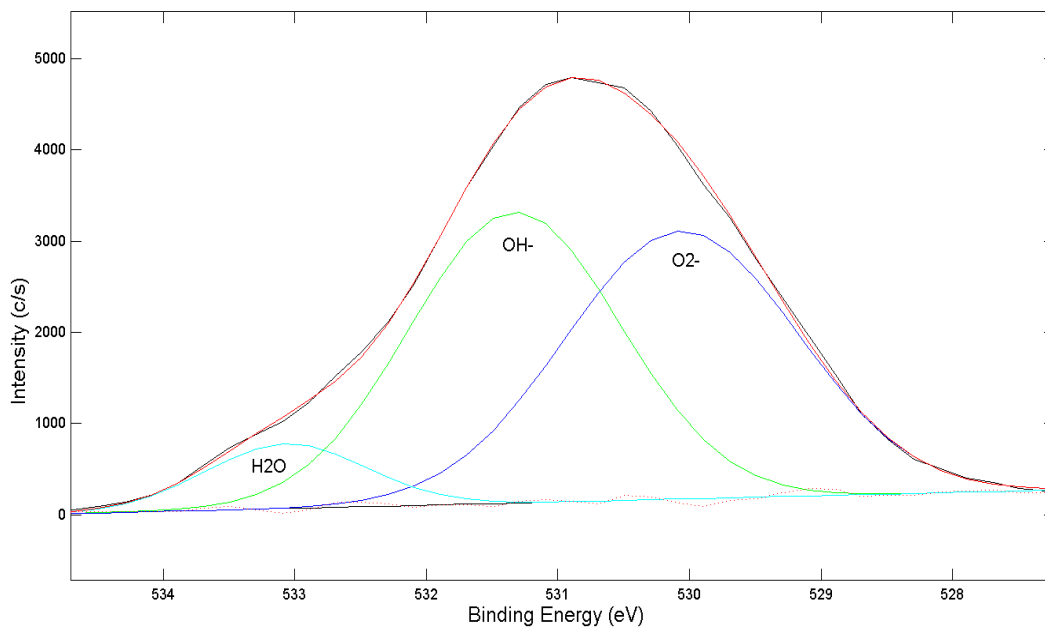


Fig. 4.15 Fitting of the O 1s spectra for the chromate coating with dipping time 30 s. (O^{2-} : 530.1 ± 0.2 eV, OH^- : 531.3 ± 0.2 eV and H_2O : 533.1 ± 0.2 eV).

4.6.3 Photo-reduction of Cr(VI) species

Fig. 4.16 shows the sequentially acquired Cr 2p XPS spectra for the sample with dipping time 60 s. The peak near 579 eV attributed to Cr(VI) becomes smaller after the first measurement which took about 45 minutes X-ray radiation. About 17 % of Cr(VI) was reduced after the first measurement and afterwards the reduction rate became slow and the percentage of Cr(VI) remained about 33% of the total chromium (see Fig. 4.17). The atom ratio of oxygen to chromium has also slightly decreased. This may imply that some decomposition of Oxo-Cr(VI) species has happened.

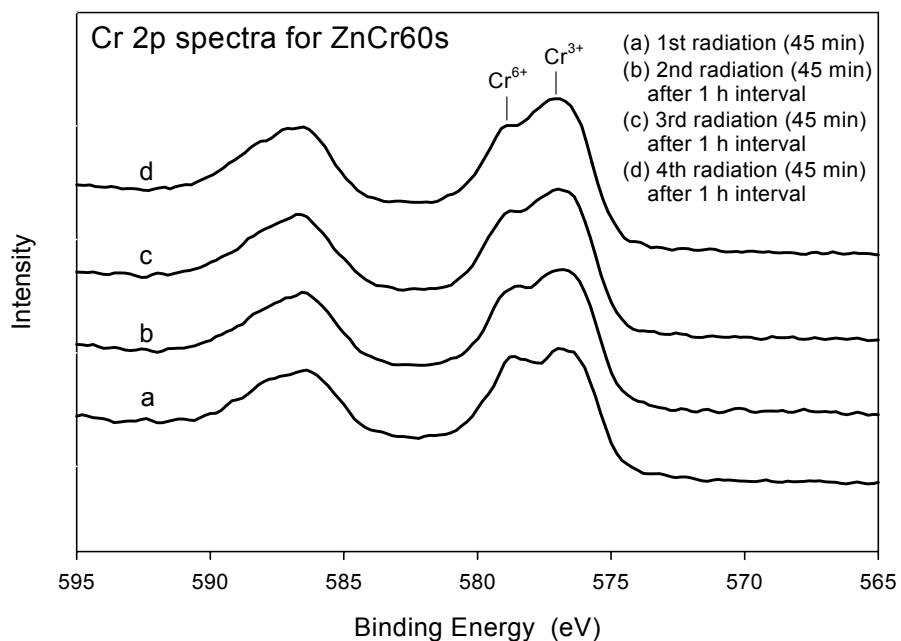


Fig. 4.16 Cr 2p spectra acquired sequentially with an interval of 60 min without X-ray radiation for a chromate coating (dipping time 60 s). Each spectrum acquisition takes 45 min.

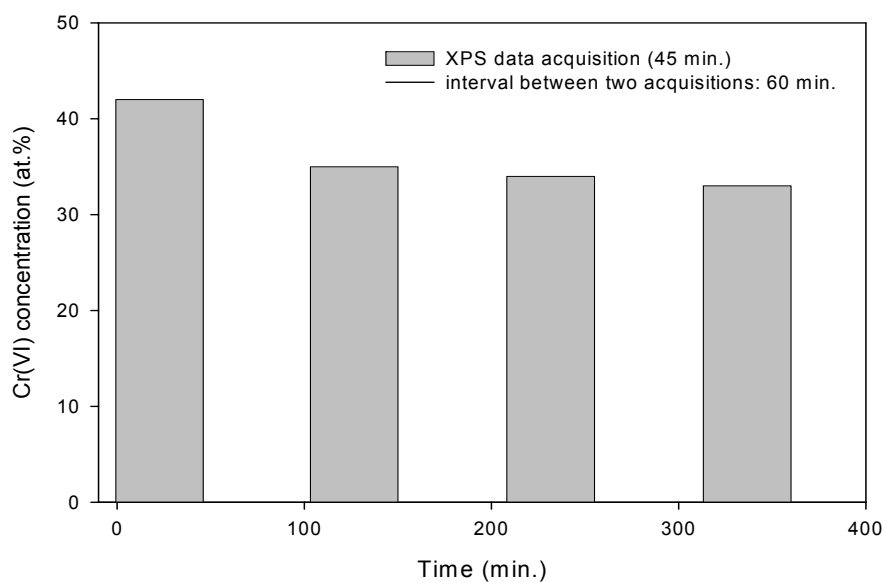


Fig. 4.17 Cr(VI) concentration changes with time in the vacuum chamber. Each XPS spectrum acquisition takes 45 min. and there is no X-ray radiation in the intervals (60 min.) between acquisitions.

4.6.4 Chromate layer after exposure to NaCl solution

Chromated zinc specimens with dipping time 10 s (ZnCr10s) and 30 s (ZnCr30s) were immersed in a quiescent 0.01 M NaCl solution (pH 6) for 24 h. After immersion, the specimens were dried in flowing air and the compositions of the coatings were analysed using XPS. Fig. 4.18 shows an XPS spectrum acquired from the sample (ZnCr30s-2) that was exposed to the 0.01 M NaCl solution for 24 h. The composition change is significant; the intensity of the Cr 2p signal has decreased and the Zn signal increased after the immersion test. The atomic percentage for elements of O, Cr, S and Zn presented in the surface layer before and after the immersion test is shown in Table 4.4. The amount of chromium for the sample ZnCr30s decreased from 23% as-chromated to 10% after immersion.

Fig. 4.19 shows the Cr 2p spectra for the chromated coatings (ZnCr30s) before and after immersion. The Cr(VI) peak at 579.2 eV became smaller than before. The fitting of Cr 2p spectra showed that the ratio of Cr(VI) to total Cr decreased to 1:4. Similar results are obtained for the sample ZnCr10s (see Table 4.4).

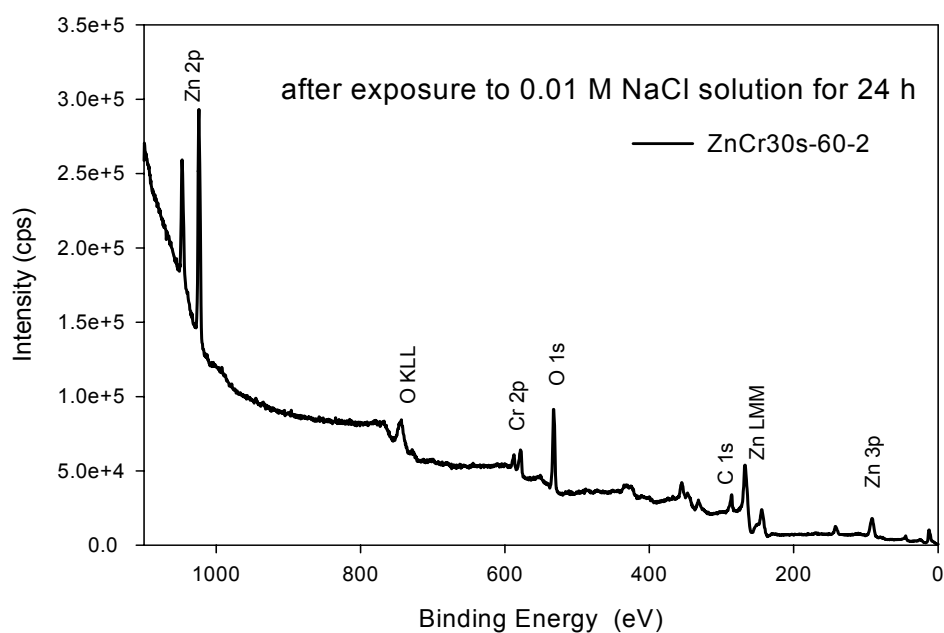


Fig. 4.18 XPS spectrum for a chromated zinc sample after immersion in 0.01 M NaCl solution (pH 6) for 24 h.

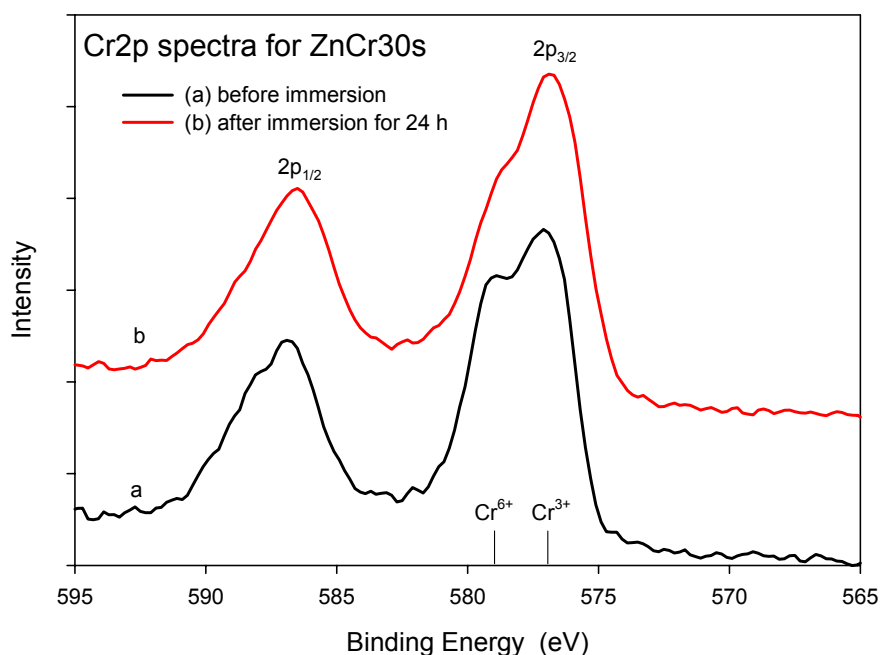


Fig. 4.19 Cr 2p spectra for the chromate coatings (ZnCr30s) (a) before and (b) after immersion in 0.01 M NaCl solution for 24 h.

Table 4.4 Atomic percentage of elements in the surface layer of chromate coatings before and after exposure to 0.01 M NaCl solution

Sample	O	S	Cr	Zn	Cr(VI)/Cr (ratio)
ZnCr30s-1 unexposed	75	2	23	0	0.4
ZnCr30s-2 exposed	50	1	10	39	0.25
ZnCr10s-1 unexposed	77	2	21	0.2	0.35
ZnCr10s-2 exposed	63	1	13	22	0.25

4.7 FTIR analysis

The composition of the Cr(VI) coatings on zinc sheet was also analyzed by means of FTIR. In order to distinguish the Cr(VI)-O and Cr(III)-O absorption bands, standard CrO₃ powder, Cr₂O₃ powder and 1 M sodium sulfate solution were analyzed using

FTIR. The reflection absorbance IR spectra were obtained on a NexusTM spectrometer from Nicolet using OMNIC software. The powder and solution samples were analyzed using an attenuated total reflection (ATR) method. The chromate coating on zinc sheet was analyzed using a reflection-absorption method. The sheet was laid on a flat sample support. The IR beam was incident on the sample surface at 84° to the normal. The detector used was a liquid nitrogen cooled MCT-B detector. The spectra were recorded in the 4000 to 400 cm⁻¹ range with a resolution of 4 cm⁻¹.

Fig. 4.20 shows the IR spectra for CrO₃ powder, Cr₂O₃ powder and 1 M sodium sulfate solution. The absorbance band at 3300 cm⁻¹ is attributed to water, and the band at 1625 cm⁻¹ is attributed to the H-O-H bending motion [27]. The band at 1100 cm⁻¹ is attributable to SO₄²⁻ [28]. The band at 953 cm⁻¹ is from vibration of Cr(VI)-O and the band at 608 cm⁻¹ is from Cr(III)-O[29,30].

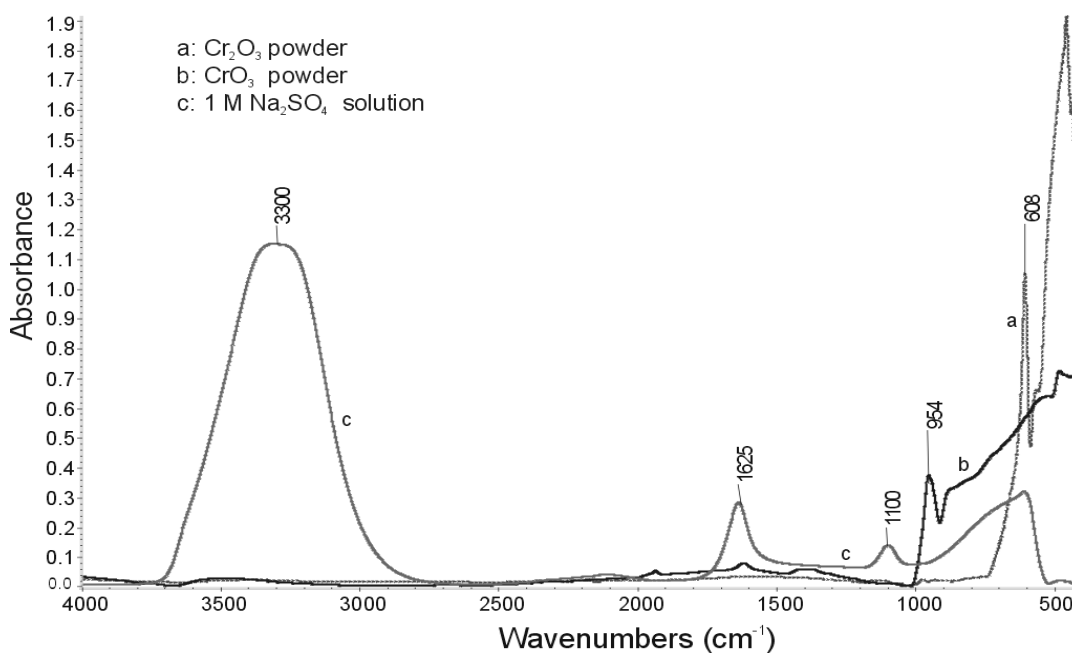


Fig. 4.20 Infrared spectra for (a) Cr₂O₃ powder, (b) CrO₃ powder and (c) 1 M sodium sulfate solution.

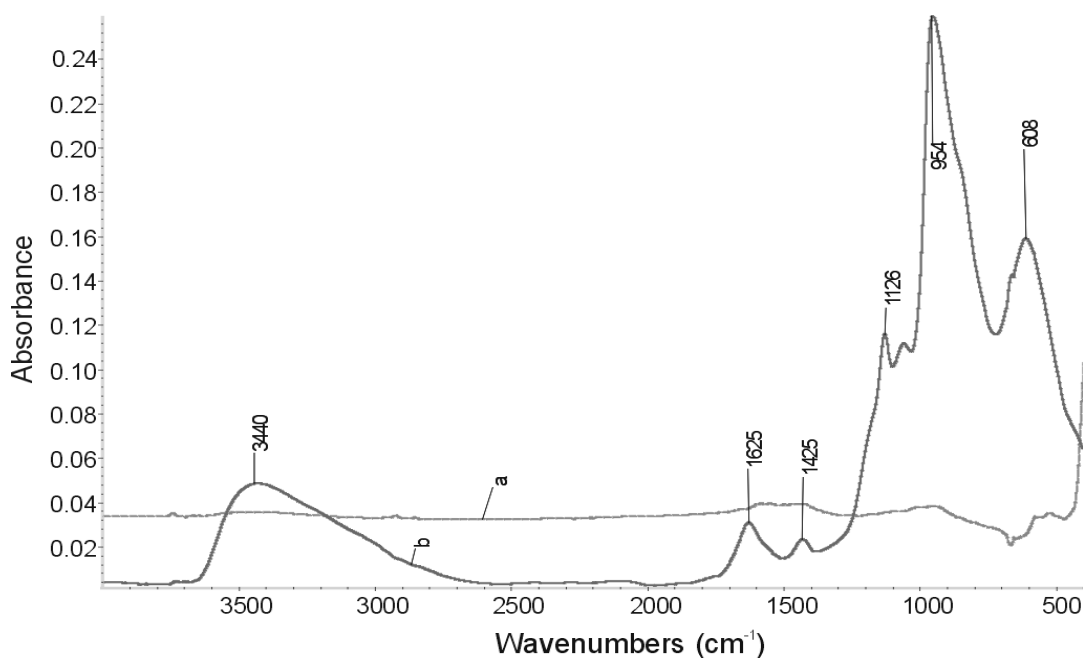


Fig. 4.21 FTIR spectra acquired from (a) a zinc substrate, (b) Cr(VI) coating on zinc sheet with dipping time 10 s.

Fig. 4.21 shows FTIR spectra acquired from (a) a zinc substrate, (b) a Cr(VI)-based coating on zinc sheet with dipping time 10 s. The broad absorption bands at 3440 and 1625 cm⁻¹ are attributable to the vibration of water or water of hydration. The band at 954 cm⁻¹ is attributable to Cr₂O₇²⁻ or CrO₄²⁻ anions [9,31,32]. The band at 1126 cm⁻¹ is from the vibration of SO₄²⁻ in the coating [28]. The band at 608 cm⁻¹ is due to the vibration of Cr(III)-O_x [29]. The peak at 1425 cm⁻¹ may be attributable to the bending vibration of water coordinated to Cr₂O₃·2H₂O [7,29].

4.8 Discussion

The SEM images presented in Fig. 4.1 show that there are no cracks in chromate coatings on zinc when the dipping time is 1 or 5 s. Microcracks emerge in the chromate coatings when the dipping times increases to 10 s. The length of crack per unit area and the average width of the cracks in the coatings increase with the dipping time. This can be attributed to the fact that, as reported in the literature [1], the tensile stress increases with the thickness of the coatings.

The SE results presented in Fig. 4.5 show that the thickness of the chromate layer initially increases rapidly with dipping time. After 60 seconds, the thickness of the layer approaches a maximum. This indicates that the reduction of Cr(VI) and the precipitation of Cr(III) oxides/hydroxides on the zinc surface are initially fast and afterwards slow down. This may be due to the previously deposited chromate layer covering the zinc surface and decreasing the driving force of the formation of the chromate layer. Zinc dissolution can continue but is limited by diffusion. A maximum content of zinc oxide detected at the interface between the chromate layer and the zinc substrate gives a piece of evidence.

The AES depth profiles presented in Fig. 4.9 and the XPS analysis results (in Table 4.2) show that Cr, O, S and Zn are present in the chromate coatings. The sulphur is from the sulphate in the coating bath. The concentrations of S and Zn are very low at the outer surface of the coating. The ratio of oxygen to chromium is about 3, if the 10% O 1s peak attributed to adsorbed water in the coating is taken out. The top chromate layer contains hexavalent and trivalent chromium oxides or hydroxides. The ratio of Cr(VI) to Cr (III) is about 4 : 6. AES depth profiles show that the concentration of chromium decreases with the depth in the chromate layer.

The photo-reduction of Cr(VI) during the XPS analysis has been observed, as suggested in literature[20]. The damage by X-ray radiation may have resulted from the following effects: “coulombic explosion”; direct ejection of photoelectrons from the valence band; the production of secondary electrons in the material as well as Bremsstrahlung[20,33]. It was reported[20] that the dominant mechanism leading to photo-reduction is the “coulombic explosion”. For example, under x-ray radiation, ejection of a core photoelectron from Cr results in an Auger process in the valence band of O²⁻ in which a temporary positive charge can be imparted to the oxygen ion. In maximum valence compounds, such as Cr⁶⁺ that have no 3d electrons to fill deeper core holes, electrons in the valence band of the oxygen ion may fill the ionized core states of the chromium. This leads to changes in the chromium oxidation state.

The Cr(VI) content in a chromate layer may be under-estimated by XPS due to the photo-reduction effect, not saying to use Ar⁺ to sputter the surface to get depth profile of

chromium in valence of +6 in the layer. In order to minimize photodecomposition, the counting time has to be limited at the expense of a high signal to noise ratio. The reduction of the chromium was less than 17% when acquisition time was limited to 45 min. If the analysis conditions remain constant, then it is still possible to use XPS to semi-quantitatively analyse the Cr species in the top chromate layer and it is useful to use XPS to determine the composition change on the surface after corrosion tests.

After immersion in 0.01 M NaCl solution for 24 h, the amount of Cr in the chromate layer is less than that of the as-chromated sample (see Table 4.4). After the immersion test, the signal of Zn increased significantly, which is attributable to zinc dissolution and the deposition of hydroxide/oxide on the surface. This may lead to the decrease of the relative percentage of chromium in the XPS analysis. However, the Cr 2p spectra show that the ratio of Cr(VI) to total Cr decreased to 1:4. The decrease of the content of Cr(VI) means that partial chromate species in the chromate layer indeed has dissolved. The dissolved Cr(VI) species can be released to the solution and transport to near defects to be reduced to Cr(III) oxides/hydroxides, leading to passivate the defects.

4.9 Conclusions

1) No cracks in the chromate coatings on zinc have been observed when the dipping time is 1 or 5 s. Microcracks appear in the coatings when the dipping time increases to 10 s or longer. The length of crack per unit area and the crack size increase with dipping time in the chromate bath.

2) The thickness of the chromate coatings increases with dipping time in the chromating baths. The layer grows fast within initial 30 seconds, and after 60 seconds it approaches a maximum.

3) Both XPS and FTIR analyses show that the chromate layer contains Cr(VI) and Cr(III). Limiting the acquisition time to 45 min or less, the photo-reduction of Cr(VI) during the XPS analysis can be less than 17% and a semi-quantitative assessment of the Cr species is possible. The Cr(VI) content varies from 32 to 42% of the total chromium in the outermost layer of the coating when the dipping time changes from 1 s to 60 s.

4) AES depth profiles show that chromium oxides are the main components in the chromate coatings on zinc. The zinc oxide is mainly located at the interface between the chromium oxides and the zinc substrate.

5) After immersion in the 0.01 M NaCl solution for 24 h, zinc oxide/hydroxide are observed on the surface of the chromate coatings. The relative amount of chromium, mainly Cr(VI), has decreased.

References

1. N. M. Martyak, *Surf. Coat. Technol.*, 88 (1996) 139.
2. N. M. Martyak, J. E. McCaskie and L. Harrison, *Metal Finishing*, 94 (1996) 65.
3. X. Zhang, C. van den Bos, W. G. Sloof, H. Terryn, A. Hovestad and J. H. W. de Wit, in: *Corrosion Science in The 21st Century*, Manchester, UK, 7-11 July, 2003; B. Cottis (Ed.), *J. Corros. Sci. Engineering*, Vol. 6, paper 57 (2003) (ISSN 1466-8858).
4. R. M. A. Azzam and N. M. Bashara, *Ellipsometry And Polarized Light*, 2nd ed., (Elsevier Science B.V., 1987).
5. H. G. Tompkins, *A User's guide to Ellipsometry*, (Academic Press, Inc., USA, 1993).
6. J. N. Hilfiker and R. A. Synowicki, *Semiconductor Fabtech*, 5th Edition (1996).
7. P. Campestrini, S. Bohm, T. Schram, H. Terryn and J. H. W. de Wit, *Thin Solid Film*, 410 (2002) 76.
8. T. Schram, J. De Laet and H. Terryn, *Thin Solid Film*, 313-314 (1998) 727.
9. F. Petit, H. Debontride, M. Lenglet, G. Juhel and D. Verchere, *Appl. Spectroscopy*, 49 (1995) 207.
10. Computer Program, *WVASE32TM*, version 3.386, J.A. Woollam Co., Inc., Lincoln, USA, 1991.
11. R. E. Galindo, A mesoscopic approach to the study of thin protective coatings by Positron Beam Analysis and Scanning Electron Microscopy, thesis, PhD Thesis, Delft University of Technology, The Netherlands, 2003.
12. A. F. Makhov, *Sov. Phys. Solid State*, 2 (1961) 1934.
13. P. C. Dastoor, in: *Surface Analysis Methods in Materials Science*, 2nd ed., D. J. O'Connor, B. A. Sexton and R. St. C. Smart (Eds.), Springer, Germany, 2003, Chap. 6, p. 155-174.
14. M. P. Seah, *Surf. Interface Anal.*, 9 (1986) 85.

15. D. Briggs and M. P. Seah, *Practical Surface Analysis*, 2nd ed., (John Wiley & Sons, London, 1990).
16. *Operators's Multipak Software Manual - version 6.0*, (Physical Electronics Inc., Chanhassen, USA, 1998).
17. M. H. Kibel, in: *Surface Analysis Methods in Materials Science*, 2nd ed., D. J. O'Connor, B. A. Sexton and R. St. C. Smart (Eds.), Springer, Germany, 2003, Chap. 7, p. 175-201.
18. A. E. Hughes and R. J. Taylor, *Surf. Interface Anal.*, 25 (1997) 223.
19. Y. Yoshikawa and J. F. Watts, *Surf. Interface Anal.*, 20 (1993) 379.
20. G. P. Halada and C. R. Clayton, *J. Electrochem. Soc.*, 138 (1991) 2921.
21. A. G. Schrott, G. S. Frankel, A. J. Davenport, H. S. Isaacs, C. V. Jahnes and M. A. Russak, *Surf. Sci.*, 250 (1991) 139.
22. D. Chidambaram, G. P. Halada and C. R. Clayton, *Appl. Surf. Sci.*, 181 (2001) 283.
23. M. T. Anthony and M. P. Seah, *Surf. Interface Anal.*, 6 (1984) 95.
24. J. F. Moulder, W. F. Stickle, P. E. Sobol and K. D. Bomben, *Handbook of X-ray photoelectron spectroscopy*, (Perkin-Elmer Corp., 1992).
25. J.-O. Nilsson, S.-E. Hörnström, E. Hedlund, H. Klang and K. Uvdal, *Surf. Interface Anal.*, 19 (1992) 379.
26. B. S. Norgren, M. A. J. Somers, W. G. Sloof and J. H. W. de Wit, in: 12th Scandinavian Corrosion Congress & Eurocorr '92, 1992; P. J. Tunturi (Ed.), 1 (The Corrosion Society of Finland, Espoo, Finland, 1992) pp. 139-149.
27. R. A. Nyquist and R. O. Kagel, *Infrared spectra of inorganic compounds*, (Academic Press, Inc, New York, 1971).
28. J. Kasparek and M. Lenglet, *La Revue de Métallurgie - CIT*, 94 (1997) 713.
29. J. T. Vandeberg, D. G. Anderson, J. K. Duffer, J. M. Julian, R. W. Scott, T. M. Sutliff and M. J. Vaickus, *An infrared spectroscopy atlas for the coatings industry*, (Federation of Societies for Coating Technology, Philadelphia, 1980).
30. L. Xia and R. L. McCreery, *J. Electrochem. Soc.*, 145 (1998) 3083.
31. M. Lenglet, F. Petit and J. Y. Malvaut, *Phys. Stat. Sol. (a)*, 143 (1994) 361.
32. M. Handke, A. Stoch, S. Sulima, P. L. Bonora, G. Busca and V. Lorenzelli, *Mater. Chem.*, 7 (1982) 7.
33. J. Cazaux, *Appl. Surf. Sci.*, 20 (1985) 457.

Chapter 5

Electrochemical Characterization of Cr(VI)-based Conversion Coatings

5.1 Introduction

In chapter 4, the morphology and the composition of chromate coatings with different dipping times in the chromating bath have been investigated using surface analytical methods. The results show that the surface structure and even compositions of the coatings change with the dipping time. The morphology and the composition of the coatings on zinc play an important role in protecting zinc from corrosion[1,2].

A variety of methods such as gravimetric, electrochemical and solution analysis methods enable the determination of the corrosion rates of metals [3,4]. Gravimetric mass loss and solution analysis for metallic cations provide historical or integrated mass loss from corrosion over some period of time. Electrochemical methods, for example, polarization resistance measurements, enable determination of instantaneous interfacial reaction rates, such as corrosion rates and exchange current densities from a single experiment [3,4]. The corrosion rate of a metal can be evaluated by means of the polarization resistance, since the corrosion rate is inversely proportional to the polarization resistance[4]. Electrochemical measurements such as polarization and EIS measurements can be used for evaluating the corrosion rate of chromate treated zinc in an aqueous environment (see Chapter 2).

In this chapter, the corrosion behavior of unchromated and chromated zinc (with different dipping times) is studied using polarization and electrochemical impedance spectroscopy (EIS) measurements.

5.2 Experimental

5.2.1 Open circuit potential and polarization measurements

The chromate coatings on zinc were prepared as described in Chapter 4. The open-circuit potential (OCP) and potentiodynamic polarization measurements were carried out in a glass cell containing a treated or untreated zinc sheet, platinum counter electrode and a reference electrode (saturated calomel electrode: $E^0 = 0.241$ V vs. NHE). In the aerated 0.01 M NaCl solution (pH 6), the solution was open to air and the specimen was left in the solution for 1 h at open circuit before the polarization measurements. To obtain the polarization curves, the potential was scanned from the OCP to 0.25 V versus the OCP to get the anodic parts and from the OCP to -0.25 V_{SCE} to get the cathodic parts. The scan rate was 0.167 mV/s. All experiments were duplicated and carried out at room temperature (22°C).

5.2.2 Impedance measurements

The electrochemical impedance spectroscopy (EIS) measurements on Cr(VI)-coated zinc were carried out in the aerated 0.01 M NaCl solution. The counter electrode was a concentric piece of flat platinum net that was parallel to the surface of the zinc disc. The reference electrode was an Ag/AgCl/Cl⁻ (saturated KCl) electrode ($E^0 = 0.197$ V vs. NHE), which was specially designed for EIS measurements. The impedance response was measured using a Solartron 1255 frequency response analyzer coupled with a Solartron 1287 Potentiostat. The frequency range was 60 kHz to 0.01 Hz, and a 10 mV *a.c.* amplitude around the OCP was used to obtain a weak current response. The impedance data were analyzed using ZView software [5].

5.2.3 Determination of corrosion rate

1) Tafel slopes and linear polarization

Assuming that both the anodic and cathodic processes are in the linear Tafel region at the corrosion potential, the corrosion current, i_{corr} , can be written as [6]

$$i_{corr} = i_{0,a} \exp\left(\frac{2.3(E_{corr} - E_{r,a})}{\beta_a}\right) = i_{0,c} \exp\left(-\frac{2.3(E_{corr} - E_{r,c})}{\beta_c}\right) \quad (5.1)$$

where E_{corr} is the corrosion potential, which is determined by the reversible potentials of the two processes taking place as well as by their exchange-current densities and Tafel slopes, β_a and β_c ; E_r is the reversible potential corresponding to the system at equilibrium with no current passing; subscripts a and c refer to the anodic and cathodic process, respectively (see Fig. 5.1).

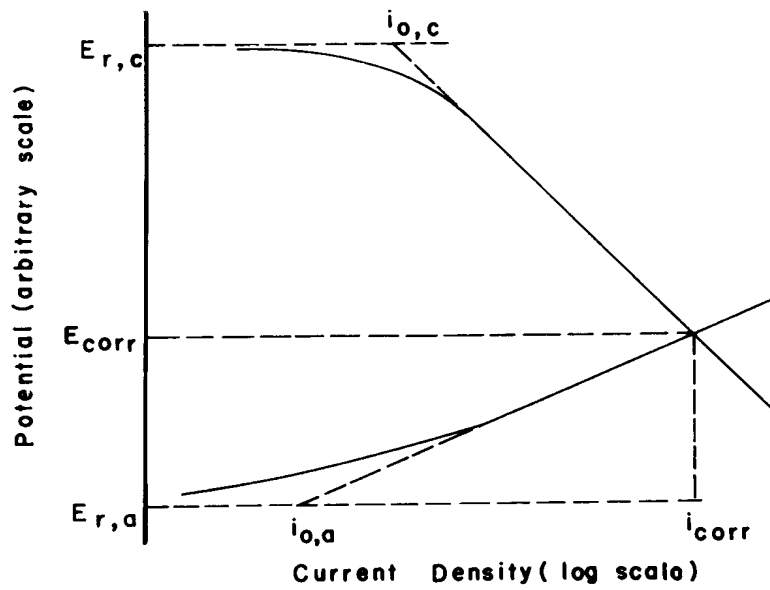


Fig. 5.1 Mixed potential and corrosion current in spontaneous corrosion (Ref. [6]).

If the metal is polarized anodically or cathodically with respect to its corrosion potential, the current that flows is

$$i = i_{0,a} \exp\left(\frac{2.3(E - E_{r,a})}{\beta_a}\right) - i_{0,c} \exp\left(-\frac{2.3(E - E_{r,c})}{\beta_c}\right) \quad (5.2)$$

Combining equation (5.2) with equation (5.1) yields

$$i = i_{corr} \left[\exp\left(\frac{2.3(E - E_{corr})}{\beta_a}\right) - \exp\left(-\frac{2.3(E - E_{corr})}{\beta_c}\right) \right] \quad (5.3)$$

This equation is useful because it permits the electrochemical determination of the corrosion rate i_{corr} by extrapolation of the $E/\log i$ plot from high values of the $E - E_{corr}$ on either the anodic or cathodic side to the corrosion potential (i.e. Tafel extrapolation), or by measurements of i as a function of E in the vicinity of E_{corr} (i.e. linear polarization). The applicability of this relationship relies on the presence of a single charge transfer controlled anodic reaction and single charge transfer controlled cathodic reaction.

In the Tafel extrapolation method, the Tafel region must extend over a current range of at least one order of magnitude to ensure reasonable accuracy [3]. In many systems this cannot be achieved because of interference from concentration polarization and other extraneous effects. The Tafel region is usually distorted if more than one reduction process occurs.

The disadvantage of the Tafel extrapolation method can be largely overcome by using a linear polarization analysis[3]. Many investigators have experimentally observed that the applied current density is approximately a linear function of the electrode potential within a few millivolts of polarization from the corrosion potential (see Fig. 5.2). Equation (5.3) can be mathematically linearized by taking its series expansion and by neglecting higher terms when $\Delta E/\beta < 0.1$. Then the polarization resistance, R_p ($\text{Ohm}\cdot\text{cm}^2$), can be written as[7]

$$R_p = \left[\frac{\Delta E}{\Delta i} \right]_{(E - E_{corr}) \rightarrow 0} = \left(\frac{\beta_a \beta_c}{2.3 i_{corr} (\beta_a + \beta_c)} \right) \quad (5.4)$$

The corrosion current density i_{corr} can be written as

$$i_{corr} = \left(\frac{\beta_a \beta_c}{2.3 R_p (\beta_a + \beta_c)} \right) = \frac{k}{R_p} \quad (5.5)$$

where k is a proportional constant, which is dominated by the smaller of the two anodic and cathodic Tafel slopes, if they are not equal. Equation 5.5, the well known Stern-Geary equation, is also applicable in situations where the corrosion is under mass transport control. Cathodic mass transport control results in $k = \beta_a/2.3$, since $\beta_c \rightarrow \infty$. Similarly, anodic mass transport control results in $k = \beta_c/2.3$. If R_p , β_a and β_c are known, the corrosion rate can be determined using equation (5.5).

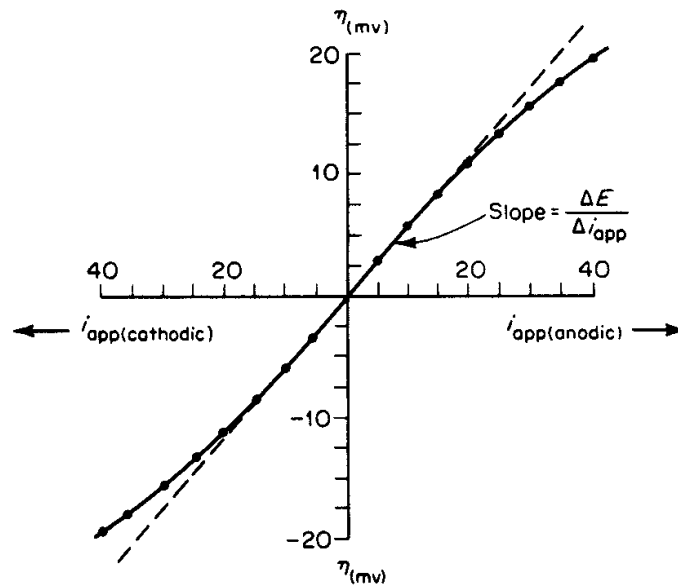


Fig. 5.2 Applied current linear-polarization curve (Ref. [3,4]). The applied current density is a linear function of the electrode potential within a few millivolts of polarization from the corrosion potential.

The anodic Tafel slope for the metal as calculated from low polarization data approaches the value $2.3RT/2F \approx 29.5$ mV/decade of current for zinc and galvanized coatings in phthalate-buffered 0.1 M NaCl solution, pH 5.3 [8]. For zinc in 1 M NaCl solution, the Tafel slopes are $\beta_a = 25$ mV, $\beta_c \rightarrow \infty$ (pH 3.8) and $\beta_a = 16$ mV, $\beta_c = 330$ mV (pH 5.8)[9]. The Tafel slopes are between 15 and 40 mV/decade of current for zinc dissolution in solutions containing Cl^- , Br^- , I^- , SO_4^{2-} and acetate [10]. For zinc corrosion in a neutral aerated 3% NaCl solution, the value of k is about 10 mV, determined by gravimetric method [11].

2) EIS and equivalent circuits

Polarization resistance can also be measured using electrochemical impedance spectroscopy (EIS). EIS measurements involve applying a small-amplitude sinusoidal voltage waveform, $E(\omega)$, over a wide range of frequencies and measuring the current response, $i(\omega)$. The electrochemical impedance, $Z(\omega)$ ($\text{Ohm}\cdot\text{cm}^2$), is a frequency-dependent proportionality factor, which can be written as

$$Z(\omega) = \frac{E(\omega)}{i(\omega)} = Z'(\omega) + jZ''(\omega) \quad (5.7)$$

where E is the *a.c.* voltage across the circuit, $E = E_0 \sin(\omega t)$; i is the *a.c.* current density through the circuit, $i = i_0 \sin(\omega t + \alpha)$; t is time (s); $Z'(\omega)$ is the real component of impedance, $Z'(\omega) = |Z(\omega)| \cos(\alpha)$; $Z''(\omega)$ is the imaginary component of impedance, $Z''(\omega) = |Z(\omega)| \sin(\alpha)$; $|Z(\omega)|$ is the impedance magnitude, $|Z(\omega)| = (Z'(\omega)^2 + Z''(\omega)^2)^{1/2}$; $j^2 = -1$; and α is the phase angle, $\alpha = \tan^{-1} Z''(\omega)/Z'(\omega)$.

Fig. 5.3 shows the electrical equivalent circuit commonly used to represent an electrochemical interface undergoing corrosion, where R_{el} is the electrolyte resistance, C_{dl} is the double layer capacitance, R_{ct} is the charge transfer resistance, and W is the Warburg impedance [12-14].

Circuit (a) in Fig. 5.3 is used for simple charge transfer controlled reaction at a planar electrode surface and in this case $R_p = R_{ct}$. The polarization resistance, R_p , can be estimated by taking the difference between $Z(\omega)$ obtained at low and high ω ($R_p = Z_{\omega \rightarrow 0} - Z_{\omega \rightarrow \infty}$). The capacitive element C_{dl} can be substituted by a constant phase element (CPE). The impedance of a CPE is given by the equation

$$Z_{CPE} = Y_0^{-1} (j\omega)^{-n} \quad (5.8)$$

where Y_0 is the admittance constant of the CPE (in s^n/Ω), ω is the angular frequency (rad/s), n the CPE exponent, $n = \alpha/(\pi/2)$ (α is the constant phase angle of the CPE). The CPE becomes a pure capacitor when $n = 1$ [15]. The capacitance of the double layer can be estimated using the equation [16]:

$$C = Y_0^{1/n} R^{(1-n)/n} \quad (5.9)$$

where R is the resistance parallel to the CPE.

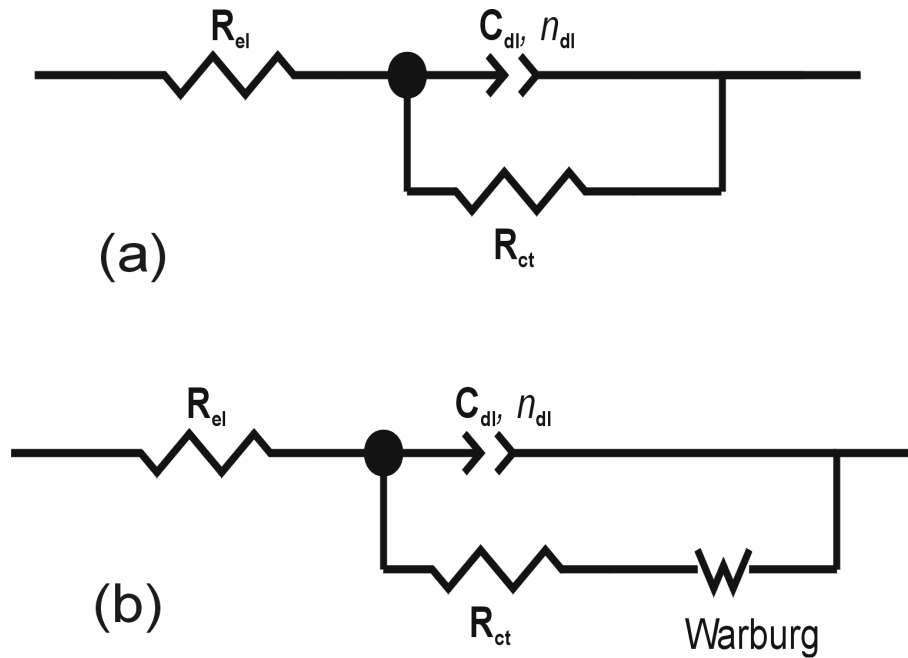


Fig. 5.3 Electrical equivalent circuit commonly used to represent an electrochemical interface undergoing corrosion, (a) for a nearly instantaneous charge transfer controlled reaction at a planar electrode surface, (b) in the case of mass transport limitations [13,14].

Circuit (b) in Fig. 5.3 is used in the case of mass transport limitations. There are two kinds of finite length Warburg element. In the case of short circuit terminus (*i.e.* $Z''_D \rightarrow 0$ when $\omega \rightarrow 0$), the Warburg impedance can be described as[4,17]

$$Z_D(\omega) = R_D \left[\frac{\tanh \sqrt{j\omega s}}{\sqrt{j\omega s}} \right] \quad (5.10)$$

where $s = l_{eff}^2 / D$, here l_{eff} is the actual finite diffusion length and D is the diffusivity of the diffusing species. In the case of open circuit terminus (*i.e.* Z''_D continues to increase

at very low frequencies, similar to the behavior of a capacitance), the Warburg impedance can be described as[5]

$$Z_D(\omega) = R_D \left[\frac{\text{ctnh}\sqrt{j\omega s}}{\sqrt{j\omega s}} \right] \quad (5.11)$$

where s has the same definition as described above.

In both cases, the value of $Z_D(\omega)$ approaches R_D as $\omega \rightarrow 0$. The diffusion resistance, R_D , also contributes to the polarization resistance. Therefore, $R_p = R_{ct} + R_D$, assuming that $R_{ct} + R_D \gg R_{el}$.

In real corrosion systems, the reaction processes are often complicated because of inhomogeneity of the electrode surface. For a system with an oxide film on the electrode surface, two or three time constants may be needed to fit the EIS spectra. For example, Fig. 5.4 shows four equivalent circuits used in modeling different electrochemical systems with two time constants, where Q_{ij} are capacitive elements which can be replaced with CPEs. Ilevbare and Scully used the circuits in Fig 5.4 (a) and (b) to model a porous or defective anodic film on aluminum alloys exposed to 0.1M $\text{Na}_2\text{SO}_4 + 0.005 \text{ NaCl}$ and to 0.1M $\text{Na}_2\text{SO}_4 + 0.005 \text{ NaCl} + 0.0038 \text{ M H}_2\text{CrO}_4$ (pH 6) solutions [18]. It was reported that the model in Fig. 5.4 (a) was better for earlier in the exposure time before pores developed, while the model in Fig. 5.4 (b) was better for later times when pores developed. Deslouis et al. [19,20] used an equivalent circuit similar to the circuit in Fig. 5.4 (a) with substitution of a Warburg element for R_3 to model the zinc/0.5 M Na_2SO_4 (pH 5.7) interface. Ende et al. [21] used an equivalent circuit in Fig. 5.4 (a) by adding a Warburg element in series with R_3 to model chromate conversion coated aluminum in 0.1 M Na_2SO_4 solution (pH 6.5). Goeminne and Campestrini et al. [22,23] used the equivalent circuit in Fig. 5.4 (c) to model chromate conversion coated aluminum alloys in 0.1 ~ 0.6 M K_2SO_4 and in 3% NaCl solutions. The equivalent circuit in Fig. 5.4 (d) was used to model a semiconductor-electrolyte interface [24,25]. It is also known that different equivalent circuits can explain EIS data in an equivalent manner [24,26]. In fact, the four equivalent circuits in Fig. 5.4 are non-distinguishable circuits for equal CPE exponents [26]. When choosing an equivalent circuit, first of all, the physical processes involved have to be considered. Secondly, the

goodness of the fit, the continuity and the simplicity are also criteria [24,27]. If circuits give equally good fits, the one with the smallest number of elements should be used [24].

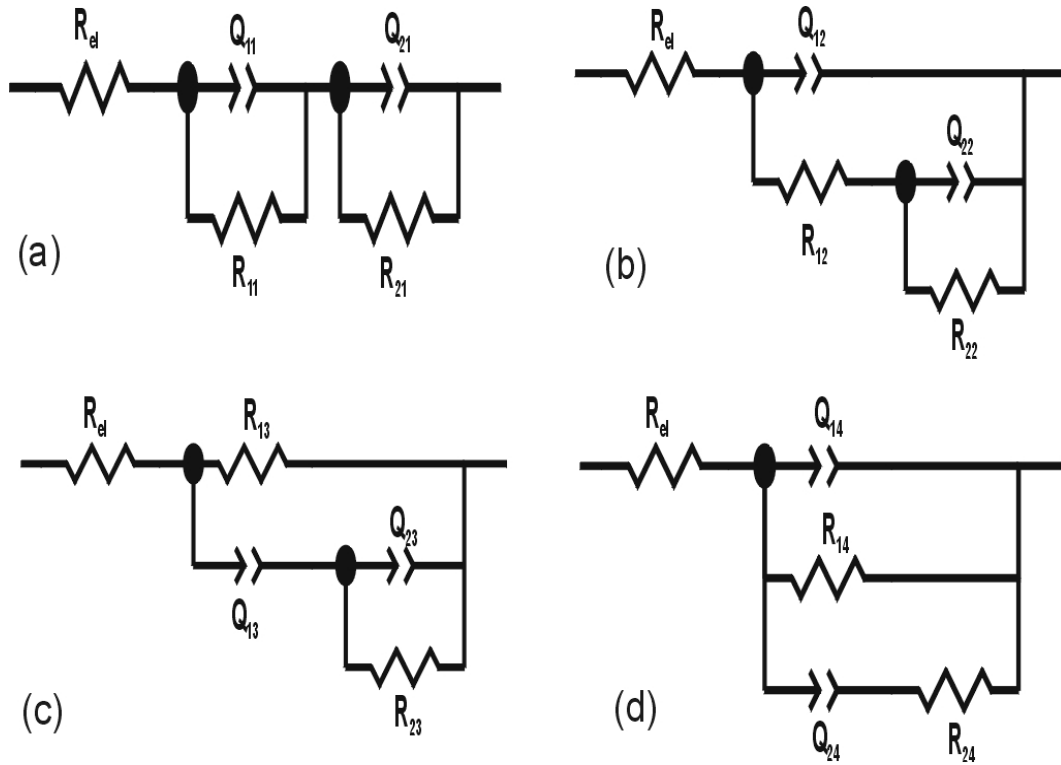


Fig. 5.4 Four possible circuits which can have the same impedance at all frequencies when the parameters of the circuit are properly interrelated [26].

5.3 Results and discussion

5.3.1 Polarization measurements

Fig. 5.5 shows the polarization curves for the bare zinc in 0.01 M NaCl solution (open to air). The average OCP value for bare zinc in the solution is about $-0.97 V_{SCE}$. The anodic polarization (AP) curves show that the anodic reaction, $Zn \rightarrow Zn^{2+} + 2e^-$, is very active. In the cathodic polarization (CP) curves, there is a diffusion-limited current density, which is of the order of $10^{-5} A/cm^2$. This is attributable to the diffusion of oxygen to the zinc/electrolyte interface. This indicates that the corrosion rate of zinc is controlled by the cathodic reaction, $2H_2O + O_2 + 4e^- \rightarrow 4OH^-$.

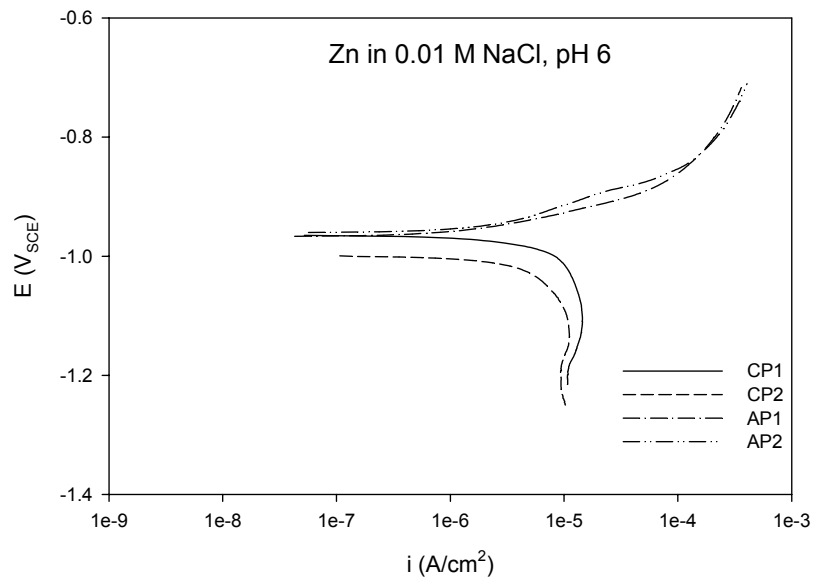


Fig. 5.5 Cathodic (CP) and anodic (AP) polarization curves for zinc sheets in 0.01 M NaCl solution, pH 6.

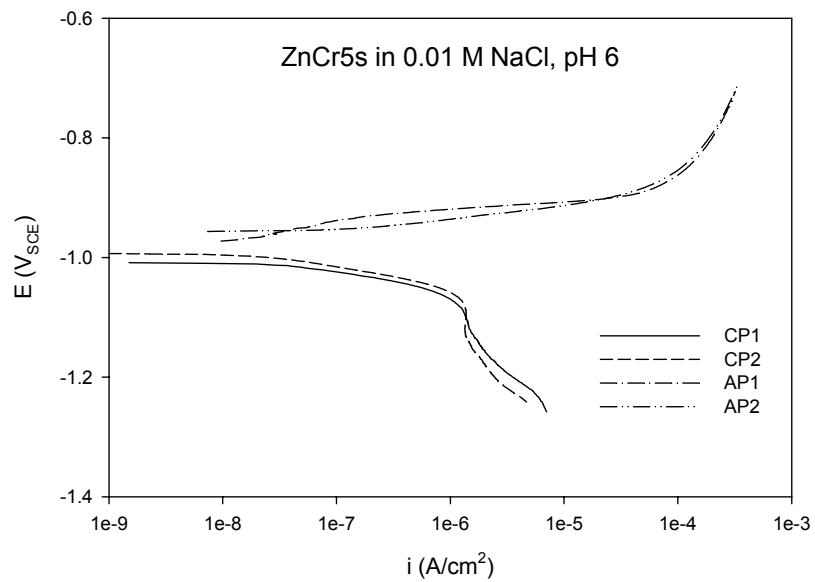


Fig. 5.6 Cathodic (CP) and anodic (AP) polarization curves for the Cr(VI) coated zinc sheets (with dipping time 5 s) in 0.01 M NaCl solution, pH 6.

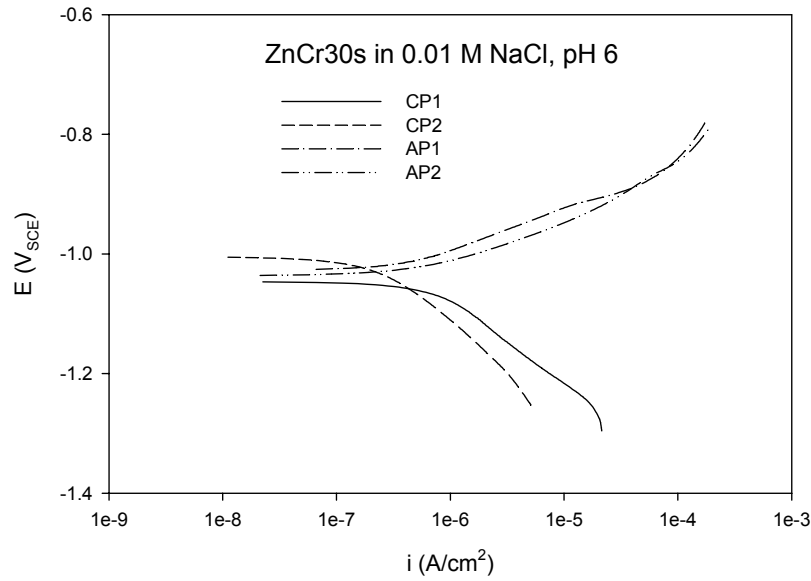


Fig. 5.7 Cathodic (CP) and anodic (AP) polarization curves for the Cr(VI) coated zinc sheets (with dipping time 30 s) in 0.01 M NaCl solution, pH 6.

Table 5.1 Corrosion potential and current density calculated from the cathodic (CP) and anodic (AP) polarization curves using Rp-fit.

Samples			Solution open to air		
			E_{corr} (V _{SCE})	R_p (k Ω ·cm ²)	i_{corr} (μ A/cm ²)
Bare Zn	1	CP	-0.97	4.2	2.4
		AP	-0.97	8	1.3
	2	CP	-0.99	4.9	2.2
		AP	-0.96	6	1.7
Cr(VI) coated Zn (5s)	1	CP	-1.01	160	0.06
		AP	-0.98	630	0.02
	2	CP	-0.99	270	0.04
		AP	-0.96	32	0.3
Cr(VI) coated Zn (30s)	1	CP	-1.05	26	0.4
		AP	-1.03	34	0.3
	2	CP	-1.01	100	0.1
		AP	-1.04	28	0.4

The corrosion current values were estimated using a linear polarization method. The slopes of the relevant polarization curves within 10 mV of the open-circuit potential were estimated and substituted into the Stern-Geary equation, *i.e.* $i_{corr} = k/R_p$ (see equation 5.5). A value of 10 mV was assumed for k , the proportionality constant in the Stern-Geary relationship. Values of the corrosion potential and estimated corrosion current density for each sample are presented in Table 5.1. The polarization resistance for bare zinc in the solution is $4.2 \sim 8 \text{ k}\Omega\cdot\text{cm}^2$.

Fig. 5.6 shows the polarization curves in 0.01 M NaCl solution for the Cr(VI) coated zinc with dipping time of 5 s. The OCP of the Cr(VI) coated zinc with dipping time of 5 s is close to the OCP of the bare zinc, and is around $-0.98 \text{ V}_{\text{SCE}}$. However, the corrosion current density is much smaller than for the bare zinc. The average corrosion current density for the Cr(VI) coating ($0.1 \text{ }\mu\text{A}/\text{cm}^2$) is smaller than for the bare zinc ($1.9 \text{ }\mu\text{A}/\text{cm}^2$). First of all, this benefits from the chromium oxides/hydroxides that cover the active zinc surface and reduce the reaction area of zinc. The current density in Table 5.1 is calculated using the whole exposure area of the coated samples since the true local current density is unknown. According to the mixed-potential theory, when both the anodic and cathodic reaction rates are reduced, the corrosion potential may remain nearly the same.

For the Cr(VI) coated zinc with dipping time of 30 s, the OCP is about 60 mV more negative than for the bare zinc, and is around $-1.03 \text{ V}_{\text{SCE}}$ (see Fig. 5.7), but the current density is greater ($0.3 \text{ }\mu\text{A}/\text{cm}^2$) than for the coating with dipping time 5 s ($0.1 \text{ }\mu\text{A}/\text{cm}^2$). This is because these coatings have more anodic reaction area than the Cr(VI) coatings with dipping time 5 s, since from chapter 4, we know that the coatings with dipping time of 30 s have wider cracks than the coatings with dipping time of 5 s. If we assume that the cathodic reaction rate is reduced on the same level for both kinds of coating, then the mixed potential will be more negative for the coating for which the anodic reaction rate is reduced less.

5.3.2 Impedance measurements

Fig. 5.8 shows the complex impedance plot for bare zinc after exposure to 0.01 M NaCl solution for 1 h. The charge transfer resistance for this sample is about $6 \text{ k}\Omega\cdot\text{cm}^2$, and the polarization resistance is about $4.5 \text{ k}\Omega\cdot\text{cm}^2$, which is consistent with the results obtained from polarization measurements.

Fig. 5.9 shows the Bode impedance plots for two bare zinc specimens after exposure to the solution for 1 h. The polarization resistance obtained from the measurements is reproducible.

For the bare zinc in the aerated NaCl solution (open to air), as described above, zinc dissolution is active. In order to build up a model to simulate the zinc corrosion in the solution, first a simple model in Fig. 5.10 with an equivalent circuit in Fig. 5.3 (a) was used to fit the impedance spectra. Then, in considering that there is usually a thin oxide layer formed in air, a two-time-constant equivalent circuit in Fig. 5.4 (a) was also used to fit the impedance data in the frequency range of $7000 \sim 0.1 \text{ Hz}$. A constant phase element (CPE) was used to represent the non-ideal capacitive response of the system. The capacitance of the double layer can be estimated using the equation (5.9). The fit results are presented in Table 5.2. The fit error is evaluated using $\delta Z/Z = (Z - Z_c)/Z$, where Z is for measured value and Z_c is for the calculated value from the model. The results are presented in Fig. 5.11 (a). It shows that the relative error for the real impedance is less than 2%, while for the imaginary part is as large as 22% at high frequencies. When the equivalent circuit in Fig. 5.4 (a) was used, the fit results show that the error is less than 1% for the real part and less than 5% for the imaginary impedance part (see Fig. 5.11(b)). The added capacitive element Q_{21} (C_p) and resistance R_{21} (R_{cp}) produce a relaxation time at high frequencies, which is attributable to the oxide layer on the zinc surface. The value of R_{cp} is very small, which indicates that the oxide layer is too thin to affect the charge transfer resistance R_{ct} .

Furthermore, in order to fit an adsorption-reaction arc (below-axis response) in Fig. 5.8, a pseudo-inductance (L) in parallel with a resistance (R_2) was added in series with R_1 (see Fig. 5.12). The fitted results are present in Fig. 5.13. Now the charge transfer resistance is estimated as $R_{ct} = R_1 + R_2 = 6 \text{ k}\Omega\cdot\text{cm}^2$, where the polarization resistance

approaches the value of $R_{cp} + R_1 = 5 \text{ k}\Omega \cdot \text{cm}^2$, since when $\omega \rightarrow 0$, the impedance of the inductance $Z_L \rightarrow 0$.

Table 5.2 Fit results of the EIS data using different models for bare zinc after exposure to the solution for 1 hour (R , in units $\text{k}\Omega \cdot \text{cm}^2$; Y_0 , in units $10^{-6} \text{ s}^n \cdot \Omega^{-1} \cdot \text{cm}^{-2}$, and C , in units $\mu\text{F}/\text{cm}^2$).

Model	R_{el}	Y_0 (C_p)	n_0	R_{cp}	Y_{01} (C_{dl})	n_1	R_{ct}	χ^2
Fig. 5.3(a)	1.2				26.5 (17.2)	0.806	6.2	7×10^{-4}
Fig. 5.4(a)	1.2	80.2 (18.8)	0.767	0.1	25.1 (17.5)	0.837	6.1	1×10^{-4}

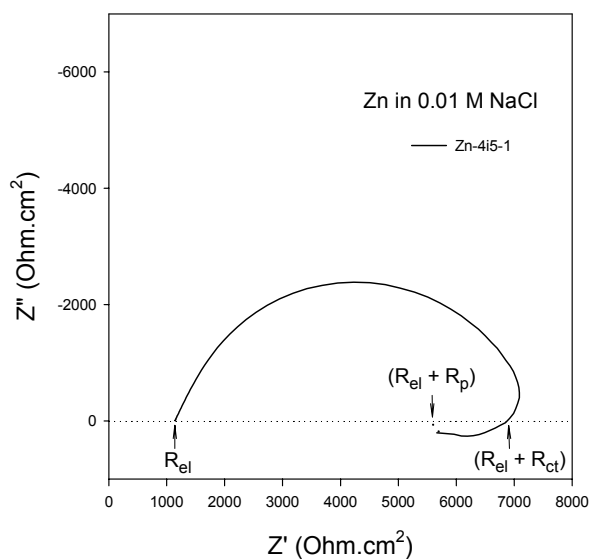


Fig. 5.8 Complex impedance plot for bare zinc after exposure to 0.01 M NaCl solution for 1 h.

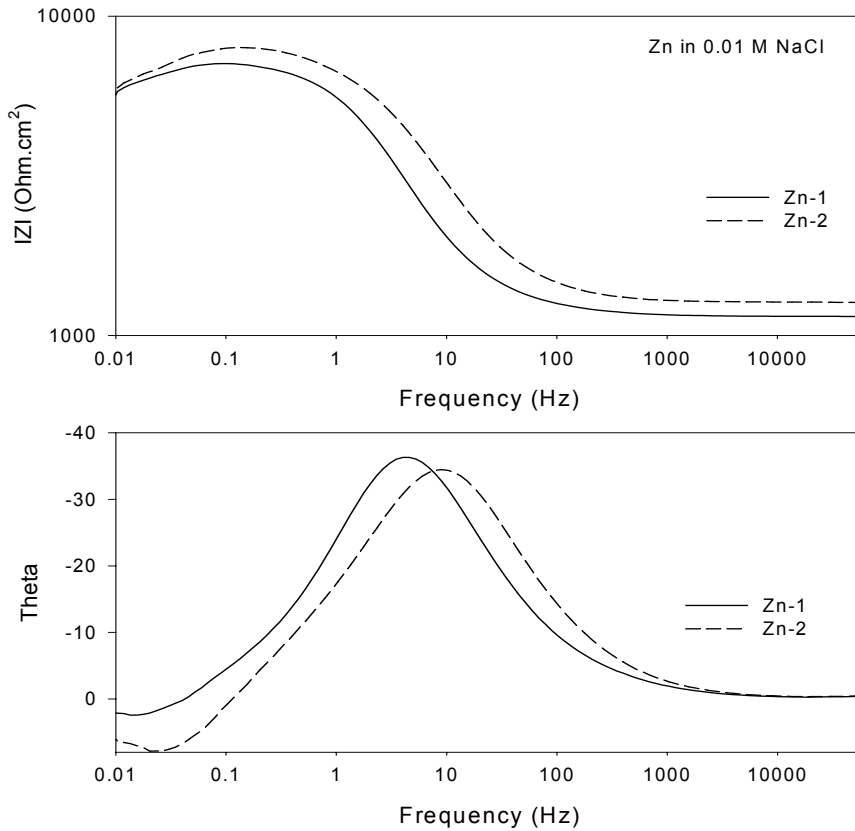


Fig. 5.9 Bode impedance plots for two zinc specimens after immersion in 0.01 M NaCl solution (pH 6, open to air) for 1 h.

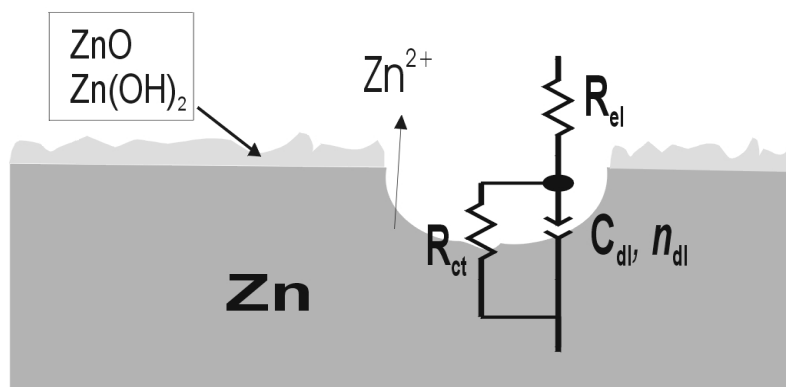
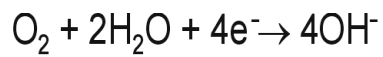


Fig. 5.10 Schematic model for bare zinc in 0.01 M NaCl solution with an equivalent circuit in Fig. 5.3 (a).

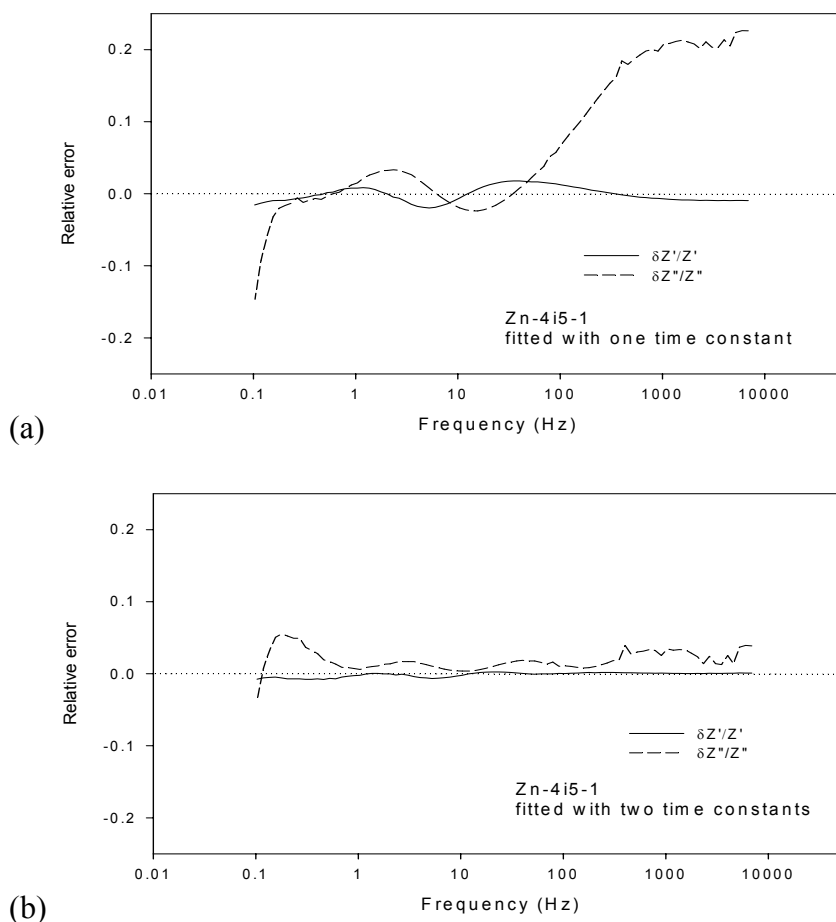


Fig. 5.11 Relative errors of using (a) one-time-constant model in Fig. 5.3 (a) and (b) two-time-constant model in Fig. 5.4 (a) to fit the impedance for a bare zinc sample Zn-4i5-1 exposed to the solution for 1 h.

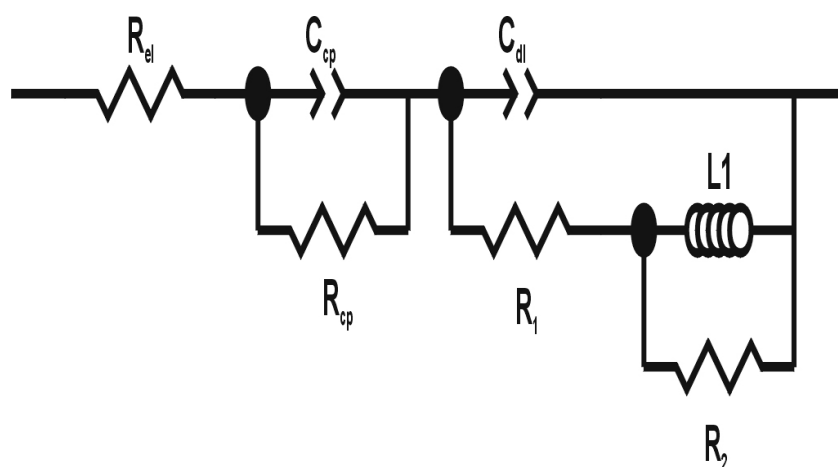


Fig. 5.12 Equivalent circuit for modeling a zinc specimen exposed to 0.01 M NaCl solution for 1 h.

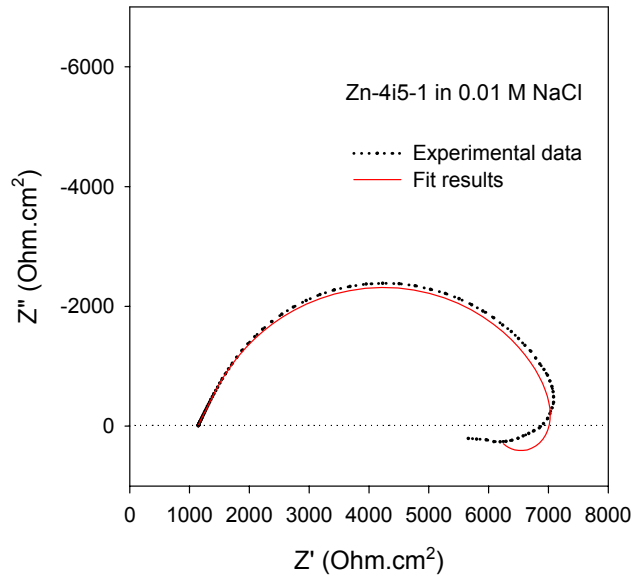


Fig. 5.13 experimental data and fitted results using equivalent circuit in Fig. 5.11 for the zinc sample exposed in 0.01 M NaCl solution for 1 h. The fitting values, given $\chi = 3 \times 10^{-3}$, are $R_{el} = 1.15 \text{ k}\Omega \cdot \text{cm}^2$, $Y_0 (C_p) = 72 \times 10^{-6} \text{ s}^n \cdot \Omega^{-1} \cdot \text{cm}^{-2}$, $n_0 = 0.788$, $R_{cp} = 0.092 \text{ k}\Omega \cdot \text{cm}^2$, $Y_{01} (C_{dl}) = 25.4 \times 10^{-6} \text{ s}^n \cdot \Omega^{-1} \cdot \text{cm}^{-2}$, $n_1 = 0.834$, $R_1 = 4.89 \text{ k}\Omega \cdot \text{cm}^2$, $L_1 = 6354 \text{ H} \cdot \text{cm}^2$, $R_2 = 1.13 \text{ k}\Omega \cdot \text{cm}^2$.

Fig. 5.14 shows the Bode impedance plots for bare zinc as a function of immersion time in the NaCl solution. The impedance decreases with time within 5 hours, and afterwards it increases with time. This indicates that the pitting process happened [28]. The impedance increase afterwards is due to the deposition of corrosion products on the surface of zinc.

The adsorption-reaction arc was only found in measurements for zinc exposed to the solution for 1 h. After immersion for 2 h, no positive phase angle was measured. In order to simplify the fitting processes, the simple model in Fig. 5.3 (a) was used to fit the experimental impedance data in the frequency range 1000 ~ 0.1 Hz for zinc in the solution. Fig. 5.15 shows the calculated capacitance and charge transfer resistance against immersion time in the solution. It shows that the capacitance of the double layer increases and the charge transfer resistance decreases with the exposure time. The

capacitance for the bare zinc, C_{dl} , measured after exposure to the solution for 1 h, is about $17 \mu\text{F}/\text{cm}^2$, and after 5 h, it becomes $370 \mu\text{F}/\text{cm}^2$. The charge transfer resistance, R_{ct} , decreases from $6.2 \text{ k}\Omega\cdot\text{cm}^2$ to $1.4 \text{ k}\Omega\cdot\text{cm}^2$ after 5 h. The increase in C_{dl} with immersion time can be attributed to the increase of the exposure area caused by corrosion [29,30].

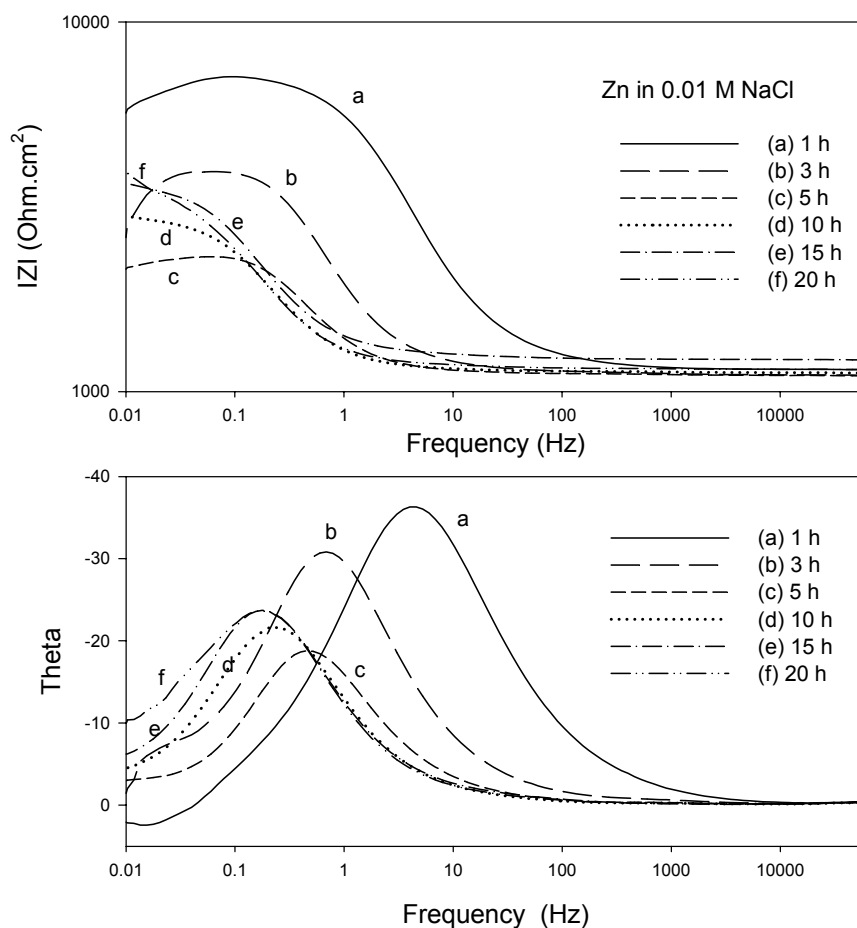


Fig. 5.14 Bode impedance plots as a function of exposure time for the bare zinc in 0.01 M NaCl solution.

Fig. 5.16 shows the Bode impedance plots for the Cr(VI) coatings (with different dipping times in the chromating bath) measured after exposure to the NaCl solution for 1 h. Compared with Fig. 5.14, Fig. 5.16 shows that all the chromate coated zinc have larger impedance than the bare zinc. Among the Cr(VI) coatings, the coating with dipping time of 5 s has the largest impedance.

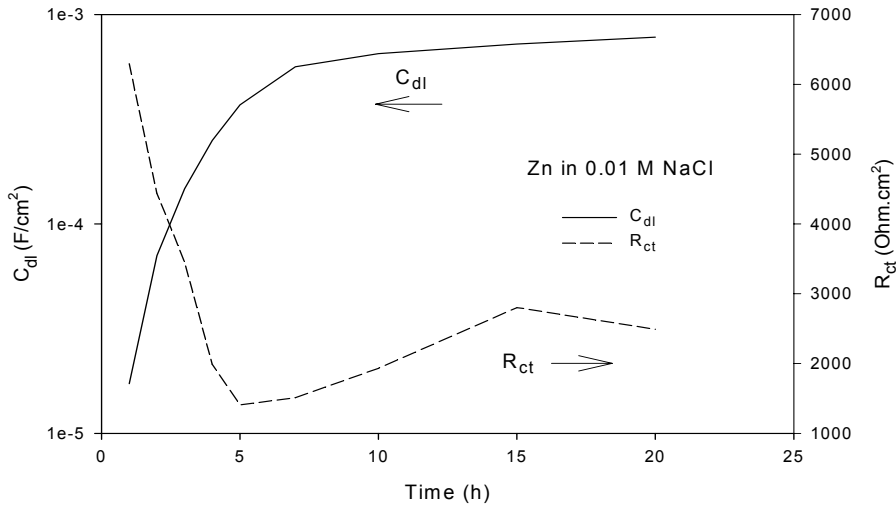


Fig. 5.15 Capacitance and charge transfer resistance as a function of exposure time for zinc in 0.01 M NaCl solution.

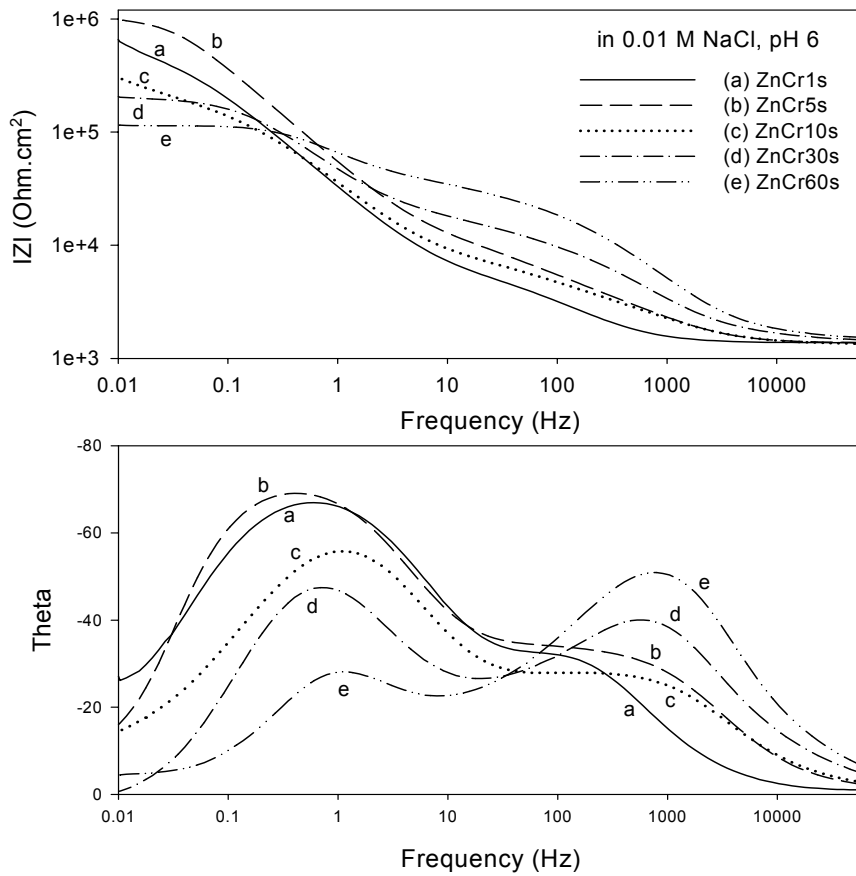


Fig. 5.16 Bode impedance plots for the Cr(VI) coatings (with different dipping times) in 0.01 M NaCl solution.

The phase-frequency curves show two maximums of phase angle located at high and low frequency sides, respectively, for every sample. This means that there are at least two time constants in the whole frequency range. According to the surface structures of the chromate conversion coatings on zinc discussed in Chapter 4, a schematic model for the chromated zinc in NaCl solution was made and shown in Fig. 5.17. The possible equivalent circuits are present in Fig. 5.18. In these circuits, R_{el} is the electrolyte resistance, C_p the capacitance of the chromate layer, R_{cp} the resistance in the pores of the chromate coating, C_{dl} the double-layer capacitance and R_{ct} the charge transfer resistance of the electrode reaction effects, C_d and R_d the capacitance and resistance of the oxygen diffusion effect [31].

Fig. 5.19 shows the experimental and fitted curves for a ZnCr5s specimen exposed to the solution for 6 h using equivalent circuit in Fig. 5.18 (a). This fit gives $\chi^2 = 3.2 \times 10^{-6}$. The fitting errors for the real and the imaginary parts of impedance are present in Fig. 5.20. The relative error is less than 1% for both the real and the imaginary impedance below 10^4 Hz. The same experimental data was also fitted with the equivalent circuit in Fig. 5.18 (b), and this fit gives $\chi^2 = 9.3 \times 10^{-5}$. In this case, the fitting errors for both the real and the imaginary parts of the impedance have exceeded 1% (see Fig. 5.21). From the fit goodness, the equivalent circuit in Fig. (a) is better than the circuit in Fig. 5.18 (b) for this system.

The EIS spectra for all the Cr(VI) coatings were fitted using equivalent circuit in Fig. 5.18 (a) in order to compare the capacitive and resistive parameters. The partial results are present in Table 5.3. The first EIS measurement for each specimen was done after exposure to solution for 1 h. It shows that except for the ZnCr5s coating, the admittance Y_0 (C_p) decreases with the thickness, and the resistance in the pores increases with the thickness of the coatings. It is physically reasonable since the capacitance is inversely proportional to the thickness of the layer when the relative dielectric constant and surface area are constant. The ZnCr5s coating has a small admittance Y_0 (C_p) than the ZnCr10s and the ZnCr30s coatings, which is attributable to smaller exposure surface area than the other coatings since this coating has no crack.

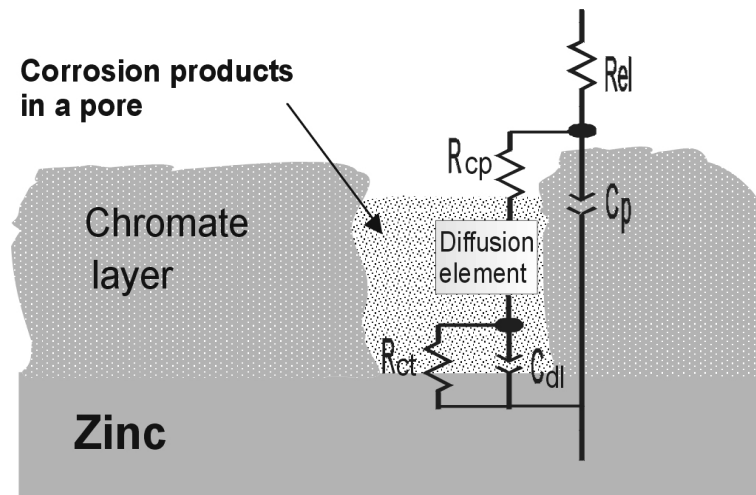


Fig. 5.17 Schematic model of chromate conversion coatings on zinc in 0.01 M NaCl solution with an equivalent circuit.

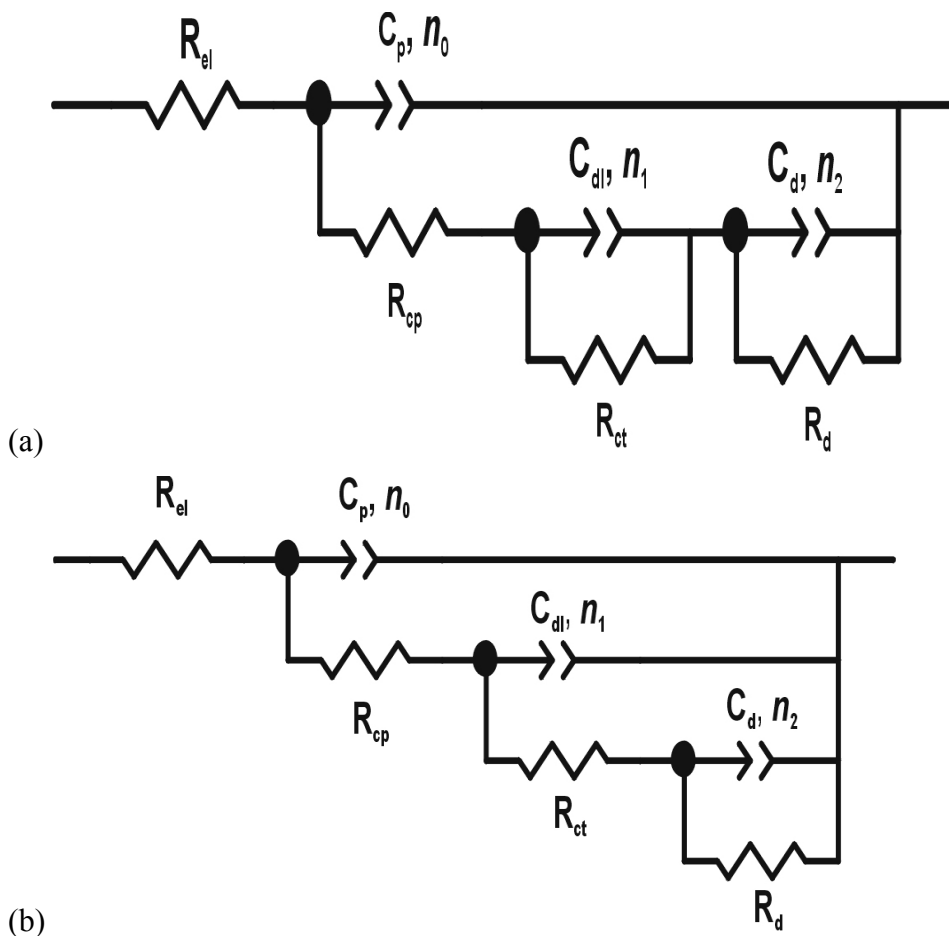


Fig. 5.18 Possible equivalent circuits for modeling chromate-coated zinc in 0.01 M NaCl solution.

Table 5.3 Best-fitting parameters of the EIS data for Cr(VI) coatings on zinc in 0.01 M NaCl solution (R_s in units $k\Omega\cdot\text{cm}^2$ and Y_0 , in units $10^{-6} \text{ s}^n\cdot\Omega^{-1}\cdot\text{cm}^{-2}$).

Sample	OCP	Exposure Time (h)	R_{el}	Y_0 (C_p)	n_0	R_{cp}	Y_{01} (C_{dl})	n_1	R_{ct}	Y_{02} (C_d)	n_2	R_d
ZnCr	-1.01	1	1.4	1.18	0.860	3.0	8.94	0.641	2.0	5.38	0.853	545
1 s		16	1.4	1.68	0.833	2.9	12	0.62	4.4	4.82	0.852	1370
ZnCr	-0.98	1	1.4	0.29	0.868	2.4	4.71	0.592	8.4	3.56	0.881	1208
5 s		16	1.4	0.46	0.831	3.3	3.82	0.65	7.6	3.35	0.86	3322
ZnCr	-1.02	1	1.3	1.01	0.747	4.1	1.65	0.902	1.9	5.67	0.81	210
10 s		16	1.4	1.9	0.698	1.9	7.85	0.576	4.0	4.62	0.852	1339
ZnCr	-1.00	1	1.4	0.45	0.771	12	7.17	0.642	8.5	4.88	0.883	176
30 s		16	1.4	0.77	0.719	0.2	5.44	0.475	11	4.26	0.865	795
ZnCr	-1.02	1	1.5	0.14	0.845	22	1.91	0.717	14	4.69	0.843	83
60 s		16	1.6	1.17	0.778	11	7.31	0.807	4.0	3.34	0.851	280

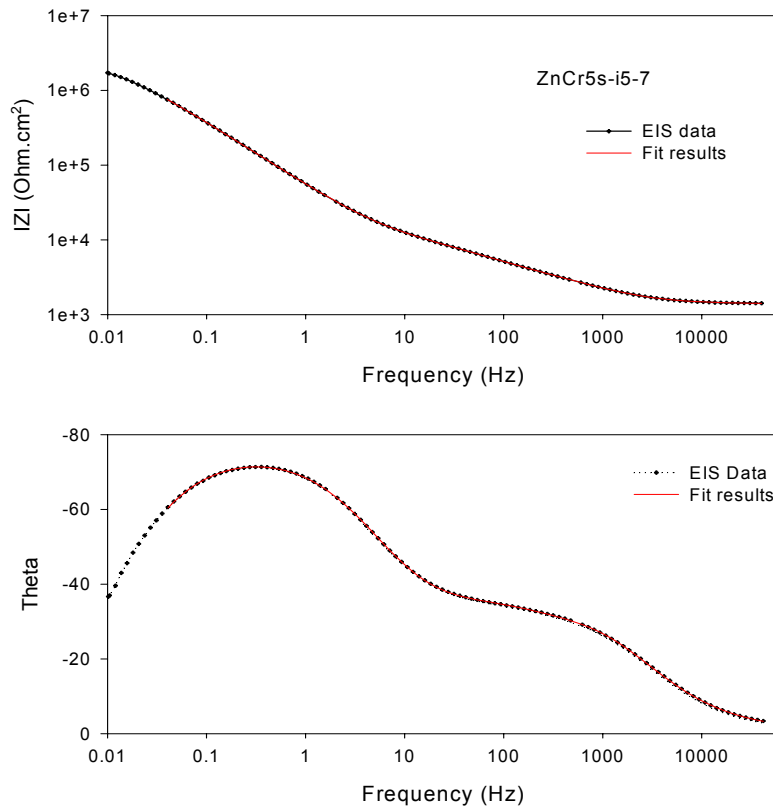


Fig. 5.19 Experimental data and fit results (Bode plots) for a ZnCr5s sample exposed to the solution for 6 h, using the equivalent circuit in Fig. 5.17 (a), given $\chi^2 = 3.2 \times 10^{-6}$.

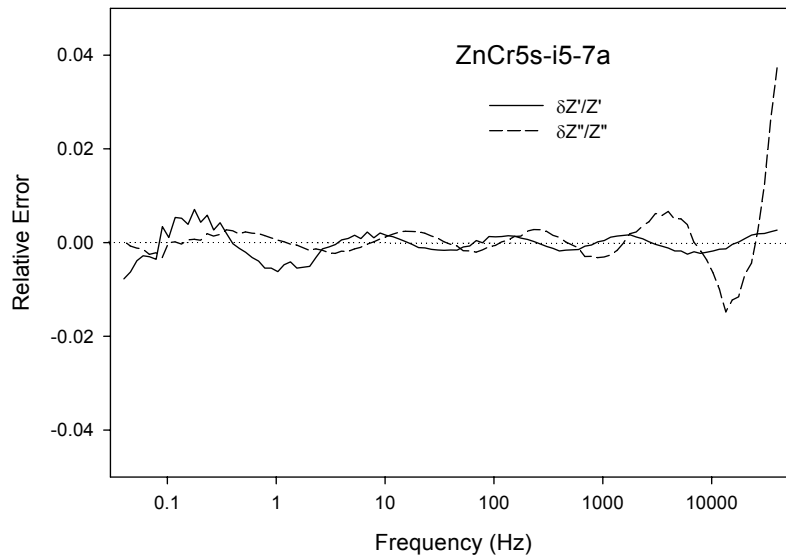


Fig. 5.20 Relative error of using the model in Fig. 5.18 (a) to fit the impedance spectra for a sample ZnCr5s exposed to the solution for 6 h.

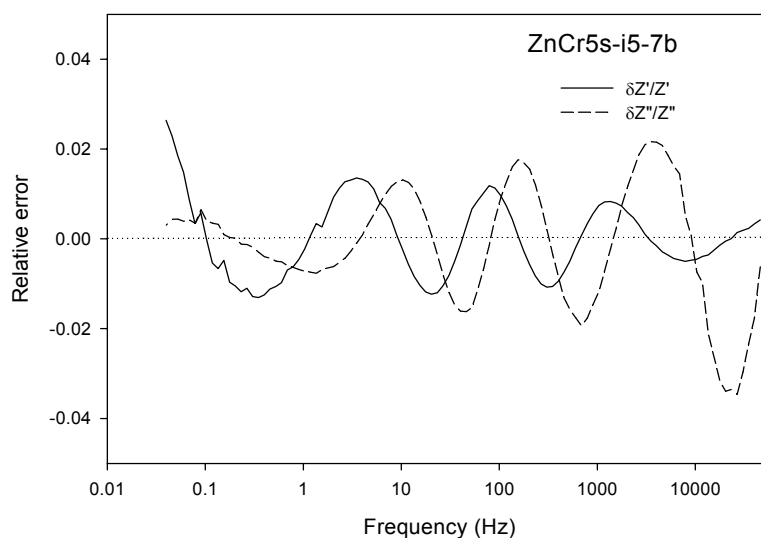


Fig. 5.21 Relative error of using the model in Fig. 5.18 (b) to fit the impedance spectra for a sample ZnCr5s exposed to the solution for 6 h.

Fig. 5.22 shows the Bode impedance plots as a function of exposure time for a Cr(VI) coating with dipping time 5 s. The shape of the phase angle versus frequency graph changes significantly with time on the low frequency side, while on the high frequency side it changes little. This indicates that corrosion has taken place at zinc/electrolyte interface, at bottom of pores in the coating, while the chromate layer has changed little for this coating.

Fig. 5.23 shows the CPE parameters Y_0 and n_0 (C_p) for a Cr(VI) coating with dipping time 5 s as a function of exposure time. The value of Y_0 increases slightly with exposure time, while the exponent of CPE (n_0) decreases with exposure time. This may be attributable to the decrease of the thickness of the coating owing to the dissolution of the adsorbed Cr(VI) species on the surface, or to the increase of the relative dielectric constant of the coating owing to the uptake of water [32].

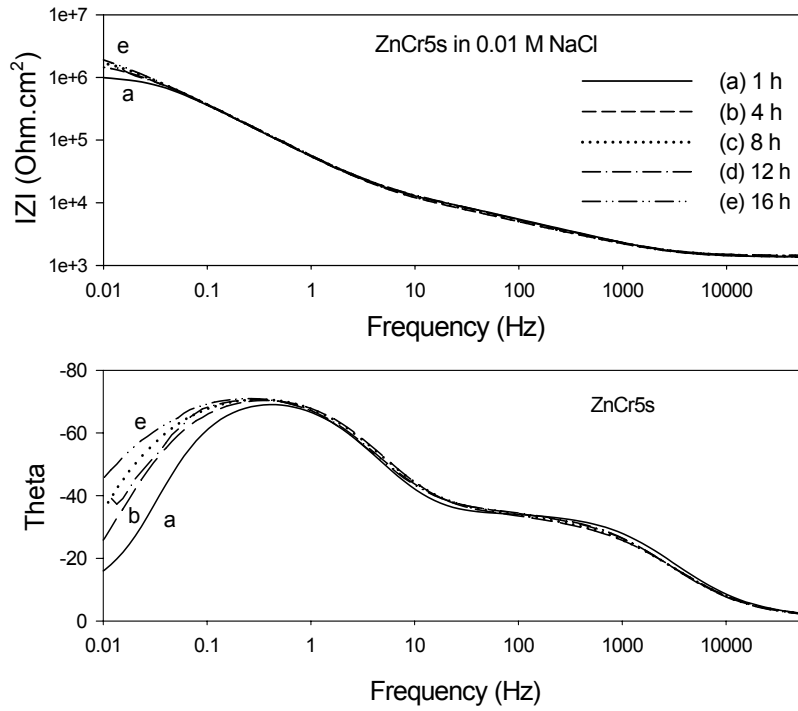


Fig. 5.22 Bode impedance plots as a function of immersion time for a Cr(VI) coating with dipping time 5 s.

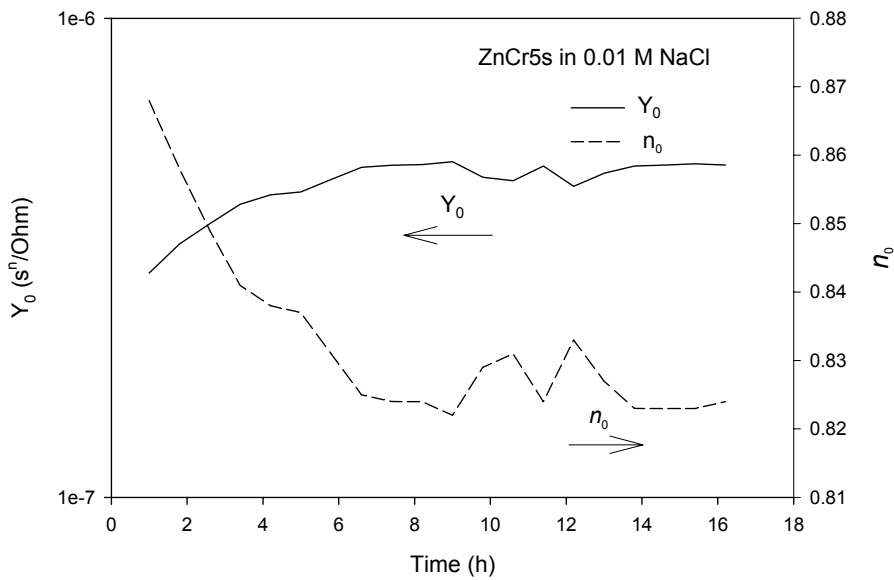


Fig. 5.23 The CPE parameters Y_0 and n_0 (C_p) for a Cr(VI) coating with dipping time 5 s as a function of exposure time.

Fig. 5.24 shows the admittances Y_{01} (C_{dl}) and Y_{02} (C_d) for a Cr(VI) coating with dipping time 5 s as a function of exposure time. The admittance for the double layer (Y_{01}) decreases slightly with time, while the Y_{02} for the diffusion it does not significantly change. It also indicates that the reaction area and the diffusion length has not significantly changed within 16 h.

The resistive parameters R_{cp} , R_{ct} and R_d for a Cr(VI) coating with dipping time 5 s as a function of exposure time are presented in Fig. 5.25. The charge transfer resistance decreases initially, and increases slowly afterwards. Both the resistance in the pores of the coating and the diffusion resistance increase with exposure time. It suggests that in the corrosion process, some corrosion products will fill the pores and consequently it will increase the corrosion resistance.

Fig. 5.26 shows the Bode impedance plots as a function of exposure time for a Cr(VI) coating with dipping time 30 s. The shape of the phase angle versus frequency curves changes significantly with exposure time not only at low frequency, but also on the high frequency side. It means that not only corrosion happened at flaws, but also the chromate layer changed significantly. The capacitance of the layer increased with exposure time, since the maximum phase angle at high frequency side decreased with time. The fit results also show that the admittance Y_0 increased from 0.45 to 0.77 $s^n/\Omega \cdot cm^2$, while the n , exponent of CPE, decreased from 0.771 to 0.719. The resistance in pores decreased from 12 to 0.2 $k\Omega \cdot cm^2$. This suggests that the zinc underneath is open to the electrolyte.

Fig. 5.27 shows the calculated polarization resistance ($R_p = R_{cp} + R_{ct} + R_d$) as a function of exposure time for the Cr(VI) coatings with different dipping times. For all the chromated zinc specimens, the corrosion resistance increases with exposure time during the measurements. Among these specimens, the corrosion resistance decreases in the following order: R_p (ZnCr5s) > R_p (ZnCr1s) > R_p (ZnCr10s) > R_p (ZnCr30s) > R_p (ZnCr60s), within 16 h in the solution.

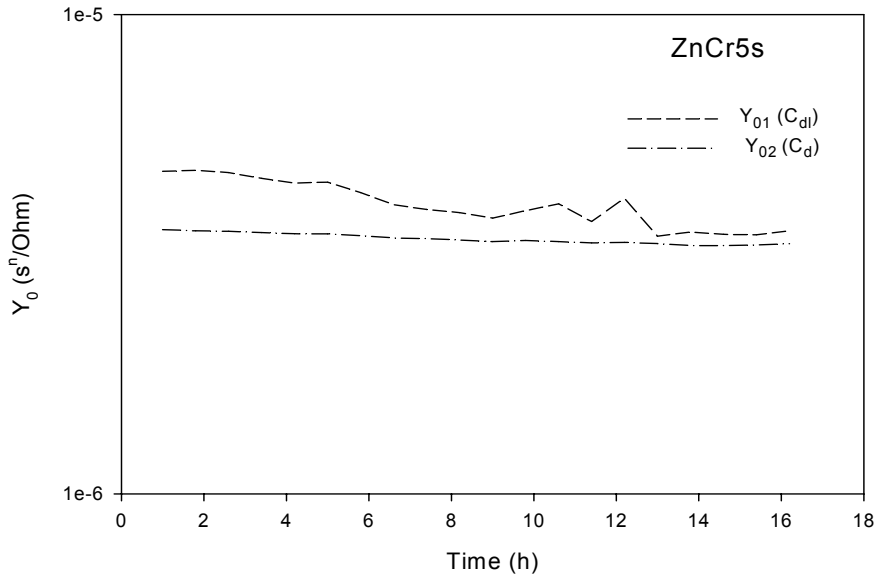


Fig. 5.24 $Y_{01} (C_{dl})$ and $Y_{02} (C_{ad})$ for a Cr(VI) coating with dipping time 5 s as a function of exposure time in the solution.

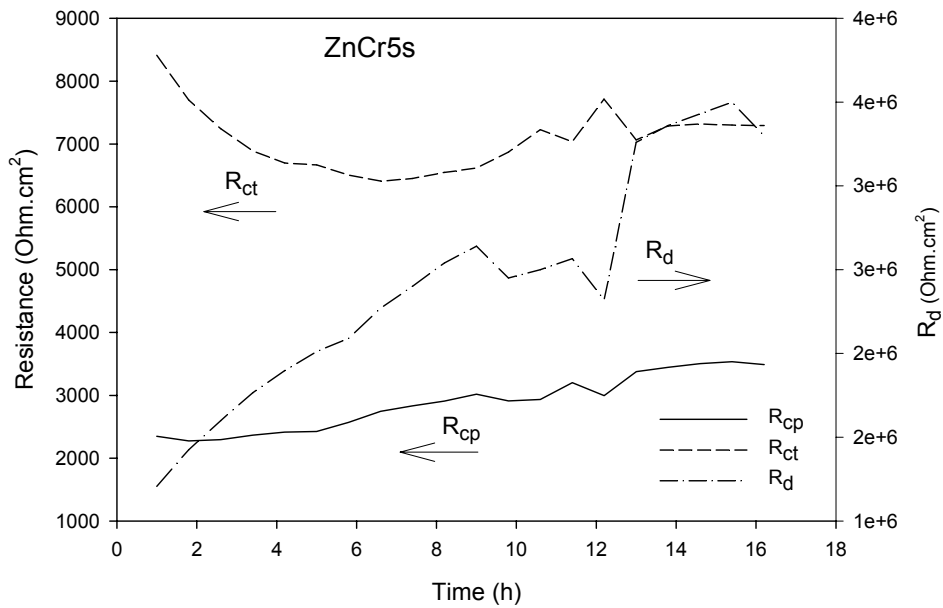


Fig. 5.25 The resistive parameters R_{cp} , R_{ct} and R_d for a Cr(VI) coating with dipping time 5 s as a function of exposure time.

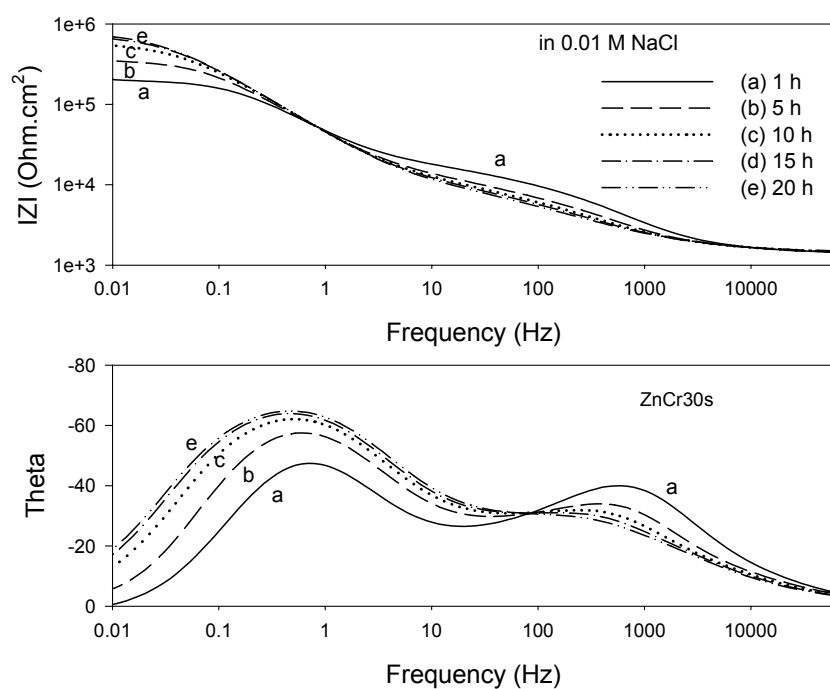


Fig. 5.26 Bode impedance plots as a function of immersion time for a Cr(VI) coating with dipping time 30 s.

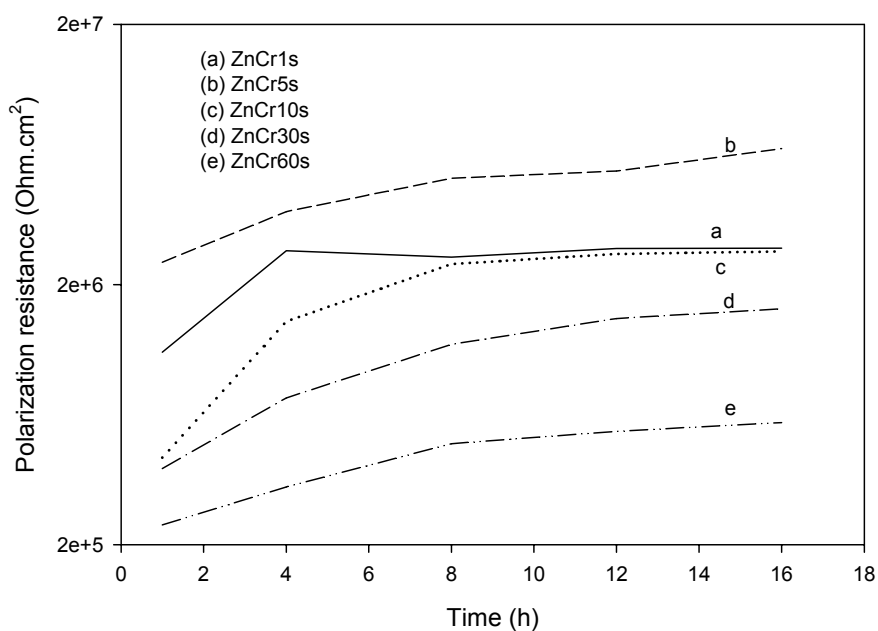


Fig. 5.27 Polarization resistance as a function of exposure time in 0.01 M NaCl solution for Cr(VI) coatings (with different dipping time).

Fig. 5.28 shows topography for the ZnCr10s and ZnCr30s samples after exposure to the solution for 24 hours. The corrosion morphology indicates that the corrosion is localized. The coating around the pits is intact. The pitting starts at flaws such as pores and cracks in the coating and then goes deeply and laterally, until the chromate coating is detached (see Fig. 5.29 (a)). The pitting geometry of the chromated zinc sheets shows a preferred orientation (see Fig. 5.29 (b)). This is also observed in passivated zinc monocrystals by other authors [33].

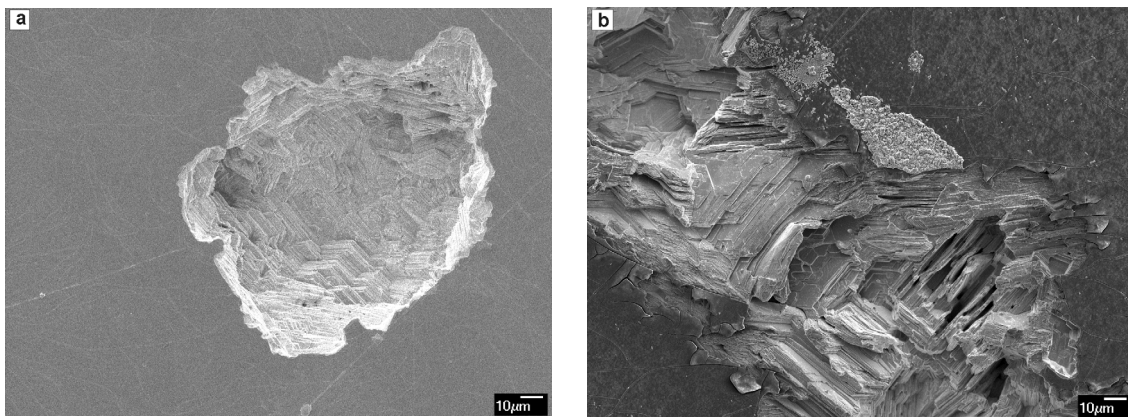
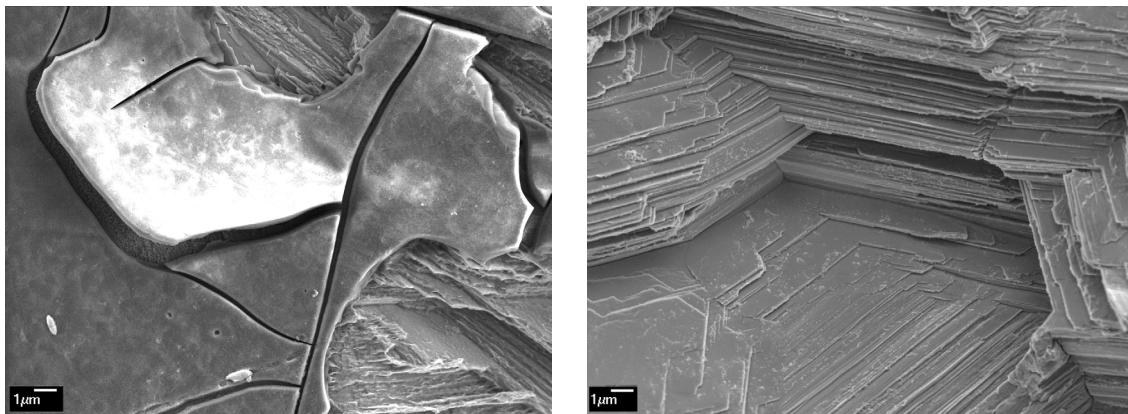


Fig. 5.28 SEM images for chromate coatings on zinc sheets, (a) ZnCr10s, (b) ZnCr30s after immersion in 0.01 M NaCl for 24 h.



(a) (b)
Fig. 5.29 SEM images for the ZnCr30s specimen after immersion in 0.01 M NaCl for 24 h: (a) the detached chromate coating, (b) zinc preferred corrosion orientation.

The results show that the morphology of the coatings does affect the corrosion behavior of the system. Flaws and cracks in the coating are the initial corrosion places [1,2]. Once the surface starts pitting, the corrosion goes under the coating and afterwards the coating collapses. The coating with dipping time of 5 s shows the greatest resistance compared to other coatings in this solution, which is attributable to the fact that the ZnCr5s coatings have fewer flaws (cracks) in the layer (see Chapter 4). The coating with dipping time of 1 s has no cracks, but the layer is too thin to have the greatest corrosion resistance. When the dipping time increases to 10 s, the coating starts to show cracks, and the size of the crack increases with the dipping time (the thickness of the coating increases with the dipping time to a certain degree). Thus, the corrosion resistance starts to decrease. The fact that the resistance increases with exposure time in the solution may be due to the corrosion products filling the pores in the coatings. The “self-healing” effect of Cr(VI) species contained in the coating may also function, but it is difficult to prove this from these impedance measurements.

5.4 Conclusions

Zinc is very active when it is exposed to 0.01 M NaCl solution. The zinc corrosion process is controlled by oxygen diffusion. The diffusion-limited current density is about 10^{-5} A/cm².

The Cr(VI) treatments significantly decrease the corrosion rate of zinc in the solution. The corrosion of Cr(VI) coated zinc is localized. The pitting starts at flaws such as pores and cracks in the coating and then goes deeply and laterally, until the chromate coating is detached.

The morphology of the coatings does affect the corrosion behavior of the system. The coating with dipping time of 5 s has fewer flaws (cracks) so that the coating has greater impedance than other coatings. Among those Cr(VI) treated zinc sheets, the corrosion resistance decreases in the following order: R_p (ZnCr5s) > R_p (ZnCr1s) > R_p (ZnCr10s) > R_p (ZnCr30s) > R_p (ZnCr60s), within 16 h in the 0.01 M NaCl solution.

References

1. N. M. Martyak, J. E. McCaskie and L. Harrison, *Metal Finishing*, 94 (1996) 65.
2. X. Zhang, C. van den Bos, W. G. Sloof, H. Terryn, A. Hovestad and J. H. W. de Wit, in: *Corrosion Science in The 21st Century*, Manchester, UK, 7-11 July, 2003; B. Cottis (Ed.), *J. Corros. Sci. Engineering*, Vol. 6, paper 57 (2003) (ISSN 1466-8858).
3. M. G. Fontana, *Corrosion Engineering*, 3rd ed., (McGraw-Hill, Inc., 1986).
4. R. G. Kelly, J. R. Scully, D. W. Shoesmith and R. G. Buchheit, *Electrochemical Techniques in Corrosion Science and Engineering*, (Marcel Dekker, Inc., New York, 2003).
5. Computer Program, *ZView for Windows*, version 2.1, Scribner Associates, Inc., Southern Pines, NC, 1998.
6. E. Gileadi, E. Kirowa-Eisner and J. Penciner, *Interfacial Electrochemistry*, (Addison-Wesley Publishing Co. Inc., 1975).
7. M. Stern and A. L. Geary, *J. Electrochem. Soc.*, 104 (1957) 56.
8. G. W. Walter, *Corros. Sci.*, 16 (1976) 573.
9. L. M. Baugh, *Electrochim. Acta*, 24 (1979) 657.
10. J. W. Johnson, Y. C. Sun and W. J. James, *Corros. Sci.*, 11 (1971) 153.
11. V. Barranco, S. Feliu Jr and S. Feliu, *Corros. Sci.*, 46 (2004) 2203.
12. X. G. Zhang, *Corrosion and Electrochemistry of Zinc*, (Plenum Press, New York, 1996).
13. F. Mansfeld, *Corrosion*, 36 (1981) 301.
14. F. Mansfeld, M. W. Kendig and S. Tsai, *Corrosion*, 38 (1982) 570.
15. E. P. M. van Westing, G. M. Ferrari and J. H. W. de Wit, *Corros. Sci.*, 34 (1993) 1511.
16. R. G. Buchheit, M. Cunningham, H. Jensen, M. W. Kendig and M. A. Martinez, *Corrosion*, 54 (1998) 61.
17. A. Pirnát, L. Mészáros, G. Mészáros and B. Lengyel, *Corros. Sci.*, 34 (1993) 1147.
18. G. O. Ilevbare and J. R. Scully, *Corrosion*, 57 (2001) 134.
19. C. Deslouis, M. Duprat and C. Tulet-Tournillon, *J. Electroanal. Chem.*, 181 (1984) 119.
20. C. Deslouis, M. Duprat and C. Tournillon, *Corros. Sci.*, 29 (1989) 13.
21. D. Ende, W. Kessler, D. Oelkrug and R. Fuchs, *Electrochim. Acta*, 38 (1993) 2577.
22. P. Campestrini, E. P. M. van Westing and J. H. W. de Wit, *Electrochim. Acta*, 46 (2001) 2631.
23. G. Goeminne, H. Terryn and J. Vereecken, *Electrochim. Acta*, 40 (1995) 479.

24. J. R. Macdonald, in: The First International Symposium on The Electrochemical Impedance Spectroscopy, Bombannes, France, 22 - 26 May, 1989; (Pergamon press, Electrochimica Acta, 1990) pp. 1483-1492.
25. M. Tomkiewicz, *Electrochim. Acta*, 35 (1990) 1631.
26. F. Berthier, J.-P. Diard and R. Michel, *J. Electroanalytical Chemistry*, 510 (2001) 1.
27. F. Geenen, *Characterisation of Organic Coatings with Impedance Measurements*, PhD thesis, Delft University of Technology, 1991.
28. F. Mansfeld, in: *Proceedings of the first international symposium on electrochemical impedance spectroscopy*, C. Gabrielli (Ed.), 35 (Pergamon Press, Bombannes, France, 1990) pp. 1533-1544.
29. L. Fedrizzi, L. Ciaghi, P. L. Bonora, R. Fratesi and G. Roventi, *J. Appl. Electrochem.*, 22 (1992) 247.
30. R. L. Zeller III and F. Savinell, *Corros. Sci.*, 26 (1986) 389.
31. E. P. M. van Westing, G. M. Ferrari and J. H. W. de Wit, *Corros. Sci.*, 36 (1994) 1323.
32. E. P. M. van Westing, G. M. Ferrari and J. H. W. de Wit, *Corros. Sci.*, 36 (1994) 957.
33. R. Guo, F. Weinberg and D. Tromans, *Corrosion*, 51 (1995) 356.

Chapter 6

Heat Effect on Corrosion Performance of Cr(VI)-Based Conversion Coatings

6.1 Introduction

It is necessary to dry chromate coatings after the chromating process, because in the wet condition the coatings are liable to mechanical damage. Furthermore, the slow removal of water from the coating at ambient temperature due to evaporation can result in pore formation and poor adhesion to the underlying zinc substrate [1]. The stability of chromate conversion coatings (CCCs) at higher temperatures is also important because passivated metal parts have to endure heat treatment during the fabrication of assemblies. For example, it is recommended that conversion coatings should be dehydrated prior to powder coating them to reduce pinhole formation [2]. It was reported that the drying temperature has little effect on the appearance of chromate coatings, but the heat treatment often results in the formation of film cracks and the transition of chromium compounds into insoluble forms [1,3]. Drying at elevated temperatures (above 50 °C) can result in the formation of brittle, cracked chromate coatings on zinc, which provide less effective corrosion protection [4].

However, the heating effect on the corrosion protection provided by the chromate coatings is strongly dependent on the nature of the metal substrate. It was reported that heating the chromate coatings on 2024 aluminium alloys degrades the coatings, while heating the magnesium substrates improves the corrosion resistance in the salt spray environment [3,5].

A progressive decrease in the Cr(VI) content of chromate coatings on aluminum alloys with increasing heating temperature was reported by Laget *et al.* [5]. For 2024 aluminum alloy, they found that this fall in the Cr(VI) content was associated with a

significant decrease in the corrosion resistance of the coating. For 1100 aluminum alloy, on the other hand, no significant change in the corrosion resistance was observed. Clearly, the effect of the drying (or heat treatment) temperature on the corrosion protection provided by chromate conversion coatings is complicated, and is strongly dependent on the nature of the metal substrate.

In this chapter, the heat effect on morphology, composition and corrosion behavior of the chromium based conversion coatings on galvanized steel and on pure zinc sheets are investigated. The possible degradation mechanism of the conversion coatings is discussed.

6.2 Experimental

6.2.1 Sample preparation

Two kinds of substrate materials are used in this study. One is electro-galvanized steel. The 1 mm thick carbon steel sheets were cut into 5×10 cm specimens. Zinc electro-deposition procedure was carried out in a bath containing 43 g/l ZnO, 32 g/l NaOH, 90 g/l NaCN at room temperature. The current density was 20 mA/cm^2 and the coating time was 30 minutes for each specimen. The average thickness of the zinc coatings was $13 \text{ }\mu\text{m}$, which was determined by X-ray fluorescence method. The X-ray fluorescence method measures the mass of coating per unit area, which can also be expressed in units of linear thickness provided that the density of the coating is known[6]. This method is based on the combined interaction of the coating and substrate with incident radiation of sufficient energy to cause the emission of secondary radiations characteristic of the elements composing the coating and substrate. The thickness of the coating can be measured in one of two ways. One is based on measuring the intensity of the X-ray fluorescence of the coating material. The intensity of the X-ray fluorescence increases as the thickness of the coating increases until it reaches a saturation level. The other is based on measuring the intensity of the X-ray fluorescence of the base material being absorbed or attenuated by the top layer. In this method the intensity of the X-ray fluorescence of the base material decreases as the thickness of the coating increases until it reaches a minimum level for a thick coating

layer. This method is generally used when measuring a coating of material with an atomic number less than that of titanium, as its low X-ray fluorescence energy cannot be detected by the proportional counter[7]. For zinc coating on steel, the first method was used and it is calibrated using pure zinc, iron and zinc coating on steel with a known thickness.

The other substrate material is rolled zinc sheet. Zinc sheet (99.95% Zn, 1 mm thick) was cut into different size for different investigations: 7.5×2.5 cm specimens for the Fourier Transform Infrared spectroscopy (FTIR) analysis, 2.0×1.6 cm specimens for the X-ray photoelectron spectroscopy (XPS) analysis and 2.0×2.0 cm specimens for electrochemical measurements. All the specimens were polished using 1 μ m diamonds as the final polishing step. The polished specimens were cleaned in acetone and ethanol for 2 minutes, sequentially.

The surfaces of specimens were activated in 0.25 % HNO₃ for 30 seconds and rinsed in deionized water before the chromating treatment was performed. Chromate coating was carried out in a bath containing 200 g/l Na₂Cr₂O₇ + 10 g/l H₂SO₄ (pH 1.2 ± 0.1) for 10 seconds at room temperature and rinsed in de-ionized water. After drying in flowing air, these samples were divided in three groups and heated in an oven at 60, 110 or 210°C for 30 minutes. These heat-treated samples were noted down as EGCr60, EGCr110, EGCr210 for chromate coatings on the EG steel; ZnCr60, ZnCr110 and ZnCr210 for chromate coatings on zinc sheet, where the numbers represent the temperature. After cooling down, they were kept in plastic boxes at least for 24 h at room temperature before surface analysis and corrosion tests. The designations of experiments are shown in Table 6.1.

Table 6.1 Details of the sample treatments and experiments.

Sample	Chromating (10 s)	Heating @ (°C)			Morphology	Composition Analysis	Corrosion Tests
		60	110	210			
EG steel	√	√	√	√	√	EDS	√
Pure zinc	√	√	√	√	√	XPS, FTIR	√

6.2.2 Morphology of chromate coatings

The surface morphology of treated and untreated specimens was investigated by means of SEM. The composition of the chromate coatings on electro-galvanized (EG) steel in a flat area and at a crack was analyzed by energy-dispersive spectrometry (EDS). The width and depth of micro cracks were measured using AFM (NanoScope III).

6.2.3 FTIR and XPS analyses

The compositions of the chromate coatings were analyzed by FTIR. The reflection absorbance IR spectra were obtained on the NexusTM spectrometer from Nicolet using OMNIC software. The specimen was laid on a flat sample support. The angle of incidence was 84 degrees. The detector used was a liquid nitrogen cooled MCT-B detector. The spectra were recorded in the 4000 to 400 cm^{-1} range with a resolution of 4 cm^{-1} .

The composition of the chromate layer was also analysed by XPS. The XPS analysis was carried out with a PHI 5400 ESCA using 400 Watt Mg K_{α} radiation (1253.6 eV). This instrument is equipped with a Spherical Capacitor Analyser (SCA) operating with a constant pass energy value. The energy scale of the spectrometer was calibrated according to the method described by Anthony *et al.* [8]. Overview spectra were obtained in the range of 0 – 1100 eV with an analyser pass energy of 71.55 eV. The intensities of Cr 2p, O 1s, C 1s, S 2p and Zn 2p photoelectron lines were recorded separately with an analyser pass energy of 35.75 eV. The electrons emitted from the specimens were detected at an angle of 45° with respect to the specimen surface. The C 1s peak (284.8 eV) was used as a reference to correct for electrostatic charging. The X-ray satellites, present in all measured spectra as a consequence of the non-monochromatic nature of the incident X-ray beam, were removed using the relative height and displacements with respect to the height and position of the Mg K_{α} . In order to assess the relative amounts of the species constituting the photoelectron lines, curve fitting was performed with symmetrical Gaussian-Lorentzian peaks after smoothing of the curve and Shirley-type subtraction of the background. The number of components to be fitted to any particular spectrum was determined by choosing the fit with the

minimum reduced chi-squared value (χ^2). Cr 2p spectra were fitted for chromium in the form of Cr_2O_3 (576.3 ± 0.2 eV), $\text{Cr}(\text{OH})_3$ or CrOOH (577.4 ± 0.2 eV) and Cr(VI) (579.2 ± 0.2 eV) in the chromate layer [9-11].

6.2.4 Open circuit potential and polarization measurements

Specimens were cut into 2×2 cm pieces. Open circuit potential (OCP) and potentiodynamic polarization measurements were done in a cell containing a platinum counter electrode and a reference electrode (saturated calomel electrode, SCE: $E^0 \approx 0.241$ V vs. NHE).

The chromated EG steel samples were immersed in 0.6 M NaCl solution for 1 hour to establish a relatively steady open circuit potential (OCP). Then polarization measurements started at -0.2 V versus OCP ending at 1 V versus OCP. The scan rate was 0.2 mV/s. Solutions with two different pH values (5.8 and 6.9 ± 0.1) were used. The pH was adjusted using HCl and NaOH. Polarization measurements were also performed in both aerated and de-aerated solution, purged by N_2 . From the polarization curves, the corrosion potential and the corrosion current were calculated using the Tafel-fit method within a range of ± 50 mV versus OCP.

For chromated pure zinc specimens, the OCP was measured in 0.01 M NaCl solution (pH 6) for 1 hour. After that, polarization measurements were obtained by scanning the potential first from OCP to -0.25 V versus OCP, then in the opposite direction to OCP and ending at +0.25V versus OCP. The scan rate was 0.167 mV/s.

6.2.5 Impedance measurements

For chromated EG steel specimens, electrochemical impedance spectroscopy (EIS) measurements were carried out in 0.6 M NaCl solution (pH 6.9 ± 0.1) after immersion for 1 hour at open circuit. The counter electrode was a platinum circular net, flat and parallel to the surface of samples. The reference electrode was an $\text{Ag}/\text{AgCl}/\text{Cl}^-$ (saturated KCl) electrode ($E^0 \approx 0.197$ V vs. NHE ≈ -0.044 V vs. SCE), which was specially designed for EIS measurements. All the potential values will be presented

against the reference of V_{SCE} . The impedance response was analyzed using a Solartron 1250 frequency response analyzer coupled with a Solartron 1286 electrochemical interface in the frequency range of 60 kHz – 0.01 Hz with 5 mV *a.c.* amplitude versus the OCP.

For the chromated pure zinc, the EIS measurements were carried out in 0.01 M NaCl solution after immersion for 0.5 hours at open circuit. The impedance response was analyzed using a Solartron 1255 frequency response analyzer coupled with a Solartron 1287 electrochemical interface in the frequency range of 60 kHz – 0.1 Hz with 10 mV *a.c.* amplitude versus the OCP.

6.3 Results

6.3.1 Heat effect on morphology of Cr(VI)-based conversion coatings

Fig. 6.1 shows the topographic image (a) and the EDS spectrum (b) for the electro-galvanized (EG) steel. Shallow pinholes were visible on the surface of zinc coating. The EDS spectrum shows that the coating was pure zinc with very little zinc oxides and carbon contamination on the surface. No Fe signal was detected. Fig. 6.2 shows the SEM images for chromate-coated specimens heated at different temperatures, (a) and (b) 60°C, (c) and (d) 110°C, (e) and (f) 210°C. After chromate coating, the shallow pinholes in the zinc coatings were covered with a chromate layer.

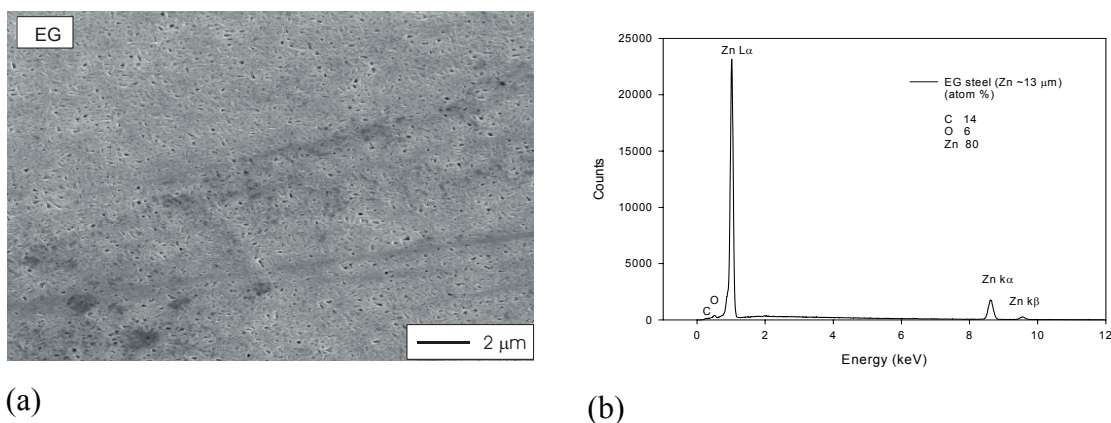


Fig. 6.1 (a) SEM image and (b) EDS spectrum for an electro-galvanized (EG) steel.

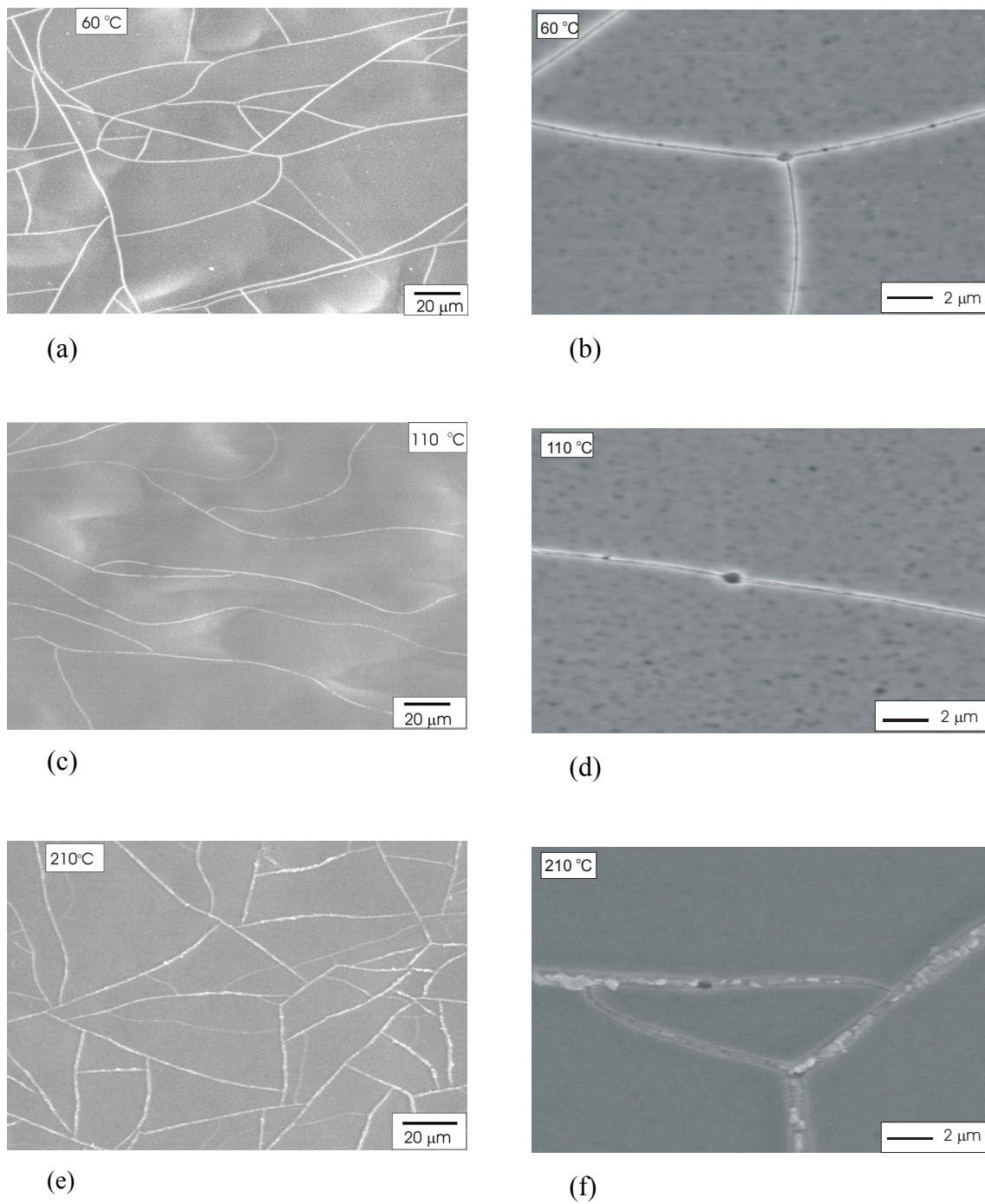


Fig. 6.2 SEM images for a chromate coating (10 sec.) on the EG steel heated at different temperatures: (a) and (b) 60°C, (c) and (d) 110°C, (e) and (f) 210°C, in an oven for 30 min.

All the chromated specimens heated at different temperatures showed microcracks in the coatings. For the chromated EG steel specimen heated at 110°C (EGCr110), the size of the microcracks was similar to the cracks in the chromated EG steel heated at 60°C (EGCr60), but the density of cracks (the length of crack per unit area) was slightly lower (see Figs. 6.2 (a), 6.2 (c) and 6.2 (e)). The width of the cracks in the chromated EG steel heated at 210°C (EGCr210) was larger than that in the coatings heated at 60°C (EGCr60) and at 110°C (EGCr110) (see Fig. 6.2 (b), 6.2 (d) and 6.2 (f)). In the cracks, the EDS spectrum shows that the chromium and oxygen contents were lower than those in the flat area, while the zinc content was higher (see Figs. 6.3 (a) and (b)). Moreover, zinc oxides (white) were visible along the cracks in the EGr210 samples under the electron microscope.

The AFM topography and the section analysis results for the coatings heated at 60, 110 and 210°C are shown in Figs. 6.4, 6.5 and 6.6, respectively. The depth of the microcracks was about 57 nm in the EGr60 sample and 122 nm in the sample EGr210. The depth of the microcracks in the EGr110 sample was less than 115 nm. The width of the cracks for samples heated at 60 or 110°C varied in a range of 200 - 600 nm, no significant difference was observed between these two kinds of samples due to the inhomogeneous width distribution of microcracks. With samples heated at 210°C, the width of cracks varied from 300 to 800 nm. Protuberant crack edges were observed.

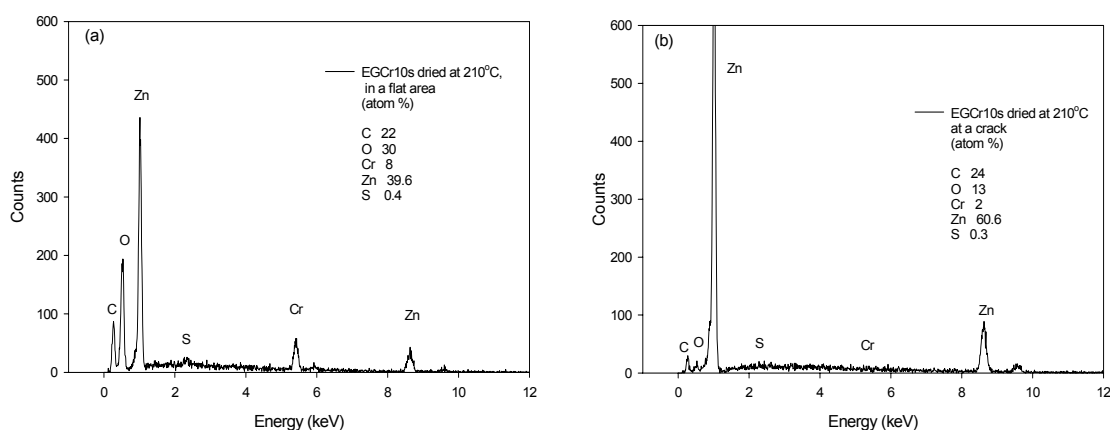


Fig. 6.3 EDS spectra (a) in a flat area and (b) inside a crack of the chromate coating on the EG steel (10 sec.) heated at 210°C in an oven for 30 min.

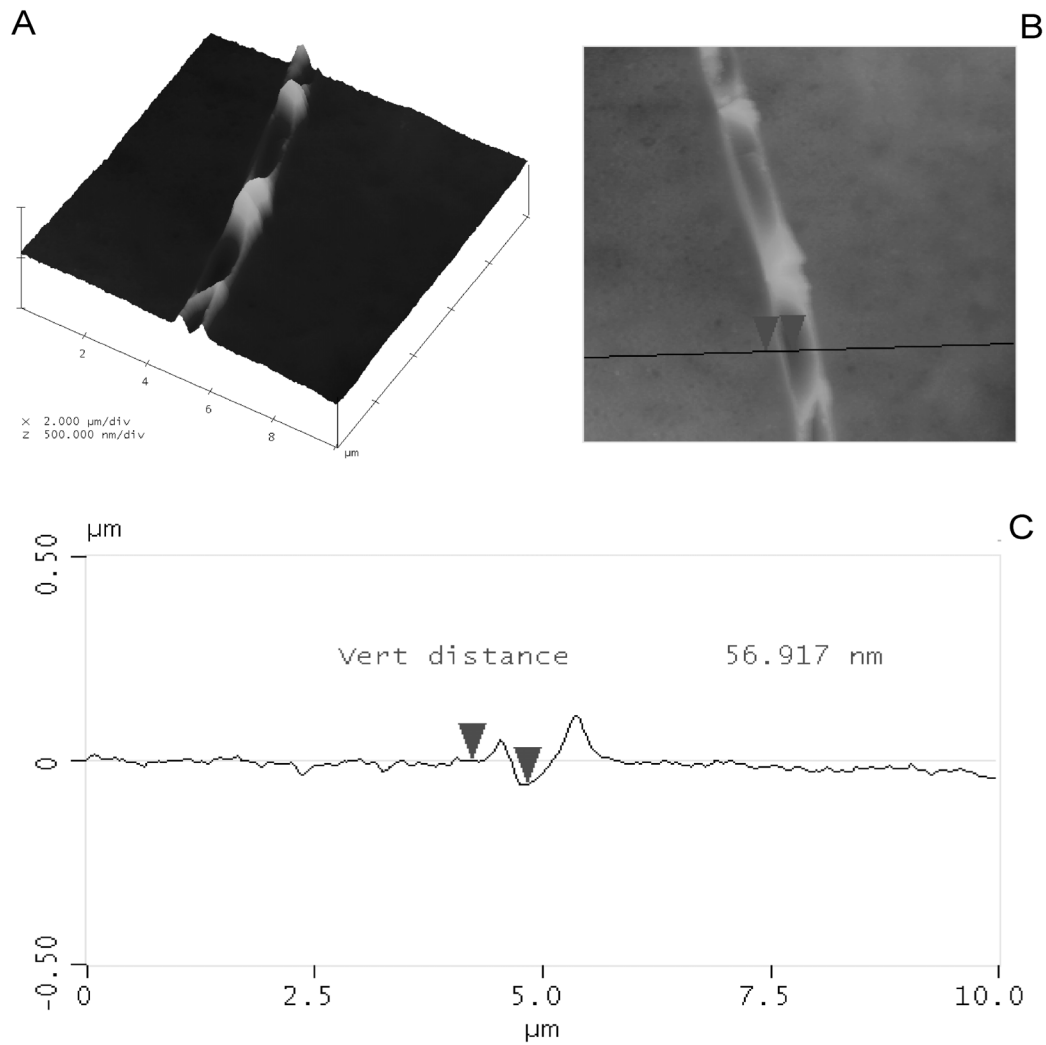


Fig. 6.4 Topographic images: (A) 3D and (B) 2D, and (C) topographic line scan along the line in (B) for a coating on the EG steel heated at 60°C in an oven for 30 min.

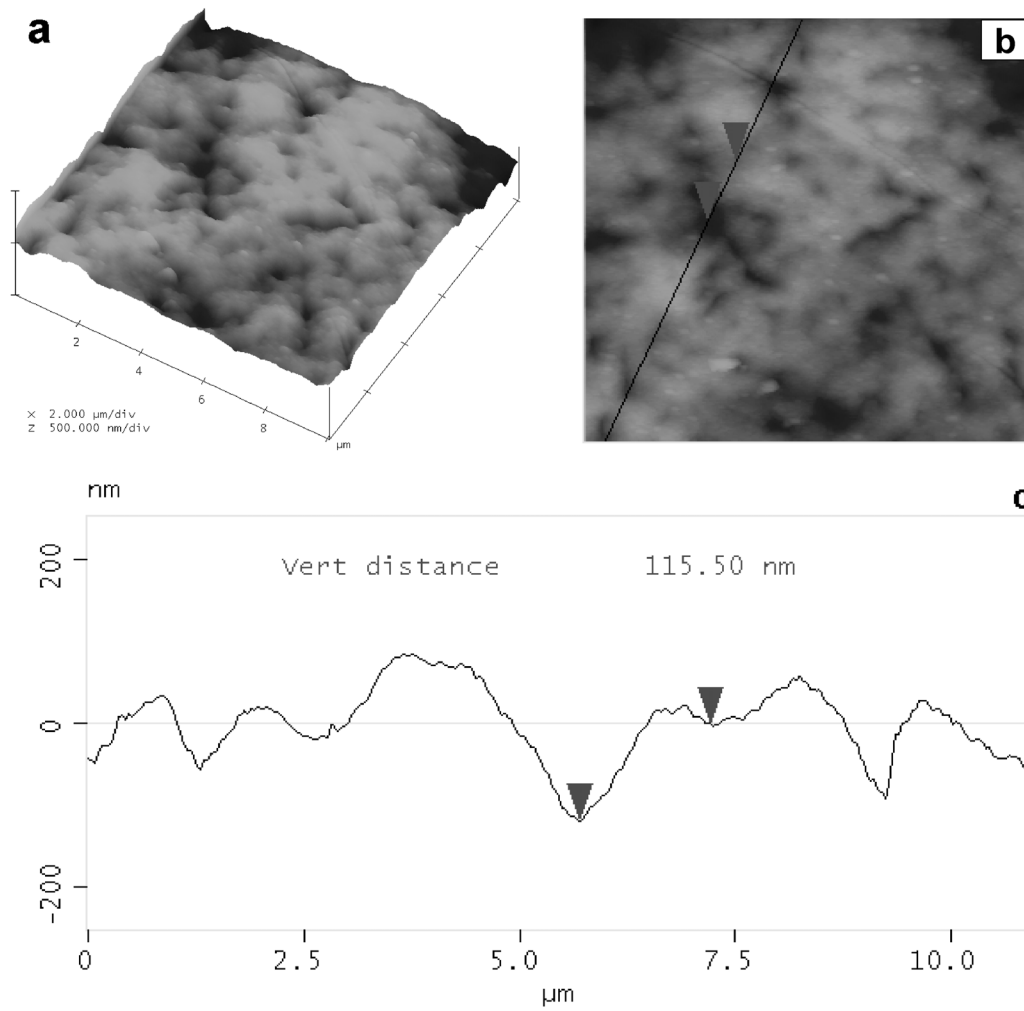


Fig. 6.5 Topographic images: (A) 3D and (B) 2D, and (C) topographic line scan along the line in (B) for a coating on the EG steel heated at 110°C in an oven for 30 min.

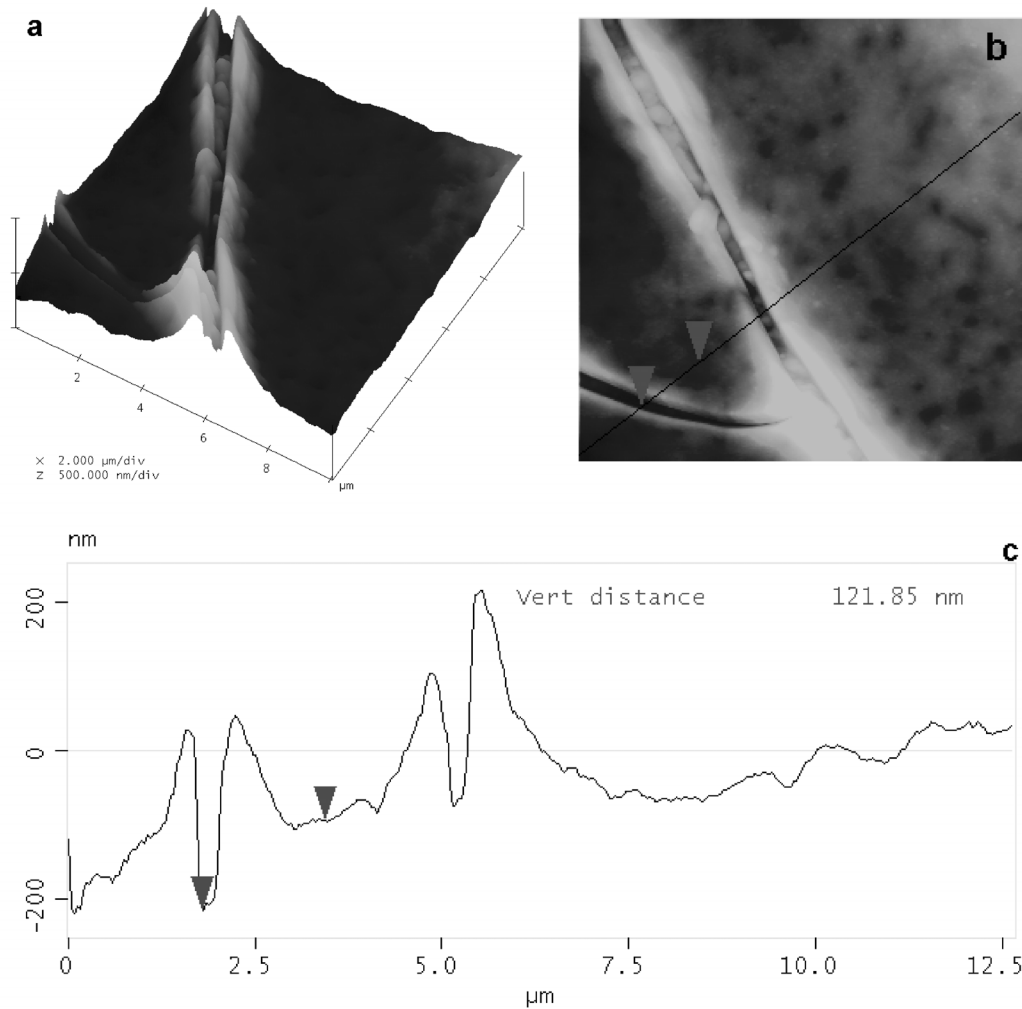


Fig. 6.6 Topographic images: (A) 3D and (B) 2D, and (C) topographic line scan along the line in (B) for a coating on the EG steel heated at 210°C in an oven for 30 min.

Figs. 6.7 shows the SEM images for chromate-coated pure zinc heated at different temperatures, (a) 60, (b) 110 and (c) 210°C. Microcracks were also observed in these coatings. The width of the cracks, for a coating heated at 60°C, was about 90 nm. For a coating heated at 110°C, it was about 110 nm and for a coating heated at 210°C, it was 300 nm. However, concerning the crack density, *i.e.* the length of crack per unit area, the coating heated at 110°C showed the lowest crack density. The same crack densities were also observed under an optical microscope (no optical micrographs are presented here), so the formation of the microcracks cannot be attributed to the vacuum conditions inside the scanning electron microscope.

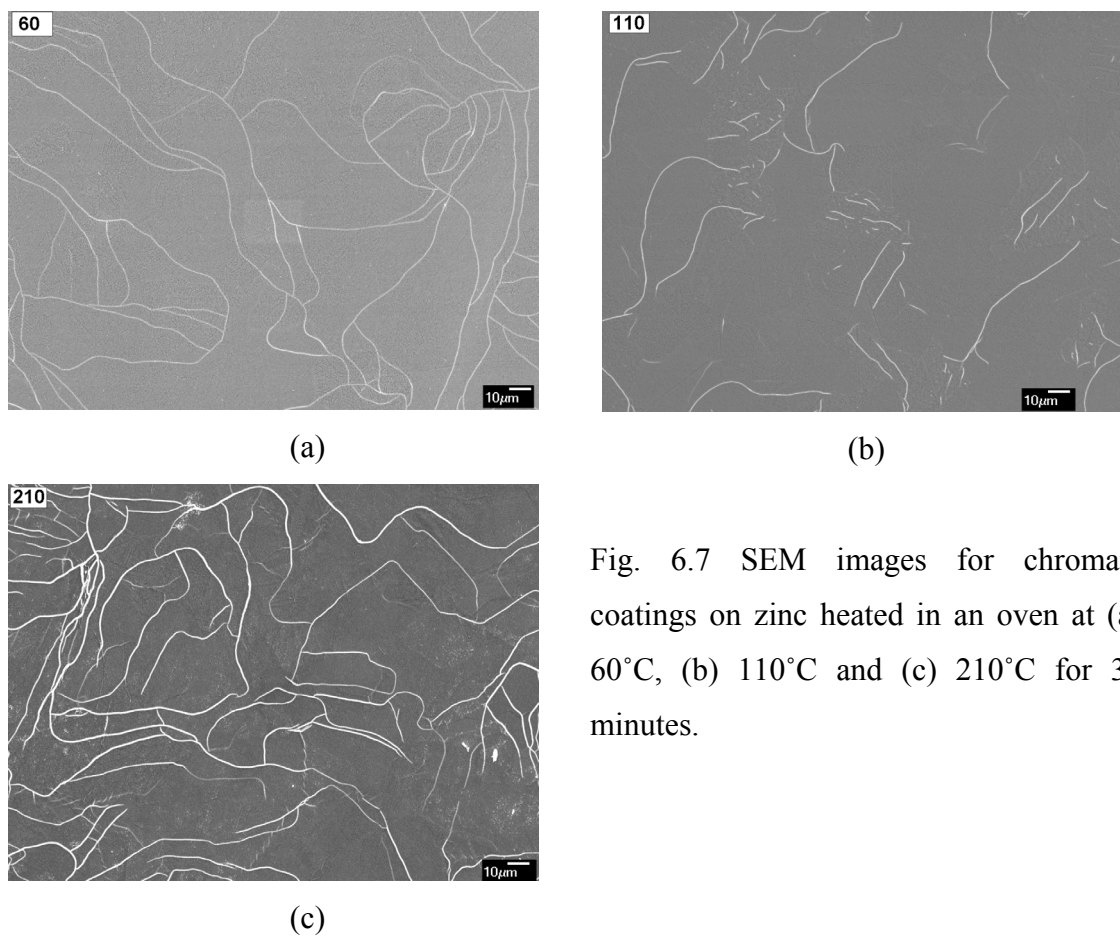


Fig. 6.7 SEM images for chromate coatings on zinc heated in an oven at (a) 60°C, (b) 110°C and (c) 210°C for 30 minutes.

6.3.2 Thermal reduction of Cr(VI) species in the coatings

Fig. 6.8 shows the vibration spectra for the chromated pure zinc samples heated at 60, 110 and 210°C. Almost all the peaks in these spectra become shorter with the increase of the drying temperature, except for the peaks in the range of 607 ~ 677 cm^{-1} . The vibration bands around 607 and 677 cm^{-1} are attributed to Cr_2O_3 . The bands between 860 and 948 cm^{-1} are attributed to the $\text{Cr}_2\text{O}_7^{2-}$ or CrO_4^{2-} anions due to the ν_1 and ν_3 vibrations, respectively [12,13]. The band at 1126 cm^{-1} is attributed to SO_4^{2-} [14]. The broad absorption band observed between 3000 and 3620 cm^{-1} is attributed to water or water of hydration, and the H-O-H bending motion at 1620 cm^{-1} is also seen [15]. The peaks at 1060 and 1426 cm^{-1} may be attributed to the bending vibration of water coordinated to the $\text{Cr}_2\text{O}_3 \cdot 2\text{H}_2\text{O}$ [16,17].

Fig. 6.8 shows that the area underneath the broad peak at 3440 cm^{-1} is smaller for the chromate coatings heated at the higher temperatures (110 and 210°C), suggesting that the dehydration of the coating was significant for these samples. Concerning the Cr(VI) species, it is important to observe that, for the chromate coating heated at 210°C , the peak at 948 cm^{-1} becomes lower and narrower while the peak near 677 cm^{-1} becomes taller than for the sample heated at 60°C . For the specimen heated at 110°C , both peaks become lower than for the sample heated at 60°C . These changes suggest that a certain fraction of Cr(VI) species is transferred to Cr(III) compounds when the specimen is heated at a higher temperature.

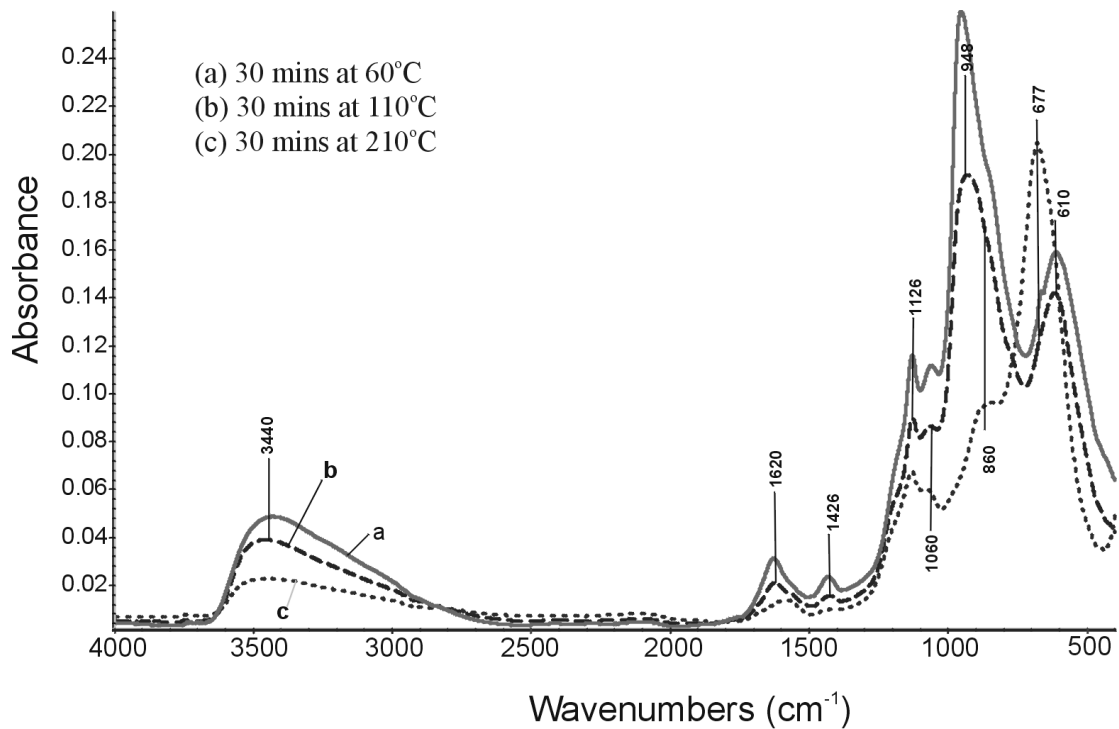


Fig. 6.8 FTIR vibration spectra for three chromated pure zinc samples: (a) heated at 60°C , (b) 110°C and (c) 210°C for 30 minutes.

Fig. 6.9 shows the vibration spectra obtained from a single chromated pure zinc sample sequentially heated at 60 , 110 and 210°C for 30 minutes at each temperature. Again, dehydration with an increase of temperature was observed. The peak at 948 cm^{-1}

(Cr VI) becomes shorter and the peaks near 677 cm^{-1} (Cr III) become taller, again showing that a certain fraction of Cr(VI) species has been transferred to Cr(III) compounds after drying at higher temperatures.

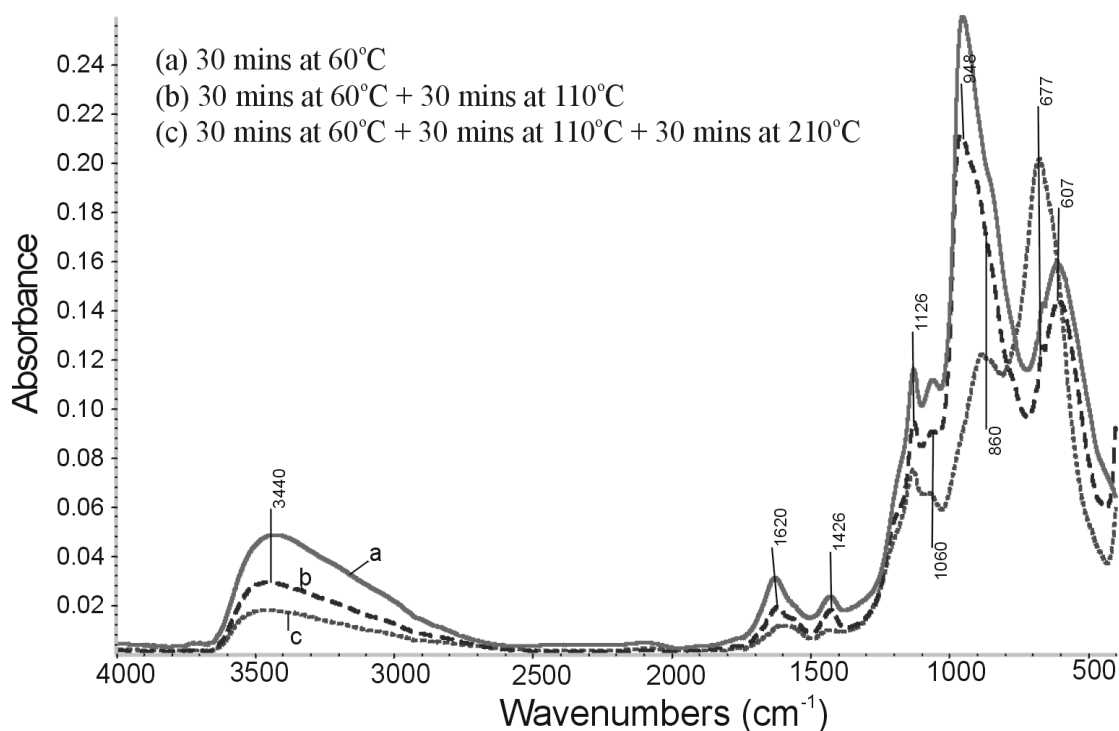


Fig. 6.9 FTIR vibration spectra obtained from a single chromated pure zinc sample sequentially heated at: (a) 60, (b) 110 and (c) 210°C for 30 minutes at each temperature.

Fig. 6.10 shows XPS spectra for the chromate coatings on zinc heated at 60, 110 and 210°C. This picture shows the presence of C, O, Cr, Zn and S in the top layer of the coatings. XPS analyses showed that when the drying temperature was increased, the carbon and zinc signals also increased, while the oxygen signal decreased. Of course, the oxidation of zinc would result in an increase of the oxygen content. However due to the dehydration of the chromate layer the net result is a loss of oxygen.

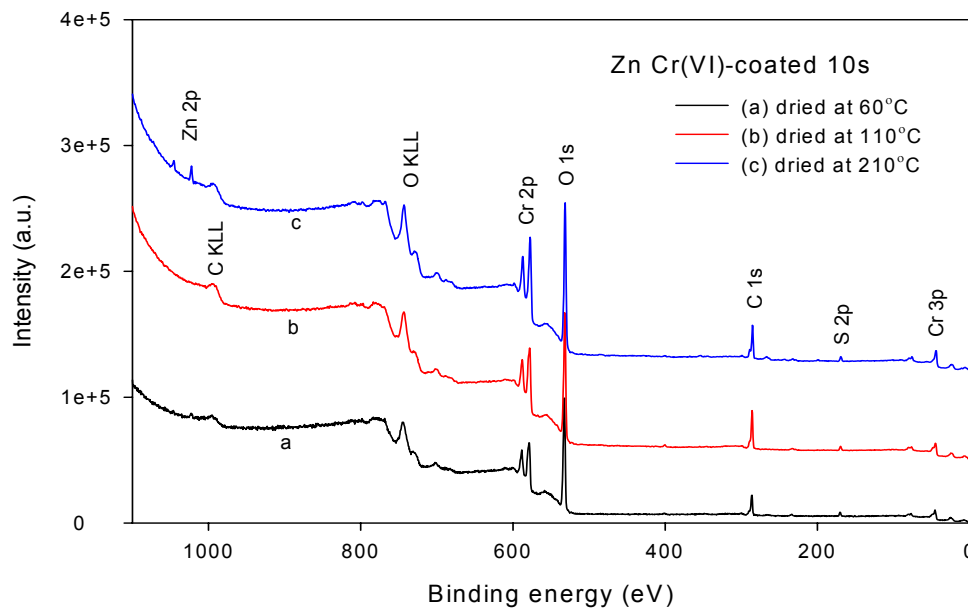


Fig. 6.10 XPS spectrum for a chromate coating heated at 60°C.

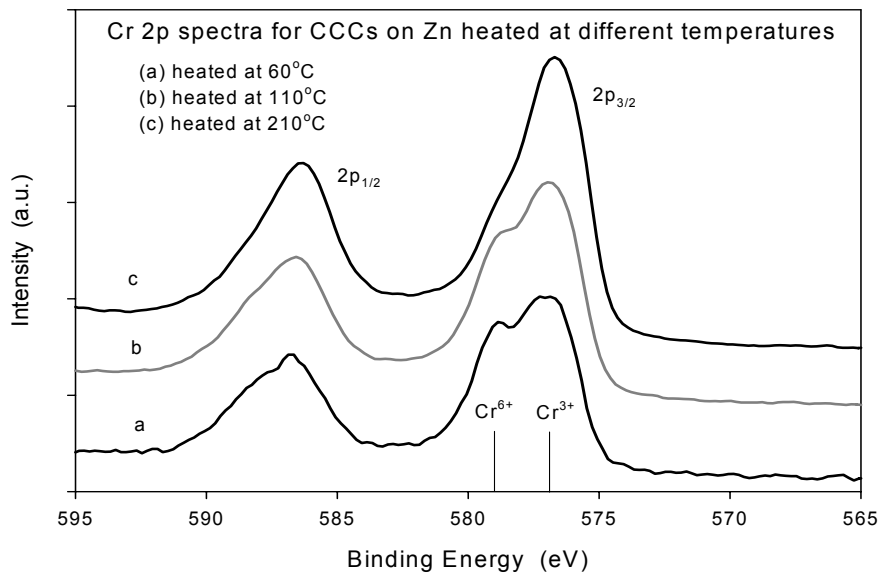


Fig. 6.11 Cr 2p XPS spectra for chromate coatings heated at different temperatures.

Fig. 6.11 shows the Cr 2p XPS spectra for chromate coatings heated at different temperatures. The peak at 579.2 eV is attributed to Cr(VI). This peak becomes shorter for the coatings heated at higher temperatures. By increasing the drying temperature

from 60 to 110 and 210°C, the ratio of Cr(VI) to total chromium in the coating decreased from 35% to 32% and 12%, respectively.

6.3.3 Open circuit potential

The open circuit potential, for all chromated EG steel specimens, dropped to more negative values at the beginning of the exposure. After a short time, it climbed to more positive values and slipped down again for all the chromated samples in the aerated 0.6 M NaCl solution (open to air), pH 5.8 (see Fig. 6.12 (A)). It reached its relatively stable state slowly within 1 hour and the values were in the range of -1.02 to -1.03 V_{SCE}. The OCP for the chromated samples was about 40 mV more positive than for zinc coatings (~ -1.07 V_{SCE}) in this solution. The OCP for all samples in the aerated solution at pH 6.9 had a similar behavior.

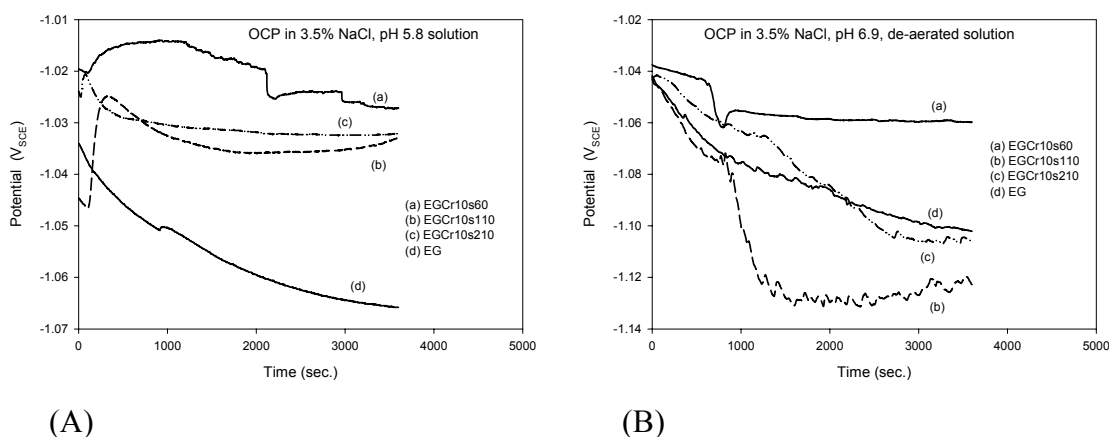


Fig. 6.12 Open circuit potential for samples in (A) quiescent 0.6 M NaCl (pH 5.8) and (B) de-aerated 0.6 M NaCl (pH 6.9) solution.

However, in de-aerated solutions (purged with N₂), the OCP for all the chromated samples was more negative than in aerated solutions. The open circuit potential measured in the de-aerated 0.6 M NaCl solution at pH 6.9, is presented in Fig. 6.12 (B). A similar behavior was observed for samples in the de-aerated solutions at pH 5.8. In this case, a potential drop and recovery process was observed only for the chromate coatings heated at 60°C. For the coatings heated at 110 or 210°C, the OCP dropped

down even further than that of the non-chromated EG steel samples. The OCP of the EGCr60 samples was still about 40 mV more positive than for the EG steel sample.

The open circuit potential of the chromate coatings moving to the negative direction in the initial tens seconds can be explained by the “re-hydration” of the chromate coatings (see Fig. 6.12). Electrolyte can access the zinc through defects of the chromate coatings. This enables zinc dissolution at defects so that it drives the potential to the negative direction. After a while, the adsorbed soluble chromates in the coating may dissolve and diffuse into defects. The Cr(VI) species can be reduced to insoluble Cr(III) compounds, which consumes electrons and causes the potential to rise. The precipitation of Cr(III) oxides/hydroxides may form a temporary passive layer to hinder the further dissolution of zinc. Passivation is also improved by direct reduction of oxygen. The corrosion products of zinc such as zinc oxide/hydroxide, may form at defects and fill the pores in the coatings, which influences the OCP value of the system. The OCP reaches a temporary stable value when dissolution and repairing processes balance out. In the de-aerated solution (see Fig. 6.12 (B)), less oxygen is available to passivate the active sites compared to samples in the aerated solution. The OCP for all the samples has moved to more negative values in the de-aerated solution.

6.3.4 Polarization curves

The polarization curves measured for chromated and unchromated EG steel in 0.6 M NaCl solutions are shown in Figs. 6.13(1) - 6.13(4). The corrosion potentials and the corrosion current density calculated from the polarization curves are shown in Table 6.2. In the quiescent solutions, the chromate coatings heated at 60°C showed a more negative corrosion potential of 100 mV than for the coatings heated at 110 or 210°C and even more negative than for the untreated EG steel. All the chromated samples showed lower corrosion currents (i_c) than the non-chromated samples (see Fig. 6.13 (1) and (2)), and the samples heated at 110°C (EGCr110) showed the lowest i_c in both the pH 5.8 and the pH 6.9 solutions.

In de-aerated solutions, the corrosion potential did not show much difference for all the samples (see Fig. 6.13 (3) and (4)). The corrosion currents were smaller for almost all samples except for the EGCr110 samples than those in the quiescent solution. The

EGCr110 samples remained at the lowest corrosion current near their free corrosion potentials in the de-aerated solutions.

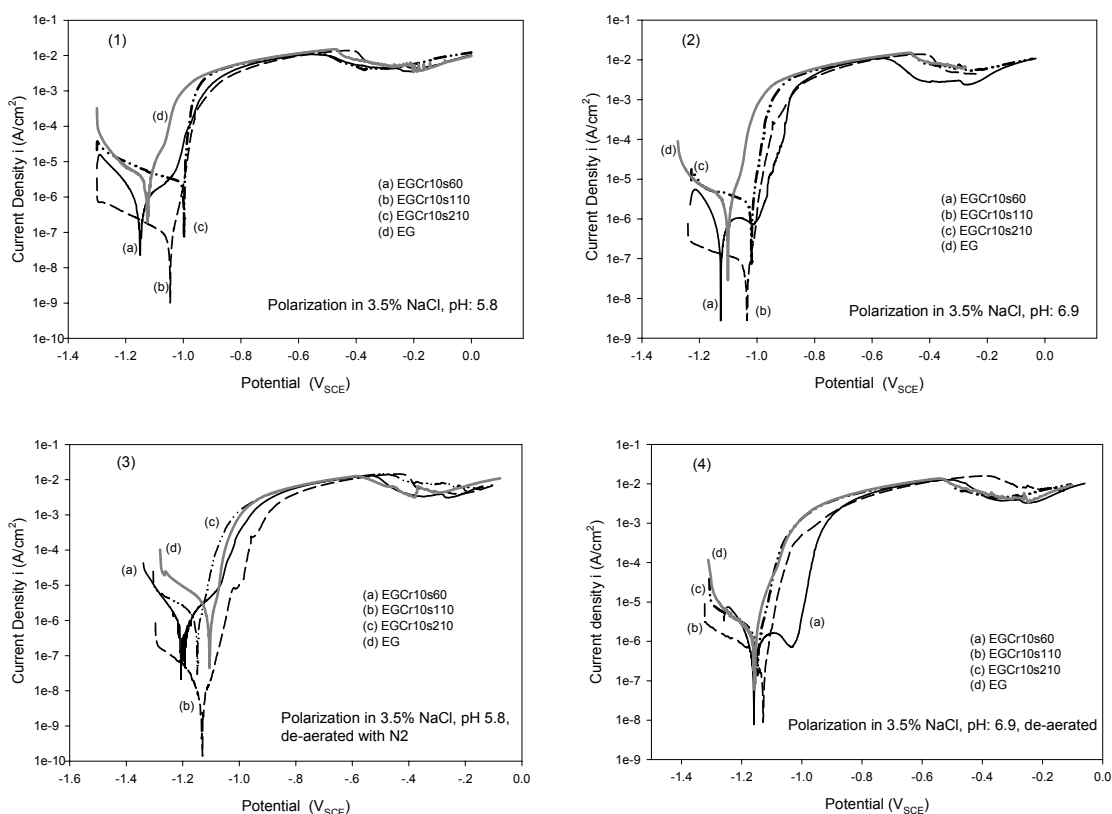
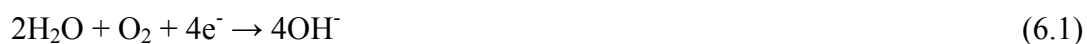


Fig. 6.13 Polarization curves for samples in 0.6 M NaCl solutions: (1) quiescent, pH 5.8; (2) quiescent, pH 6.9; (3) de-aerated, pH 5.8; and (4) de-aerated, pH 6.9.

It is worth noting that for the chromate coatings heated at 60°C (EGCr60), a passivation process in solution has been observed (see Fig. 6.13(2) and (4)). For the EGCr60 samples, the current increases with the potential at the beginning of the scan starting at the cathodic branch for a short time. This may be related to the reduction of hexavalent chromium to Cr(III) [18], which adds to the cathodic current. The reduction of Cr(VI) to Cr(III) can contribute to the formation of a passive layer at defects. The cathodic reactions[19], such as



or/and



will consume hydrogen ions and locally increase the pH value, which enables a better passivation process. When the potential reaches $-1.0 \text{ V}_{\text{SCE}}$, these samples exhibit the lowest current in the solution with pH 6.9. The range of passivity shown by the EGCr60 samples increased from 50 mV in the neutral quiescent solution to 60 mV in the neutral de-aerated solution.

Table 6.2. Corrosion potential E_c (V_{SCE}) and corrosion current i_c ($\mu\text{A}/\text{cm}^2$) calculated from polarization curves in Fig. 6.13 using the Tafel-fit method.

Samples	Solutions and results							
	0.6 M NaCl (pH: 5.8 ± 0.1)				0.6 M NaCl (pH: 6.9 ± 0.1)			
	Quiescent		De-aerated		Quiescent		De-aerated	
	E_c	i_c	E_c	i_c	E_c	i_c	E_c	i_c
EGCr60	-1.15	0.306	-1.20	0.049	-1.13	1.47	-1.16	1.17
EGCr110	-1.05	0.087	-1.13	0.006	-1.03	0.045	-1.13	0.25
EGCr210	-1.06	1.43	-1.15	1.13	-1.02	2.98	-1.15	1.87
EG steel	-1.12	3.21	-1.11	0.75	-1.10	4.58	-1.16	1.50

Fig. 6.14 shows the polarization curves obtained in aerated 0.01 M NaCl solution, for three chromate-coated specimens all heated at 60°C . The mixed potential moved about 120 mV in the negative direction against the OCP. All of the specimens showed a kind of anodic passivation behavior in a range of 160 mV. The polarization curves display a good degree of reproducibility.

Fig. 6.15 shows the polarization curves obtained in the same corrosive medium for coatings heated at the three different temperatures. Values of the corrosion potential and estimated corrosion current density for each coating and for the uncoated zinc are presented in Table 6.4. The corrosion current values were estimated from the slopes of the relevant cathodic polarization curves within 10 mV of the open-circuit potential, using the Stern-Geary equation, *i.e.* $i_{\text{corr}} = k / R_p$. A value of 10 mV was assumed for k ,

the proportionality constant in the Stern-Geary relationship; this value is typical for zinc products immersed in near-neutral chloride solutions [20,21].

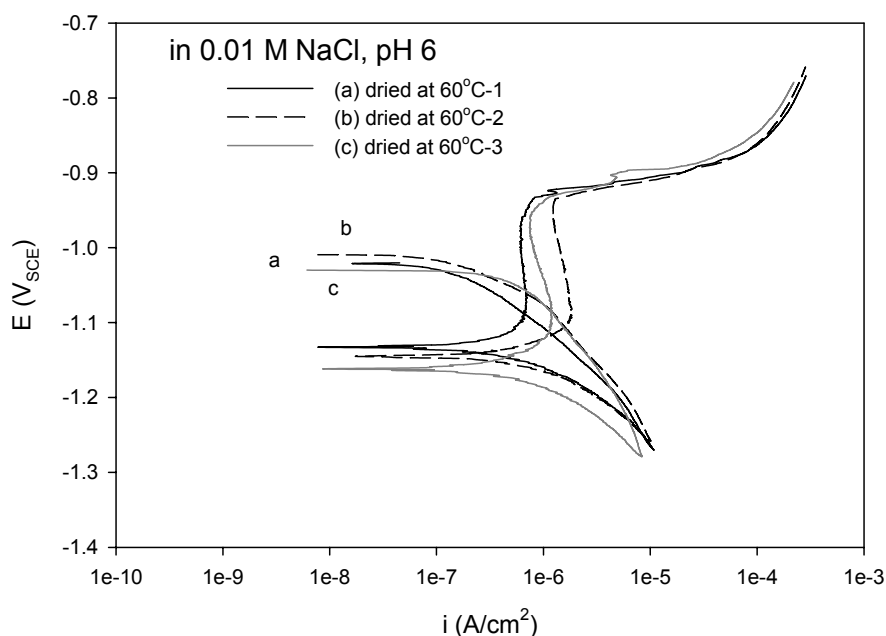


Fig. 6.14 Polarization curves for three Cr(VI) coated specimens heated at 60°C. The potential scan rate was 0.167 mV/s.

Table 6.4 Corrosion potential E_c and corrosion current i_c calculated from polarization curves in Fig. 6.15 using the R_p -fit method.

Samples	Solution open to air	
	E_{corr} (V _{SCE})	i_{corr} ($\mu\text{A}/\text{cm}^2$)
ZnCr60	-1.02	0.1
ZnCr110	-0.99	0.03
ZnCr210	-0.99	0.2
Zn	-0.98	7.7

For all the coatings, the anodic breakdown potential was almost the same, around -0.92 V_{SCE}. Only for the coating heated at 60°C did the mixed potential move in the negative direction against the OCP. Significantly, the cathodic current recorded near the

OCP was smaller for the coatings heated at 110°C than for the coatings heated at the lowest temperature (60°C). For the chromate coatings heated at the highest temperature (210°C), the cathodic current measured near the mixed potential was larger than for the coatings heated at 60°C.

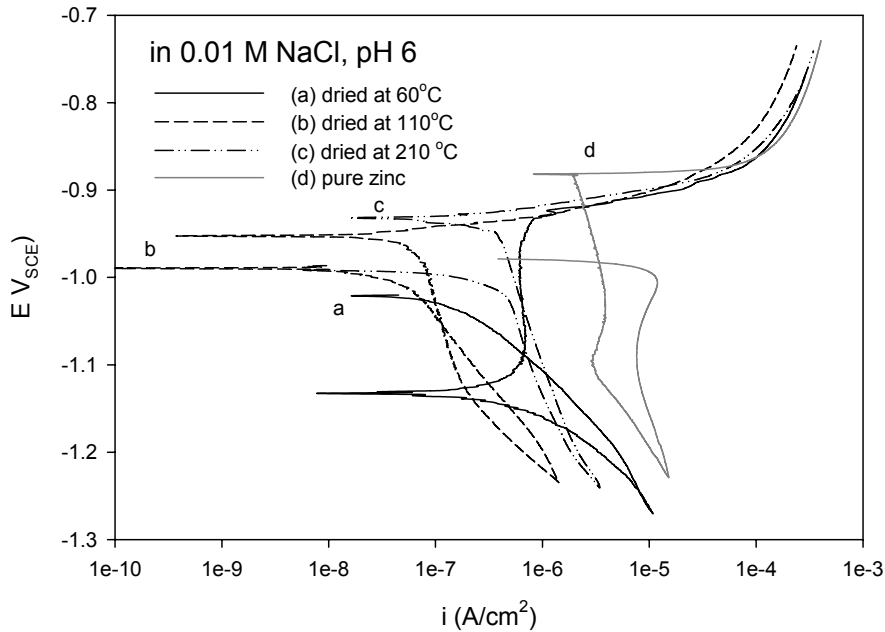


Fig. 6.15 Polarization curves for chromate coatings heated at different temperatures. The potential scan rate was 0.167 mV/s.

6.3.5 Impedance measurements

Figs. 6.16 and 6.17 present the Nyquist and Bode plots of the impedance, respectively, which were obtained after immersion in the quiescent 0.6 M NaCl solution (pH 6.9) for 2 hours for the chromate treated and untreated EG steel samples. For the chromate treated EG steel, the corrosion process occurs on the zinc surface exposed to the electrolyte through pores or defects of the chromate layer. The shape of the Bode plots suggests that there are three time constants. Fig. 6.18 shows a schematic of the chromate conversion coating on the EG steel with an equivalent circuit. In this model, R_{el} is for the electrolyte resistance, C_p for the capacitance of the chromate layer, R_{cp} for the resistance in the pores of the chromate layer, C_{dl} for the double-layer capacitance and R_{ct} for the charge transfer resistance of the electrode reaction effects. C_{ad} and R_{ad} are parameters for adsorption–reaction processes [22] and/or for oxygen diffusion

effects [23]. The elements C_{dl} and C_{ad} were substituted by constant phase elements (CPE). The impedance of a CPE is given by the equation (5.8) [24]. The capacitance of the double layer was estimated using the equation (5.9), $C = Y_0^{1/n} R^{(1-n)/n}$, where R is the resistance parallel to the CPE [25]. The impedance behavior of the chromate treated and untreated EG steel can be explained by the equivalent circuits shown in Fig. 6.19 and in Fig. 5.3 (b) respectively. The impedance data were fitted using the software Zview for windows (version 2.3d)[26]. The fitting results are shown in Table 6.3. The Chi-squared value of fit is better than 6×10^{-4} and the value of weighted sum of squares is less than 0.13.

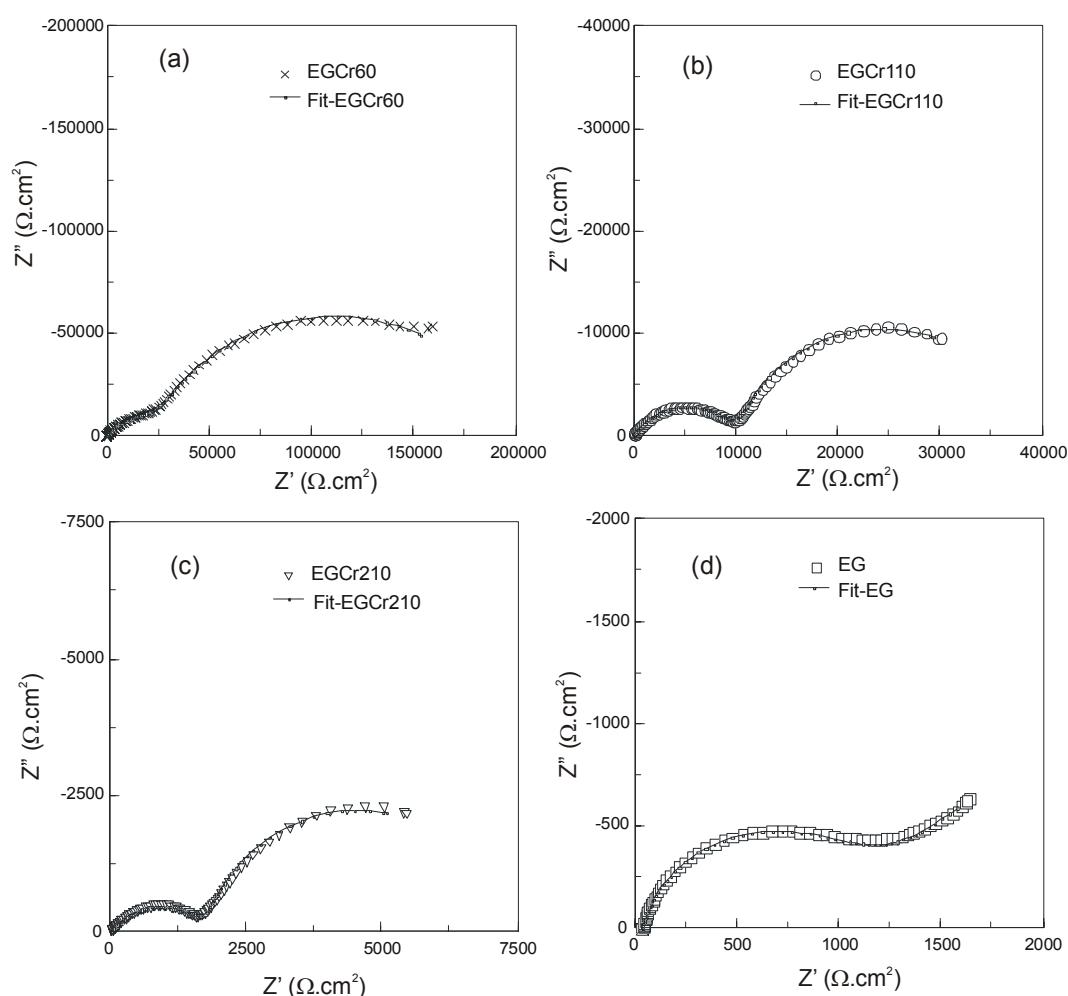


Fig. 6.16 Nyquist impedance plots obtained in the quiescent 0.6 M NaCl solution (pH 6.9) for the chromated EG samples heated at: (a) 60°C, (b) 110°C, (c) 210°C and for the EG steel (d).

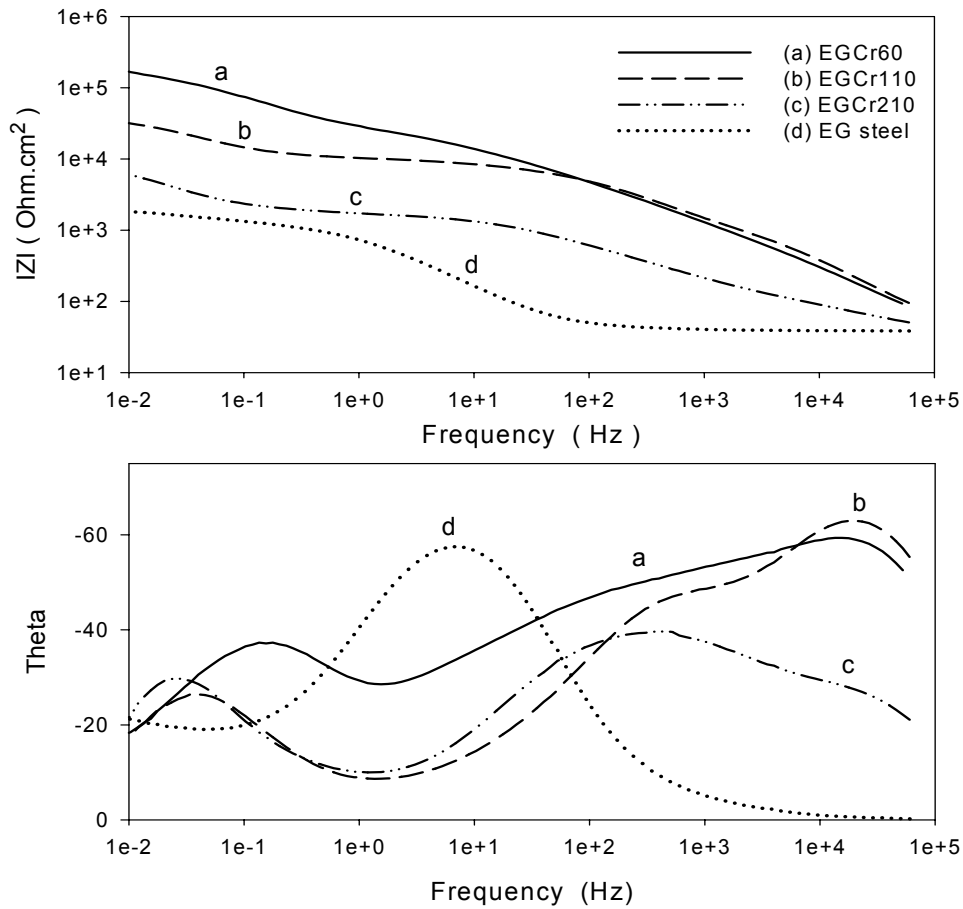


Fig. 6.17 Bode impedance plots for the chromated EG samples heated at: (a) 60°C, (b) 110°C, (c) 210°C and for non-chromated EG steel (d) in the quiescent 0.6 M NaCl solution (pH 6.9).

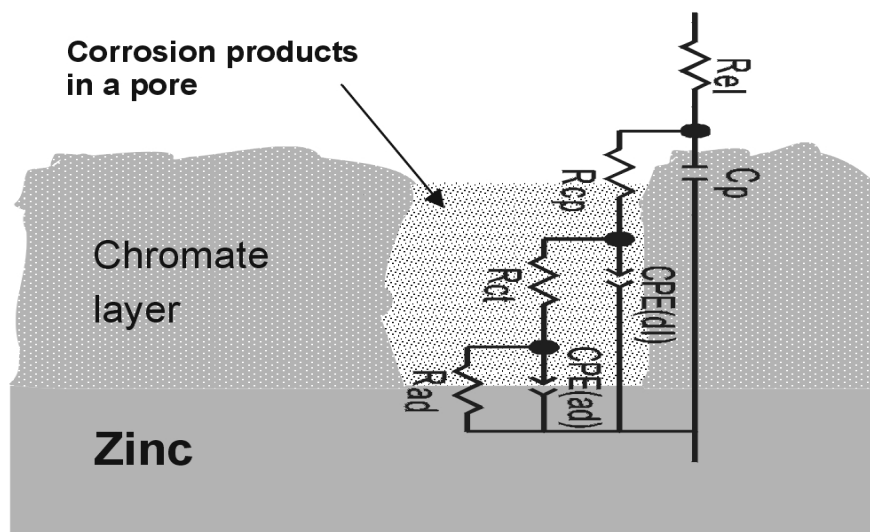


Fig. 6.18 Schematic of the chromate conversion coating on the EG steel with an equivalent circuit.

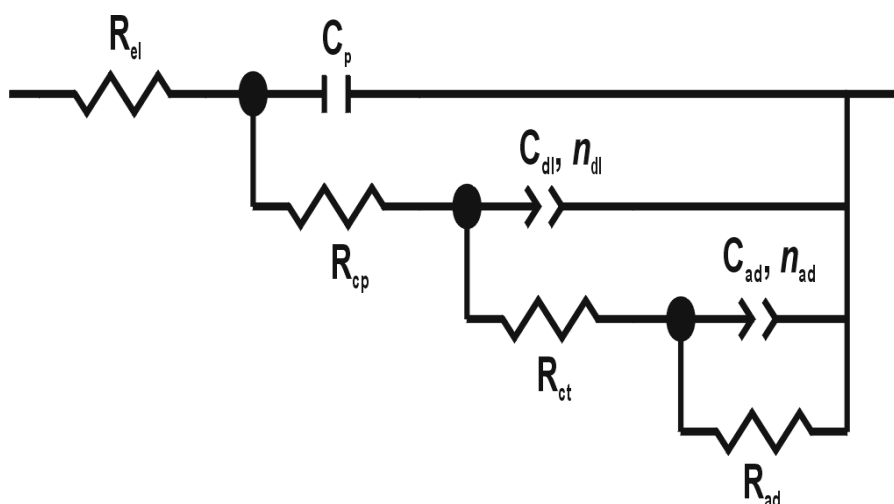


Fig. 6.19 Electrical equivalent circuits used to model the behavior of chromate coatings on electro-galvanized steel in 0.6 M NaCl solution.

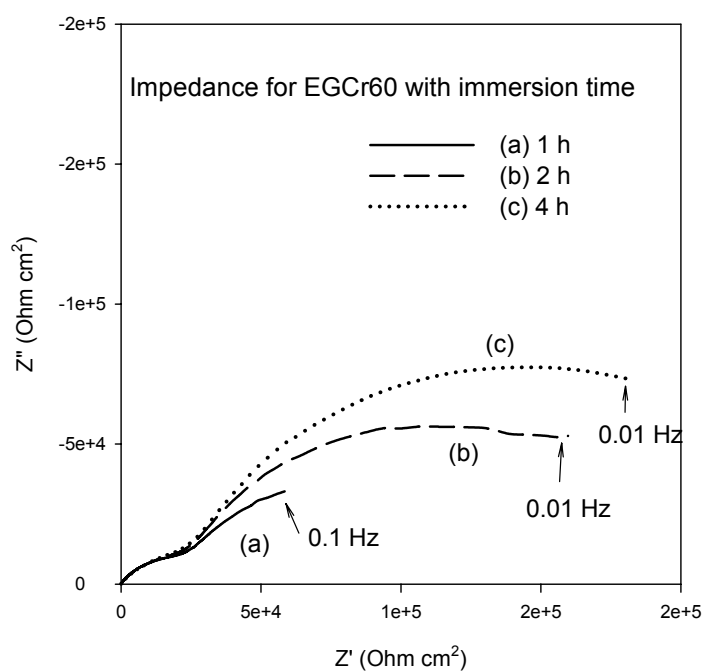


Fig. 6.20 Nyquist impedance plots with immersion time for the EGCr60 samples in the in 0.6 M NaCl solution (pH 6.9).

For the untreated EG steel samples, the impedance spectra were fitted using the equivalent circuit presented in Fig. 5.3 (b) with a capacitance C_{dl} , for the double layer, a charge transfer resistance R_{ct} and a Warburg element. This fits to a model, where zinc corrosion is at least partially diffusion controlled in neutral 0.6 M NaCl solution. The charge transfer resistance decreased and the diffusion resistance increased within 4 hours. The charge transfer resistance (R_{ct}) is about $0.9 \text{ k}\Omega\text{-cm}^2$ and the capacitance of the double layer is $186 \text{ }\mu\text{F/cm}^2$ after the specimen immersed in solution for 4 hours.

Fig. 6.20 shows the Nyquist impedance plots with the immersion time for the chromate coatings heated at 60°C . The impedance increased with time during the measurements. The fitting results show that the resistances (R_{cp} , R_{ct} and R_{ad}) increased with immersion time for all the chromate treated EG steel samples within 4 hours (see Table 6.3). This can be attributed to the corrosion products filling the pores in the coatings. The C_{dl} values increase with immersion time for all the coatings, which can be attributed to the increase of the exposure area caused by corrosion [27,28]. The larger value of a capacitance means that either the layer is thinner or the area of the layer is larger. For the chromate coatings heated at 210°C , all the values of capacitance (C_p , C_{dl} and C_{ad}) are larger and all the resistances (R_{cp} , R_{ct} and R_{ad}) are smaller than for the coatings heated at 60 or 110°C . This suggests that the coatings have become thinner after drying at higher temperatures, and that the cracks in the layer make the real exposure area larger. The wider and deeper cracks observed in the EGCr210 samples by SEM and AFM (see Figs. 6.2 and 6.6) give a piece of evidence of the layer having larger real surface area which can be exposed to the solution.

For the coatings heated at 60°C , the values of resistance in pores (R_{cp}) are smaller and the capacitance values of the double layer (C_{dl}) are larger than for the coatings heated at 110°C . However, for the coatings heated at 60°C , the capacitance values due to the adsorption reaction and diffusion (C_{ad}) are smaller and the resistances due to the charge transfer (R_{ct}) and adsorption or diffusion (R_{ad}) are much larger than for the coatings heated at 110°C . The whole impedance for the coatings heated at 60°C is larger than for the coatings heated at 110°C .

Table 6.3 Best-fitting parameters of the EIS data for chromated and unchromated EG steel (R , $\Omega\cdot\text{cm}^2$ and C , $\mu\text{F}/\text{cm}^2$) (see Figs. 6.16 – 6.20).

Samples	Immersion Time (h)	OCP V_{SCE}	R_{el}	C_{p}	R_{cp}	C_{dl}	R_{ct}	C_{ad}	R_{ad}
EGCr 60°C	1	-1.06	42	0.037	211	1.0	35 k	19	91 k
	2	-1.06	42	0.037	234	1.4	37 k	20	171 k
	4	-1.06	43	0.037	252	1.9	43 k	18	241 k
EGCr 110°C	1	-1.03	47	0.034	509	0.24	4.2 k	488	6 k
	2	-1.05	46	0.034	585	0.29	9.7 k	303	29 k
	4	-1.06	45	0.032	680	0.32	15 k	192	56 k
EGCr 210°C	1	-1.03	42	0.16	45	3.8	1.5 k	1848	2.5 k
	2	-1.03	42	0.3	49	4.0	1.8 k	2081	5.6 k
	4	-1.03	43	0.12	76	4.5	2.8 k	2195	7.7 k
EG Steel (Blank)	1	-1.09	39	--	--	117	1.4 k	5743	1.2 k
	2	-1.10	39	--	--	155	1.1 k	$W_{0\text{-T}}$ 28.5	$W_{0\text{-R}}$ 1518
	4	-1.11	38	--	--	186	0.9 k	$W_{0\text{-T}}$ 77.6	$W_{0\text{-R}}$ 2255

Fig. 6.21 shows the Nyquist plots of impedance for (A) the chromate coatings heated at different temperatures and (B) a pure zinc specimen in aerated 0.01 M NaCl solution (pH 6). For the coatings heated at 60 and 110°C, two capacitive loops were observed, while for the coatings heated at 210°C, only one capacitive loop was observed. The capacitive loop at high frequencies is related to the chromate layer and the loop observed at lower frequencies is related to the double layer at the zinc/electrolyte interface [27]. The impedance diagram for a pure zinc specimen (with no chromate coating) is too small compared to that for the chromated specimens. It is enlarged and shown in Fig. 6.21 (B). It shows that zinc corrosion is charge transfer controlled dissolution in the NaCl solution. The charge transfer resistance is about $5.5 \text{ k}\Omega\cdot\text{cm}^2$ in this case.

Fig. 6.22 shows the Bode plots of impedance for the coatings heated at different temperatures. It shows that all the chromate coatings have larger impedance than the bare zinc. However, among the chromate coatings, the coating heated at 110°C has the largest impedance and the coating heated at 210°C has the lowest impedance, which is consistent with the results of the polarization measurements. The phase versus frequency curves show that there are two time constants for the coatings heated at 60 and 110°C, while for the coating heated at 210°C and the pure zinc there is only one time constant.

The impedance data for the chromated pure zinc heated at 60 and 110°C can be explained using the equivalent circuit shown in Fig. 6.23, while for the chromated zinc heated at 210°C and for unchromated zinc, the data can be fitted using the circuit shown in Fig. 5.3 (a). The fitted results are shown in Table 6.5.

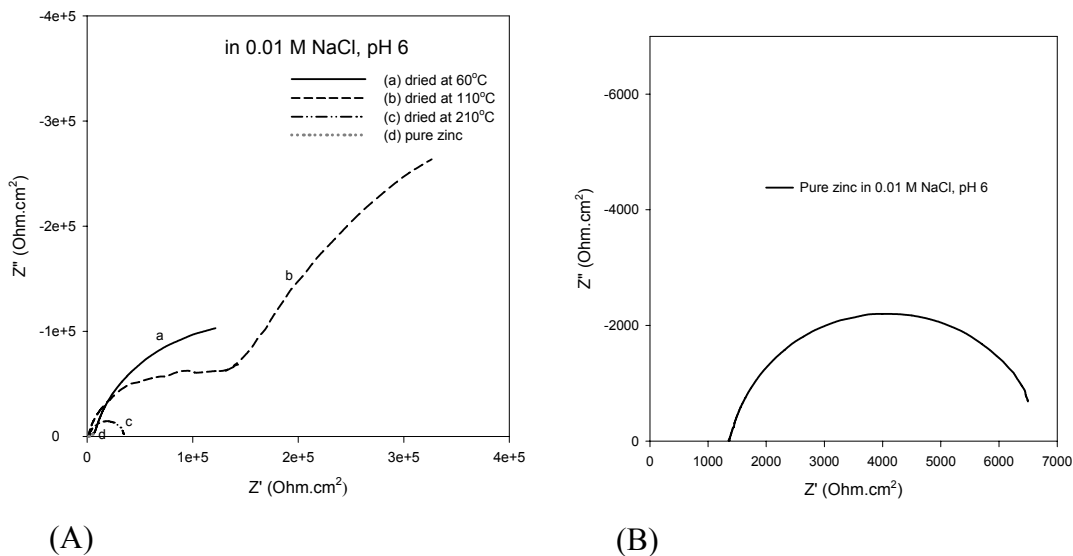


Fig. 6.21 The Nyquist impedance plots for (A) the chromate coatings heated at different temperatures and (B) non-chromated pure zinc in aerated 0.01 M NaCl solution (pH 6).

The larger impedance shown by the chromated specimens compared to the bare zinc can be attributed to the barrier nature of chromate coatings. The chromium hydroxides/oxides in the coatings hinder the access of anions such as chloride and

oxygen to the metal [29]. Furthermore, the hydrophobicity of the chromate coatings will also hamper the access of oxygen dissolved in the solution to the zinc.

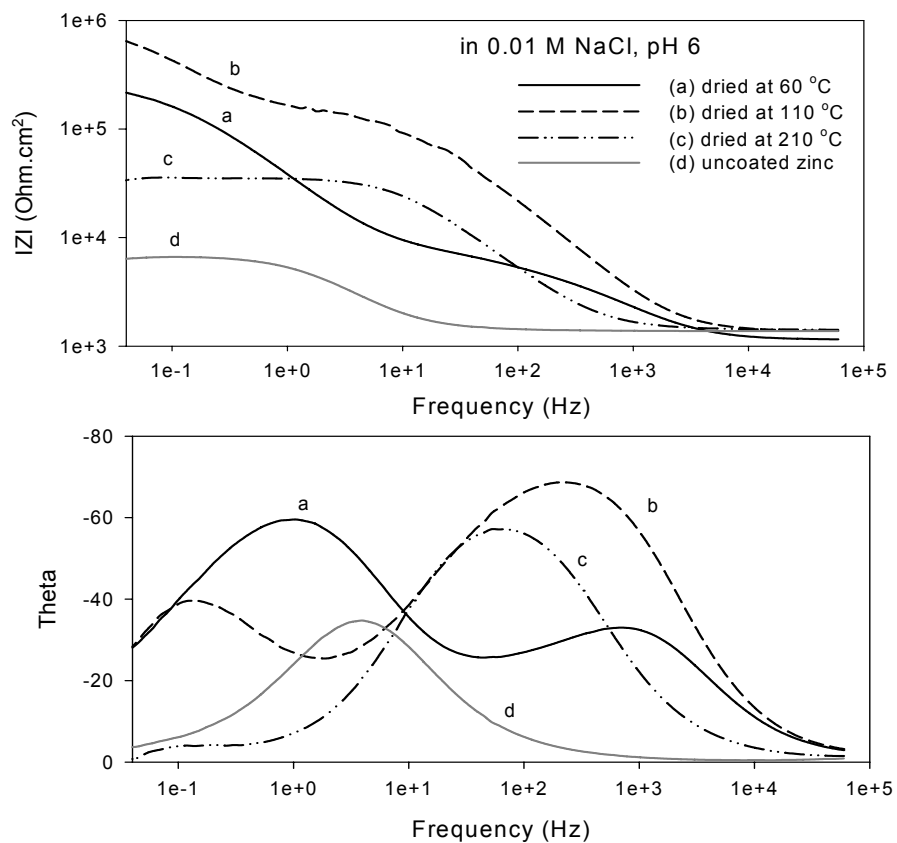


Fig. 6.22 The Bode impedance plots for the Cr(VI) coatings heated at different temperatures.

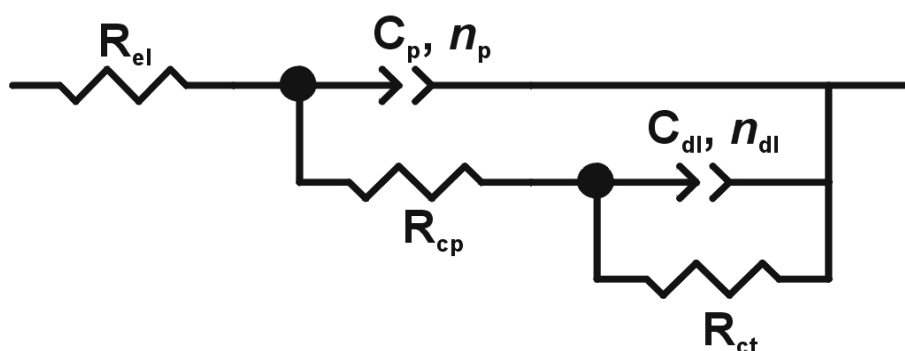


Fig. 6.23 Equivalent circuits used to model the behavior of chromate coatings (heated at 60 and 110 °C) in 0.01 M NaCl solution.

Table 6.5 Best-fitting parameters of the EIS data for chromated and unchromated zinc (R, $k\Omega\cdot cm^2$ and C, $\mu F/cm^2$) (see Figs. 6.21 – 6.23).

Sample	R_{el}	C_p	R_{cp}	C_{dl}	R_{ct}
ZnCr60	1.1	0.14	6	6.6	298
ZnCr110	1.3	0.094	138	4.2	779
ZnCr210	1.4	--	--	0.44	34
Zn	1.4	--	--	20	5.5

6.4 Discussion

The heating process hardens chromate coatings and increases abrasive resistance of the surface [1]. However, the different heating temperatures have different effects on the morphology of chromate coatings on the EG steel and consequently affect the corrosion properties of the coatings.

First, the drying process is responsible for the formation of microcracks in the chromate coatings[30]. Microcracks exist in all greenish chromate coatings on EG steel when heated in air. During the drying process, the gel-like film formed is dehydrated in air and the film shrinks so that microcracks develop. Martyak reported that microcracks result from the internal tensile stress initiated during the chromate treatment process and the tensile stress increases with the thickness of the chromate coatings [31]. In the cases studied, the chromating conditions in solution were kept constant. Only the drying temperature was changed. Thus, the different morphologies of the chromated specimens are due to the different drying temperatures. The protrusion of the crack edges results from the shrinking of coatings due to dehydration. The formation and expansion of zinc oxides under the microcracks may also contribute to the protrusion of the crack edges. A mixture of zinc oxide and chromium oxides existing at the interface between chromate layer and zinc layer has been detected by Auger electron spectroscopy (AES) depth profile analyses [32].

The chromate coatings heated at 210°C have wider and deeper microcracks than the coatings heated at 60 and 110°C. The corrosion current for the samples heated at 210°C is larger and the impedance is smaller than the samples heated at 60 and 110°C (see Tables 6.2 and 6.3). This means that drying at higher temperature (210°C), as suggested in literature [1], causes significant degradation of the chromate coatings. The microcracks are the weak places where corrosion can easily start [33]. The wider and deeper the cracks, the smaller the corrosion resistance will be. The chromate coatings heated at 110°C having a lower corrosion current density can be attributed to fewer microcracks in these coatings than for the coatings heated at other temperatures (see Figs. 6.2 and 6.7).

The drying process also affects the Cr(VI) species in the coatings[34]. A progressive decrease of the Cr(VI)/total Cr ratio with temperature was observed by Laget *et al.* [5] for aluminum alloys. It has also been reported that the loss of “self-healing” effect of the chromates is mainly due to dehydration, which makes the Cr(VI) species immobile or insoluble, rather than to the reduction of Cr(VI) in the coating [3,35]. Another observation reported in literature is that the thermal effect on the corrosion resistance of chromate coatings depends on the substrate. Laget *et al.* attributed the fact that heating treatments do not affect the corrosion resistance of chromate coatings on Al-1100 alloy to the good corrosion resistance of the relatively pure aluminum substrate [5]. Gallaccio *et al.* observed that, in salt-fog tests, heating chromate coatings on electroplated zinc to above 75 °C resulted in marked damage, but conversely that heating chromate coatings on magnesium improves the protection provided by the coatings [3].

In our case, Fourier Transform Infrared Spectrometry and XPS analyses of the chromate coatings have shown that the relative ratio of Cr(VI)-O species to Cr(III)-O compounds decreases after drying at higher temperatures. It means that the drying process does indeed cause Cr(VI) to be reduced to Cr(III). The polarisation curves obtained on the chromate coatings heated at 60°C suggest that a kind of anodic passivation behaviour exists in a range of 160 mV, and all of the chromated specimens, independent of the drying temperature, showed approximately the same anodic breakdown potential, $-0.92 V_{SCE}$. All of the chromated specimens showed a more negative corrosion potential than the uncoated zinc in the 0.01 M NaCl solution,

suggesting that this kind of conversion coating has a cathodic inhibitive effect on the corrosion of zinc: the corrosion rate of zinc is controlled by the cathodic reaction. For the coatings heated at 110°C, the ratio of Cr(VI)/total Cr did decrease with respect to the ratio for the coatings heated at 60°C, but this reduction was small and was not significant enough to have a negative effect on the corrosion behavior of the coated specimens.

According to Mansfeld, the high electrochemical impedance values of chromate conversion coatings are only of secondary importance, and the corrosion protection is mainly provided by mobile Cr(VI), which inhibits the initiation and propagation of pits (for example during salt spray tests) [36]. Buchheit *et al.* reported a correlation between salt spray test results and electrochemical impedance measurements, but chromate conversion coatings can pass salt spray tests with comparatively low coating resistance values [25], again indicating that active protection resulting from the presence of mobile Cr(VI) in the coating is probably more important.

Both the polarization and the EIS measurements showed that the corrosion of zinc is controlled by the cathodic reaction and the diffusion processes. The chromate treated EG steel specimens heated at 60°C showed a more negative corrosion potential than the untreated EG steel in the 0.6 M NaCl solution. This suggests that this kind of coatings has a cathodic inhibitive effect in the corrosion of zinc. Compared to the non-treated EG steel and pure zinc, the chromate treated specimens have larger impedance which can be attributed to the barrier nature of chromate coatings. The chromium hydroxides/oxides in the coatings hinder the anions such as chloride and oxygen to access the metal [29]. The increase of the impedance with the immersion time for all the chromate treated specimens may be explained by the consumption of oxygen and the corrosion products filling in the pores may cause more difficult for the transport of the oxygen.

On the other hand, the soluble Cr(VI) species existed in the coatings may have “self-healing” effect : the Cr(VI) species can be reduced to Cr(III) and form an insoluble Cr(III) oxide/hydroxide layer which may repair the defects in the coatings. It was reported that the loss of “self-healing” effect of the chromates is mainly due to the dehydration which makes the Cr(VI) species immobile [35] or insoluble [3] rather than reduction of Cr(VI) in the coating. However, the decrease of the relative ratio of Cr(VI)

to Cr(III) with rising of the drying temperatures means that the drying process may also cause Cr(VI) to be reduced to Cr(III). At lower Cr(VI) concentrations in the layer, the “self-healing” ability will also diminish.

From the polarization measurements, the coatings heated at 110°C had a smaller current than the coatings heated at other temperatures. However, the coatings heated at 60°C showed passivity. The reduction of Cr(VI) in the layer may increase the cathodic current, but it enables a better passivation process. This indicates that the coatings heated at 60°C have an active protection to zinc from corrosion. The EIS results show that the impedance for the chromated EG steel heated at 60°C is larger than the coatings heated at 110 or 210°C. This suggests that the corrosion resistance of the chromate coatings heated at 60°C is better than the coatings heated at 110°C. Anyhow, the favorable drying temperature for the chromate coatings on the EG steel is between 60 and 110°C.

6.5 Conclusions

Electrochemical measurements showed that chromate coatings improve the corrosion resistance of zinc and the electro-galvanized steel. The drying process has a significant effect on the coating morphology and the corrosion performance of the chromate coatings in the NaCl solutions. All of the chromate coatings investigated in this study showed microcracks in the layer. The width and depth of these cracks increased with the drying temperature. The chromate coatings heated at 110°C had the lowest corrosion current at the free corrosion potential and the corrosion rate was controlled mainly by cathodic reaction. Drying at a moderate temperature (110°C) appeared to increase the corrosion resistance with respect to drying at 60°C. However, the chromate coatings heated at a lower temperature (60°C) showed passivity, which may be attributed to hexavalent chromium being reduced to trivalent chromium thus temporarily repairing some defects. Heating at higher temperatures (210°C) degraded the chromate coatings by widening the cracks and reducing the mobility of the soluble Cr(VI) species. The thermal reduction of Cr(VI), detected by FTIR and XPS, is probably responsible for the decrease of the Cr(VI) content of the layer. Thus, drying at

moderate temperatures makes chromate coatings hard, but on the other hand, it will reduce the “self-healing” effect of the soluble chromates. A favorable drying temperature for the chromate treated electro-galvanized steel is between 60 and 110°C.

References

1. T. Biestek and J. Weber, *Conversion Coatings*, (Portcullis Press Ltd., Redhill, 1976).
2. N. R. Short, J. K. Dennis and S. O. Agbonlahor, *Trans IMF*, 66 (1988) 107.
3. A. Gallaccio, F. Pearlstein and M. R. D'Ambrosio, *Metal Finishing*, (1966) 50, 57.
4. M. E. Roper, *Metal Finishing Journal*, 14 (1968) 286, 294.
5. V. Laget, C. Jeffcoate, H. S. Isaacs and R. G. Buchheit, in: *Corrosion and corrosion control in saltwater environments*, D. A. Shifler, P. M. Natishan, T. Tsuru and S. Ito (Eds.), 99-26 (The electrochemical society, INC., Pennington, NJ 08534-2839, USA, 2000) pp. 173-182.
6. in: *Annual Book of ASTM Standards, Vol 03.05, B 568 - 91*, Annual Book of ASTM Standards, Vol 03.05, B 568 - 91 1992,
7. N. E. Yanaki, *Metal Finishing*, (1997) 33.
8. M. T. Anthony and M. P. Seah, *Surf. Interface Anal.*, 6 (1984) 95.
9. A. E. Hughes and R. J. Taylor, *Surf. Interface Anal.*, 25 (1997) 223.
10. J.-O. Nilsson, S.-E. Hörnström, E. Hedlund, H. Klang and K. Uvdal, *Surf. Interface Anal.*, 19 (1992) 379.
11. B. S. Norgren, M. A. J. Somers, W. G. Sloof and J. H. W. de Wit, in: *12th Scandinavian Corrosion Congress & Eurocorr '92, 1992*; P. J. Tunturi (Ed.), 1 (The Corrosion Society of Finland, Espoo, Finland, 1992) pp. 139-149.
12. M. Lenglet, F. Petit and J. Y. Malvaut, *Phys. Stat. Sol. (a)*, 143 (1994) 361.
13. F. Petit, H. Debontride, M. Lenglet, G. Juhel and D. Verchere, *Appl. Spectroscopy*, 49 (1995) 207.
14. J. Kasperek and M. Lenglet, *La Revue de Métallurgie - CIT*, 94 (1997) 713.
15. R. A. Nyquist and R. O. Kagel, *Infrared spectra of inorganic compounds*, (Academic Press, Inc, New York, 1971).
16. P. Campestrini, S. Bohm, T. Schram, H. Terry and J. H. W. de Wit, *Thin Solid Film*, 410 (2002) 76.
17. J. T. Vandenberg, D. G. Anderson, J. K. Duffer, J. M. Julian, R. W. Scott, T. M. Sutliff and M. J. Vaickus, *An infrared spectroscopy atlas for the coatings industry*, (Federation of Societies for Coating Technology, Philadelphia, 1980).

18. M. Kendig and S. Jeanjaquet, *J. Electrochem. Soc.*, 149 (2002) B47-B51.
19. M. P. Gigandet, J. Faucheu and M. Tachez, *Surf. Coat. Technol.*, 89 (1997) 285.
20. V. Barranco, S. Feliu Jr and S. Feliu, *Corros. Sci.*, 46 (2004) 2203.
21. L. M. Baugh, *Electrochim. Acta*, 24 (1979) 657.
22. J. R. Macdonald, in: *The First International Symposium on The Electrochemical Impedance Spectroscopy*, Bombannes, France, 22 - 26 May, 1989; Pergamon press, *Electrochimica Acta*, 1990) pp. 1483-1492.
23. C. Pérez, A. Collazo, M. Izquierdo, P. Merino and X. R. Nóvoa, *Corrosion*, 56 (2000) 1220.
24. E. P. M. van Westing, G. M. Ferrari and J. H. W. de Wit, *Corros. Sci.*, 34 (1993) 1511.
25. R. G. Buchheit, M. Cunningham, H. Jensen, M. W. Kendig and M. A. Martinez, *Corrosion*, 54 (1998) 61.
26. Computer Program, *ZView for Windows*, version 2.1, Scribner Associates, Inc., Southern Pines, NC, 1998.
27. L. Fedrizzi, L. Ciaghi, P. L. Bonora, R. Fratesi and G. Roventi, *J. Appl. Electrochem.*, 22 (1992) 247.
28. R. L. Zeller III and F. Savinell, *Corros. Sci.*, 26 (1986) 389.
29. S. Turgoose, in: *Chemical inhibitors for corrosion control*, B. G. Clubley (Ed.), The Royal Society of Chemistry, Manchester, 1990, p. 72-88.
30. X. Zhang, S. Böhm, A. J. Bosch, E. P. M. van Westing and J. H. W. de Wit, *Materials and Corrosion*, 55 (2004) 501.
31. N. M. Martyak, *Surf. Coat. Technol.*, 88 (1996) 139.
32. X. Zhang, C. van den Bos, W. G. Sloof, H. Terryn, A. Hovestad and J. H. W. de Wit, *Surf. Engineering*, 20 (2004) 244.
33. N. M. Martyak, J. E. McCaskie and L. Harrison, *Metal Finishing*, 94 (1996) 65.
34. X. Zhang, C. van den Bos, W. G. Sloof, H. Terryn, A. Hovestad and J. H. W. de Wit, in: *Corrosion science in the 21st century*, Manchester, UK, 7-11 July, 2003; B. Cottis (Ed.), *J. Corros. Sci. Engineering*, Vol. 6, paper 57 (2003) (ISSN 1466-8858).
35. V. Laget, H. S. Isaacs, C. S. Jeffcoate and R. G. Buchheit, in: *Proc. of 2nd International symposium on aluminum surface science and technology*, 2000; H. Terryn (Ed.), UMIST, Manchester, England, UK, 2000) pp. 295-300.
36. F. Mansfeld, *Corrosion*, 54 (1998) 595.

Chapter 7

Investigation of Cr(VI) and Cr(III)-Based Conversion Coatings on Zinc Using SKP and SKPFM

7.1 Introduction

Under atmospheric conditions, a thin water layer is often formed on the surface of metals by adsorption or condensation. Because the water layer is so thin, it is difficult to use conventional electrochemical techniques to study atmospheric corrosion. The well-established Kelvin probe (KP) technique (vibrating capacitor method) used for measuring the work function of a metal in a vacuum [1,2], has been adapted to measure the Volta potential of a metal surface which is covered with a thin electrolyte layer without touching the surface [3-5]. It has been reported that this Volta potential is correlated to the corrosion potential of the metals [3].

Scanning Kelvin probe force microscopy (SKPFM) is a relatively new technique which is a combination of the well-known Kelvin probe technique and atomic force microscopy (AFM)[6-9]. It can measure the surface topography and potential distribution on a line-by-line basis using metal-coated silicon tips that are electronically conducting. Schmutz and Frankel [9] reported that for a number of pure metals, the Volta potential values measured in air with the SKPFM (relative to the potential of Ni) after immersion in de-ionized water or 0.5 M NaCl for 30 min. are linearly related to the open-circuit potentials measured in the solutions just before the samples are removed.

In this chapter, the Volta potential distribution across the boundary between a Cr(VI) or a Cr(III) coating and untreated zinc is measured using scanning Kelvin probe (SKP) in a humid chamber and using the SKPFM technique in air before and after

exposing the samples to 0.01 M NaCl solution. The inhibition of zinc corrosion by the Cr(VI) and Cr(III)-A coatings is discussed according to the mixed potential theory.

7.2 Principles of Kelvin Probe and Scanning Kelvin probe force microscopy

7.2.1 Kelvin probe technique

The Kelvin probe consists of a vibrating reference electrode connected with the sample via a voltage source (see Fig. 7.1) [10]. The tip of the probe and the surface of the metal sample under study constitute a capacitor. The probe vibration produces a periodic fluctuation in capacitance (C) given by

$$C = \frac{\epsilon\epsilon_0 S}{d_0 + d_1 \sin(\omega t)} \quad (7.1)$$

where ϵ is the dielectric constant, ϵ_0 the permittivity of vacuum, S the plate area, d_0 the mean distance between the tip of the probe and sample surface, d_1 the amplitude of vibration and ω the vibration frequency.

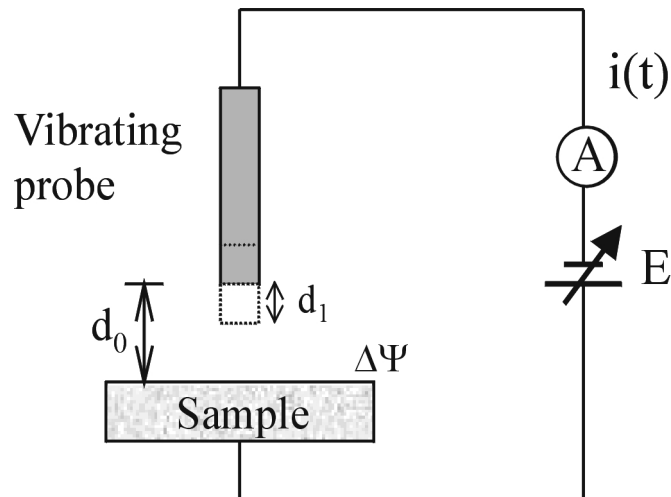


Fig. 7.1 Schematic illustration of the Kelvin probe for measuring the Volta potential of a sample using the vibrating capacitor method.

If any Volta potential difference ($\Delta\Psi$) exists between the probe and the sample surface, an alternating current will flow in the external circuit. If a DC voltage (E) is switched into the circuit, then the alternating current (i) is given by

$$i = \frac{dQ}{dt} = (\Delta\Psi + E) \frac{dC}{dt} = -\varepsilon\varepsilon_0 S (\Delta\Psi + E) \frac{\omega d_1 \cos(\omega t)}{[d_0 + d_1 \sin(\omega t)]^2} \quad (7.2)$$

and if $d_0 \gg d_1$, the relationship simplifies to

$$i = \frac{dQ}{dt} = (\Delta\Psi + E) \frac{dC}{dt} = -\varepsilon\varepsilon_0 S (\Delta\Psi + E) \frac{\omega d_1 \cos(\omega t)}{d_0^2} \quad (7.3)$$

The alternating current vanishes when $\Delta\Psi = -E_{i=0}$. The Volta potential difference $\Delta\Psi$ can be measured by means of a lock-in amplifier.

Stratmann et al. [3] reported that the Volta potential difference measured by the Kelvin probe is related to the corrosion potential measured by a micro reference electrode. The relationship between the corrosion potential E_{corr} and the Volta potential $\Delta\Psi$ follows

$$E_{corr} = \left(\varepsilon_{ref} + \frac{A^{Ref}}{F} - X_{EL}^{Gas} \right) + \Delta\Psi_{EL}^{Ref} \quad (7.4)$$

where ε_{ref} is the half cell potential of the reference electrode/electrolyte interface, which is a constant, A^{Ref} the work function of the probe electrode in contact with the given atmosphere, F the Faraday constant, X_{EL}^{Gas} the surface potential at the interface solution/gas and $\Delta\Psi_{EL}^{Ref}$ the Volta potential difference between the electrolyte and a Kelvin probe. In a given environment and Kelvin probe the parameters in the parenthesis are constants and this relationship simplifies to

$$E_{corr} = const + \Delta\Psi_{EL}^{Ref} \quad (7.5)$$

This correlation was experimentally proved by measuring the corrosion potential E_{corr} of a surface, covered by an electrolyte layer (1 mm thick, in air) with a Luggin-capillary, and simultaneously the Volta potential difference $\Delta\Psi_{EL}^{\text{Ref}}$ with a Kelvin probe [3].

7.2.2 Scanning Kelvin probe force microscopy

The SKPFM is a technique combining the well-known Kelvin probe and atomic force microscopy (AFM). The invention of the AFM provided the ability to profile insulators with very high spatial resolution [11]. Martin et al. demonstrated the capability of AFM in getting topography and the surface potential map of metals and semiconductors [12,13].

The tip and the specimen surface under study constitute two plates of a capacitor as in the Kelvin probe, but the SKPFM measures the Volta potential using a null-force method. The different surface potentials between two materials cause electrostatic force due to the separation-dependent capacitance C . This force F is of the form[13]

$$F = \frac{1}{2}(\Delta\Psi)^2 \frac{\partial C}{\partial z} \quad (7.6)$$

where z is the distance between tip and specimen. If an external potential $U_0 + U_1 \sin(\omega_p t)$ is applied to the tip, the force becomes

$$F = \frac{1}{2} \frac{\partial C}{\partial z} [\Delta\Psi + U_0 + U_1 \sin(\omega_p t)]^2 \quad (7.7)$$

where ω_p is a resonant frequency of the tip. The amplitude of vibration of the tip d_A will be given by

$$d_A = B \times \left[(\Delta\Psi + U_0)^2 + \frac{U_1^2}{2} + 2(\Delta\Psi + U_0)U_1 \sin(\omega_p t) - \frac{U_1}{2} \cos(2\omega_p t) \right] \quad (7.8)$$

where B is the calibration factor relating potential difference to amplitude of vibration, and includes the elastic response of the tip as well as $(\partial C / \partial z)$. The vibration amplitude

of the tip can be easily monitored during the operation of AFM. The amplitude of vibration of the tip at ω_p is proportional to the product $(\Delta\Psi+U_0)U_1$. If a mixed DC and AC bias is applied to the tip, and the DC level is adjusted until the AC vibration of the tip at ω_p is zero, then at this point the DC offset U_0 is equal in magnitude and opposite in sign to the Volta potential difference $\Delta\Psi$ between the specimen and the tip.

Topography and Volta potential mapping are usually performed in two line-scans (each line is scanned twice) [6]. The topography is scanned in the first trace using “tapping mode”. During this scan no external voltage is applied to the tip to keep the long-range electrostatic interactions small. After each line of the topography scan, the feedback loop controlling the vertical piezo is turned off. The tip is lifted from the surface (lift mode) and retraces over the same topography at a set distance from the surface (lift height) while using an AC-modulated feedback to measure the Volta potential.

The contamination, oxide layer, trapped surface charges and even the topography of the surface may affect the Volta potential difference measured by means of SKPFM in air[14]. In the case of a passive surface, where a thin oxide layer covers the surface of metal, the interface might preferably be described as a semiconductor/electrolyte interface [15]. The Volta potential has not been defined for a semiconductor/electrolyte interface, but the concept of the metal/electrolyte interface can be adapted to this type of interface since it is related to the charge distribution on the surface [8]. When the film is thin (1~2 nm thick), the direct electron transfer occurs easily by a tunneling mechanism between the metal electrode and the redox species. As the thickness of a surface layer increases, the electron transfer takes place between the electron level in the film and the electron level in the redox species (indirect electron transfer) [15]. Although a passivated metal surface is different from a bare metal surface, the potential measured by this technique is strongly related to the Volta potential difference, and this potential does not vary for distances between the tip and the measured surface from 100 nm to a few micrometers[8].

7.3 Experimental methods

7.3.1 Sample preparation

Pure zinc sheets, 0.5 mm thick, were used as substrates. Before applying a Cr(VI) or a Cr(III) coating, the specimens for the KP and open circuit potential measurements were cut into 2×2 cm specimens, and for the SKPFM analysis into 1×0.5 cm specimens. The surfaces to be analysed were polished using 1 μm diamond grains in the final step. The specimens were ultrasonically cleaned in acetone and ethanol for 2 minutes, respectively, and dried in flowing air.

A Cr(VI) conversion coating was applied to only the half of the polished zinc surface to make a chromate/zinc boundary. The Cr(VI) treatment was carried out in a bath containing 200 g/L $\text{Na}_2\text{Cr}_2\text{O}_7$ + 10 g/L H_2SO_4 (pH 1.1-1.3) for 5 or 60 s at room temperature ($\sim 20^\circ\text{C}$). The Cr(VI) treated area was rinsed in de-ionized water for 10 s, while the untreated zinc area was intact. The treated samples were dried using a hair-dryer first, and then was heated in an oven at 60°C for 30 minutes.

The Cr(III)-A treatment was carried out in a commercial solution, Permapass ImmunoxTM 3K (pH 1.8). Half of each polished zinc specimen was treated in the bath for 60 seconds at room temperature ($\sim 20^\circ\text{C}$). The treated area was dipped in de-ionized water for 10 s and the untreated zinc area was intact. These treated samples were dried in an oven at 70°C for 30 minutes.

7.3.2 Kelvin probe measurements

The Volta potential of partly treated zinc specimens was measured by using the UBM Kelvin probe at Corus. The probe was made from CrNi wire with a diameter of 150 μm . The specimen and the atmosphere chamber were fixed to an X-Y axis stage, which could be moved two-dimensionally with respect to the probe under computer control. The probe was attached to a Z-axis stage and was driven with a piezo-actuator. The distance between the probe tip and the specimen electrode could be adjusted. The

scanning height was 75 μm . The analysis area was 10×10 mm. First, the samples were scanned in air at room humidity and room temperature. Then they were scanned in a humid chamber (RH 96%).

7.3.3 Scanning Kelvin probe force microscopy measurements

Scanning Kelvin probe force microscopy (SKPFM) analysis was performed with a commercial AFM (Digital instrument Nanoscope III Multimode)[6]. The cantilevers were coated with a thin layer of Pt-Ir. The topography of the samples was scanned using the tapping mode without a voltage applied to the tip. The Volta potential was measured using the lift mode while the distance between the tip and the surface of samples was 100 nm. The topography and potential map across the boundary between the untreated area and the Cr(VI) treated area were obtained using SKPFM in air at room temperature before and after immersion in 0.01 M NaCl solution for 24 h.

7.4 Results and discussion

7.4.1 Cr(VI)-treated zinc

Fig. 7.3 shows the Volta potential map across the boundary between the Cr(VI) treated area (left side) with dipping time 5 s and the untreated area (right side) on a zinc specimen obtained using SKP (a) in air (RH 22%) and (b) in humid chamber (RH 96%). The potential in the Cr(VI) treated area is about 200 mV more negative than that of the bare zinc at 22% RH. When the humidity was increased to 96% RH, the Volta potential difference between the two sides decreased to about 50 mV.

Fig. 7.2 shows the Volta potential map obtained from the Cr(VI) treated surface with dipping time 60 s on the left side and untreated zinc area on the right side. At 22% RH, the Volta potential difference between the Cr(VI) coating and bare zinc is about -300 mV and at 96% RH about -250 mV.

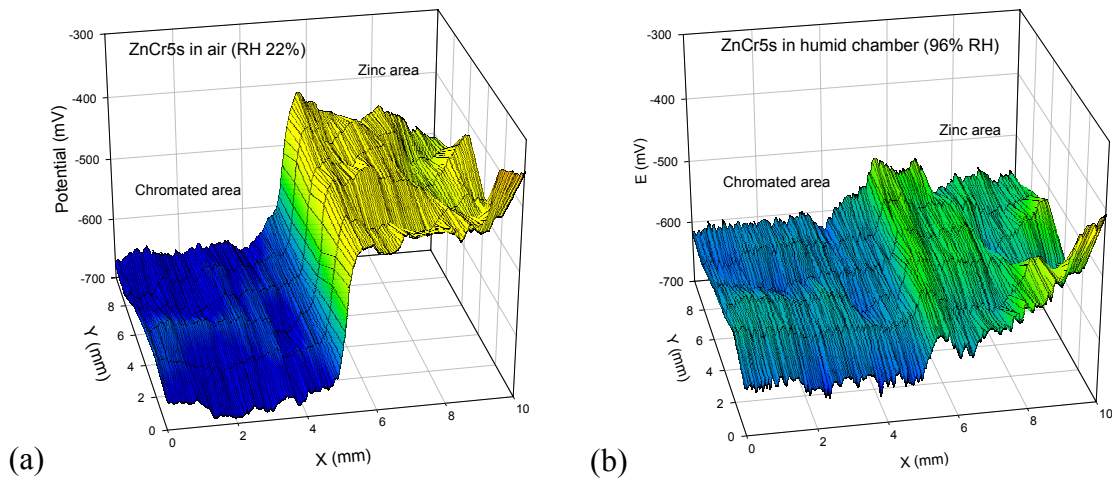


Fig. 7.2 Volta potential maps across the boundary between the Cr(VI) treated area (left side, with dipping time 5 s) and the untreated area (right side) on zinc surface obtained using SKP (a) in air (RH 22%) and (b) in a humid chamber (RH 96%).

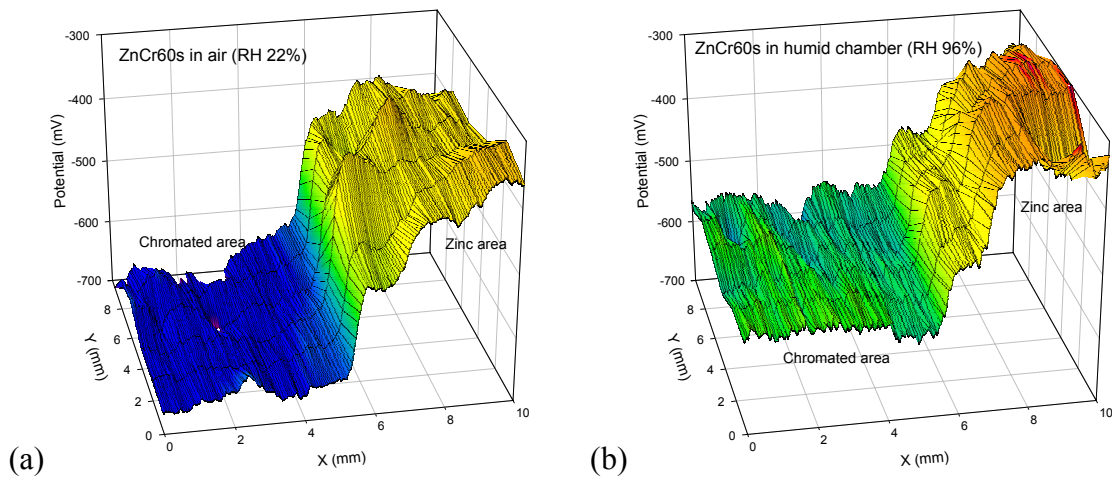


Fig. 7.3 Volta potential maps across the boundary between the Cr(VI) treated area (left side, with dipping time 60 s) and the untreated area (right side) on zinc surface obtained using SKP (a) in air (RH 22%) and (b) in a humid chamber (RH 96%).

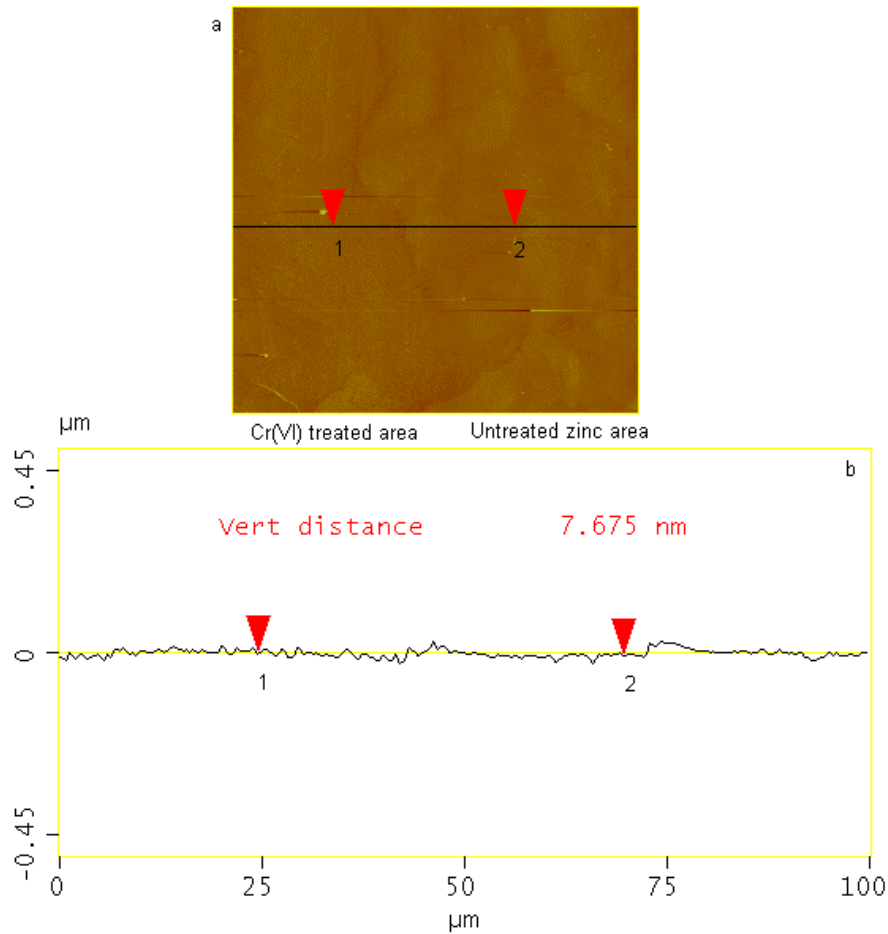


Fig. 7.4 (a) Topography (Z range: 1 μm) and (b) the topography scan along the line shown in (a) measured using SKPFM in air across the boundary between untreated area (right side) and Cr(VI) treated area (with a dipping time of 5 s, left side).

Fig. 7.4 presents (a) topography (Z range: 1 μm) and (b) the topography scan along the line shown in (a) measured using SKPFM in air across the boundary between untreated area (right side) and Cr(VI) treated area (with a dipping time of 5 s, left side). The topography does not show any boundary between the Cr(VI) treated area and the untreated zinc area. The average roughness of the scanned surface area is about 10 nm.

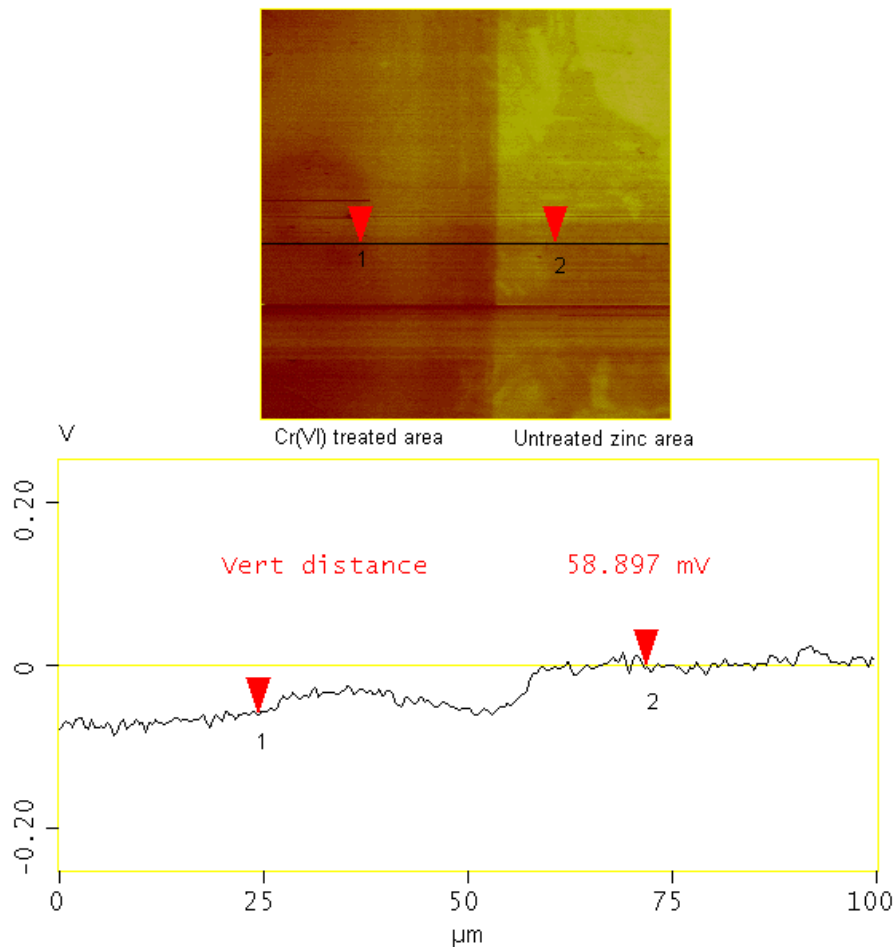


Fig. 7.5 (a) Volta potential map and (b) the Volta potential scan along the line shown in (a) measured using SKPFM in air across the boundary between untreated area (right side) and Cr(VI) treated area (left side) on the same sample as in Fig. 7.4.

Fig. 7.5 shows (a) the Volta potential map (in the same area as in Fig. 7.4) and (b) the Volta potential scan along the horizontal line shown in (a) across the boundary between the untreated area (right side) and the Cr(VI) treated area (with a dipping time of 5 s, left side) obtained using SKPFM. The Volta potential map shows that the potential in the Cr(VI) treated area is lower than that in the bare zinc area. The scan line (b) shows that the potential difference is about 60 mV between the chromated and non-chromated areas.

Fig. 7.6 shows (a) the topography in the same area of the sample as shown in Fig. 7.4 and (b) the topography scan along the line shown in (a) measured using SKPFM in air across the boundary between untreated zinc area (right side) and Cr(VI) treated area

(left side), after immersion in 0.01 M NaCl solution for 24 h. The topography shows that the surface in the zinc area becomes rougher than before. Fig. 7.7 shows the Volta potential map measured in the same area. The potential in the Cr(VI) treated area is still more negative than that in the untreated zinc area. The potential difference between the two areas increased to 200 mV. This suggests that the untreated zinc area was corroded and zinc oxide/hydroxide was deposited on the surface, which increased the potential difference.

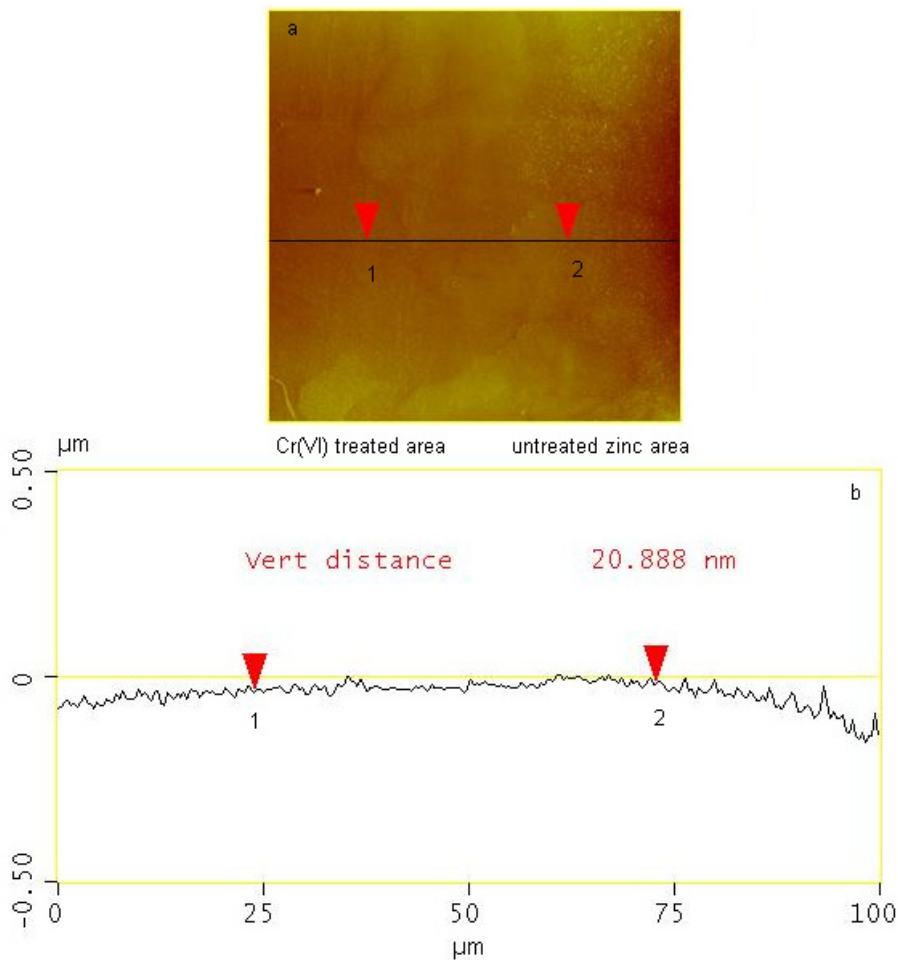


Fig. 7.6 (a) Topography (the same area as shown in Fig. 7.4) and (b) the topography scan along the line shown in (a) measured using SKPFM in air across the boundary between untreated zinc area (right side) and Cr(VI) treated area (left side), after immersion in 0.01 M NaCl solution for 24 h.

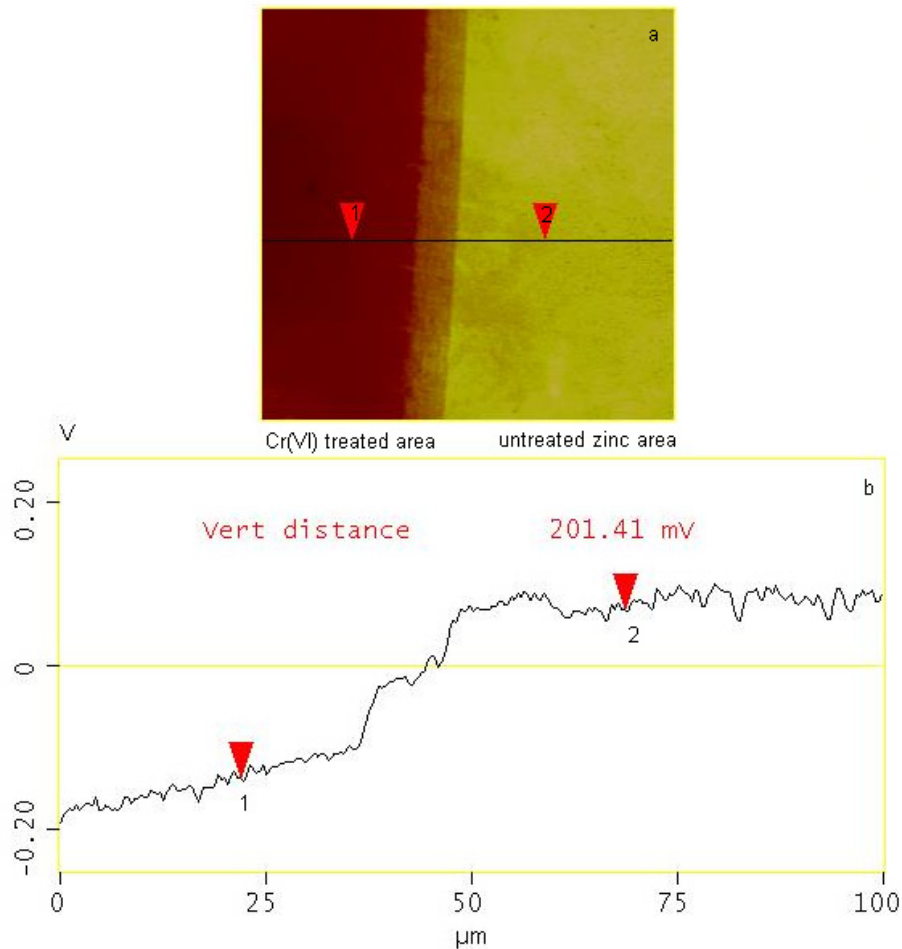


Fig. 7.7 (a) Volta potential map (in the same area shown in Fig. 7.6) and (b) the Volta potential scan along the line shown in (a) measured using SKPFM in air across the boundary between untreated area (right side) and Cr(VI) treated area (with a dipping time of 5 s, left side), after immersion in 0.01 M NaCl solution for 24 h.

7.4.2 Cr(III)-A treated zinc

Fig. 7.8 shows the Volta potential map obtained using the SKP across the boundary between bare zinc area and Cr(III)-A coated area (with a dipping time of 10 s) in a humidity of (a) 40% RH and (b) 96% RH. The potential in the coated area is about 200 mV more negative than the uncoated zinc measured in a humidity of 40% RH and 600 mV more negative measured in a humidity of 96% RH. When the humidity decreased to 40% RH, the potential difference decreased to about 200 mV again. Stratmann and coworkers [3] reported that a cathodic potential shift immediately after wetting resulted from the superposition of the anodic metal dissolution and the cathodic rust reduction

(Fe contaminated by SO₂). Here in the case of Cr(III)-A treated zinc, the reason why the potential difference increased so much (600 mV) in a high humidity needs further investigation.

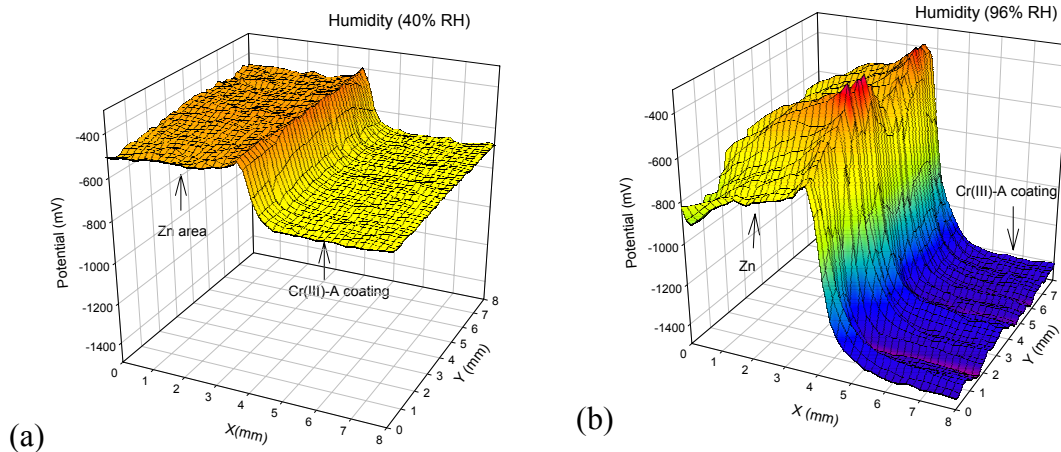


Fig. 7.8 Volta potential map across the boundary between the untreated Zn area (left side) and Cr(III)-A treated zinc with a dipping time 10 s (right side), obtained by means of SKP in a chamber: (a) humidity: 40% RH, (b) humidity: 96% RH at room temperature.

Fig. 7.9 shows (a) topography (Z range: 2 μm) and (b) the topography scan along the line shown in (a) using SKPFM in air across the boundary between untreated zinc area (left side) and Cr(III)-A treated area (with a dipping time of 60 s, right side). The topography shows that there is a small step between the untreated bare zinc area and the Cr(III)-A treated area. The Cr(III)-A treated area is slightly rougher and higher (~ 85 nm) than the untreated area.

Fig. 7.10 shows (a) the Volta potential map in the same area of the sample as shown in Fig. 7.9 and (b) the Volta potential scan along the line shown in (a) measured using SKPFM in air. The potential in the Cr(III)-A treated area is about 200 mV more negative than the untreated zinc area, which is in agreement with the results obtained using SKP in a humid environment 40% RH.

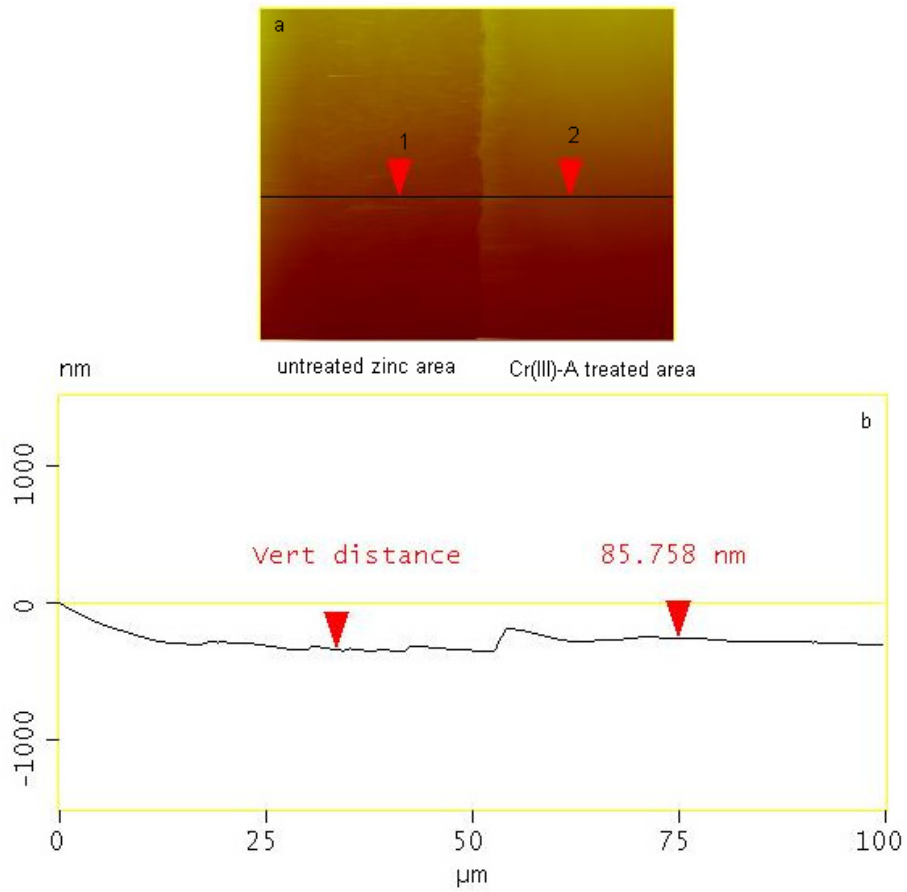


Fig. 7.9 (a) Topography (Z range: $2\ \mu\text{m}$) and (b) topography scan along the line shown in (a) measured using SKPFM in air across the boundary between untreated zinc area (left side) and Cr(III)-A treated area (with a dipping time of 60 s, right side).

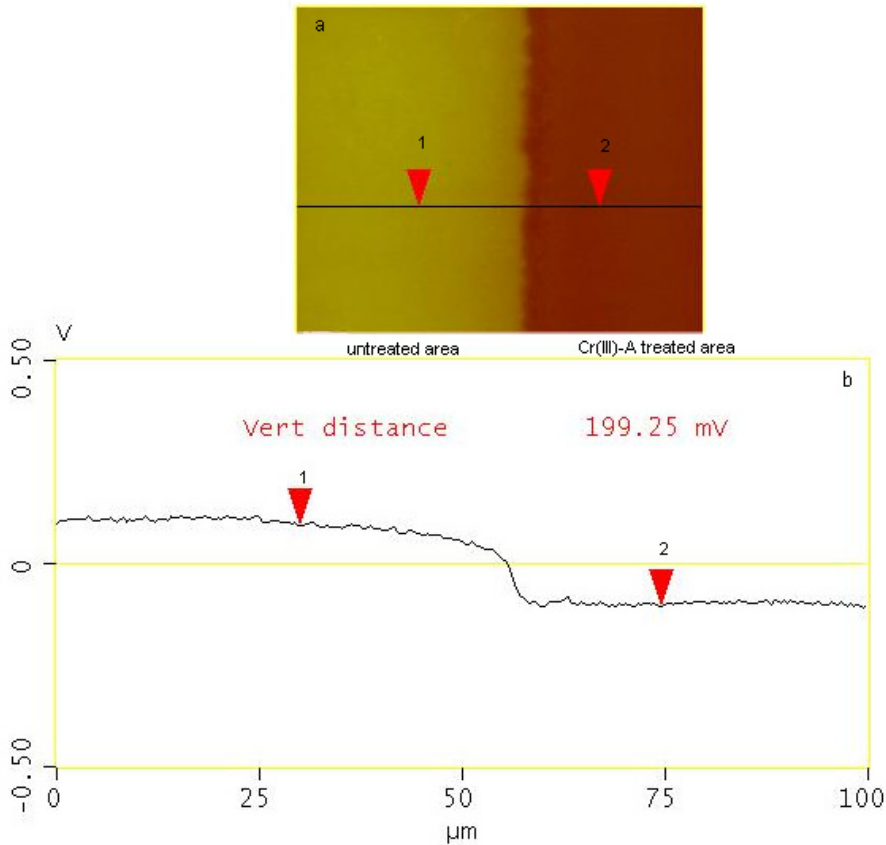


Fig. 7.10 (a) Volta potential map in the same area of the sample shown in Fig. 7.9 and (b) the Volta potential scan along the line shown in (a) measured using SKPFM in air across the boundary between untreated zinc (left side) and Cr(III)-A treated area (with a dipping time of 60 s, right side).

7.4.3 Open circuit potential

Fig. 7.11 shows the open circuit potential as a function of time, for the untreated zinc, Cr(III)-A and Cr(VI) treated zinc with dipping time 60 s, measured in 0.01 M NaCl solution (open to air) using a KCl-saturated silver-silver chloride reference electrode ($E^0 = 0.197$ V vs. NHE) in a general three-electrode cell. The open circuit potentials of the Cr(VI) coatings are lower than those of the bare zinc samples in the solution. The potential difference between the Cr(VI) treated samples and bare zinc samples varies from 40 to 80 mV. This is in reasonably good agreement with the Volta potential difference measured by means of the SKP in a humid chamber and by means of SKPFM in air.

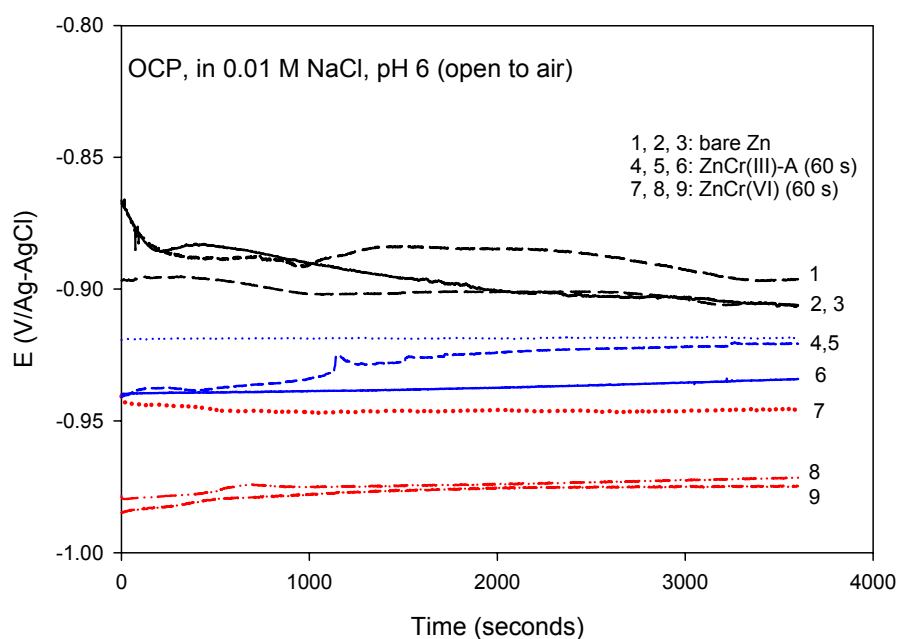


Fig. 7.11 Open circuit potential versus time, for the untreated zinc, the Cr(III)-A treated zinc (with dipping time 60 s) and the Cr(VI) treated zinc (with dipping time 60 s), measured in 0.01 M NaCl solution (open to air) using KCl saturated silver-silver chloride reference electrode in a general three electrodes cell.

According to the mixed potential theory [16], if the cathodic reaction rate keeps constant and the anodic reaction is inhibited, the corrosion potential will move in the positive direction (see Fig. 7.12). If the anodic reaction rate keeps constant and the cathodic reaction is inhibited, the corrosion potential will move in the negative direction. If both the reaction rates are inhibited the potential may not change, but in any case, the corrosion rate will decrease.

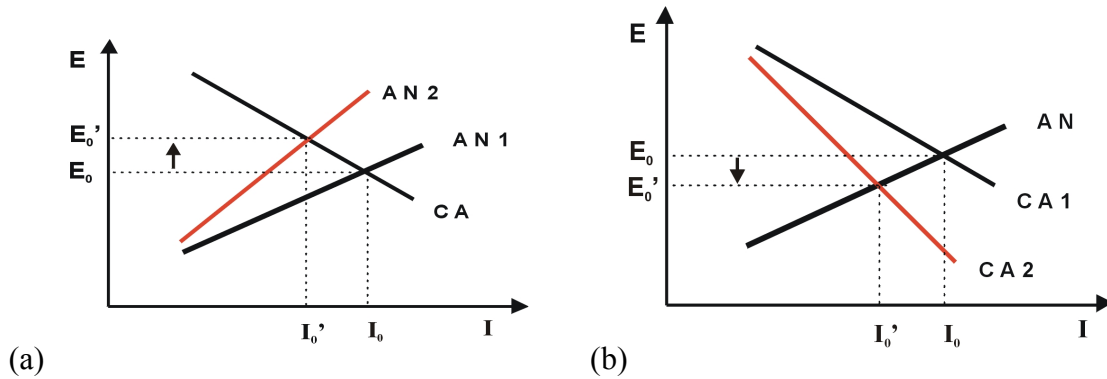


Fig. 7.12 Mixed potential theory in the case of anodic inhibition (a) and cathodic inhibition (b) of the corrosion of metals.

Here the absolute values of the corrosion potential measured by means of SKP or SKPFM may be not important, since as described in section 7.2, the contamination, oxide layer, trapped surface charges and even the topography of the surface may affect the Volta potential difference, and even the OCP values measured in different solution or at different time may be different. The important thing is that the relative potential difference between the treated part and the untreated part measured by three different techniques showed similar results.

The Volta potential differences measured using SKP and SKPFM, and the OCP measured in 0.01 M NaCl solution show that Cr(VI) coatings have a negative potential with respect to bare zinc. These results are qualitatively in agreement with the results obtained by L. Forget et al.[17]. Forget et al. measured Volta potential difference between chromate treated and untreated hot dip galvanized steel using UBM SKP at a relative humidity of 95%. They reported that the potential on the chromated area was about -600 mV (with Cr/Ni reference) which was more negative than that in the untreated HDG area. The potential difference was about 70 mV when using chromic acid treatment, while using an industrial chromating bath (containing small amount of phosphates) this potential difference increased to about 180 mV. After 17 h exposure to 0.01 M NaCl the potential difference between chromated area and unchromated area increased as high as 1 V. The potential of the chromated part remained the same as before while the potential of unchromated part increased. This potential shift was attributed to the coverage of the corrosion products which slow down the dissolution of zinc.

The results described above suggest that the Cr(VI) and Cr(III)-A based treatments can cathodically inhibit the corrosion of zinc in solution[17]. Polarization measurements described in chapter 5 for the Cr(VI)-treated and untreated zinc in 0.01 M NaCl solution showed that the rate of zinc corrosion in 0.01 M NaCl solution is controlled by the cathodic reaction. The corrosion current is reduced when the potential shifts in the negative direction. The Cr(III)-A coating can function as a barrier layer, hindering the transport of oxygen to the zinc substrate and consequently retarding the corrosion of zinc [18]. The corrosion behavior of the Cr(III)-A treated zinc in 0.01 M NaCl solution will be further described in chapter 8 of this thesis.

The Cr(VI)-based coatings contain chromium oxides/hydroxides in the form of Cr(III) and Cr(VI) [19]. If the Cr(III) oxides/hydroxides have the function as cathodic inhibitors, the Cr(VI)-based coatings can have the function as well. From this point of view, these measurements have not yet shown clearly the role played by the Cr(VI) species in the coatings.

7.4 Conclusions

The Volta potential differences between the Cr(VI)-treated and untreated zinc, and between the Cr(III)-A treated and untreated zinc, have been measured by means of SKP in a humid chamber and SKPFM in air. Both techniques show that the Cr(VI) and Cr(III)-A treated zinc both have lower Volta potentials than the untreated zinc.

The open circuit potentials (OCP) measured in 0.01 M NaCl solution show that the OCP of the Cr(VI)-treated zinc is lower than that of untreated zinc, which is qualitatively correlated with the differences in Volta potential measured by means of SKP and SKPFM.

The negative potentials of the Cr(VI) and the Cr(III)-A treated zinc against the untreated zinc measured by all these techniques (SKP, SKPFM, and OCP techniques) suggest that both coatings inhibit the cathodic reaction in the corrosion of zinc.

The effect of humidity on Volta potential is not completely understood. More work is required to interpret this phenomenon.

References

1. I. D. Baikie, S. Mackenzie, P. J. Z. Estrup and J. A. Meyer, *Rev. Sci. Instrum.*, 62 (1991) 1326.
2. H. Baumgartner and H. D. Liess, *Rev. Sci. Instrum.*, 59 (1988) 802.
3. M. Stratmann and H. Streckel, *Corros. Sci.*, 30 (1990) 681.
4. A. Tahara and T. Kodama, *Corros. Sci.*, 42 (2001) 655.
5. S. Yee, R. A. Oriani and M. Stratmann, *J. Electrochem. Soc.*, 138 (1991) 55.
6. P. Campestrini, *Microstructure-related Quality of Conversion Coatings on Aluminium Alloys*, thesis, Delft University of Technology, The Netherlands, 2002.
7. F. Andreatta, *Local Electrochemical Behaviour of 7xxx Aluminium Alloys*, thesis, Delft University of Technology, The Netherlands, 2004.
8. V. Guillaumin, P. Schmutz and G. S. Frankel, *J. Electrochem. Soc.*, 148 (2001) B163-B173.
9. P. Schmutz and G. S. Frankel, *J. Electrochem. Soc.*, 145 (1998) 2285.
10. H. N. McMurray and D. A. Worsley, R. G. Compton and G. Hancock (Eds.), Blackwell Science Ltd., 1997, Chap. 4.
11. G. Binnig, C. F. Quate and Ch. Gerber, *Phys. Rev. Lett.*, 56 (1986) 930.
12. H. O. Jacobs, H. F. Knapp, S. Müller and A. Stemmer, *Ultramicroscopy*, 69 (1997) 39.
13. Y. Martin, D. W. Abraham and H. K. Wickramasinghe, *Appl. Phys. Lett.*, 52 (1988) 1103.
14. M. Nonnenmacher, M. P. O'Boyle and H. K. Wickramasinghe, *Appl. Phys. Lett.*, 58 (1991) 2921.
15. N. Sato, *Electrochemistry at metal and semiconductor electrodes*, (Elsevier science B.V., Amsterdam, 1998).
16. M. G. Fontana, *Corrosion Engineering*, 3rd ed., (McGraw-Hill, Inc., 1986).
17. L. Forget, J. Delhalle and Z. Mekhalif, *Mater. Corros.*, 52 (2001) 181.
18. X. Zhang, C. van den Bos, W. G. Sloof, H. Terryn, A. Hovestad and J. H. W. de Wit, *Surf. Eng.*, 20 (2004) 244.
19. X. Zhang, W. G. Sloof, A. Hovestad, E. P. M. van Westing, H. Terryn and J. H. W. de Wit, *Surf. Coat. Technol.*, in press.

Chapter 8

Physical and Electrochemical Characterization of Cr(III)-Based Conversion Coatings

8.1 Introduction

Chromium is present in chromate conversion coatings (CCCs) with both Cr(III) and Cr(VI) oxidation states. Cr(VI) is present mainly in the outer layer of the coating [1-3]. Previously reported work [4] indicates that the effectiveness of protection depends on the amount of hexavalent chromium that is released [5,6]. This is supported by the fact that when a chromate coating is scratched, the substrate metal is protected against corrosion by soluble chromate species emerging from the surface around the damaged site. Other work [7] indicates that the insoluble part of chromate coatings is decisive for corrosion resistance, while the soluble part (Cr(VI)) has only a supplementary effect on the resistance of the coatings. When the soluble Cr(VI) species have completely leached out of the coating, the remaining insoluble part of the coating still retains a major part of the original protective properties. Another theory suggests that the protective action of chromate coatings involves the adsorption of polar molecules from the chromate solution. The adsorbed oxo-Cr(VI) species on the oxide surface can inhibit corrosion by discouraging the adsorption of depassivating anions such as chloride[8].

Trivalent chromium-based conversion treatments are worth studying, because they are considered to be commercially acceptable alternatives to conventional Cr(VI) treatments for certain applications[9]. A trivalent chromium system for zinc, containing nitrate as an oxidant and sodium hypophosphite as a complexant to increase the stability of the Cr(III) in the treatment bath, is discussed in a paper by Barnes *et al.* [10]. Like the conventional Cr(VI)-based process, this Cr(III)-based treatment involves a redox reaction: the zinc surface is oxidised while the oxidising agent in the treatment bath is

reduced. As in the Cr(VI)-based process, the reduction of the oxidant neutralizes hydrogen ions, bringing about a localised pH increase and making possible the precipitation of trivalent chromium as an insoluble hydroxide. It has been claimed that the corrosion protection provided by coatings of this type can be as good as that provided by hexavalent chromate coatings[10]. The colour and thickness of the coatings formed in this Cr(III)-based treatment can be altered by modifying the solution composition, pH, temperature and immersion time. For the newest generation of trivalent chromium coatings, the corrosion resistance does not significantly diminish after subjecting to high temperatures (150 °C) for 1 hour, as is the case with hexavalent chromate treatments [11].

In this chapter, the nature and corrosion properties of the Cr(III) coatings on pure zinc disc and on electro-galvanized (EG) steel are studied and compared with Cr(VI) coatings. The inhibition of zinc corrosion in solutions containing Cl^- by Cr(VI) and Cr(III) are discussed.

8.2 Experimental

8.2.1 Materials

Two substrates were used in this investigation. One is pure zinc (99.95%) discs with a diameter of 11.3 mm (*i.e.* area = 1 cm²) and a thickness of 2 mm, which was used as rotating disc electrodes. All discs were mechanically polished using 1 μm diamonds in the final polishing step. The other was 1 mm thick carbon steel sheet, which was cut into 2×2 cm pieces and each pieces was polished before electro-galvanizing (EG). The electro-galvanizing process was described in chapter 6. A 16 μm thick zinc layer was electro-deposited on the polished carbon steel. These specimens were used as stationary electrodes.

8.2.2 Cr(VI) and Cr(III) treatments

The discs and sheets were ultrasonically cleaned in acetone for 2 minutes and then in ethanol for another 2 minutes. The surfaces were activated in 0.25 % HNO_3 for 10

seconds and then rinsed in de-ionized water before Cr(VI) or Cr(III) treatments. The Cr(VI) coating was carried out in the 200 g/l $\text{Na}_2\text{Cr}_2\text{O}_7$ + 10 g/l H_2SO_4 bath (pH 1.2). The process was described in chapter 4.

The Cr(III) treatments were carried out in two different commercial solutions. One bath was Permapass Immunox™ 3K (pH 1.8), which contains fluoride and sulfate as accelerators. The specimens were treated in the bath for 10, 30 or 60 seconds at room temperature (~ 20°C). After rinsing in de-ionized water these coatings were dried in an oven at 70 °C for 30 minutes. The other bath was Permapass™ 7012 (pH 2.0), which contains phosphate. The specimens were treated in the bath at 30°C for 10, 30, or 60 seconds. These coatings were rinsed in de-ionized water and then dried in an oven at 100 °C for 30 minutes. The details of the conversion treatments are shown in Table 8.1.

Table 8.1 Details of the conversion treatments

Coating	Treatment solution	pH	Immersion time (s)	Drying temperature (°C)
Cr(III)-A	Permapass Immunox™ 3K	1.8	10, 30, 60	70
Cr(III)-B	Permapass™ 7012	2.0	10, 30, 60	100
Cr(VI)	200 g/l $\text{Na}_2\text{Cr}_2\text{O}_7$ + 10 g/l H_2SO_4	1.2	10, 60	60

8.2.3 Analysis of morphology and thickness of the coatings

The morphology of Cr(VI) and Cr(III) coatings before and after exposure to 0.01 M NaCl solution was investigated under the Field Emission Scanning Electron Microscope, JSM-6500F. The thickness of the Cr(VI) and the Cr(III) coatings was measured by spectroscopic ellipsometry (SE). The SE analysis was performed with a J.A. Woollam Co. VASE (see chapter 4 for details). The thickness of the coatings was calculated by fitting the ellipsometric Ψ and Δ spectra using a two-layer optical model and the WVASE software from J.A. Woollam Co. [12,13].

8.2.4 Composition analysis of the coatings

The surface layers of Cr(VI) and Cr(III) coatings on zinc discs were analysed by means of X-ray photoelectron spectroscopy (XPS), Auger electron spectroscopy (AES) and Fourier transform infrared spectroscopy (FTIR). These analysis methods are described in chapter 4. For the AES analysis, a 40 nm gold layer was deposited on the chromated zinc in order to increase the conductivity of the surface. Alternate sputtering (rastered) and data acquisition were used to obtain the concentration-depth profiles for two locations on each sample. The sample surface was rastered using a 2 keV Ar ion beam over an area of $4 \times 4 \text{ mm}^2$ with emission current 20 mA and argon pressure 20 mPa. The data process is described in chapter 4 of this thesis.

8.2.5 Open circuit potential and polarization measurements

For the rotating electrodes (treated and untreated zinc discs), the open-circuit potential (OCP) and potentiodynamic polarization measurements were carried out in a glass cell containing a rotating disc, platinum counter electrode and a reference electrode (saturated calomel electrode: $E^0 = 0.241 \text{ V vs. NHE}$) connected with a Luggin capillary. Using rotating disc electrode (RDE) is to make the electrode surface uniformly accessible to reacting species. All the experiments were performed at room temperature. In the aerated 0.01 M NaCl solution (pH 6), the solution was open to air and the rotating disc was left in the solution for 0.5 ~1 h at open circuit before the polarization measurements. In the de-aerated 0.01M NaCl solutions with and without chromate inhibitors, the solution was purged with N_2 for 1 h before and then continuously during the measurements, and the samples were immersed in the solution for 5 minutes at open circuit before starting the polarization measurements. The pH was adjusted to 6 by adding NaOH. To obtain the polarization curves, the potential was scanned from the OCP to 0.25 V versus the OCP to get the anodic parts and from the OCP to $-1.6 \text{ V}_{\text{SCE}}$ to get the cathodic parts. The disc rotation speed was 600 rpm. The scan rate was 0.167 mV/s.

For the stationary electrodes (treated and untreated EG steel sheets), the polarization measurements were carried out in a cell containing a treated or untreated EG steel sheet,

platinum counter electrode and a reference electrode, described in chapter 5 of this thesis. The specimen was left in 0.01 M NaCl solution (open to air) for 1 hour at open circuit before the polarization measurements. The polarization curves were obtained by scanning the potential from the OCP to -0.25 V versus the OCP, and then in the opposite direction, ending at $+0.25$ V versus the OCP.

8.2.6 Impedance measurements

The electrochemical impedance spectroscopy (EIS) measurements were carried out in the 0.01 M NaCl solution (open to air). The counter electrode was a concentric piece of flat platinum net that was parallel to the surface of the zinc disc. The reference electrode was an Ag/AgCl/Cl⁻ (saturated KCl) electrode ($E^0 = 0.197$ V vs. NHE), which was specially designed for EIS measurements. The impedance response was measured using a Solartron 1255 frequency response analyzer coupled with a Solartron 1287 electrochemical interface. The frequency range was 60 kHz to 0.1 Hz, and a 10 mV *a.c.* amplitude around the OCP was used to obtain a weak current response. For the Cr(VI) and the Cr(III)-A coated rotating zinc discs, the rotation speed was 600 rpm. The EIS measurements started after leaving the rotating discs at open circuit for 0.5 h.

For the Cr(VI), the Cr(III)-A and the Cr(III)-B coated stationary EG steel sheet specimens, the EIS measurements started after immersion in the 0.01 M NaCl solution at open circuit for 1 h. For the Cr(VI) and the Cr(III)-B coated EG steel sheet specimens, the impedance as a function of exposure time in the 0.6 M NaCl solution was also measured.

8.3 Results

8.3.1 Morphology of the coatings

The color of the Cr(VI) coating on zinc discs with dipping time of 60 s is brown and the Cr(VI) coating on the EG steel with dipping time of 10 s is yellow-green. The color of the Cr(III)-A coatings on zinc disc and on the EG steel are blue. The color of the Cr(III)-B coatings on the EG steel is slightly iridescent yellow.

Fig. 8.1 shows SEM images of a Cr(III)-A coating on a zinc disc. No cracks can be observed in this coating, but preferentially etched zones are revealed. On some grains, the coating has a smooth appearance in the SEM. On other grains, it has a rougher appearance. Rougher areas can be seen in Fig. 8.1 (a) and in the upper part of Fig. 8.1 (b). Fig. 8.2 shows SEM images of a Cr(VI) coating on a zinc disc. Fig. 8.2(b) is an enlarged image of an area in Fig. 8.2(a). Microcracks are visible in this coating, which are attributable to the tensile stress in the coatings resulting from the drying process[14,15].

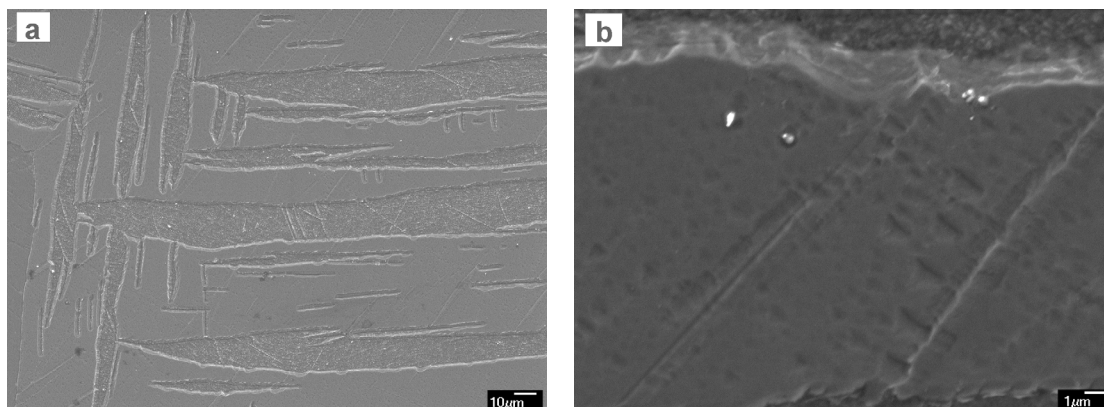


Fig. 8.1 SEM image of a Cr(III)-A coated zinc disc (dipping 60 s) dried at 70 °C for 30 minutes in an oven.

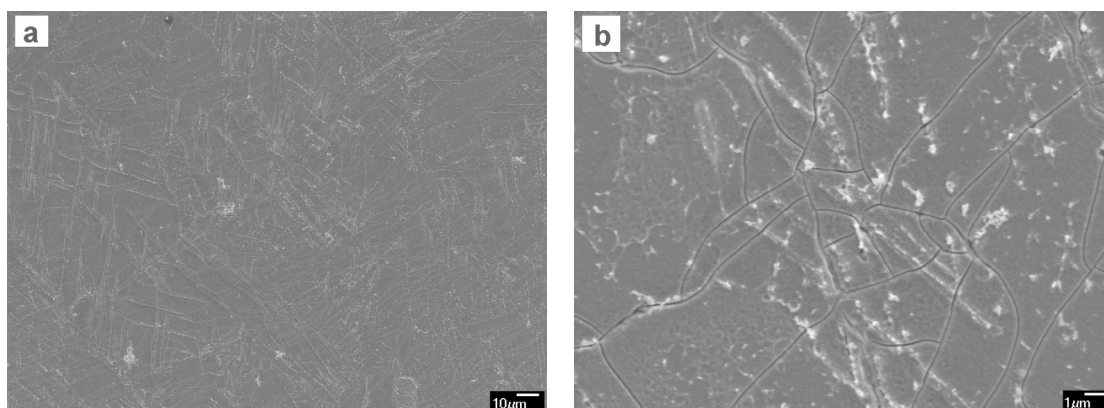
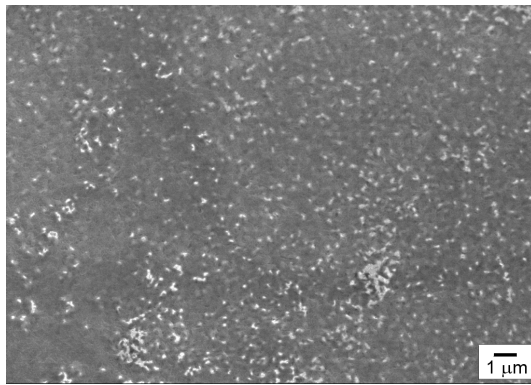
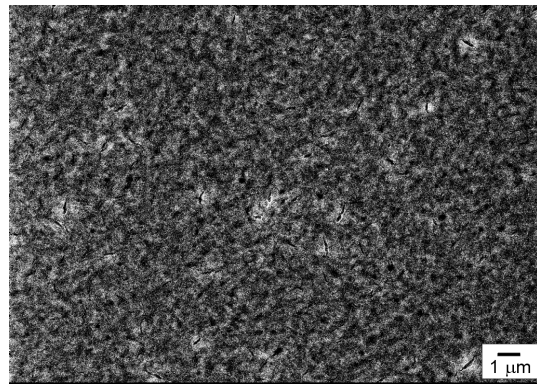


Fig. 8.2 SEM image of a Cr(VI) treated zinc disc (dipping 60 s) dried at 60 °C for 30 minutes in an oven.

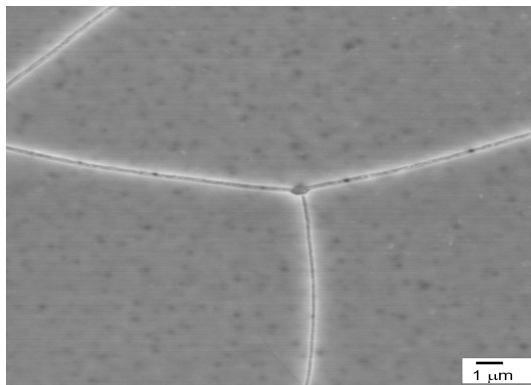
Fig. 8.3 shows SEM images for (a) a Cr(III)-A coating, (b) a Cr(III)-B coating and (c) a Cr(VI) coating on EG steel sheet specimens. For the Cr(III)-A and the Cr(III)-B coatings, no cracks can be observed. The surface of the Cr(III)-B coating is rougher than the surface of the Cr(III)-A coating. Microcracks are visible in the Cr(VI) coating, and the cracks are about 200 nm wide [16].



(a) Cr(III)-A treatment: 60 s.



(b) Cr(III)-B treatment: 60 s.



(c) Cr(VI) treatment: 10 s.

Fig. 8.3 SEM images of the different conversion coatings on the EG steel: (a) Cr(III)-A coating, (b) Cr(III)-B coating and (c) Cr(VI) coating.

8.3.2 Thickness of the coatings

Fig. 8.4 shows the experimental and fitted ellipsometric data for Cr(III) coated zinc: (a) Ψ spectra and (b) Δ spectra. The thickness of each coating was calculated by fitting the acquired SE spectra using a two-layer optical model previously used to model the optical properties of chromium conversion coatings on aluminum [12,13]. The two layers are the coating layer and an interface layer between the coating and the substrate.

The refractive index n of the chromate layer is unknown and is modeled as a function of the wavelength λ using a Cauchy dispersion relation whose terms are fitted during the regression processing: $n = A + B/\lambda^2$, where A and B are constants and λ is the wavelength. Strictly, this dispersion relation describes the dependence of n on λ for a fully transparent dielectric material. For chromate coatings (and other materials that are not fully transparent) an absorption factor should also be included. Nevertheless, it has been confirmed that the use of this dispersion relationship to model the optical properties of chromium coatings is acceptable [12]. A wavelength range of 400 to 1700 nm was chosen for data fitting.

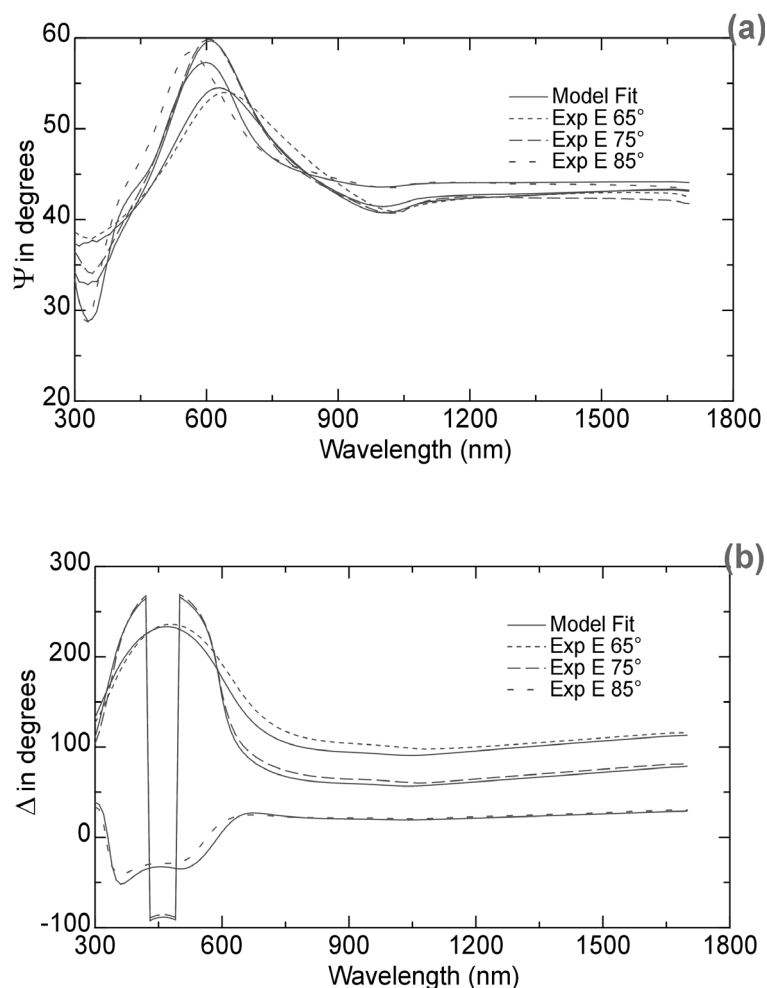


Fig. 8.4 Experimental and fitted ellipsometric data for Cr(III)-A coated zinc (with dipping time 60 s): (a) Ψ spectra and (b) Δ spectra.

The fitted value of the refractive index, n , for a wavelength of 600 nm is 1.69 for the Cr(VI) coating and 1.70 for the Cr(III)-A coating on zinc discs. These values of n are consistent with the values given in reference [12] for chromate conversion coatings on aluminum. The fitting results for the coatings on zinc discs are presented in Table 8.2. For a dipping time of 60 s, the thickness of the Cr(VI) coating on zinc disc is about 400 nm. The Cr(III)-A coating is much thinner, 88 nm, than the Cr(VI) coating within the same dipping time.

Table 8.2 Fitting results, using a two-layer optical model with a Cauchy dispersion relation, for the conversion coatings on zinc disc with dipping time of 60 s (see text for details)[†].

Sample	d_1 (nm)	d_2 (nm)	$d_{\text{tot}}=d_1+d_2$ (nm)	A	B	EMA %	MSE
Cr(VI) coating	357 ± 8	48 ± 1	405	1.683 ± 0.025	0.0041 ± 0.0022	66	21.34
Cr(III)-A coating	85.3 ± 0.9	2.5 ± 0.4	88	1.689 ± 0.011	0.0048 ± 0.0013	66	11.44

[†]Where d_1 is the thickness of the chromate layer; d_2 is the thickness of the interface layer between the chromate layer and the zinc substrate; EMA consists of 66% Cauchy and 34% of the zinc substrate in the interface layer; MSE is the “mean square error” of the fitting results (which equals 1 for a perfect fit).

Fig. 8.5 shows the thickness of the Cr(III)-A and B coatings on the EG steel specimens as a function of the dipping time in the coating baths measured by SE. Within 30 seconds, the thickness of the Cr(III)-A coating is thicker than the Cr(III)-B coating, but when the dipping time increases to 60 seconds the Cr(III)-A coating reaches its maximum thickness, about 90 nm, while the Cr(III)-B coating reaches a thickness of 250 nm.

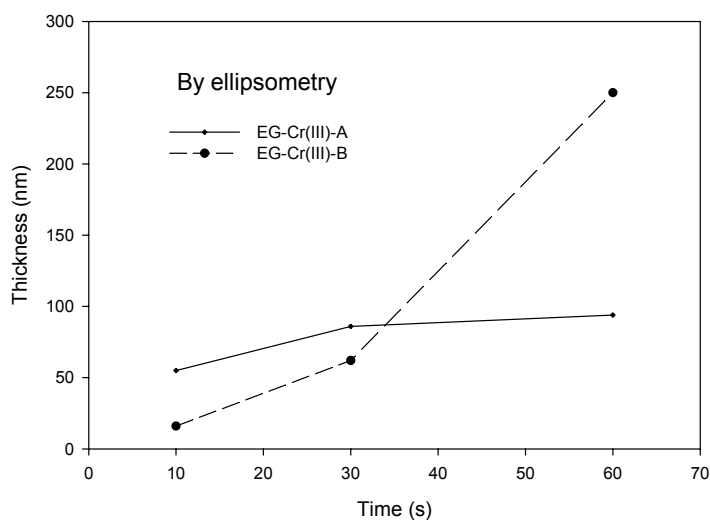


Fig. 8.5 Thickness of the Cr(III)-A and B coatings on electro-galvanized steel measured by spectroscopic ellipsometry.

8.3.3 Composition of the coatings

Fig. 8.6 shows the overview XPS spectra acquired from (a) a Cr(VI) coating and (b) a Cr(III)-A coating on zinc discs. This figure shows that there are C, Cr, O and S signals from the Cr(VI) coating. The C is considered to be due to exposure to ambient air. Thus, the surface layer of the Cr(VI) coating contains mainly Cr, O, and S. For the Cr(III)-A coating on zinc, a strong signal from Zn was also detected besides Cr, O and S. This means that zinc oxides/hydroxides also exist within the surface layer of these coatings.

Fig. 8.7 shows the overview XPS spectrum acquired from a Cr(III)-B coating on zinc. This figure shows that there are C, Cr, O and P signals, but there is no S signal detected from this coating by XPS. The atomic percentage of elements is 4% C, 55% O, 14% Cr 25% Zn and 2% P in the surface layer. This indicates that some phosphate is present in the Cr(III)-B coating.

Fig. 8.8 shows the Cr 2p spectra acquired from the Cr(VI) coating and both Cr(III) coatings. For the Cr(VI) coating, the peak at the binding energy of 579.2 eV is

attributable to Cr(VI) [17-19]. For the Cr(III) coatings, no Cr(VI) peak was observed near 579.2 eV.

Fig. 8.9 shows the Cr $2p_{3/2}$ curves for the Cr(VI) coating, fitted using three components, Cr(VI), Cr(OH)₃ and Cr₂O₃. The fitting results show that the ratio of Cr(VI) to total Cr is about 0.4. About 40% of the Cr is in the form Cr(OH)₃, and 20 % in Cr₂O₃. For the Cr(III) coating on zinc, no Cr(VI) is present in the surface layer. About 60% of the chromium in the Cr(III) coating is in the form of Cr(OH)₃, and about 40% is in the form of Cr₂O₃.

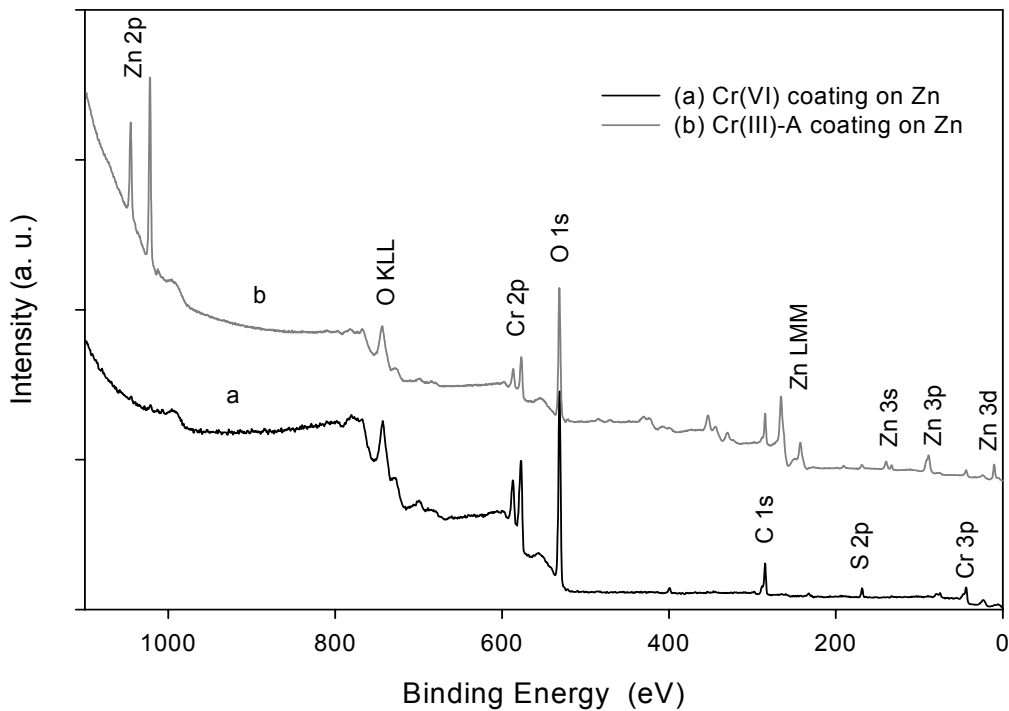


Fig. 8.6 XPS spectra for (a) a Cr(VI) coating, (b) a Cr(III)-A coating on pure zinc discs analyzed using Mg K α (1253.6 eV) X-rays.

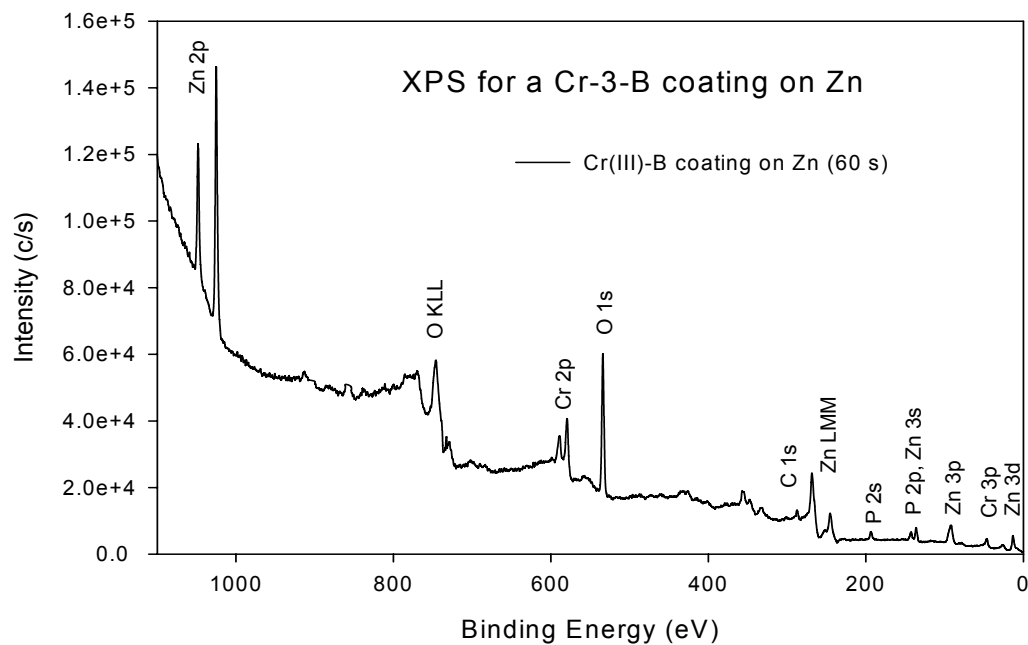


Fig. 8.7 XPS overview spectrum for a Cr(III)-B coating on pure zinc (60 s).

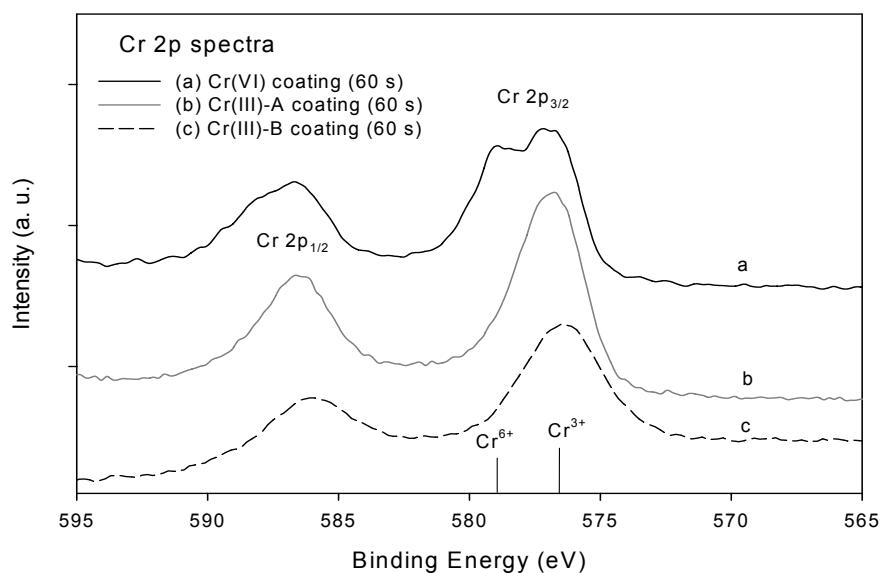


Fig. 8.8 Cr 2p spectra for the Cr(VI), Cr(III)-A and Cr(III)-B coatings on zinc.

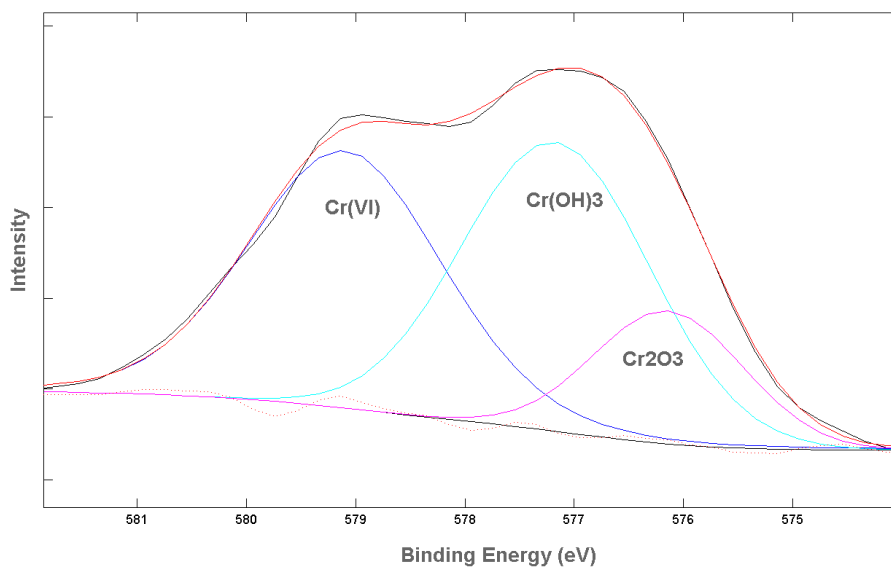


Fig. 8.9 Fitting of a Cr 2p_{3/2} curve for a Cr(VI) coating on a pure zinc disc with dipping time of 60 s. (Cr₂O₃: 576.3 ± 0.2 eV, Cr(OH)₃ or CrOOH: 577.3 ± 0.2 eV and Cr(VI): 579.2 ± 0.2 eV).

Fig. 8.10 shows FTIR spectra acquired from (a) a zinc substrate, (b) a Cr(III)-A coating on zinc with dipping time 30 s and (c) a Cr(III)-B coating on zinc with dipping time 60s and (d) a Cr(VI)-based coating on zinc sheet with dipping time 10 s. The broad absorption band at 3440 cm⁻¹ is attributable to water or water of hydration, and the H-O-H bending motion at 1625 cm⁻¹ can also be observed [20]. The band at 960 cm⁻¹ can be attributed to Cr₂O₇²⁻ or CrO₄²⁻ anions [21-23]. The band near 1126 cm⁻¹ can be attributed to SO₄²⁻ in the Cr(III)-A coating [24] and PO₄³⁻ in the Cr(III)-B coating [23]. The vibration bands at 580, 642 and 836 cm⁻¹ are attributable to Cr(III)-O_x. The peak at 1425 cm⁻¹ may be attributable to the bending vibration of water coordinated to Cr₂O₃·2H₂O [12,25]. For both of the Cr(III) coatings, no band at 960 cm⁻¹ has been observed, which means that no Cr(VI) exists in these coatings.

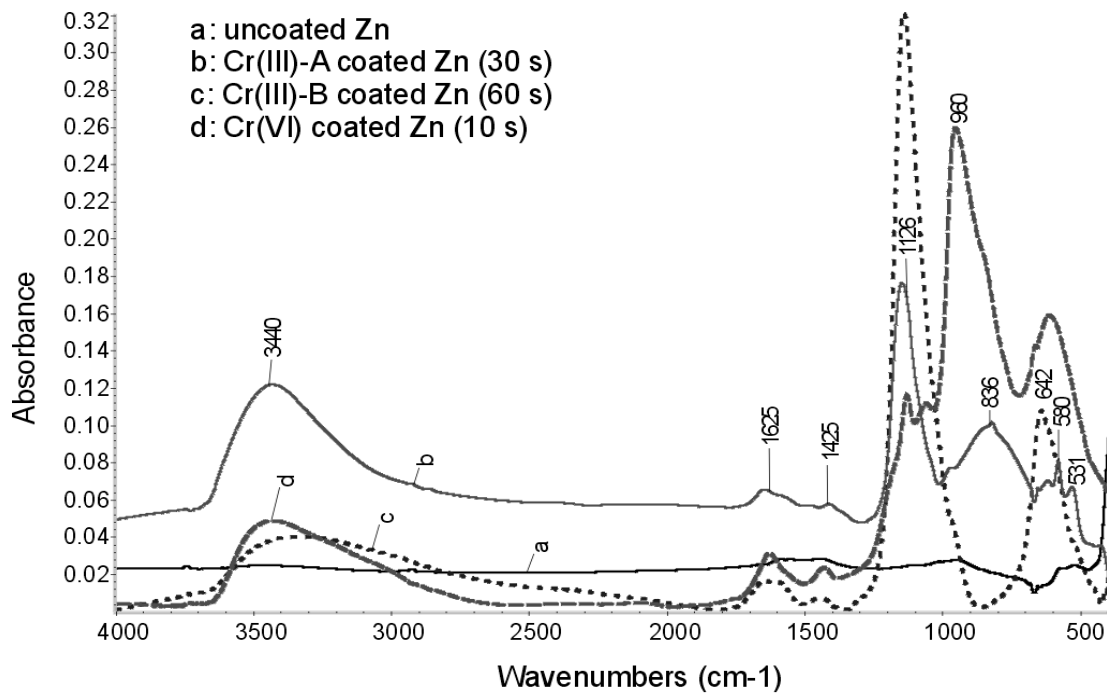


Fig. 8.10 FTIR spectra acquired from (a) a zinc substrate, (b) a Cr(III)-A coating on zinc with dipping time 30 s, (c) a Cr(III)-B coating on zinc with dipping time 60 s and (d) Cr(VI) coating on zinc sheet with dipping time 10 s.

Fig. 8.11 shows the AES depth profiles for (a) a Cr(III)-A coating, (b) a Cr(III)-B coating and (c) a Cr(VI) coating on zinc. It shows that the Cr(III)-B coating is thicker than the Cr(III)-A coating with the same dipping time (60 s). Both the Cr(III)-A and B coatings contain a mixture of chromium oxides and zinc oxide through the layer, and the content of zinc oxide is more than chromium oxides. For the Cr(VI) coating with dipping time of 10 s, a longer sputtering time is needed than for the Cr(III)-B coating with dipping time of 60 s. The depth-profiles show that zinc oxide in the top layer of the Cr(VI) coating is less than 4%.

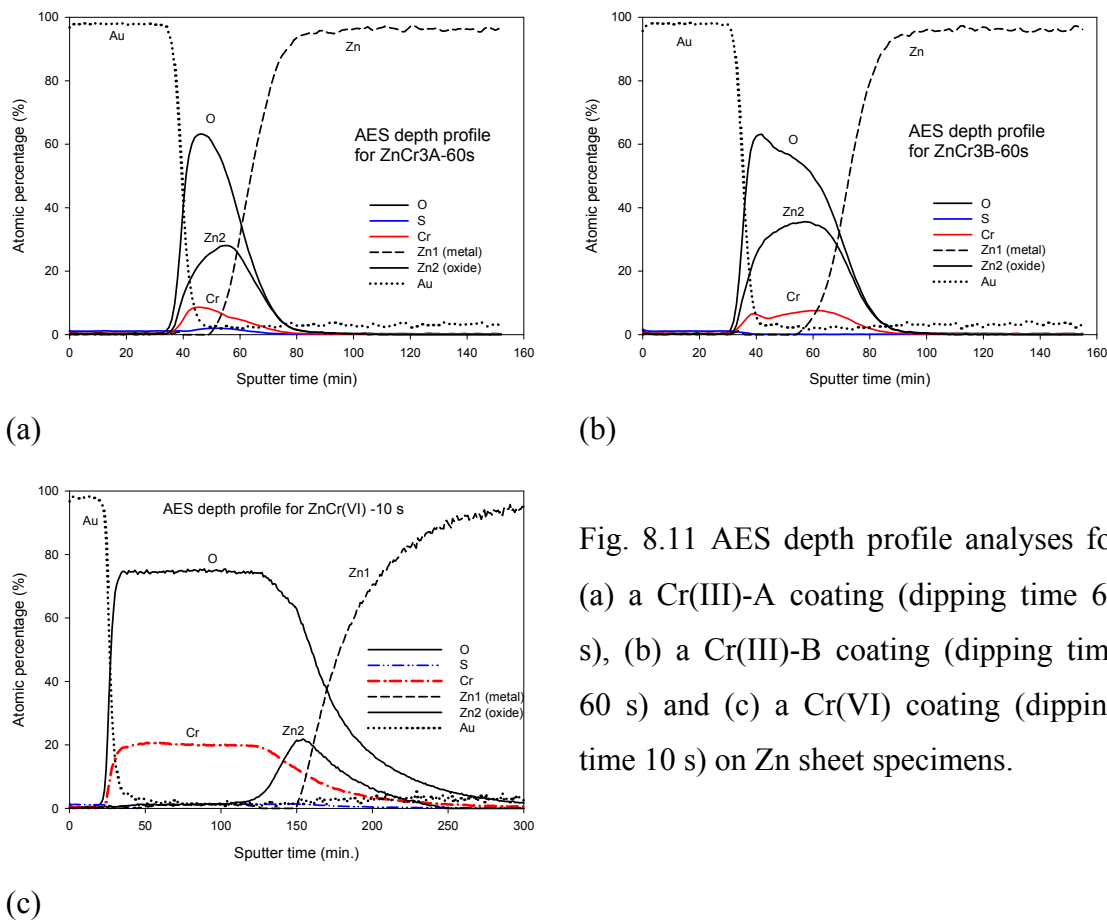


Fig. 8.11 AES depth profile analyses for (a) a Cr(III)-A coating (dipping time 60 s), (b) a Cr(III)-B coating (dipping time 60 s) and (c) a Cr(VI) coating (dipping time 10 s) on Zn sheet specimens.

8.3.4 Corrosion resistance of the Cr(VI) and the Cr(III)-A coated zinc discs

The Cr(VI) and the Cr(III)-A coated zinc discs were characterized using a rotating disc electrode in aerated (open to air) and de-aerated (bubbling with N_2) 0.01 M NaCl solution, respectively. Fig. 8.12 shows the OCP versus time curves for the bare zinc, the Cr(VI) and the Cr(III)-A coatings on zinc discs in aerated 0.01 M NaCl solution. Three measurements were made for each kind of sample. For bare zinc, the potential is initially more negative than for the Cr(VI) and the Cr(III) coated zinc. The potential increases and reaches a maximum in 10 to 20 minutes. After 30 minutes, the potential settles at a relatively stable value. The stable OCP for bare zinc is about $-0.93 V_{SCE}$. For the Cr(VI) and the Cr(III) coated zinc, the OCP shows less change, and is always around $-1.0 V_{SCE}$.

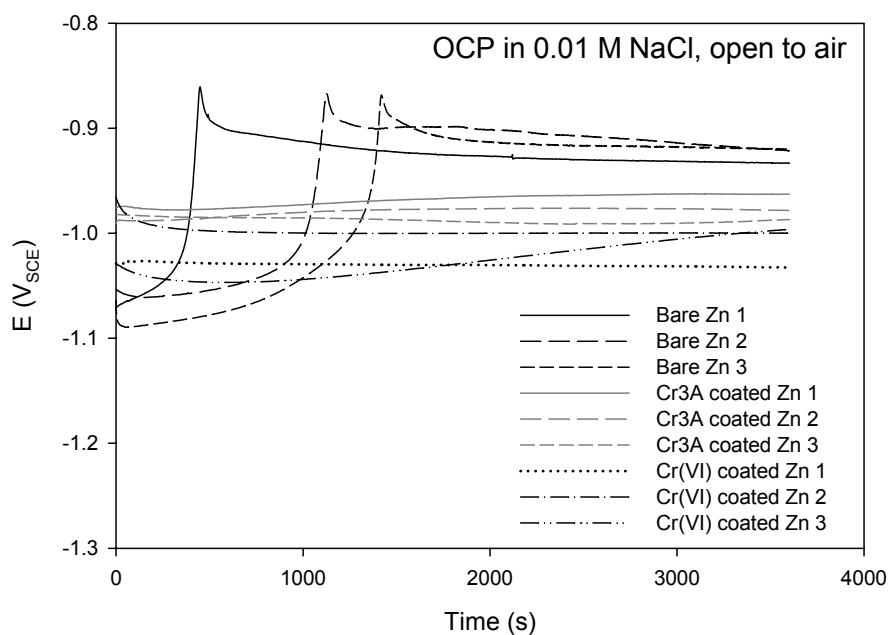


Fig. 8.12 Potential-time curves for bare zinc, Cr(III)-A and Cr(VI) coatings on zinc in 0.01 M NaCl solution (pH 6).

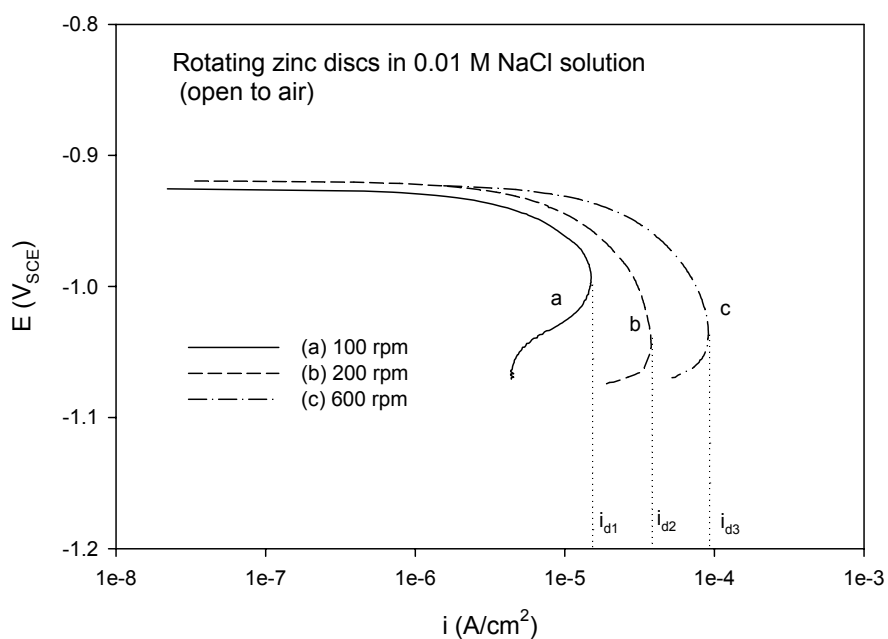


Fig. 8.13 Cathodic polarization curves as a function of rotation speed for bare zinc discs in 0.01 M NaCl solution (open to air).

Fig. 8.13 shows the cathodic polarization curves as a function of rotation speed for bare zinc discs in aerated 0.01 M NaCl solution (open to air). For each rotation speed there is a limiting current density, i_d . It suggests that the cathodic reaction rate on the zinc disc electrode is controlled by the oxygen diffusion to the zinc/electrolyte interface.

Fig. 8.14 shows that the limiting current density is proportional to the square root of the rotation speed, $\omega^{1/2}$. The diffusional boundary layer thickness can be estimated according to the equation[26,27]:

$$\delta_d = 1.61D^{1/3} \nu^{1/6} \omega^{-1/2} \quad (8.1)$$

When rotation rate is 600rpm, the thickness of the diffusion layer is about 10 μm , where $D = 2 \times 10^{-5} \text{ cm}^2/\text{s}$, $\nu = 1 \text{ cp}$ at 20 °C [5,28].

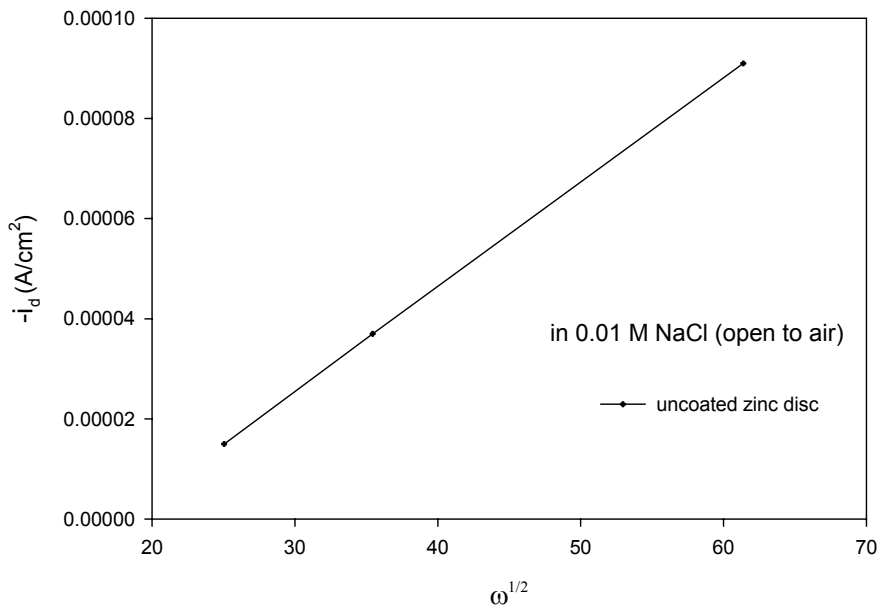


Fig. 8.14 The limiting current density as a function of the rotation speed of zinc disc in 0.01 M NaCl solution (open to air).

Fig. 8.15 shows the anodic and cathodic polarization curves for the Cr(VI)-coated, the Cr(III)-A coated and bare zinc electrodes in aerated 0.01 M NaCl solution. The anodic polarization curves are similar for both the Cr(VI)- and the Cr(III)-A coated zinc. The cathodic polarization curves, however, are significantly different. The bare zinc discs show the largest cathodic current density, and the Cr(VI) coatings show the smallest current density.

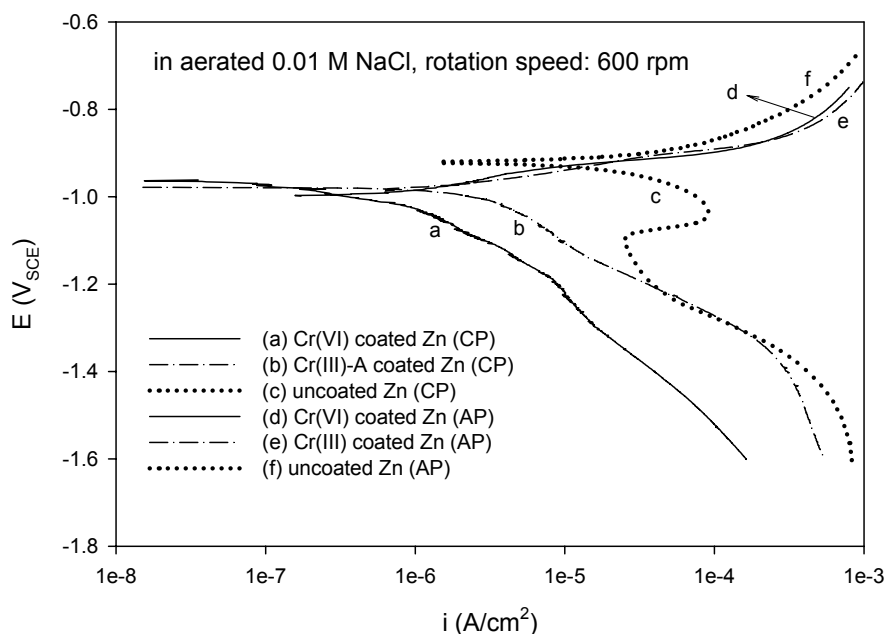


Fig. 8.15 Cathodic (CP) and anodic (AP) polarization curves for Cr(VI) and Cr(III)-A coated zinc in aerated 0.01 M NaCl solution.

The corrosion current values were estimated from the slopes of the relevant polarization curves within 10 mV of the open-circuit potential, using the Stern-Geary equation 5.5. A value of 10 mV was assumed for k , the proportionality constant in the Stern-Geary relationship; this value is typical for zinc products immersed in near-neutral chloride solutions[29]. Values of the corrosion potential and estimated corrosion current density for each coating and for a bare zinc surface are presented in Table 8.3. The current densities presented in Table 8.3 are the currents per unit surface area of each sample. For the coated samples, however, the true local current density is unknown, since the actual reaction area is unknown. The measurements were repeated

at least three times. For the uncoated and the Cr(III)-A coated zinc, the reproducibility was good. For the Cr(VI)-coated zinc, the reproducibility was relatively poor because the density of microcracks in the Cr(VI) coatings was not reproducible.

Fig. 8. 16 shows the polarization curves for the Cr(VI) and the Cr(III)-A coated zinc in the de-aerated 0.01 M NaCl solution. The corrosion potentials and corrosion currents are presented in Table 8.3. In this solution, the open-circuit potentials move to more negative potentials. For the uncoated zinc, the OCP value is $-1.1 \text{ V}_{\text{SCE}}$, which is more negative than for the Cr(VI) and the Cr(III)-A coated zinc. The current peak at about $-1.24 \text{ V}_{\text{SCE}}$ for uncoated zinc is attributable to the cathodic reduction of the zinc oxide formed in air on the surface, *i.e.* $\text{ZnO} + 2\text{H}^+ + 2\text{e}^- \rightarrow \text{Zn} + \text{H}_2\text{O}$ ($E = -0.439 - 0.059 \text{ pH} / \text{V}_{\text{NHE}}$) [30]. For both the uncoated zinc and the Cr(III)-A coated zinc, the corrosion current density becomes significantly less than that measured in the aerated solution. The corrosion current density for the Cr(III)-A coated zinc is similar to that for the Cr(VI) coated zinc.

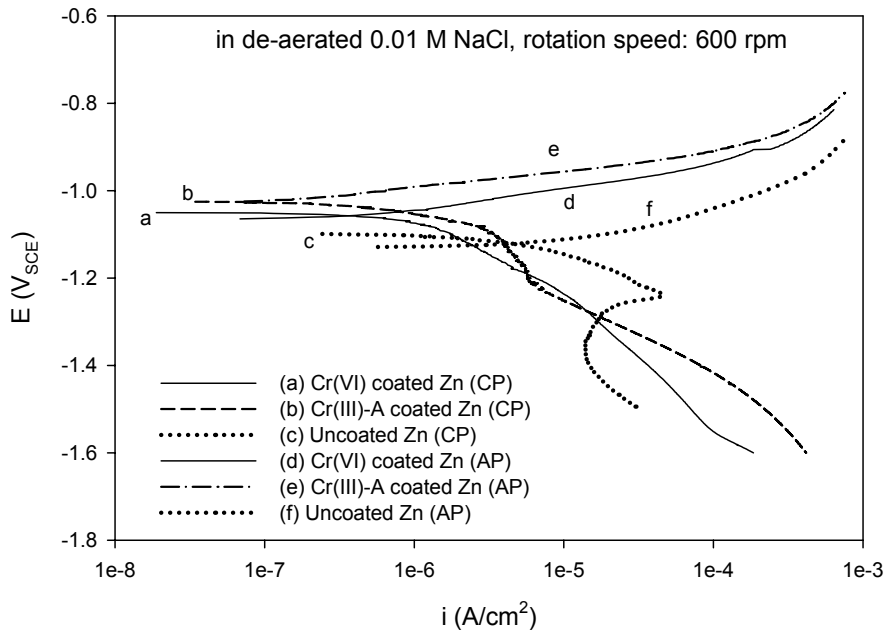


Fig. 8.16 Cathodic (CP) and anodic (AP) polarization curves for Cr(VI) and Cr(III)-A coated zinc in de-aerated 0.01 M NaCl solution.

Fig. 8. 17 shows the Bode impedance plots for a Cr(III)-A coating, a Cr(VI) coating of coating and an uncoated zinc disc obtained after immersion in the aerated 0.01 M NaCl solution for 0.5 hours. This figure shows that the Cr(VI) coatings have the largest impedance and the uncoated zinc surface has the smallest impedance.

Table 8.3 Average corrosion potential and corrosion current density calculated from the cathodic (CP) and anodic (AP) polarization curves using Rp-fit.

Samples		Solution open to air		De-aerated solution	
		E_{corr} (V _{SCE})	i_{corr} (μA/cm ²)	E_{corr} (V _{SCE})	i_{corr} (μA/cm ²)
Cr(VI) coated	CP	-0.99 ± 0.03	0.4 ± 0.1	-1.07 ± 0.02	0.4 ± 0.2
Zn (60s)	AP	-1.00 ± 0.01	0.7 ± 0.3	-1.08 ± 0.02	0.5 ± 0.2
Cr(III)-A coated	CP	-0.97 ± 0.03	0.9 ± 0.3	-1.01 ± 0.02	0.4 ± 0.1
(60s)	Zn AP	-1.00 ± 0.01	0.9 ± 0.2	-1.06 ± 0.03	0.4 ± 0.2
Bare	CP	-0.92 ± 0.01	11 ± 2	-1.10 ± 0.01	2.1 ± 0.3
Zn	AP	-0.94 ± 0.02	20 ± 5	-1.13 ± 0.01	5.9 ± 0.4

Fig. 8. 18 presents the Nyquist impedance plots for an uncoated zinc disc obtained in the aerated 0.01 M NaCl solution. The shape of these Nyquist diagrams suggests that the corrosion of pure zinc is a charge-transfer-controlled dissolution reaction [31,32]. These impedance data can be fitted with a simple equivalent circuit in Fig. 5.3(a). The fitting results are shown in Table 8.4. The Chi-squared value from the fitting is smaller than 8×10^{-4} (the smaller this value is, the better is the fitting results).

The capacitance for the uncoated zinc, C_{dl} , measured after exposure to the solution for 0.5 h, is 45 μF/cm², and after 1 h, it becomes 33 μF/cm². The charge transfer resistance, R_{ct} , decreases from 0.9 kΩ·cm² to 0.42 kΩ·cm² after 1 h.

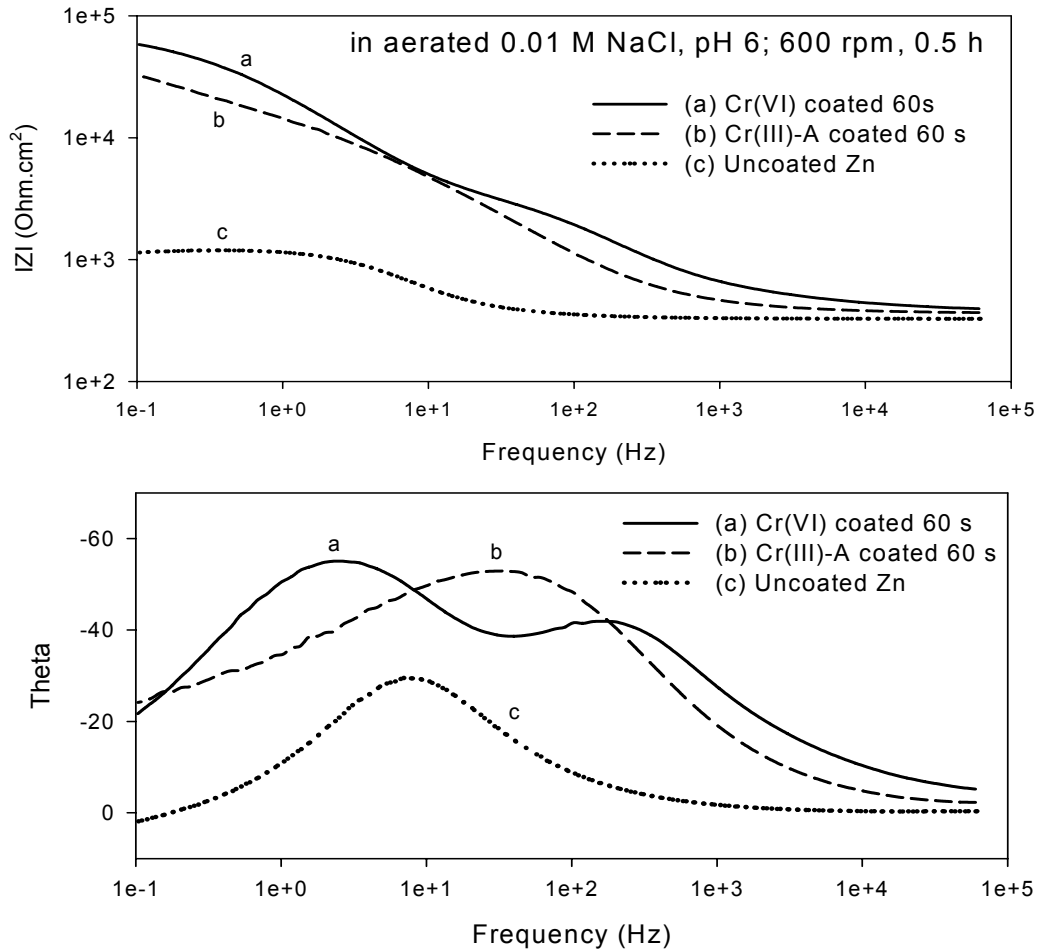


Fig. 8.17 Bode impedance plots after 0.5 h for a Cr(VI) coating, a Cr(III)-A coating and uncoated zinc in aerated 0.01 M NaCl solution.

Fig. 8. 19 shows the Nyquist impedance plots for (1) a Cr(VI) coating and (2) a Cr(III)-A coating obtained as a function of immersion time in the aerated 0.01 M NaCl solution. The impedance diagrams for the Cr(VI) coated zinc discs clearly show two capacitive loops (see Fig. 8. 19 (1)). The response of these coatings to an applied potential perturbation can be modeled with the equivalent circuit proposed in Fig. 8.20. The elements in this circuit are described as in chapter 5. Here only two time constants are considered, since the diffusion effect is much weaker than in the stationary solution. The capacitive response of the coating determines the behavior of the system at high frequencies, and the capacitive response of the double layer determines the behavior at lower frequencies [31]. When a conversion coating is present on the surface, the

corrosion takes place on the zinc surface exposed to the electrolyte through pores or defects in the coating. For the Cr(VI) coating, the second capacitive loop (*i.e.* the low frequency loop) changes significantly with immersion time: the fitting results in Table 8.4 indicate that the charge-transfer resistance R_{ct} increases within the first hour of immersion and then decreases. Meanwhile, the resistance associated with the pores in the coating, R_{cp} , decreases slightly with time. The charge transfer resistance may increase during the first hour of immersion because a certain time span is required for the Cr(VI) species to move to defects in the coating and bring about an effective “repair”. On the other hand, the duration of this “self-healing” ability is limited, because the reduction of Cr(VI) to Cr(III) is irreversible. When the soluble, mobile Cr(VI) species have been consumed, and are no longer able to maintain an effective state of passivity over the entire coated surface, then the corrosion resistance starts to decrease again.

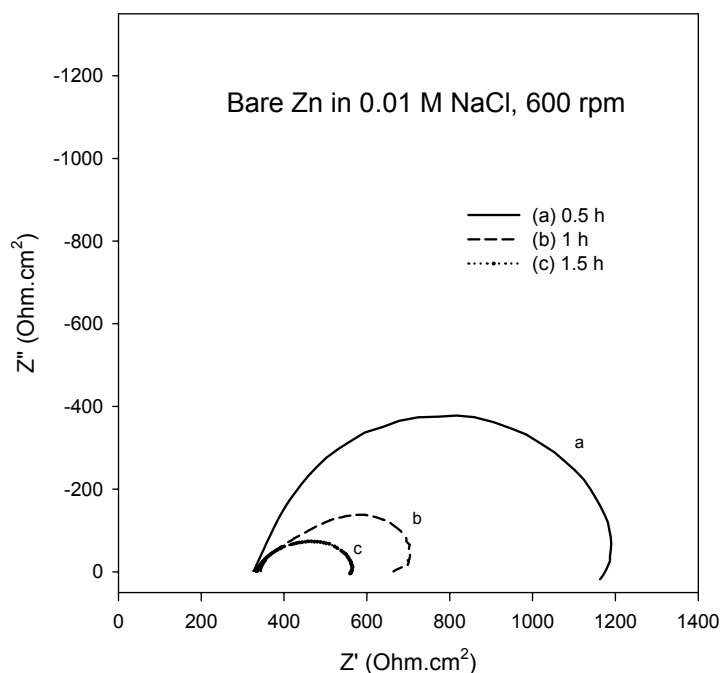


Fig. 8.18 Complex impedance plot obtained in aerated 0.01 M NaCl solution for uncoated zinc.

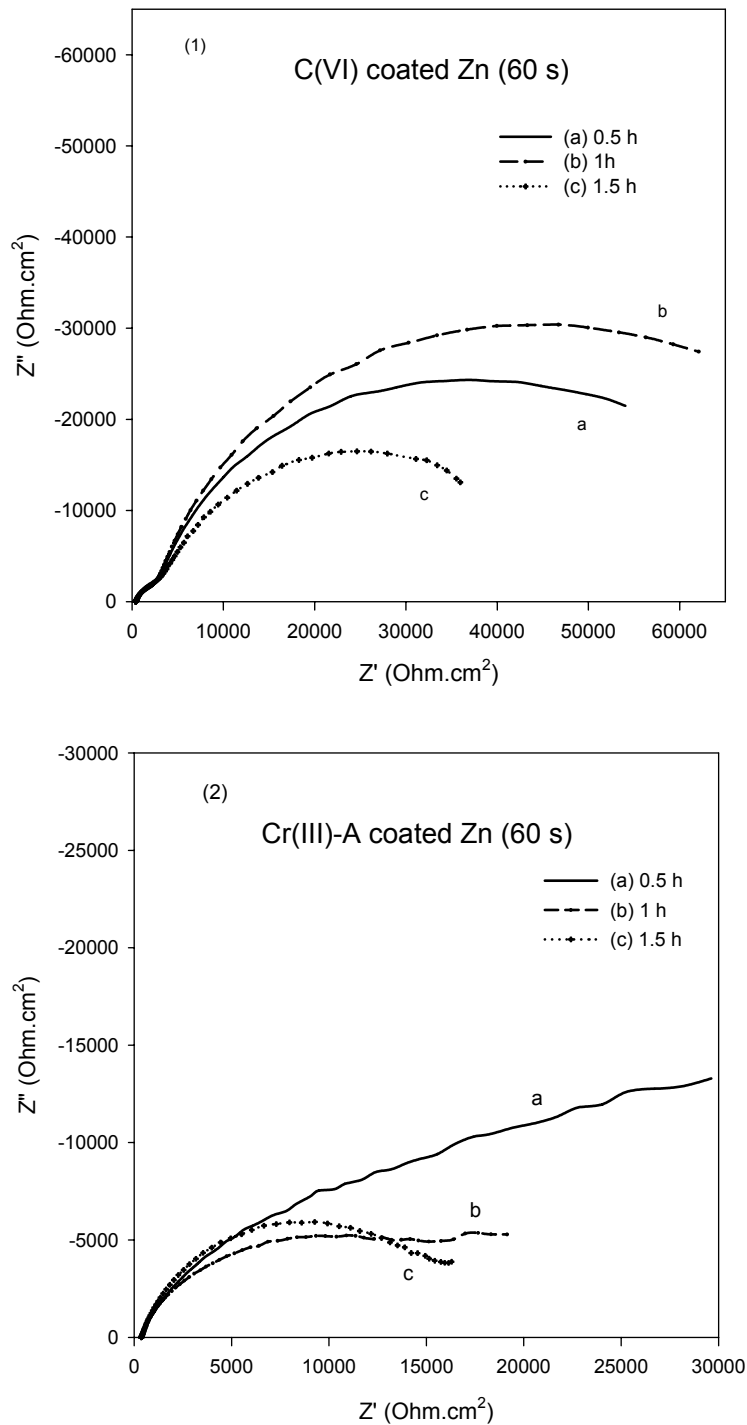


Fig. 8.19 Complex impedance plots obtained in aerated 0.01 M NaCl solution for (1) Cr(VI) coated Zn and (2) Cr(III)-A coated Zn.

For the Cr(III)-A treated zinc (see Fig. 8.19 (2)), the capacitive loop related to the coating is not as well defined as that for the Cr(VI) coated zinc. The apparent increase of the double-layer capacitance with time may be explained by an increase of the

reacting surface area due to the corrosion. No increase in the magnitude of R_{ct} during the first hour of immersion can be seen. R_{ct} decreases as a function of time, perhaps reflecting the fact that no Cr(VI) species are present, so that there is no self-healing effect.

Table 8.4 Fitting results from the EIS data acquired from Cr(VI) and Cr(III)-A coatings on Zn discs in 0.01 M NaCl solution using circuit in Fig. 8.20. The data obtained from bare zinc specimens were fitted using circuit (a) in Fig. 5.3 (R , in units $k\Omega \cdot cm^2$; Y_0 , in units $10^{-6} s^n \cdot \Omega^{-1} \cdot cm^{-2}$ and C , in units $\mu F \cdot cm^{-2}$).

Samples	Time (h)	OCP (V_{SCE})	R_{el}	Y_0 (C_p)	n_0	R_{cp}	C_{dl}	R_{ct}
Cr(VI) coated Zn (60 s)	0.5	-1.00	0.39	6.8	0.677	6.8	2.9	66
	1	-1.00	0.39	5.4	0.707	5.7	3.4	80
	1.5	-1.00	0.39	4.0	0.768	5.2	6.7	42
Cr(III)-A coated Zn (60s)	0.5	-0.98	0.37	8.3	0.752	16	37	32
	1	-0.98	0.37	7.5	0.786	9.6	57	17
	1.5	-0.99	0.37	11	0.798	16	688	8.3
Pure Zn	0.5	-0.90	0.33	--	--	--	45	0.90
	1	-0.90	0.34	--	--	--	33	0.42
	1.5	-0.90	0.33	--	--	--	33	0.25

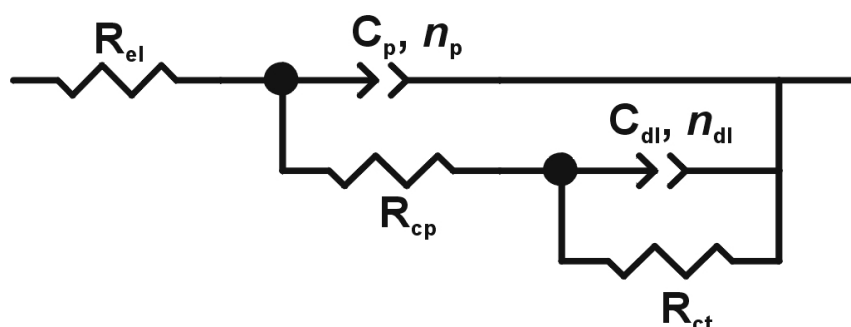


Fig. 8.20 An equivalent circuit for modeling the Cr(VI) and the Cr(III)-A coated zinc rotating discs in aerated 0.01 M NaCl solution.

Fig. 8.21 shows the topography of (a) a Cr(VI) and (b) a Cr(III)-A coated zinc disc after exposure to 0.01 M NaCl solution with a rotation speed of 600 rpm for 5 hours. For the Cr(VI) coated zinc, white corrosion products are visible near cracks. For the Cr(III)-A coated zinc, pits are observed. For both types of coating on zinc, corrosion is localized.

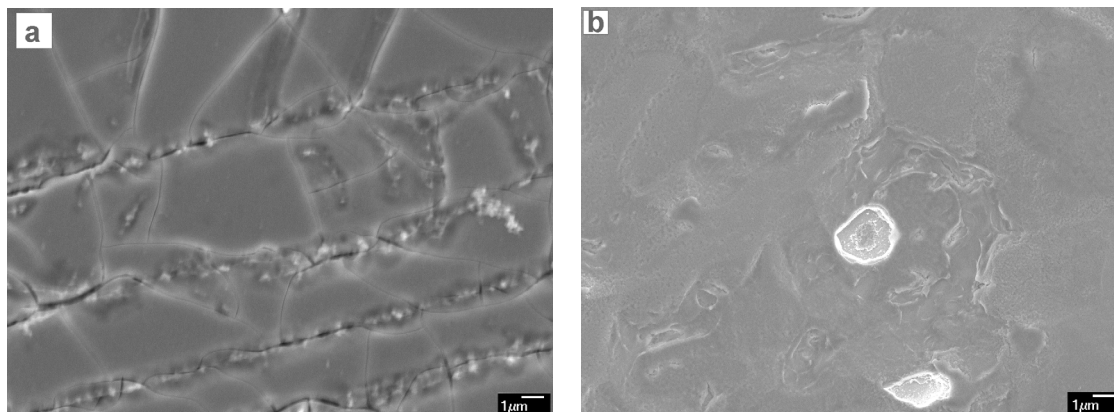


Fig. 8.21 SEM images of (a) a Cr(VI) and (b) a Cr(III)-A coated zinc disc after immersion in 0.01 M NaCl solution for 5 h (rotation speed: 600 rpm).

8.3.5 Corrosion inhibition through the reduction of Cr(VI) in the solution

In the Cr(VI) coatings, some Cr(VI) species are adsorbed on the surface of the coating and on the walls of the pores in the coatings. These adsorbed Oxo-Cr(VI) species may dissolve in the solution when the coating is exposed to an electrolyte. Therefore we can ask the question: as a strong oxidizing agent, how do the Oxo-Cr(VI) species function in inhibiting the corrosion of zinc?

Fig. 8.22 shows the cathodic polarization curves for zinc discs in de-aerated 0.01 M NaCl solution containing different concentrations of sodium dichromate. With the addition of sodium dichromate to the solution, the mixed potential (corrosion potential) moves in the positive direction. With the addition of 0.001 M sodium dichromate to the solution the mixed potential changes about 250 mV, and as more dichromate is added, the potential moves further. It indicates that the Oxo-Cr(VI) species in the solution have an anodic inhibition effect on the corrosion of zinc.

In Fig. 8.22, a sharp current peak exists between -1.01 and -1.05 V_{SCE} in all the solutions with different concentrations of sodium dichromate. This peak has an area of 2.3 - 5.3 mC/cm^2 and this area varies little with the concentration of $Cr(VI)$ in the solution. This peak may be due to the reduction of adsorbed zinc ions [33], since this potential is near the reduction of zinc ions (-0.763 $V_{NHE} \approx 1.004$ V_{SCE} [28]). This peak is also possibly due to the reduction of chromium species on the surface of the zinc disc [34].

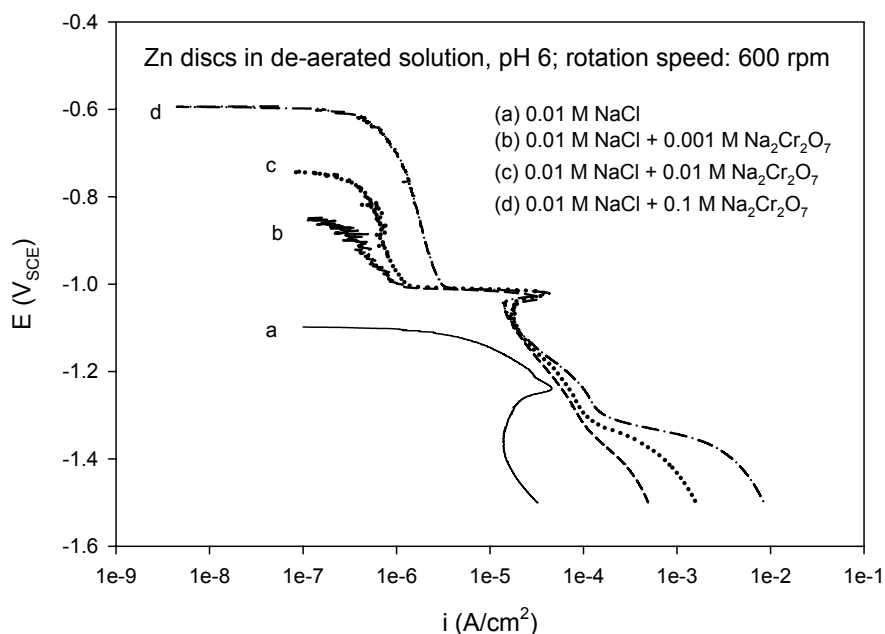


Fig. 8.22 Cathodic polarization curves for zinc discs in de-aerated 0.01 M NaCl with or without chromate inhibitors.

In order to see the composition change, a zinc sample cathodically polarized from the OCP to -1.01 V_{SCE} (onset of the current peak) and a sample polarized from the OCP to -1.05 V_{SCE} (end of the current density peak, see Fig. 8.23) were analyzed using XPS. Cr signal has been observed on the surface of both samples. Fig. 8.24 shows the Cr 2p peaks obtained from the two samples. The chromium detected on both surfaces is mainly in the form of $Cr(III)$ oxides and hydroxides. It indicates that some $Cr(VI)$ species at the zinc/electrolyte interface have been reduced and deposited on the surface of zinc. Zinc signal has also been observed on the surface of the two samples (see Fig. 8.25). A characteristic Auger peak Zn LLM is at the binding energy 265.4 eV that is

from zinc oxide[35]. This does not exclude the possibility that zinc oxidized in air after the cathodic polarization measurements.

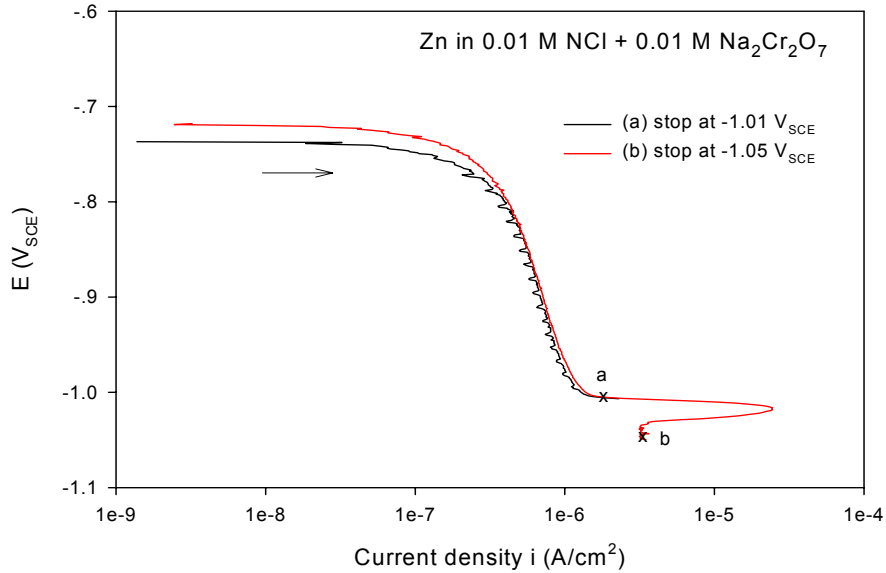


Fig. 8.23 Cathodic polarization curves for two zinc samples in de-aerated 0.01 M NaCl + 0.01 M Na₂Cr₂O₇ solution (pH: 6): (a) from OCP to $-1.01 V_{SCE}$ (onset of the current peak) and (b) from OCP to $-1.05 V_{SCE}$ (end of the current density peak).

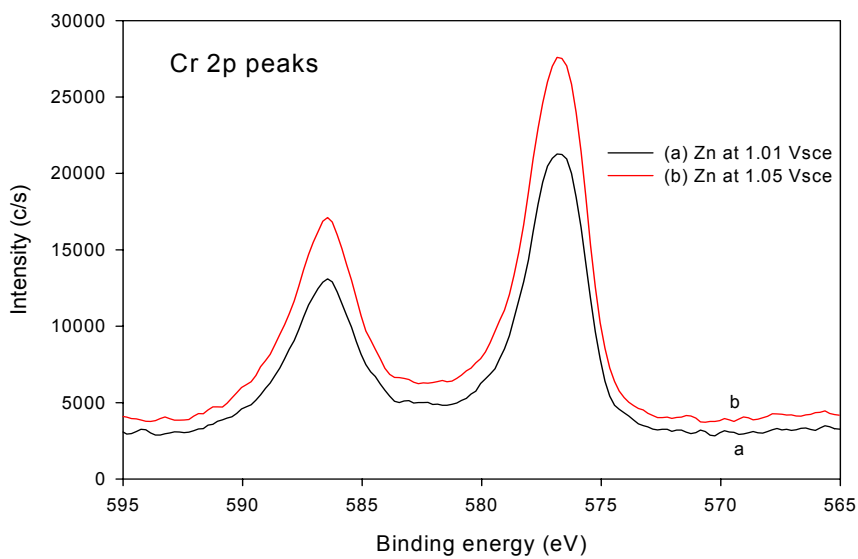


Fig. 8.24 Cr 2p peaks obtained from the two zinc samples after cathodic polarized in de-aerated 0.01 M NaCl + 0.01 M Na₂Cr₂O₇ solution (pH: 6) as described in the text.

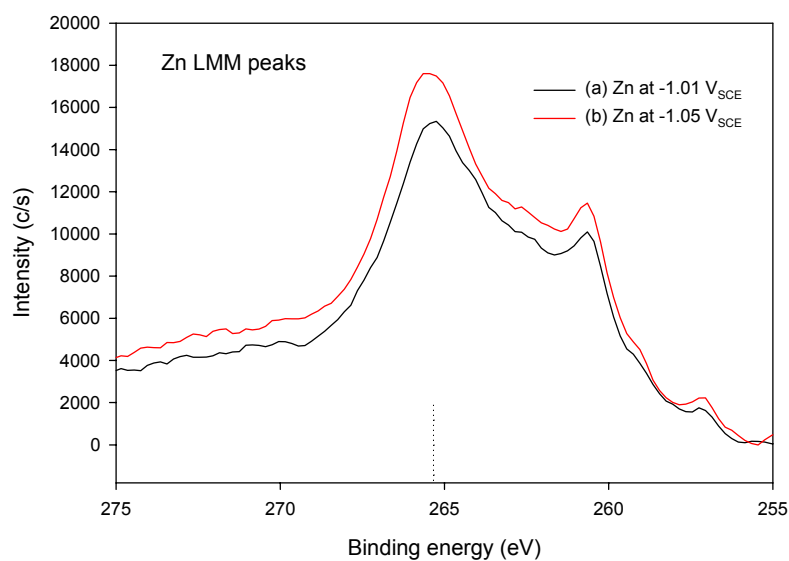


Fig. 8.25 Zn LMM peaks obtained from the zinc samples cathodically polarized in de-aerated 0.01 M NaCl + 0.01 M Na₂Cr₂O₇ solution (pH: 6) as described in the text.

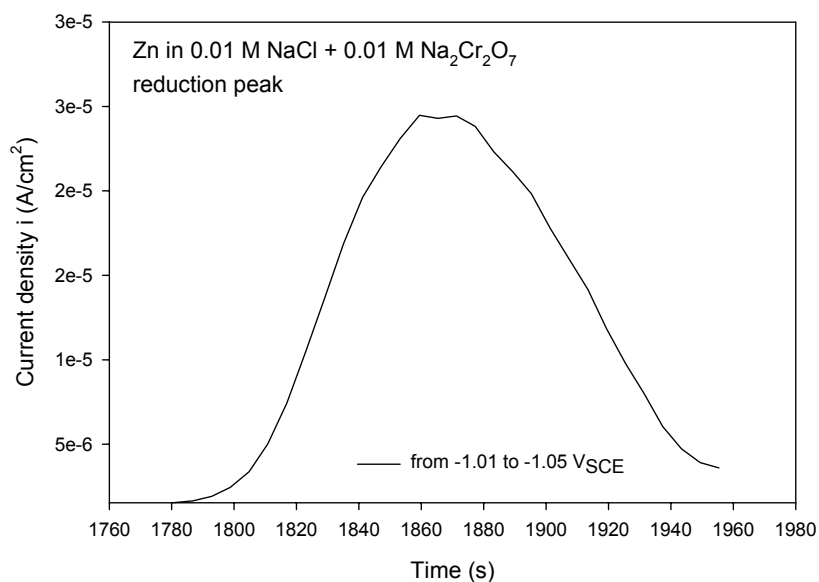


Fig. 8.26 Cathodic current density peak for a zinc disc in de-aerated 0.01 M NaCl + 0.01 M Na₂Cr₂O₇ solution between -1.01 and -1.05 V_{SCE}.

Fig. 8.26 shows the cathodic current density peak obtained from a zinc disc in de-aerated 0.01 M NaCl + 0.01 M Na₂Cr₂O₇ solution between -1.01 and -1.05 V_{SCE} (see also Fig. 8.23). This peak has an area of 2.3 mC/cm², which is in agreement with the results reported by Clark et al.[34]. Clark and coworkers have measured the reduction peaks which have an area of 1.1-2.5 mC/cm² for copper and glassy carbon electrodes in 0.1M NaCl + 0.05 M K₂Cr₂O₇ solution, and the area varied little with Cr(VI) concentration, electrode material, and potential in the range of +0.2 to -0.6 V_{Ag/AgCl} (E⁰ = 0.197 V versus NHE). This reduction peak was attributed to the reduction of Cr(VI) to Cr(III), and corresponds to formation of approximately a monolayer of Cr(III) oxy-hydroxide[34].

8.3.6 Corrosion resistance of the Cr(VI), the Cr(III)-A and the Cr(III)-B coated EG steel

Fig. 8.27 shows the polarization curves for three specimens of the Cr(III)-B coated EG steel in the aerated 0.01 M NaCl solution. The open circuit potential (OCP) is about -0.98 V_{SCE}. The breakdown potential (defined as the potential at which the anodic current exceeds 10⁻⁵ A/cm²) is between -0.91 and -0.94 V_{SCE}.

Fig. 8.28 shows the polarization curves for a Cr(III)-A, a Cr(III)-B, a Cr(VI) coating and a bare EG steel specimen in the solution. There is not much difference in breakdown potential for the chromium treated specimens, but for the untreated EG steel E_b is more negative than for the chromium treated specimens. The corrosion current values were estimated from the slopes of the relevant cathodic polarization curves within 10 mV of the open-circuit potential, using the Stern-Geary equation 5.5, as described above. Values of the corrosion potential and estimated corrosion current density for each coating and for the uncoated EG steel are presented in Table 8.5. The corrosion current decreases in the following order: i_c (EG steel) > i_c (Cr(III)-A) > i_c (Cr(III)-B) > i_c (Cr(VI)). This suggests that the corrosion resistance of the Cr(III)-B coating is greater than that of the thinner Cr(III)-A coating, but less than that of the Cr(VI) coating.

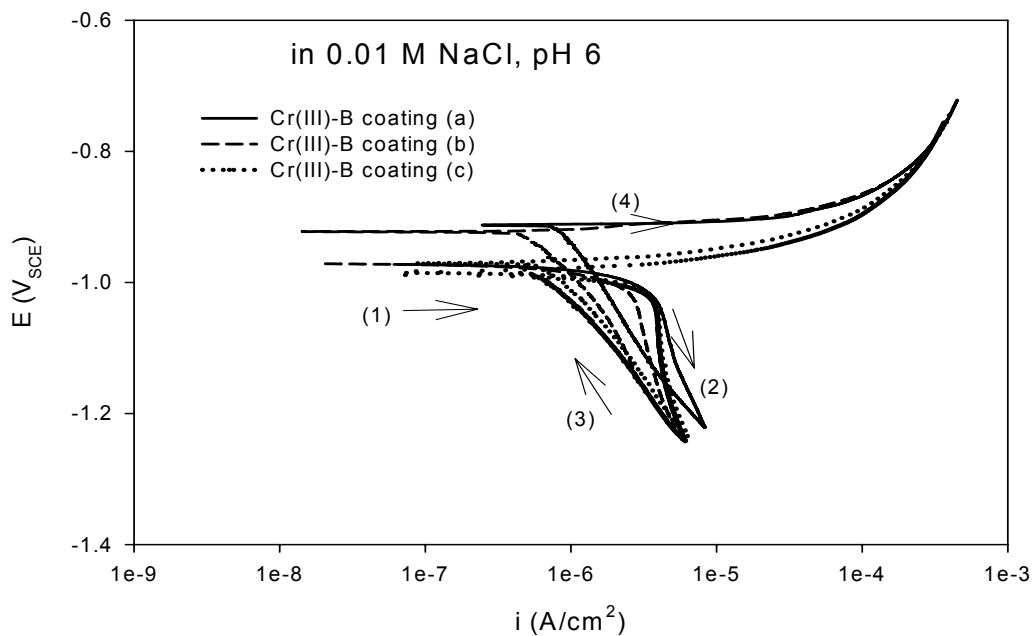


Fig. 8.27 Polarization curves for three Cr(III)-B coated specimens (with dipping time of 60 s) exposed to aerated 0.01 M NaCl solution.

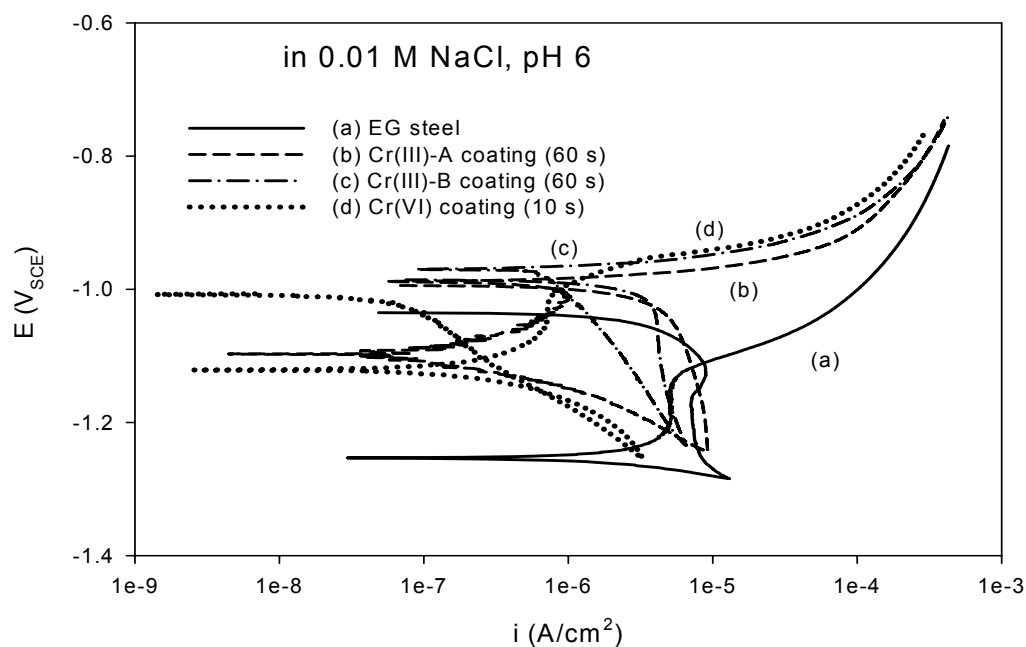


Fig. 8.28 Polarization curves for (a) EG steel, (b) Cr(III)-A, (c) Cr(III)-B and (d) Cr(VI) coatings in aerated 0.01 M NaCl solution.

Table 8.5 Corrosion potential and current density after 1 hour in aerated 0.01 M NaCl solution calculated from the cathodic polarization curves (in Fig. 8.28) using Rp-fit.

Samples	Solution open to air	
	E_{corr} (V _{SCE})	i_{corr} ($\mu\text{A}/\text{cm}^2$)
EG steel	-1.03	1.7
Cr(III)-A coated EG steel (60 s)	-0.99	1.5
Cr(III)-B coated EG steel (60 s)	-0.97	1.1
Cr(VI) coated EG steel (10 s)	-1.00	0.12

Fig. 8.29 shows the Bode impedance plots for (a) the bare EG steel, (b) Cr(III)-A, (c) Cr(III)-B and (d) Cr(VI) coatings obtained after immersion in the 0.01 M NaCl solution for 0.5 hours (the relevant Nyquist plots are not presented here). When a conversion coating is present on the surface, the corrosion takes place in the pores or defects in the coatings. The shape of the phase angle vs. frequency curve for the Cr(VI) coating indicates that the impedance has two separate capacitive components *i.e.* there are two time constants. The capacitive response at higher frequencies can be attributed to the capacitive behavior of the chromate coating, while the capacitive response at lower frequencies can be attributed to the double layer [31]. For the two types of Cr(III)-coating and the bare EG steel, the impedance has only a single capacitive component *i.e.* there is only one time constant. The magnitude of the impedance shown in Fig. 8.29 increases in the following order: $|Z|$ (EG steel) < $|Z|$ (Cr(III)-A) < $|Z|$ (Cr(III)-B) < $|Z|$ (Cr(VI)), which is consistent with the polarization results.

Fig. 8.30 shows SEM images for (a) a Cr(III)-B coating (60 s) and (b) a Cr(VI) coating (10 s) on EG steel after immersion in 0.01 M NaCl solution for 24 h. Both coatings exhibit localized corrosion, since pits are visible in both coatings. However, some pits in the Cr(III)-B coating are much bigger than those in the Cr(VI) coating. This supports the electrochemical data suggesting that the Cr(VI) coating has a larger corrosion resistance than the Cr(III)-B coating.

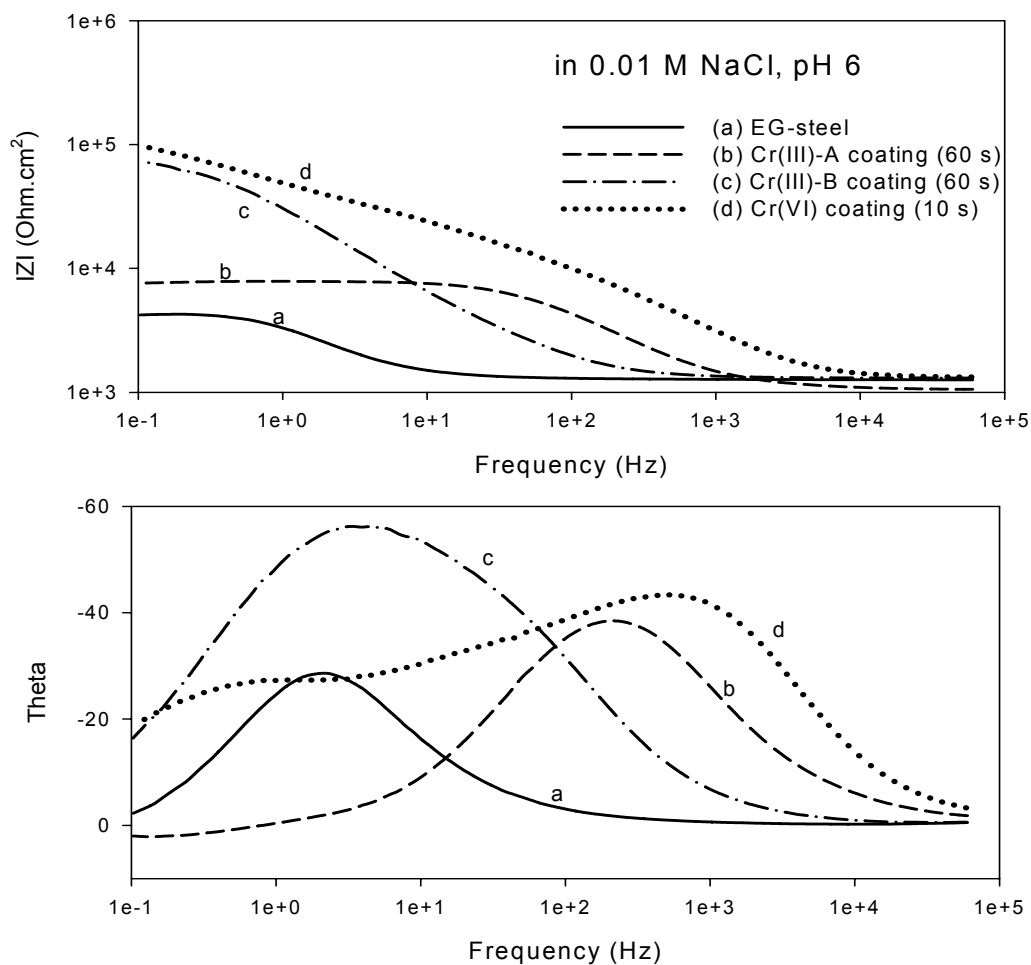


Fig. 8.29 The Bode impedance plots for the three different coatings and untreated EG steel obtained after immersion in the solution for 0.5 h.

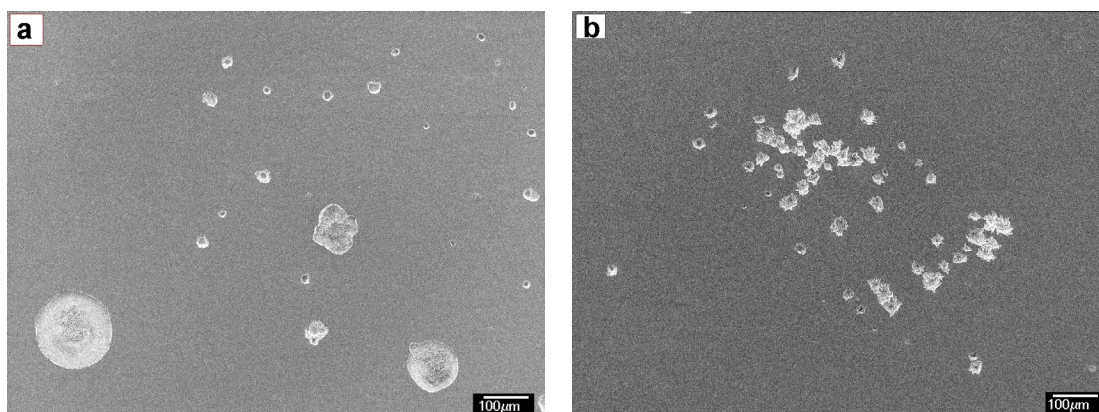


Fig. 8.30 SEM images of the coated EG steel specimens after exposure to aerated 0.01 M NaCl solution for 24 h: (a) Cr(III)-B coating (60 s) and (b) Cr(VI) coating (10 s).

Fig. 8.31 shows the Bode plots of impedance for a Cr(VI) and a Cr(III)-B coating on the EG steel in 0.6 M NaCl solution (open to air). The impedance data have been fitted using the equivalent circuit in Fig. 5.18 (b). Some fitting results are presented in Table 8.6. The meaning of the elements is as defined in chapter 5.

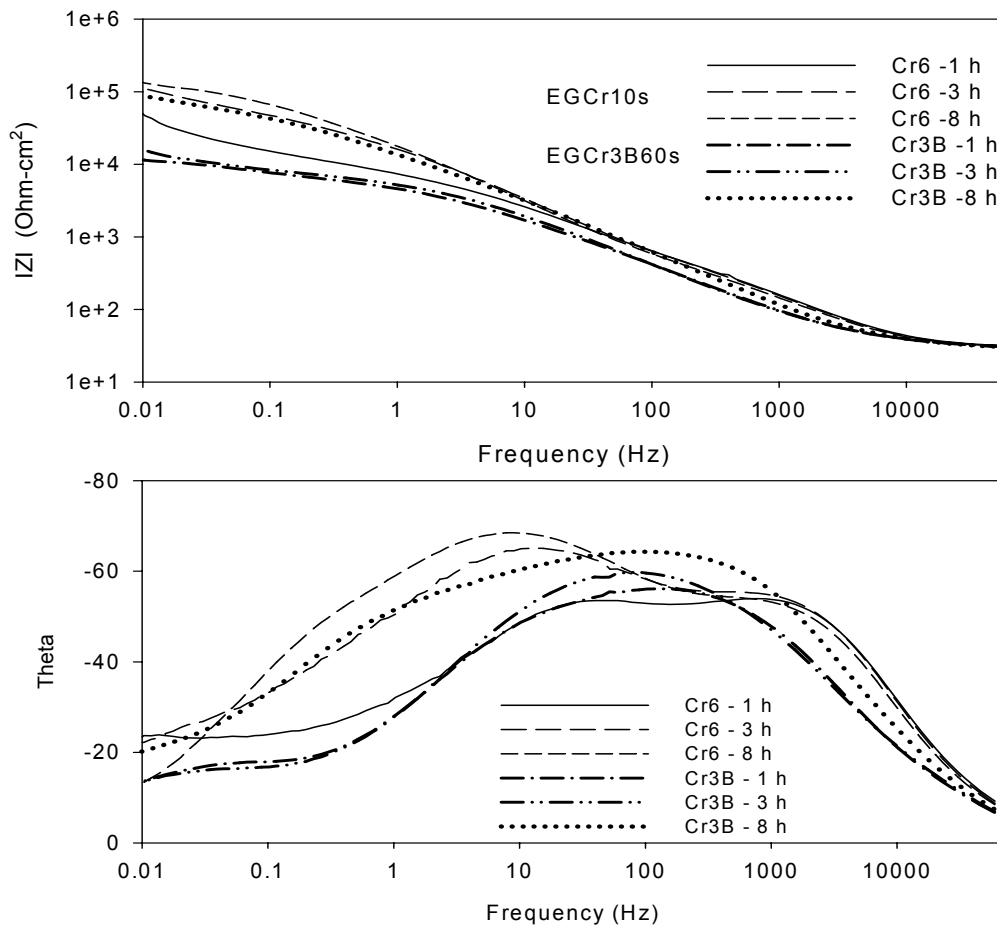


Fig. 8.31 Bode impedance plots for a Cr(VI) coating (10 s) and a Cr(III)-B coating (60 s) on the EG steel, as a function of immersion time in aerated 0.6 M NaCl solution.

Table 8.6 Best-fit parameters for the EIS data obtained from Cr(VI) and Cr(III)-B coatings on the EG steel in aerated 0.6 M NaCl solution (all resistances R , in units $\Omega \cdot \text{cm}^2$ and all admittances Y_0 , in units $10^{-6} \text{ s}^n \cdot \Omega^{-1} \cdot \text{cm}^{-2}$).

Sample	OCP	Exposure	R_{el}	Y_0	n_0	R_{ep}	Y_{01}	n_1	R_{ct}	Y_{02}	n_2	R_{d}
	V_{SCE}	Time (h)		(C_p)			(C_{d1})			(C_d)		
Cr(VI)	-1.06	1	30	4.4	0.828	582	12.6	0.701	7.9 k	94	0.597	18 k
10 s		3	30	5.2	0.816	787	5.0	0.815	28.7 k	27.2	0.583	84 k
		8	29	6.2	0.804	764	4.4	0.842	59 k	17.6	0.805	65 k
Cr(III)-B	-1.06	1	30	22.7	0.718	3735	19	0.76	3 k	420	0.65	8.3 k
60 s		3	30	3.0	0.875	34	19.7	0.681	7.2 k	378	0.618	9.8 k
		8	31	0.6	1	24	11	0.728	5.6 k	11	0.485	96 k

Fig. 8.32 shows the residual errors after fitting of the impedance data, measured for (a) the Cr(VI) and (b) the Cr(III)-B coatings on the EG steel after exposure to the solution for 8 h, using the equivalent circuit in Fig. 5.18 (b). The fitting errors are less than 3% for both the real part and the imaginary part of the measured impedance over most of the investigated frequency range.

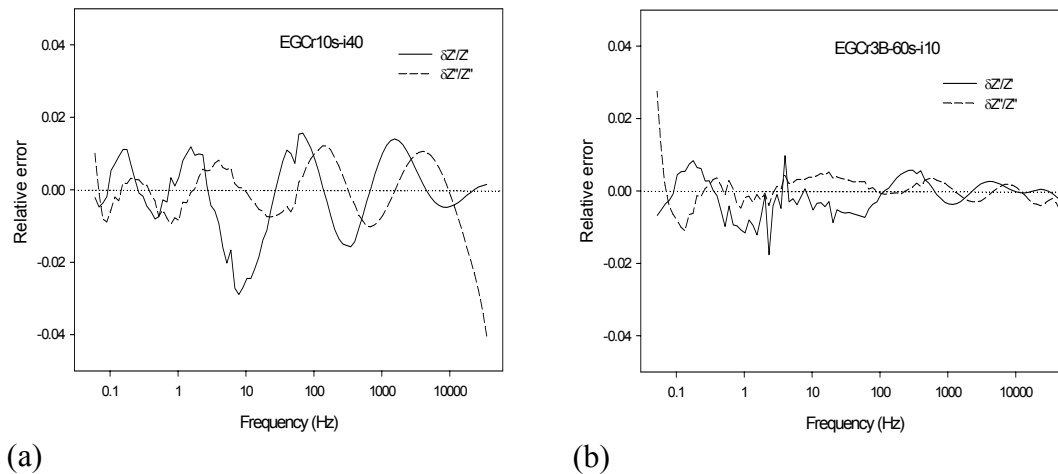
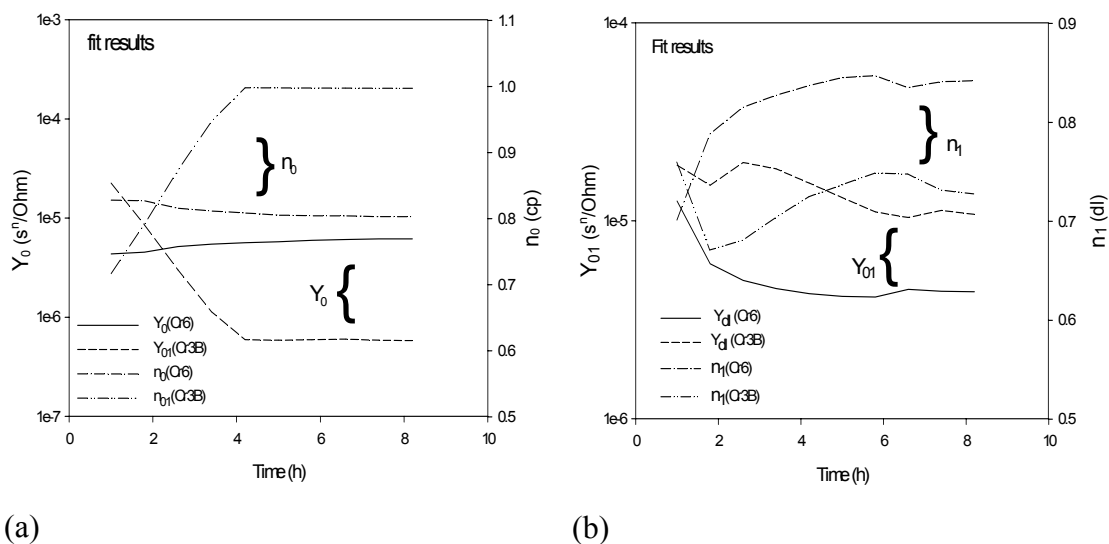


Fig. 8.32 Residual error after fitting impedance data using the model in Fig. 5.18(b): (a) the Cr(VI) coating, (b) the Cr(III)-B coating after exposure to the aerated 0.6 M solution for 8 h.

Fig. 8.33 shows the fitting results, (a) admittance Y_0 and CPE exponent n_0 for the coating layer, (b) admittance Y_{01} and CPE exponent n_1 for the double layer as a function of exposure time for the Cr(VI) and the Cr(III)-B coatings on the EG steel in aerated 0.6 M NaCl solution. The admittance Y_0 for the Cr(III)-B coating decreases with exposure time, and after 4 h, it becomes a pure capacitor (i.e. $n_0 = 1$). This suggests that the corrosion product deposition thickens the layer during the corrosion process, filling and blocking the pores in the coating. However, the admittance Y_{01} of the double layer is greater for the Cr(III)-B coating ($11 \text{ s}^n \cdot \Omega^{-1} \cdot \text{cm}^{-2}$) than for the Cr(VI) coating ($4.4 \text{ s}^n \cdot \Omega^{-1} \cdot \text{cm}^{-2}$) after exposure to the solution for 8 h. It indicates that the corrosion area in the Cr(III)-B coating is larger than in the Cr(VI) coating, though the Cr(III)-B layer is

like a capacitor. This is due to the fact that the corrosion product, zinc oxide/hydroxide, does not completely passivate the zinc surface as Cr(VI) does.



(a) (b)
 Fig. 8.33 Fitting results: (a) admittance Y_0 and CPE exponent n_0 of the coating layer, (b) Y_{01} and n_1 of the double layer as a function of exposure time for the Cr(VI) and the Cr(III)-B coatings on the EG steel in aerated 0.6 M NaCl solution.

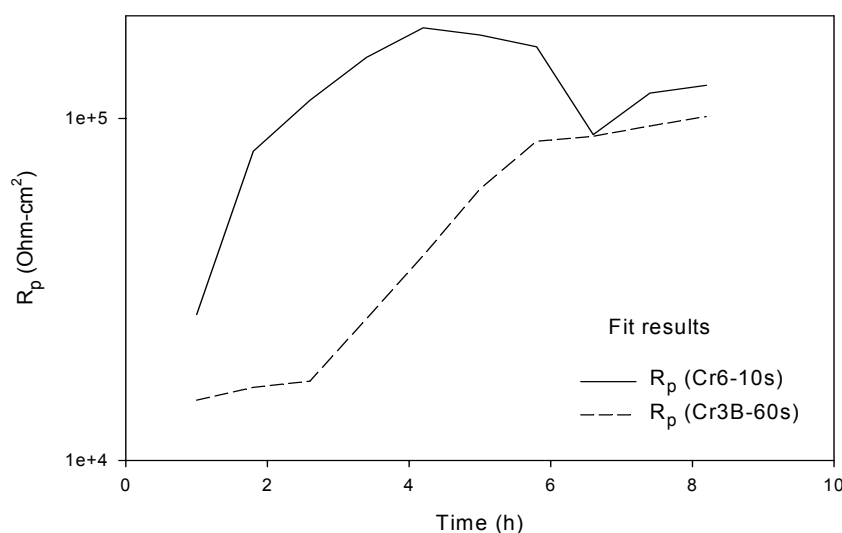


Fig. 8.34 Fit results: polarization resistance as a function of exposure time for the Cr(VI) and the Cr(III)-B coatings on the EG steel in aerated 0.6 M NaCl solution.

Fig. 8.34 shows the fitted values of the polarization resistance ($R_p = R_{cp} + R_{ct} + R_d$) as a function of exposure time in the solution. For the Cr(VI) coating, the polarization resistance increases with exposure time during the first four hours. After 4 h it drops down and after 7 h it rises again slightly. For the Cr(III)-B coating, the polarization resistance is lower than for the Cr(VI) coating. However, it increases with exposure time during the whole experimental period and it is comparable with the resistance of the Cr(VI) coating after 6 h.

8.4 Discussion

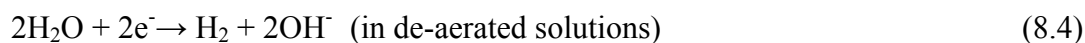
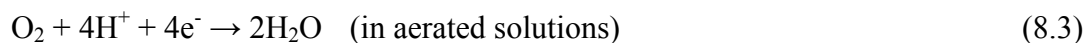
The SEM images show that no cracks have been observed in the Cr(III)-A coating on zinc, but preferentially etched zones are visible, suggesting that the Cr(III)-A coating formation process is influenced by the orientation of individual zinc grains. There are microcracks in the Cr(VI) coatings on zinc, which are attributable to the tensile stresses developed in these coatings during the chromating and drying processes[14,15].

It is easier to form a thicker oxide film on zinc in the Cr(VI) bath than in the Cr(III) baths. Although a thick layer can be formed on zinc in the Cr(III)-B coating bath, within the same dipping time, the Cr(VI) coating grows considerably faster than the Cr(III)-B coating. On the other hand, a thicker Cr(VI) coating tends to crack more easily because the tensile stress inside the coating increases with its thickness [14]. The XPS and the FTIR analyses show that there are both Cr(VI) and Cr(III) species in the Cr(VI) coating, while in the Cr(III) coatings, no Cr(VI) has been detected. The AES depth profiles show that the Cr(III)-A and B coatings both consist of mixed Cr/Zn oxides, and that the content of zinc oxide is more than the content of chromium oxides.

After exposure to 0.01 M NaCl solution, both coatings on zinc discs showed localized corrosion. The corrosion of the Cr(VI) and Cr(III) coated zinc started at flaws such as cracks and pores in these coatings [36].

In near-neutral aerated solution containing Cl^- anions, the corrosion of zinc is controlled by the diffusion of oxygen (see Fig. 8. 13), as reported by other researchers

[32,37,38]. Zinc corrosion in a near-neutral aqueous environment involves the following half-reactions [31,32,39]:



and



The presence of oxygen in the solution accelerates the corrosion by depolarization of the cathodic areas. Without oxygen, the cathodic reaction on zinc is very slow. The current density is much less for the bare zinc in the de-aerated solution than in the aerated solution (see Table 8.3). It is well known that hydrogen evolution on zinc surfaces is slow, because the hydrogen overpotential is very high [40]. Thus, by hindering the transport of oxygen to the zinc surface, the corrosion of zinc can be retarded.

The polarization measurement results show that both Cr(VI) and Cr(III) coatings on zinc can reduce the cathodic current at potentials close to the free corrosion potential. Although the Cr(III)-A coating on zinc discs is much thinner (88 nm) than the Cr(VI) coating (405 nm), the cathodic current measured on this Cr(III)-A coating in the aerated 0.01 M NaCl solution is significantly smaller than the cathodic current measured on the bare zinc surface. The Cr(III)-B coating is thicker than the Cr(III)-A coating on the EG steel, and the polarization resistance of the Cr(III)-B coating is greater than the Cr(III)-A coating. In the 0.6 M NaCl solution, the polarization resistance of the Cr(III)-B coating increases with exposure time within 8 h, and after 6 h, its resistance is comparable with the Cr(VI) coatings with a similar thickness. Acting as a barrier layer, the Cr(III) coatings can hinder the transport of oxygen to the zinc substrate and consequently retard the corrosion of zinc. The impedance measurements also support this idea because the impedance for the Cr(III) coatings is much larger than that for the bare zinc surface.

The inhibition of the corrosion of zinc by the Cr(III)-based coatings, however, is still less effective than that by the Cr(VI) coating (in the studied cases). In the aerated 0.01

M NaCl solution, the cathodic reaction rate for the Cr(VI) coated zinc is much lower than that for Cr(III)-coated zinc. The Cr(VI) coatings contain not only chromium(III) oxides/hydroxides but also Cr(VI) species (see Fig. 8.8 and 8.9). Most of the Cr(VI) species are either adsorbed onto the surface of the chromium(III) oxides or locked into pores in the coating [8,41]. Although microcracks were present in the Cr(VI) coating, the coating was thicker than the Cr(III) coating, and this resulted in an increase of the oxygen diffusion length in the coating. Furthermore, the adsorbed soluble Cr(VI) species in the coating are mobile and can be reduced to Cr(III), $\text{Cr}^{6+} + 3\text{e}^- \rightarrow \text{Cr}^{3+}$. Thus, the Cr(VI) coatings can protect zinc surfaces in several different ways: the trivalent chromium oxide layer acts as a barrier layer and the dissolvable hexavalent chromium in the layer can diffuse to nearby defects and temporarily repair them, which is the so-called “self-healing” effect.

Experimental results show that the mixed potential for the zinc disc moves 250 mV in the positive direction when a small amount of dichromate (0.001M $\text{Na}_2\text{Cr}_2\text{O}_7$) is added to the de-aerated 0.01 M NaCl solution (pH 6) (see Fig. 8.22). The current near the mixed potential is limited to less than $1 \mu\text{A}/\text{cm}^2$. These results suggest that the small amount of dichromate has changed the kinetics of the corrosion of zinc. Once a passive layer has formed on the surface, the access of further anions to the metal is hindered[34].

However, for the Cr(VI) coatings, it is notable that the “self-healing” effect depends on the amount of mobile Cr(VI) species available in the layer. As the Cr(VI) species are consumed, the efficiency of the “self-healing” effect diminishes. The observed increase of the electrochemical impedance of the Cr(VI) coated zinc discs during the first hour of immersion and subsequent decrease may indicate that the duration of the “self-healing” effect is limited.

8.5 Conclusions

Results show that with the same dipping time in the conversion treatment baths, the Cr(VI) coating is thicker than the Cr(III) coatings on zinc. In the surface layer of the Cr(VI) coating, the ratio of Cr(VI) to Cr(III) is about 2:3. No Cr(VI) species are found

in both kinds of Cr(III) coating. The AES depth profiles show that the both Cr(III)-A and B coatings consist of mixed Cr/Zn oxides, and even the content of zinc oxide is more than the content of chromium oxides.

Both the Cr(VI) and Cr(III)-based coatings can retard the cathodic reaction by hindering the transport of oxygen to the substrate metal. Although the Cr(III)-based coating is very thin, its impedance is many times larger than that of the bare zinc surface. The Cr(III)-B coating is thicker than the Cr(III)-A coating on the EG steel, and the polarization resistance of the Cr(III)-B coating is greater than the Cr(III)-A coating. However, for the cases investigated, the Cr(III)-based coatings inhibit the corrosion of zinc in chloride-containing solutions less effectively than Cr(VI) coatings, even when microcracks are present in the Cr(VI) coatings. The different corrosion resistance of the two types of coating is attributed to the difference in the thickness and the availability of Cr(VI) species in the Cr(VI) coatings.

References

1. T. Biestek and J. Weber, *Conversion Coatings*, (Portcullis Press Ltd., Redhill, 1976).
2. H. E. Townsend and R. G. Hart, *J. Electrochem. Soc.*, 131 (1984) 1345.
3. L. Xia, E. Akiyama, G. Frankel and R. McCreery, *J. Electrochem. Soc.*, 147 (2000) 2556.
4. W. E. Pocock, *Metal Finishing*, 52 (1954) 48.
5. M. Kendig and S. Jeanjaquet, *J. Electrochem. Soc.*, 149 (2002) B47-B51.
6. J. Zhao, L. Xia, A. Sehgal, D. Lu, R. L. McCreery and G. S. Frankel, *Surf. Coat. Technol.*, 140 (2001) 51.
7. E. Akiyama, A. J. Markworth, J. K. McCoy, G. S. Frankel, L. Xia and R. L. McCreery, *J. Electrochem. Soc.*, 150 (2003) B83-B91.
8. M. Kendig, R. Addison and S. Jeanjaquet, *J. Electrochem. Soc.*, 146 (1999) 4419.
9. P. C. Wynn and C. V. Bishop, *Trans IMF*, 79 (2001) B27-B30.
10. C. Barnes, J. J. B. Ward, T. S. Sehmbhi and V. E. Carter, *Trans IMF*, 60 (1982) 45.
11. A. Gardner and J. Scharf, *Soc. Automot. Eng.*, [Spec. Publ.], SP-1614 (2001) 91.
12. P. Campestrini, S. Bohm, T. Schram, H. Terryn and J. H. W. de Wit, *Thin Solid Film*, 410 (2002) 76.
13. T. Schram, J. De Laet and H. Terryn, *Thin Solid Film*, 313-314 (1998) 727.
14. N. M. Martyak, *Surf. Coat. Technol.*, 88 (1996) 139.
15. X. Zhang, C. van den Bos, W. G. Sloof, H. Terryn, A. Hovestad and J. H. W. de Wit, in: *Corrosion science in the 21st century*, Manchester, UK, 7-11 July, 2003; B. Cottis (Ed.), *J. Corros. Sci. Engineering*, Vol. 6, paper 57 (2003) (ISSN 1466-8858).
16. X. Zhang, S. Böhm, A. J. Bosch, E. P. M. van Westing and J. H. W. de Wit, *Materials and Corrosion*, 55 (2004) 501.
17. A. E. Hughes and R. J. Taylor, *Surf. Interface Anal.*, 25 (1997) 223.
18. J.-O. Nilsson, S.-E. Hörnström, E. Hedlund, H. Klang and K. Uvdal, *Surf. Interface Anal.*, 19 (1992) 379.
19. B. S. Norgren, M. A. J. Somers, W. G. Sloof and J. H. W. de Wit, in: *12th Scandinavian Corrosion Congress & Eurocorr '92*, 1992; P. J. Tunturi (Ed.), 1 (The Corrosion Society of Finland, Espoo, Finland, 1992) pp. 139-149.
20. R. A. Nyquist and R. O. Kagel, *Infrared spectra of inorganic compounds*, (Academic Press, Inc, New York, 1971).
21. M. Lenglet, F. Petit and J. Y. Malvaut, *Phys. Stat. Sol. (a)*, 143 (1994) 361.
22. M. Handke, A. Stoch, S. Sulima, P. L. Bonora, G. Busca and V. Lorenzelli, *Mater. Chem.*, 7 (1982) 7.

23. F. Petit, H. Debontride, M. Lenglet, G. Juhel and D. Verchere, *Appl. Spectroscopy*, 49 (1995) 207.
24. J. Kasparek and M. Lenglet, *La Revue de Métallurgie - CIT*, 94 (1997) 713.
25. J. T. Vandenberg, D. G. Anderson, J. K. Duffer, J. M. Julian, R. W. Scott, T. M. Sutliff and M. J. Vaickus, *An infrared spectroscopy atlas for the coatings industry*, (Federation of Societies for Coating Technology, Philadelphia, 1980).
26. E. Gileadi, E. Kirowa-Eisner and J. Penciner, *Interfacial Electrochemistry*, (Addison-Wesley Publishing Co. Inc., 1975).
27. R. G. Kelly, J. R. Scully, D. W. Shoesmith and R. G. Buchheit, *Electrochemical Techniques in Corrosion Science and Engineering*, (Marcel Dekker, Inc., New York, 2003).
28. *Handbook of Chemistry and Physics*, 56 ed., (CRC Press, Inc., USA, 1975).
29. V. Barranco, S. Feliu Jr and S. Feliu, *Corros. Sci.*, 46 (2004) 2203.
30. B. R. W. Hinton and L. Wilson, *Corros. Sci.*, 29 (1989) 967.
31. L. Fedrizzi, L. Ciaghi, P. L. Bonora, R. Fratesi and G. Roventi, *J. Appl. Electrochem.*, 22 (1992) 247.
32. X. G. Zhang, *Corrosion and Electrochemistry of Zinc*, (Plenum Press, New York, 1996).
33. C. Cachet and R. Wiart, *J. Appl. Electrochem.*, 20 (1990) 1009.
34. W. J. Clark and R. L. McCreery, *J. Electrochem. Soc.*, 149 (2002) B379-B386.
35. J. F. Moulder, W. F. Stickle, P. E. Sobol and K. D. Bomben, *Handbook of X-ray photoelectron spectroscopy*, (Perkin-Elmer Corp., 1992).
36. N. M. Martyak, J. E. McCaskie and L. Harrison, *Metal Finishing*, 94 (1996) 65.
37. S. Turgoose, in: *Chemical inhibitors for corrosion control*, B. G. Clubley (Ed.), The Royal Society of Chemistry, Manchester, 1990.
38. D. C. H. Nevison, in: *ASM Handbook*, 9th ed., ASM International, Materials Park, Ohio, 1987, Vol. 13.
39. L. M. Baugh, *Electrochim. Acta*, 24 (1979) 657.
40. U. R. Evans, *The corrosion and oxidation of metals*, (Edward Arnold Ltd., London, 1960).
41. P. McCluskey, *Trans IMF*, 74 (1996) 119.

Chapter 9

Salt Spray Testing of Cr(VI) and Cr(III) Treated Zinc

9.1 Introduction

The salt spray (fog) test is one of the most widely used accelerated test methods for evaluating the corrosion protection provided by coatings on metals [1-3]. The intent of the salt spray test is to compare the relative corrosion resistance of specimens or evaluate the differences between a test sample and a part that has been previously tested and shown to provide satisfactory service [1]. This test has many advantages such as standardized protocols (ASTM B117 [4], DIN 50021 [5]) for conducting the exposure and evaluating the results, simple procedure and the ability to discriminate. Although there is a lack of evidence that this test gives consistent reproducible results from one test chamber to another and one time to another, the test is continuously used since this is the standard that has been accepted by the industry for severe corrosion testing, and it has been used historically for this purpose[6].

In the work described in this chapter, Cr(VI)-based coatings with different dipping times and Cr(III)-based coatings have been investigated using the neutral salt spray test according to the standard DIN 50021 method. The aim is to compare the durability of these coatings in a salt fog.

9.2 Experimental

Pure zinc (99.95%) sheets were cut into 10×5 cm pieces. The specimens were ultrasonically cleaned in ethanol for 2 min. The surfaces were activated in 0.25% nitric acid for 30 s and rinsed in de-ionized water. The specimens were then treated in Cr(VI)

bath (see chapter 5) with dipping time of 1, 5, 10 or 60 s, and in Cr(III)-A or Cr(III)-B bath with dipping time 60 s (see chapter 8). The details of these treatments are described in Table 9.1.

Table 9.1 Details of the samples treated in Cr(VI), Cr(III)-A and Cr(III)-B baths.

Sample code	Treatment	Dipping time (s)
1	Cr(VI)	1
2	Cr(VI)	1
3	Cr(VI)	1
4	Cr(VI)	5
5	Cr(VI)	5
6	Cr(VI)	5
7	Cr(VI)	10
8	Cr(VI)	10
9	Cr(VI)	10
10	Cr(VI)	60
11	Cr(VI)	60
12	Cr(VI)	60
13	Cr(III)-B (Permapass 7012)	60
14	Cr(III)-B (Permapass 7012)	60
15	Cr(III)-B (Permapass 7012)	60
16	Cr(III)-A (Permapass 3K Immunox)	60

The neutral salt spray testing of these treated samples was performed in the laboratory of TNO in Eindhoven according to the DIN 50021 protocol [5]. The samples were exposed to a 5% NaCl (pH 6.5) fog in a salt spray chamber at 35°C for 483 hours. The coverage of the sample surfaces by the white corrosion products was recorded.

9.3 Results and discussion

The percentage of the surfaces covered with white corrosion products are shown in Table 9.2. White corrosion products were first observed, after 23 hours, on the surfaces of the samples treated with Cr(III) baths, and on the Cr(VI)-treated specimens with dipping time 1 s (see Fig. 9.1). More than 5% of the surface area was covered with white rust after 23 hours for the sample treated in the Cr(III)-A bath. After 45 hours, white rust covered more than 5% of the surface areas of the samples treated in the Cr(III)-B bath or in the Cr(VI) bath with dipping time 1s.

Table 9.2 Results of the salt spray test for the Cr(VI), the Cr(III)-A and the Cr(III)-B treated zinc.

Sample code	23 hrs	45 hrs	73 hrs	203 hrs	231 hrs	483 hrs
1	<1 %*	1-5 %	5 %	10 %	10 %	80 %
2	<5 %	5-10 %	20 %	50 %	50 %	80 %
3	5-10 %	5-10 %	20 %	50 %	50 %	80 %
4	0 %	0 %	0 %	0 %	1-5 %	< 5 %
5	0 %	0 %	0 %	0 %	1 %	1-5 %
6	0 %	0 %	0 %	<1 %	1-5 %	5 %
7	0 %	0 %	0 %	0 %	0 %	0 %
8	0 %	0 %	0 %	0 %	0 %	< 1 %
9	0 %	0 %	0 %	0 %	0 %	0 %
10	0 %	0 %	0 %	0 %	0 %	0 %
11	0 %	0 %	0 %	0 %	0 %	0 %
12	0 %	0 %	0 %	0 %	0 %	0 %
13	5 %	5-10 %	10 %	30 %	30 %	50 %
14	1%	5 %	5 %	5-10 %	5-10 %	30 %
15	5 %	5-10 %	10 %	40 %	40 %	50 %
16	5-10 %	5-10 %	20 %	25 %	25 %	60 %

* % = percentage of the surface covered with white corrosion products.

For the Cr(VI) treated samples with dipping time 5s, the white rust was observed on the surface after 231 hours. For the samples treated in the Cr(VI) bath for 10 or 60 s, no difference was found after exposure in the salt fog for 203 hours and even after 483 hours (see Figs. 9.2 and 9.3).

These salt spray testing data indicate that the Cr(III)-B treated zinc (60 s) has higher corrosion resistance than the Cr(III)-A treated zinc (60 s), but lower resistance than the Cr(VI) treated zinc with a shorter dipping time (5 s). This result is qualitatively consistent with the results obtained from the EIS measurements (presented in chapter 8). It confirms that the Cr(VI) treatments are more effective than the Cr(III) treatments in protecting zinc against corrosion.

For the Cr(VI) treated zinc samples, the corrosion resistance increases with the dipping time from 1 to 10 seconds. However, when the dipping time increases from 10 to 60 seconds not much difference can be observed. In chapter 5, the EIS measurements showed that the polarization resistance for the Cr(VI) treated zinc with dipping time 60 s is lower than that with dipping time 5 s. It has to be mentioned that there are some differences between the two different measurement techniques. In the EIS measurements described in chapter 5, first of all, zinc sheets were polished before doing Cr(VI) treatments, while here in the salt spray test, the zinc sheets were not polished before doing the Cr(VI) treatments, which may affect the formation of the layer. Secondly, the test solution is less concentrated (0.01 M NaCl) than the solution used in the salt spray test (5% NaCl). Furthermore, in the EIS measurements the sample surface is exposed to the bulk solution, and the impedance measurement is very sensitive to the defects in the coatings since the sample is connected with an external electrical circuit, while in the salt spray test the sample surfaces are exposed in a salt fog and there is no external circuit connected to the sample. So, some difference between the results obtained from the two different tests is to be expected.



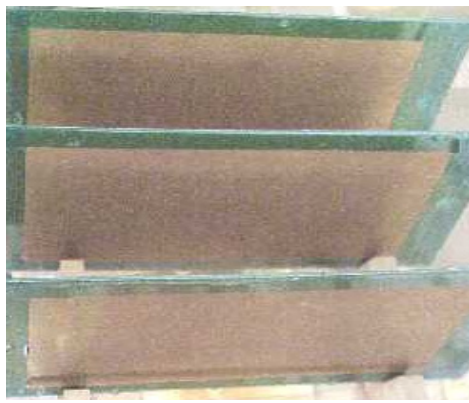
(a) Samples 1-3 (Cr(VI) 1 s)



(b) Samples 4-6 (Cr(VI) 5 s)



(c) Samples 7-9 (Cr(VI) 10 s)



(d) Samples 10-12 (Cr(VI) 60 s)



(e) Samples 13-15 (Cr(III)-B 60 s)

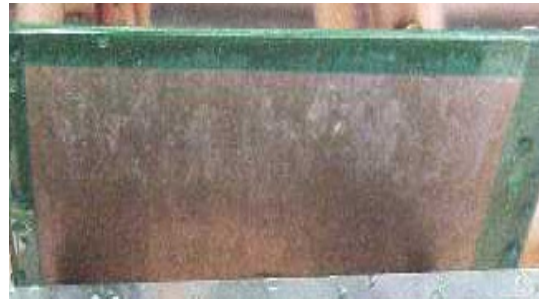


(f) Sample 16 (Cr(III)-A 60 s)

Fig. 9.1 Samples after 23 hours salt fog exposure. Cr(VI)-treated samples with dipping time (a) 1 s, (b) 5 s, (c) 10 s, (d) 60 s; (e) the Cr(III)-B treated samples (60 s) and (f) a Cr(III)-A treated sample (60 s).



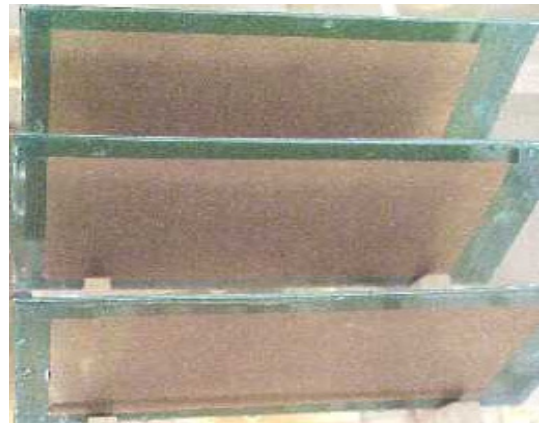
(a) Samples 2-3 (Cr(VI) 1 s)



(b) Sample 5 (Cr(VI) 5 s)



(c) Sample 9 (Cr(VI) 10 s)



(d) Samples 10-12 (Cr(VI) 60 s)



(e) Samples 14 (Cr(III)-B 60 s)



(f) Sample 16 (Cr(III)-A 60 s)

Fig. 9.2 Samples after 203 hours salt fog exposure. Cr(VI)-treated samples with dipping time (a) 1 s, (b) 5 s, (c) 10 s, (d) 60 s; (e) Cr(III)-B treated samples (60 s) and (f) a Cr(III)-A treated sample (60 s).



(a) Samples 1-3 (Cr(VI) 1 s)



(b) Samples 4-6 (Cr(VI) 5 s)



(c) Samples 8-9 (Cr(VI) 10 s)



(d) Samples 10-11 (Cr(VI) 60 s)



(e) Samples 13-15 (Cr(III)-B 60 s)



(f) Sample 16 (Cr(III)-A 60 s)

Fig. 9.3 Treated samples after 483 hours salt fog exposure. Cr(VI)-treated samples with dipping time (a) 1 s, (b) 5 s, (c) 10 s, (d) 60 s; (e) Cr(III)-B treated samples (60 s) and (f) a Cr(III)-A treated sample (60 s).

9.4 Conclusions

From the results described above, we can conclude that the corrosion resistance of Cr(III)-B treated zinc (60 s) in the salt fog environment is better than the Cr(III)-A treated zinc (60 s), but worse than the Cr(VI) treated zinc (5, 10, or 60 s), which is qualitatively in agreement with the results obtained from EIS measurements and presented in chapter 8. For the Cr(VI) treated zinc, the corrosion resistance in the salt fog environment increases with the dipping time from 1 s to 10 s. Not much difference in corrosion resistance was found between the samples treated in the Cr(VI) bath with dipping time of 10 s and 60 s after 483 hours exposure to the salt fog.

References

1. F. Altmayer, *Plat. and Surf. Fin.*, 72 (1985) 36.
2. D. Gilroy, P. J. Eddowes, I. M. Dalrymple, V. Madina, F. Seco, A. del Barrio, J. Parkes, M. Byrne, R. Byrne and E. M. Almeida, *Metal Finishing*, 94 (1996) 14.
3. R. G. Buchheit, M. Cunningham, H. Jensen, M. W. Kendig and M. A. Martinez, *Corrosion*, 54 (1998) 61.
4. *ASTM B 117-90 "Standard Method of Salt Spray (Fog) Testing"*, (Philadelphia, PA; ASTM, 1992).
5. DIN Deutsches Institut für Normung, *DIN 50021*, in: *Korrosion und Korrosionsschutz*, (Berlin, 2003).
6. B. R. Appleman, *J. Coat. Technol.*, 62 (1990) 57.

Chapter 10

General discussion

10.1 The corrosion of zinc

Zinc and its alloys oxidize easily in air to form a layer of zinc oxide/hydroxide during natural dry and wet processes. Zinc oxide/hydroxide reacts with CO₂ and atmospheric pollutants to form different corrosion products. Although some corrosion products formed on zinc surfaces may supply protection, this protection is limited, especially when exposed to an industrial or marine environment. The corrosion products could be dissolved and washed away from the zinc surface.

Zinc corrodes actively when exposed to an aqueous environment like a solution containing Cl⁻. The corrosion of zinc is an electrochemical process that involves an anodic reaction like zinc being oxidized to zinc cations, and a cathodic reaction such as oxygen reduction, water or hydrogen ion reduction. According to the charge conservation law the electrons given by zinc atoms should be equal to the electrons obtained by the oxidizing agents. The two reaction rates should be the same. The slowest reaction will control the whole process. Polarization measurements performed in this work showed that zinc corrosion is controlled by oxygen diffusion in neutral NaCl solution (see chapters 5 and 8). A localized corrosion morphology has been observed in this solution, since zinc oxide/hydroxide deposited near the corrosion sites. The corrosion products deposited on the zinc surface are a mixture of zinc hydroxide and chloride, which has been determined by means of XRD.

So, it is possible to decrease the corrosion rate of zinc by depressing the cathodic reaction, and surface treatments such as conversion coating and painting can provide protection to zinc or zinc coatings from corrosion.

10.2 Inhibition effect of Cr(III) and Cr(VI)-based conversion coatings

Chromate conversion coating (CCC) is one of the most effective treatments, which provides more corrosion resistance and increases the adhesion between primer coatings and metal substrates. However, the toxic hexavalent chromium used in the treatment is on the list of substances whose use will be forbidden in the near future. In the last few decades, many scientists have been involved in searches for alternatives to chromates and valuable results have been obtained, but a coating chemistry and technology for replacing chromate conversion in all applications still does not exist. The CCC is so effective that a thorough understanding of the mechanism of the CCC is necessary and this knowledge will be helpful in searching for alternatives to chromate treatments.

With this objective, Cr(VI) and Cr(III) based conversion coatings on zinc and electro-galvanized steel have been investigated in this PhD project. The morphology, structure, composition and corrosion performance of these coatings have been investigated using different surface analytic techniques combined with electrochemical measurements. Attention has been paid to analyzing the concentration of the Cr(VI) in the surface layer using XPS, since the Cr(VI) plays a vital role in the “self-healing” of flaws in Cr(VI) coatings.

For the Cr(VI)-based coatings on zinc, AES depth profiles show that chromium oxides are the main components in the coatings, while zinc oxide is mainly located at the interface between the chromium oxides and the zinc substrate (see chapters 4 and 8). In chapter 4, XPS and FTIR analyses show that the chromate layer contains both insoluble Cr(III) oxides/hydroxides and Cr(VI) species. It has been found that the concentration of Cr(VI) varies from 32 to 42% of the total chromium in the outermost layer of the coating when the dipping time changes from 1 s to 60 s. The concentration of Cr(VI) deeper in the coating layer was not investigated since the X-ray radiation and Ar ion sputtering would reduce chromium from +6 oxidation state to lower oxidation state. Numerous reports have shown that most of Cr(VI) species are adsorbed on to the surface of the insoluble Cr(III) oxides/hydroxides, either on the outer surface or within the pores in the coating[1-4].

The Cr(III) oxides/hydroxides in the coatings are inert, and can inhibit electron transfer, hinder the transport of oxygen to the zinc substrate and consequently cathodically inhibit the corrosion of zinc. In chapters 7 and 8, the Volta potential measurements and polarization measurements have shown that the Cr(III)-based coatings can decrease the corrosion current of zinc by inhibiting the cathodic reaction.

Polarization and EIS measurements performed in this work have indicated that the corrosion protection provided by the Cr(VI) coating is more effective than by the two types of Cr(III) coatings. The Cr(VI) species in the Cr(VI)-based coating play an important role in inhibition of the corrosion of zinc. In chapter 4, XPS analysis demonstrated that the concentration of Cr(VI) in the outermost layer increased slightly with the dipping time. The dissolution and reduction of the Cr(VI) from the coating has been observed by the XPS measurements after immersion of the Cr(VI)-coated zinc in 0.01 M NaCl solution for 24 h.

The impedance measurements (in chapter 5) show that the corrosion resistance decreased with the dipping time (longer than 10 s), because of the microcracks in the coatings which increase visibly with the dipping time. The impedance measured for the Cr(VI)-based coatings in the 0.01 M NaCl solution showed that the coating with dipping time of 5 seconds had the greatest corrosion resistance during the measurements (16 h), which indicates that the morphology of the coating is also important. The dipping time of one second may be too short to develop a layer covering the whole zinc surface, while if the dipping time is longer than 10 seconds the layer develops more microcracks during the drying process, since the tensile stress in the coating increases with the thickness of the coating [5]. So, although the adsorbed Cr(VI) species in the coatings may diffuse to and passivate some defect sites, the corrosion resistance of these coatings is not great enough. This indicates that thicker conversion coatings do not necessarily provide more corrosion protection.

The “self-healing” role of Cr(VI) species in the coatings has been demonstrated in chapter 6 using polarization measurements for the Cr(VI) coatings (with dipping time 10 seconds) on electro-galvanized steel dried at different temperatures. The concentration of Cr(VI) in the outermost layer decreased when the coatings were dried at a temperature above 60°C, determined by means of XPS. The polarization

measurements showed that only the coatings dried at a lower temperature (60°C) had significant passivity in de-aerated 3.5% NaCl solution, while the coatings dried at 110 or 210°C did not show passivity [6]. This indicates that the soluble Cr(VI) species adsorbed in the coating have the capability of passivating the zinc surface exposed to the solution.

This passivating capability of oxo-Cr(VI) has been further demonstrated in chapter 8. The cathodic polarization measurements show that the corrosion potential of zinc moved in the positive direction about 250 mV and the corrosion current density near the corrosion potential decreased to 10^{-6} A/cm² in de-aerated 0.01 M NaCl solution after adding 0.001 M sodium dichromate to the solution. XPS analyses showed that chromium oxides/hydroxides had already formed on the zinc surface when the measurements stopped at -1.01 V_{SCE}. These results suggest that the small amount of dichromate added to the solution has changed the kinetics of the corrosion of zinc: the zinc surface has become more noble than before. Moreover, indirect evidence for the role played by Cr(VI) is given by the EIS measurements, which showed that the impedance of the Cr(VI) treated zinc disc in aerated 0.01 M NaCl solution increased after 1 hour and then decreased after 1.5 hours exposure, while for the Cr(III)-A treated zinc it decreased with time.

The “self-healing” effect of Cr(VI)-based coatings has been demonstrated by many researchers by exposing coatings with artificial defects (scratches in the coating) to a salt fog. Cr(VI) coatings showed little corrosion product at the scratches, while other scratched coatings showed more corrosion products at the scratches [7]. The mechanism of self-healing exhibited by CCC films has been reported by Zhao and Frankel et al.[8]. An “artificial scratch” cell was made by placing a polished and untreated aluminium alloy sample close to a CCC-coated sample, with a 1.8 mm thick layer of 0.1 M NaCl solution. Micrographs indicated that the initially untreated alloy was protected by the presence of a CCC film. XPS measurement demonstrated that chromium in some form had been released and had deposited on an initially untreated aluminium alloy sample, which was put on the top of a CCC-treated sample and immersed in 0.1 M NaCl for 20 h. Formation of a Cr(VI)-containing deposit observable by Raman spectroscopy was more rapid in or near pits in the untreated alloy sample and the deposit was similar in spectroscopy to the original CCC film.

The soluble oxo-Cr(VI) anions are strong oxidizing agents. When a very small amount of oxo-Cr(VI) anions is added to the solution, the chromium(VI) can be reduced to chromium(III) and form Cr(III)-oxides/hydroxides which can precipitate on the metal surface. The corrosion of the metal would then be inhibited. Clark et al.[9,10] have examined the oxygen reduction reaction on copper, platinum, and glassy carbon electrodes, with regard to its inhibition by exposure of the electrode to Cr(VI)-oxo anions in NaCl solution. Their work showed that all three electrodes exhibited a mass transport limited current for the oxygen reduction reaction at sufficiently negative potentials, but this current was strongly inhibited in the presence of Cr(VI). This inhibition persisted in Cr(VI)-free solution after the electrode was rinsed thoroughly, indicating that Cr(VI) formed an irreversibly adsorbed inhibiting layer. The mechanism of inhibition involves a reduction and irreversible adsorption of Cr(III) to the surface of electrode, possibly followed by a second layer of adsorbed Cr(VI). Then the sites of adsorption are blocked. Once adsorption sites are blocked, oxygen adsorption is prevented [5].

Thus, the work carried out in this study and work performed by other researchers indicate that Cr(VI)-based coatings can protect zinc surfaces in two ways: the trivalent chromium oxide layer acts as a barrier layer and the dissolvable hexavalent chromium in the layer can diffuse to nearby defects and temporarily repair them, which is the so-called “self-healing” effect. Results from many different experiments and techniques support this conclusion.

10.3 Topics for future research

The results obtained in this work show that Cr(III)-based coatings are promising alternatives to the Cr(VI) treatment. Cr(III) treatments are easy to apply on zinc and its alloys and are commercially acceptable. Cr(III)-based treatments are especially suitable if self-healing is less important, for instance when the main function of the treatment is to improve the adhesion of paints or polymer coatings. It may be difficult to develop an alternative conversion treatment which performs as well as Cr(VI) treatment in all

applications. For some applications, it may be necessary to apply two or more treatments and rely on their synergistic effects.

This work has investigated only the corrosion properties of the Cr(VI) and the Cr(III) treated zinc without painting. The corrosion behavior of the painted system may be different. A comparison of the corrosion behavior of the Cr(VI) and Cr(III)-treated zinc with a top paint may give more insights into the performance of these conversion coatings. On this topic, the scanning vibrating electrode technique (SVET) in the corrosion laboratory at TU Delft can be employed to map the current density around the scratches (artificial defects in painted systems). SVET has already been successfully used in characterizing chromated-epoxy primer on steel and aluminum [11], and in studying the photo-degradation at metallic cut edges of organic coated galvanized steel [12].

As described in chapter 5, XPS is very powerful in analyzing the composition of a surface layer, especially in getting information about the chemical states of elements on the surface. However, using this technique to analyze a Cr(VI)-based conversion coating has some drawbacks. First of all, putting a Cr(VI)-coated zinc sample in a vacuum chamber will dehydrate the coating, since the Cr(VI)-based conversion coating contains water, which causes errors in analyzing the composition. Secondly, Cr(VI) species in a coating are easily reduced to species of lower valence under X-ray radiation which makes a precisely quantitative analysis of Cr(VI) in the coating impossible. Thirdly, ex-situ analysis and accelerated corrosion tests may not reflect the real situation of the formation and degradation of a conversion coating. So, an in-situ monitor of the composition change during the formation and degradation of the Cr(VI) and Cr(III)-based conversion coating on zinc may be more interesting.

In doing in-situ experiments, Raman spectroscopy and X-ray absorption near edge structure (XANES) are two possible choices, since both of them can distinguish Cr(VI) from Cr(III) species and can be used in air[13,14]. However, using Raman spectroscopy to analyze Cr(III) species in the conversion coating has its limitation in resolution. It was reported that Cr(III) species are not easily distinguishable in the presence of strong Raman scatterers, such as Cr(VI) species, since Cr(III) species are not strong scatterers [14,15]. XANES has been used successfully to study the mechanism of inhibition by

CCCs [16]. In XANES analysis the sample is also under radiation of X-ray, but the cross section for damage due to X-ray irradiation is inversely proportional to the $7/2$ power of the incident photon energy (i.e. $E_i^{7/2}$)[17]. The energy used in XANES analysis is almost 4.8 times that of Mg K_α X-radiation, but the damage cross section for XANES is 237 times less than that for Mg K_α XPS analysis[13]. The drawback of this technique is that information can only be obtained over the whole thickness probed, without any depth resolution[18]. In studying how a conversion coating forms on a metal, using a difference viewer imaging technique (DVIT) may be helpful to observe the nucleation and growth of a conversion layer.

References

1. M. Kendig, R. Addison and S. Jeanjaquet, *J. Electrochem. Soc.*, 146 (1999) 4419.
2. H. E. Townsend and R. G. Hart, *J. Electrochem. Soc.*, 131 (1984) 1345.
3. L. Xia and R. L. McCreery, *J. Electrochem. Soc.*, 145 (1998) 3083.
4. L. Xia, E. Akiyama, G. Frankel and R. McCreery, *J. Electrochem. Soc.*, 147 (2000) 2556.
5. N. M. Martyak, *Surf. Coat. Technol.*, 88 (1996) 139.
6. X. Zhang, S. Böhm, A. J. Bosch, E. P. M. van Westing and J. H. W. de Wit, *Materials and Corrosion*, 55 (2004) 501.
7. O. Kachurina, T. L. Metroke, E. Stesikova and E. T. Knobbe, *J. of Coatings Technol.*, 74 (2002) 43.
8. J. Zhao, G. Frankel and R. McCreery, *J. Electrochem. Soc.*, 145 (1998) 2258.
9. W. J. Clark, J. D. Ramsey, R. L. McCreery and G. S. Frankel, *J. Electrochem. Soc.*, 149 (2002) B179-B185.
10. W. J. Clark and R. L. McCreery, *J. Electrochem. Soc.*, 149 (2002) B379-B386.
11. J. He, V. J. Gelling, D. E. Tallman and G. P. Bierwagen, *J. Electrochem. Soc.*, 147 (2001) 3661.
12. S. Böhm, H. N. McMurray, S. M. Powell and D. A. Worsley, *Electrochim. Acta*, 45 (2000) 2165.
13. G. P. Halada and C. R. Clayton, *J. Electrochem. Soc.*, 138 (1991) 2921.
14. J. Zhao, L. Xia, A. Sehgal, D. Lu, R. L. McCreery and G. S. Frankel, *Surf. Coat. Technol.*, 140 (2001) 51.
15. J. Ramsey and R. McCreery, *J. Electrochem. Soc.*, 146 (1999) 4076.
16. M. W. Kendig, A. J. Davenport and H. S. Isaacs, *Corros. Sci.*, 34 (1993) 41.
17. L. C. Feldman and J. W. Mayer, *Fundamentals of Surface and Thin Film Analysis*, (North-Holland, New York, 1986).
18. S. Virtanen, P. Schmuki and H. S. Isaacs, *Electrochim. Acta*, 47 (2002) 3117.

Summary

With the aim of understanding the protective mechanism of chromate conversion coatings (CCCs) and searching for alternatives to chromate treatments, the physical natures and the corrosion properties of Cr(VI) and Cr(III) treated zinc have been investigated in this PhD project.

This PhD thesis is composed of three parts. The first part contains literature surveys of corrosion of zinc (in chapter 2) and conversion coatings (in chapter 3). The second part (chapters 4-6) covers physical and electrochemical characterization of the Cr(VI)-based conversion coatings on zinc. The third part (chapters 7-9) investigates Cr(III)-based coatings and compares the corrosion properties of Cr(VI) and Cr(III)-based coatings.

In chapter 4, the morphology, the thickness and the composition of Cr(VI) coatings on zinc sheets with different dipping times (1, 5, 10, 30 and 60 s) in the Cr(VI) bath have been investigated by means of SEM, spectroscopic ellipsometry, AES, XPS and FTIR. The results show that the thickness of the layer increases with dipping time in the bath. The microcracks appear in the coatings if the dipping time reaches 10 s or longer, and the width of the cracks increases with the dipping time. AES depth profiles show that chromium oxides are the main components in the Cr(VI) coatings. Zinc oxide is mainly located at the interface between the chromium oxides and the zinc substrate. The outermost layer of Cr(VI) coatings is composed of both Cr(VI) and Cr(III) compounds. The concentration of Cr(VI) to Cr(III) is about 2:3, determined by means of XPS. After immersion in the 0.01 M NaCl solution for 24 h, the relative amount of Cr(VI) has decreased.

In chapter 5, the corrosion behavior of untreated zinc and Cr(VI) treated zinc with different dipping times has been studied using polarization and electrochemical impedance measurements in 0.01 M NaCl solution. Zinc is very active when it is exposed to 0.01 M NaCl solution. The corrosion rate of zinc is controlled by oxygen diffusion process. The Cr(VI) treatments significantly decrease the corrosion rate of

zinc in the solution. The corrosion of Cr(VI) coated zinc starts at flaws such as pores and cracks in the coating and then propagates deeply and laterally, until the chromate coating collapses.

It is clear that the morphology of the coatings does affect the corrosion behavior of the system. Among the Cr(VI) treated zinc sheets with different dipping times, the corrosion resistance decreases in the following order: R_p (ZnCr5s) > R_p (ZnCr1s) > R_p (ZnCr10s) > R_p (ZnCr30s) > R_p (ZnCr60s), in the 0.01 M NaCl solution during the measurements (16 h). The coating with dipping time of 5 s has fewer flaws (cracks) so that the coating has greater corrosion resistance than other coatings.

In chapter 6, the effect of the drying temperature on Cr(VI) coatings on zinc and on electrogalvanized steel with dipping time of 10 s has been investigated. The drying process has a significant effect on the coating morphology and the corrosion performance of Cr(VI) coatings in NaCl solutions. Drying at a high temperature (210°C) makes chromate coatings hard, but on the other hand, it will reduce the “self-healing” effect of the soluble Cr(VI) species. The thermal reduction of Cr(VI), detected by FTIR and XPS, is probably responsible for the decrease of the Cr(VI) content of the layer. A favorable drying temperature for the chromate treated electro-galvanized steel is between 60 and 110°C.

The corrosion properties of Cr(VI) and Cr(III) coatings have been compared in chapters 7 and 8. If the zinc specimen is treated in a Cr(VI) or Cr(III)-A solution, the Volta potential in the Cr(VI) or Cr(III)-A treated zinc area is more negative than the untreated zinc area. Open circuit potential measurements also show negative potentials of the Cr(VI) and the Cr(III)-A coatings against untreated zinc. This indicates that both the Cr(VI) and the Cr(III)-A coatings can inhibit the cathodic reaction. The polarization and impedance measurements show that both the Cr(VI) and Cr(III) coatings can decrease the corrosion rate of zinc. The Cr(III)-B coating is thicker than the Cr(III)-A coating, and its corrosion resistance is greater than that of the Cr(III)-A coating. However, the inhibition of the corrosion of zinc by Cr(VI) coating is more effective than by the Cr(III) coatings, since the Cr(III) based coatings act just as barrier layer, while the Cr(VI) coatings can protect zinc surfaces in two ways: as a barrier layer and as a passivating inhibitor (“self-healing”) effect. Cr(III)-based treatments may be suitable

if self-healing is less important, for instance when the main function of the treatment is to improve the adhesion of paints or polymer coatings. For some applications, it may be necessary to apply two or more treatments and rely on their synergistic effects.

Samenvatting

In dit promotie-onderzoek zijn de fysische eigenschappen en de corrosie-eigenschappen van met Cr(VI) en Cr(III) behandeld zink onderzocht met als doel het begrijpen van het beschermingsmechanisme van chromaat conversielagen (CCCs) en een alternatief te zoeken voor chromaat behandelingen.

Het proefschrift bestaat uit drie delen. Het eerste deel bevat een overzicht van de literatuur over de corrosie van zink (hoofdstuk 2) en conversielagen (hoofdstuk 3). Het tweede deel (hoofdstukken 4-6) behandelt de fysische en elektrochemische karakterisering van de Cr(VI) conversielagen op zink. In het derde (hoofdstukken 7-9) worden op Cr(III) gebaseerde deklagen bestudeerd en worden de corrosie-eigenschappen van op Cr(VI) en Cr(III) gebaseerde deklagen vergeleken.

In hoofdstuk 4 zijn de morfologie, de laagdikte en de samenstelling van de Cr(VI) deklagen op platen zink bij verschillende dompeltijden (1, 5, 10, 30 en 60 s) onderzocht met behulp van SEM, ellipsometrie, AES, XPS en FTIR. De resultaten laten zien dat de laagdikte toeneemt met toenemende dompeltijden. Microscheuren verschijnen als de dompeltijd langer dan 10 seconden is en de breedte van de scheuren neemt toe bij langere dompeltijden. AES diepteprofielen laten zien dat chromoxides de hoofdcomponent van de Cr(VI) deklagen vormen. Zinkoxide komt voornamelijk op het grensvlak tussen de chromoxides en het zinksubstraat voor. De bovenste laag van de Cr(VI) deklagen bestaat uit zowel Cr(VI) als Cr(III) verbindingen. Met XPS is bepaald dat de concentratie van Cr(VI) en Cr(III) zich ongeveer verhoudt als 2:3. Relatief gezien neemt de hoeveelheid chroom, voornamelijk Cr(VI) af na onderdompelen in 0.01M NaCl oplossing gedurende 24 uur.

In hoofdstuk 5 is het corrosiegedrag van onbehandeld en met Cr(VI) behandeld zink met verschillende dompeltijden bestudeerd met behulp van polarisatiemetingen en electrochemische impedantie spectroscopie in 0.01M NaCl oplossingen. Zink is zeer (re)actief wanneer het wordt blootgesteld aan 0.01M NaCl oplossing. De corrosiesnelheid van zink wordt bepaald door de diffusie van zuurstof. De Cr(VI)

behandeling vermindert de corrosiesnelheid van zink in de oplossing significant. De corrosie van met Cr(VI) bedekt zink begint op fouten in de deklaag zoals poriën en barsten en verspreidt zich in de diepte en over de breedte totdat de chromaat deklaag bezwijkt.

Het is duidelijk dat de morfologie van de coatings het corrosiegedrag van het systeem beïnvloedt. De corrosieweerstand in 0.01M NaCl oplossing gedurende de metingen (16 uur) van zinken platen behandeld met Cr(VI) met verschillende dompeltijden neemt af volgens: R_p (ZnCr5s) > R_p (ZnCr1s) > R_p (ZnCr10s) > R_p (ZnCr30s) > R_p (ZnCr60s). De deklaag met dompeltijd van 5s heeft minder fouten (barsten), waardoor deze deklaag een hogere corrosieweerstand heeft dan de andere deklagen.

In hoofdstuk 6 is het effect van de droogtemperatuur op Cr(VI) deklagen op zink en op gegalvaniseerd staal met dompeltijden van 10s onderzocht. De invloed van het droogproces op de morfologie van de deklaag en op het corrosiegedrag van Cr(VI) deklagen in NaCl oplossingen is significant. Drogen bij een hoge temperatuur (210°C) maakt chromaatlagen hard, maar reduceert aan de andere kant het “zichzelf herstellende” effect van het oplosbare Cr(VI). De reductie onder invloed van temperatuur van Cr(VI), zoals waargenomen met FTIR en XPS is waarschijnlijk verantwoordelijk voor de afname van de hoeveelheid Cr(VI) in de laag. De droogtemperatuur van met chromaat behandeld gegalvaniseerd staal ligt bij voorkeur tussen de 60 en 110°C.

De corrosie-eigenschappen van Cr(VI) en Cr(III) deklagen zijn vergeleken in de hoofdstukken 7 en 8. Als het zinken monster is behandeld met een Cr(VI) of een Cr(III)-A oplossing, is de Voltapotentiaal in het met Cr(VI) en Cr(III)-A behandelde gebied negatiever dan in het onbehandelde zink gebied. Open circuit potentiaal metingen laten ook negatieve potentialen zien van de Cr(VI) en Cr(III)-A deklagen ten opzichte van onbehandeld zink. Dit geeft aan dat zowel de Cr(VI) als de Cr(III)-A deklagen de kathodische reactie kunnen remmen. De polarisatie- en impedantiemetingen laten zien dat zowel de Cr(VI) als de Cr(III)-A deklagen de corrosiesnelheid van zink kunnen verlagen. De Cr(III)-B deklaag is dikker dan de Cr(III)-A deklaag en heeft een hogere corrosieweerstand dan de Cr(III)-A deklaag. De

remming van de corrosie op zink door een Cr(VI) deklaag is echter effectiever dan die door Cr(III) deklagen, omdat de op Cr(III) gebaseerde deklagen slechts als barriërelagen fungeren en de Cr(VI) deklagen de zinkoppervlakken op twee manieren beschermen, namelijk als barriërelaag en als passiverende remmer: het “zichzelf herstellende” effect. Deklagen gebaseerd op Cr(III) behandelingen zijn geschikt als de zichzelf beschermende eigenschappen minder belangrijk zijn, bijvoorbeeld als de voornaamste functie van de behandeling is de adhesie van polymeren deklagen te verbeteren. Voor sommige toepassingen kan het noodzakelijk zijn twee of meerdere behandelingen te geven en te vertrouwen op hun synergetische effecten.

Publications

Scientific papers

X. Zhang, C. van den Bos, W.G. Sloof, H. Terryn, A. Hovestad and J.H.W. de Wit, "Investigation of Cr(III)-based conversion coatings on electro-galvanized steel", *Surface Engineering*, 20 (2004) 244-250.

X. Zhang, S. Böhm, A.J. Bosch, E.P.M. van Westing and J.H.W. de Wit, "Influence of drying temperature on the corrosion performance of chromate coatings on galvanized steel", *Materials and Corrosion*, 55 (2004) 501- 510.

X. Zhang, C. van den Bos, W.G. Sloof, H. Terryn, A. Hovestad and J.H.W. de Wit, "Effect of drying temperature on chromate conversion coatings on zinc", *J. Corros. Sci. and Engineering*, Vol. 6, Paper 57, 2003 (ISSN 1466-8858).

X. Zhang, W.G. Sloof, A. Hovestad, E.P.M. van Westing, H. Terryn and J.H.W. de Wit, "Characterization of chromate conversion coatings on zinc using XPS and SKPFM", *Surf. Coat. Technol.*, in press.

X. Zhang, C. van den Bos, W.G. Sloof, H. Terryn, A. Hovestad and J.H.W. de Wit, "Comparison of the morphology and corrosion performance of Cr(VI) and Cr(III)-based conversion coatings on zinc", *Surf. Coat. Technol.*, in press.

X. Zhang, S. Lo Russo, S. Zandolin, A. Miotello, E. Cattaruzza, P. L. Bonora and L. Benedetti, "The Pitting Behavior of Al-3103 Implanted with Molybdenum", *Corros. Sci.* 43 (2001) 85-97.

X. Zhang, S. Lo Russo, A. Miotello, L. Guzman, E. Cattaruzza, P. L. Bonora and L. Benedetti, "The corrosion behavior of Zn coating on Al-3103 alloy", *Surf. Coat. Technol.*, 141 (2001) 187-193.

G. Battaglin, E. Cattaruzza, F. Gonella, G. Mattei, P. Mazzoldi, C. Sada, and X. Zhang, "Formation of Metal-Alloy Nanoclusters in Silica by Ion Implantation and Annealing in Selected Atmosphere", *Nucl. Instr. And Meth. in Phys. Research B* 166-167 (2000) 857-863.

X.L. Zhang, J.C. Jin, J.M. Li, Z. Xie, P.D. Wang, G.B. Liu, and B. Long, "Stress Corrosion Studies of Ion Implanted Austenitic Steel", *J. Materials Sci.* 34 (1999) 2159-2162.

C. van den Bos, H.C. Schnitger, X. Zhang, A. Hovestad, H. Terryn, J.H.W. de Wit, Influence of alloying elements on the corrosion resistance of rolled zinc sheet, submitted to Corrosion Science.

Presentations, poster presentations and proceedings

X. Zhang, C. van den Bos, W.G. Sloof, H. Terryn, A. Hovestad and J.H.W. de Wit, "Investigation of Cr(III)-based conversion coatings on electro-galvanized steel",

Eurocorr 2003, Budapest, Hungary, 28th Sept. – 2nd Oct. 2003, paper No. 182, Oral presentation.

X. Zhang, C. van den Bos, W.G. Sloof, H. Terryn, A. Hovestad and J.H.W. de Wit, “Effect of drying temperature on chromate conversion coatings on zinc”, *International Symposium “Corrosion Science in the 21st Century”*, Manchester, UK, 6th – 11th July 2003, paper No. C133, Oral presentation.

X. Zhang, C. van den Bos, H. Terryn, A. Hovestad and J.H.W. de Wit, “Investigation of Cr(VI)- and Cr(III)-based conversion coatings on zinc”, *Electrochemical Methods in Corrosion Research: 8th International Symposium*, Nieuwpoort, Belgium, 4th – 9th May 2003, paper No. O-74, Oral presentation.

X. Zhang, T. Bos, A. Hovestad, E.P.M. van Westing and J.H.W. de Wit, “Electrochemical behavior of chromate and phosphate conversion coatings on zinc”, *201st Electrochemical Society Meeting*, Philadelphia, USA, 12th – 17th May 2002, Abstract No. 333, Poster.

X. Zhang, W.G. Sloof, A. Hovestad, E.P.M. van Westing and J.H.W. de Wit, “XPS studies on chromate conversion coatings on zinc”, in Proc. of *15th International Corrosion Congress*, Granada, Spain, 23rd – 27th Sept. 2002, paper No. 307, Oral presentation.

S. Böhm, X. Zhang, A.J. Bosch, E.P.M. van Westing and J.H.W. de Wit, “Zinc patina formation and dissolution in aqueous bicarbonate/carbonate solutions using electrochemical techniques”, *Eurocorr 2001*, Riva del Garda, Italy, 30th Sept. – 4th Oct. 2001, Poster.

X. Zhang, S. Böhm, A.J. Bosch, E.P.M. van Westing and J.H.W. de Wit, “Investigation of the surface structure and corrosion of chromated galvanized steel”, in Proc. of *Eurocorr 2001*, Riva del Garda, Italy, 30th Sept. – 4th Oct. 2001, paper No. 193, Oral presentation.

X. Zhang, A. Bosch, E.P.M. van Westing and J.H.W. de Wit, “Localized corrosion of chromate conversion coatings on galvanized steel”, *2nd International Workshop on Scanning Electrochemical Microscopy*, Southampton, UK, 29th June – 2nd July 2001, Poster.

C. van den Bos, X. Zhang, A. Hovestad, H. Terryn, J.H.W. de Wit, “EIS study of the corrosion behaviour of anodically coated zinc”, 6th International Symposium on Electrochemical Impedance Spectroscopy (EIS 2004), Cocoa Beach, Florida, USA, 16-21 May 2004. Poster.

C. van den Bos, X. Zhang, A. Hovestad, H. Terryn, J.H.W. de Wit, “Influence of alloying elements on the corrosion resistance of rolled zinc sheet”, 45th Corrosion Science Symposium, Sheffield, United Kingdom, 6-8 September 2004. Oral presentation by C. van den Bos.

Acknowledgements

This thesis would have been impossible but for the kind help, support and love of many people. I would like to take this opportunity to express my gratitude to all of them.

First of all, I am grateful to Prof. Hans de Wit. Hans, thank you very much for giving me a lot of motivation and freedom to do my research. Each time when I had a discussion with you I learned a lot not only about science but also about Dutch culture, and I improved my English as well. I am also grateful to Prof. Herman Terryn from Vrije Universiteit Brussel. Herman, your appointment at the NIMR and your critical scientific insight made my research more valuable and clearer. Many thanks are also due to Sake, Peter and other members in your group for helping me to use spectroscopic ellipsometry and to do AES measurements in Brussel. I have also benefited from discussion with them. I would like to thank Prof. Koen Janssens and Kristof Proost from University of Antwerp for the XANES measurements, though the results are not included in the thesis.

I am particularly grateful to Prof. Pier Luigi Bonora at Trento University. Without his recommendation I may not have come to Delft to complete this work. His trust and encouragement always stimulate me to achieve more. I am also grateful to Prof. Paolo Mazzoldi and Prof. Sergio Lo Russo for their support during my research at Padova University in Italy.

I would like to thank Erik van Westing, Albert Bosch and Siva Böhm for their kind help when I started this research work. Erik, I thank you very much for being always ready to help me and for teaching me how to interpret impedance results. Get well soon. Siva, you always have good ideas. I appreciate your friendly help.

Wim Sloof, I thank you very much for your guidance in surface analysis. Chapters 4, 6 and 8 of this thesis included your contribution. I thank Kees Kwakernaak and Han

Kiersch for training and helping me to use SEM. I also thank Niek van der Pers for teaching me how to use XRD technique.

Arjan Hovestad and Machteld van der Meulen from TNO have contributed a lot to my research on zinc deposition and conversion coatings on zinc. Thank you very much. Arjan, you helped me to understand the electrochemical reactions occurring in electro-galvanizing and conversion coating processes. I always learn new things from you when I do experiments or have a discussion with you in the TNO laboratory. Machteld, you are always available to prepare new solutions and willing to help me to prepare samples. Chapter 9 in this thesis includes your contributions.

Bart Norbart, thank you for your friendly help. You found a room for me when I had just come to Delft. You can always solve problems that anyone asks you in the corrosion group. Gerrit Bakker, thank you for the financial management.

I would like to sincerely thank Chris van den Bos. You are so kind that you always pay attention to listen to me and answer my questions whenever I appear in front of you. You read my drafts scrutinizingly and correct them carefully.

I would like to thank Paola Campestrini, Francesco Andreatta, Jeroen van den Brand. Paola and Francesco, from you I learned how to use the AFM. You are also reminding me to practise my poor Italian. Jeroen, you helped me to make the FTIR measurements which are included in the thesis. You are also a magic IT expert. You solved many problems in my computer (after your departure Wouter took this job) that saved me a lot of time.

I would also like to thank Jose and Premendra, for sharing the big sunshiny office in this group with me; thank Wouter for writing down the minutes in each BC meeting or project meeting; thank Laetitia for helping me to do SVET measurements; thank Frederik for translating the summary and propositions into Dutch. I thank my other colleagues, Peter Overkamp, Peter Beentjes, Mae, Saskia, Jaco, Zeeshan, Natalya, Hetian, Tjitte, Kas, Siu Fai, Hong Lu, Martin, Barry, Brian, Berend, for the pleasant collaboration over the past few years and making my PhD research a very nice period.

This project is organized by SenterNovem. Barbara Breimer has done a lot of work in organizing the meeting of the Steering Committee (IOP Funaz/Telmab) twice a year. From the meeting I got a lot of valuable ideas and comments that were helpful for the research. NedZink, Corus and Enthone have supplied us some materials and chemicals. I would like to take this chance to thank Marc Mertens from Enthone-OMI for the helpful discussion about the Cr(III) conversion coating. I thank Tom Bos, Raghid Hamze and Carlos Caicedo Martinez, for their help in the SKP measurements. I thank Ramón Escobar Galindo for the positron measurements. I am also grateful to Bart Koene and Gabriele Ferrari for helpful discussion during project meetings. All the members of the IOP steering committee are sincerely acknowledged.

Now I would like to thank Prof. Lihua Zhao, Prof. Jiucheng Jin and Prof. Jianming Li for the guidance of my graduate study at Hunan University in China. I thank many chinese friends in Delft. Your friendship makes me feel at home. I would like to thank Xiali Wang for teaching me to play Taiji; thank Xiaoding Xu, Yiqing Cui, Bo Song, Chuanjun Liu, Zhou Yu, Xiaonan Li, Jun Tian, Yan Wang, Yang Hua, Zheng Zeng for sharing the good times in playing volleyball. Luoxing Li, Yuxing Li, JianXing Yuan, Lianjie Zhu, Rong Wang, Jianghua Chen, Shangping Chen, Lie Zhao, Jie Zhou, Guiming Song, Shunli Shang, Mengyue Wu, Bing Zhang, Bing Hu, Bo Zhou, Yutao Pei, Xiaoguang Sun, et al., thank you very much. I am also grateful to many friends I met in Italy and in the Netherlands. My gratitude is for all of you.

Last but never the least, I would like to thank my father Jiusheng Zhang and my mother Zhangjiao Mao, because without their love and care I could not be what I am now. I would like to heartily thank my wife Yuping Peng for her love and patience during my study. You are truly a perfect friend. I would thank my parents-in-law, Rongqiu Peng and Biyu Liu (she has already left us) for their love and helping to take care of my daughter before my family came to the Netherlands. I thank my daughter Liwen for bringing me a lot of joy. I also thank my sisters, Qiumei, Aiqun, Ailan, Xiaoqi, and their families for their love.



Curriculum Vitae

The author of this PhD thesis was born on 15 January 1964 in Hunan, China. He received his M.Sc. degree at Hunan University in China in 1990. His Master thesis is “A Behavior Study on Stress Corrosion Cracking Resistance of Generator Retaining Ring Steel by Ion Implantation”. He worked as a lecturer in physics at Central South University in China from 1990 to 1997. He then worked as a visiting researcher at the National Institute of Material Physics (INFM) at the University of Padova in Italy until 2000. Since August 2000, he has been employed by Delft University of Technology as a PhD researcher supervised by Prof. dr. J.H.W. de Wit and Prof. dr. ir. H. Terryn in the Corrosion Technology and Electrochemistry research group at the department of Materials Science and Technology. During his PhD study, he took a course in “Technical Writing in English” in Delft University of Technology in 2001 and a course in “Impedance Spectroscopy” in the Electrochemical Society in Philadelphia in 2002. His PhD work deals with the formation and degradation of chromium based conversion coatings on zinc and galvanized steel. This research was carried out in collaboration with NIMR and TNO. This book is the result of this research work.